MEASURING LOW DIMENSIONAL SCHOTTKY BARRIERS OF RARE EARTH SILICIDE - SILICON INTERFACES

Andrew James Vick

Thesis submitted for the degree of DOCTOR OF PHILOSOPHY

University of York
Department of Physics

November 2011

Abstract

The focus of this study is the measurement of low dimensional Schottky barrier heights of metal silicide-silicon interfaces and the challenges of current-voltage (I/V) curve interpretation. Engineering the Schottky barrier to exploit the spin and charge of an electron and manipulate it through silicon requires careful control of the interface structure between the metal and the silicon substrate. In doing this the advantages of both magnetic materials and semiconductors can be combined in spintronics.

Current-voltage characteristics have been taken using contact probe techniques, and from these the Schottky barrier properties have been extracted using standard Schottky barrier models. Several ways of extracting the Schottky barrier height have been explored concluding with the development of a new fitting program which utilises the whole data set and includes additional factors such as image force lowering and an oxide tunnel barrier. Nickel silicide thin films on silicon(111) have been used as a test system to develop the analysis for I/V measurements.

Rare earth silicides were grown on silicon(111) and silicon(001) forming ordered interface structures, which have been extensively studied in the group at York. The rare earth silicides on silicon have attractive low Schottky barrier heights (0.4 eV). Erbium silicide islands of the order of 500 nm diameter were grown on silicon (111) and erbium silicide nanowires were grown on silicon (001) 4° offcut. Using an Omicron Nanoprobe contacts were made with the nano structures enabling the measurement of the electrical properties of the silicide and the Schottky barrier between the silicide island and the substrate.

A new growth study of manganese on erbium silicide on silicon(111) is presented as a possible way to engineer the Schottky barrier between a ferromagnetic material and silicon. Preliminary results of the I/V measurement are presented and the additional complication of an oxide layer highlighted. If engineering the Schottky barrier in this way is successful, the realisation of spintronics maybe a step closer.

Contents

Abstract 2

Acknowledgements 16

Declaration 17

1 Introduction 19

1.1 Spintronics and Schottky Barriers 21

1.2 Material Selection 24

1.2.1 Silicon Substrates 24

1.2.2 $NiSi_2$: A Test Material 26

1.2.3 Rare Earth Silicides 26

1.2.4 Manganese 27

1.3 Chapter Summary 27

2 Theory of Schottky Barriers 29

2.1 Schottky Barriers Historical 29

2.2 The Formation of a Schottky Barrier 30

2.2.1 The Schottky-Mott limit 31

2.2.2 Modelling Theories 32
2.3 Transport Mechanisms Across Schottky Barriers 33
2.3.1 Drift and Diffusion 34
2.3.2 Thermionic Emission 36
2.3.3 Schottky Effect - Image Force Lowering 37
2.3.4 Tunnelling Through the Schottky Barrier 42
2.3.5 Recombination Effects 47
2.4 Deviation from a Single Schottky Barrier 48
2.4.1 Inhomogeneous Schottky Barriers 49
2.4.2 Series Resistance 49
2.4.3 Shunt Resistance 49
2.4.4 Double Barrier 50
2.4.5 Vacuum Tunnel Barriers 50
2.5 Schottky Barriers of Nanostructures 51
2.6 Engineering the Barrier 52
2.7 Simulating Schottky Barrier I/V Curves 53
2.7.1 MATLAB Simulation Script 54
2.7.2 Parameter Trends 56
2.7.3 Low Voltage and Low Schottky Barrier Height 59

3 Experimental Techniques 61

3.1 Surface Characterisation 61
3.1.1 Electron Diffraction 62

3.1.2 Scanning Tunnelling Microscopy 64

3.1.3 Scanning Electron Microscope 65

3.2 Sample Growth 65

3.2.1 Ultra-High Vacuum 66

3.2.2 Substrate and Sample Heating 66

3.2.3 Film Thickness Monitoring 68

3.2.4 Types of Deposition Sources 68

3.3 Vacuum Systems 69

3.3.1 The Molecular Beam Epitaxy System 69

3.3.2 The York Omicron STM System 71

3.4 Interface Characterisation 73

3.4.1 Omicron Nanoprobe 73

3.4.2 I/V Measurements 75

3.4.3 Transmission Electron Microscope 78

4 Application of Analysis Methods to Nickel Silicide-Silicon Interfaces 79

4.1 The $NiSi_2$-Si Interface 79

4.1.1 Background 80

4.1.2 Interface Structure of $NiSi_2$-Si(111) 81

4.1.3 Growth 82

4.1.4 I/V Measurement 85

4.2 Graphical Fitting Methods 87

4.2.1 Logarithmic I/V Plots 87

4.2.2 Shunt Resistance 89

4.2.3 Series Resistance - Norde Plots 91

4.2.4 Series Resistance - Small Signal Evaluation 94

4.2.5 Comparing Graphical Fitting Methods 98

4.2.6 $NiSi_2$ Sample Comparison 99

4.2.7 Fitting Tolerance of the Small Signal Evaluation 100

4.3 Fitting Routine for Back-to-Back Barriers 103

4.3.1 MATLAB 103

4.3.2 IV.x - I/V Fitting Program 104

4.4 IV.x Analysis of $NiSi_2$ 107

4.4.1 Analysis of Full Applied Voltage Range 108

4.4.2 Analysis of Forward Bias Range 113

4.4.3 Inhomogeneous A-type $NiSi_2$ 116

4.5 Conclusion 116

5 Rare Earth Silicide on Si(111) 119

5.1 Rare Earth Silicides 119

5.1.1 Structure 120

5.1.2 Growth 122

5.2 I/V Measurements 127

5.2.1 I/V from Masked Dots 127

5.2.2 I/V of the Self Assembled Island-Silicon Interface 129

5.2.3 I/V Between Self Assembled Islands 131

5.2.4 Van der Pauw 133

5.3 Temperature variation of I/V Measurements 134

5.3.1 Temperature I/V Through the Self Assembled Islands 134

5.3.2 Temperature I/V Between Self Assembled Islands 138

5.4 Conclusion 139

6 Rare Earth Silicide Nanowires on Si(001) 141

6.1 Rare Earth Silicide Nanowires 141

6.1.1 Growth 142

6.2 I/V Measurements 144

6.2.1 Tunnelling 144

6.2.2 I/V of the Nanowire-Silicon Interface 145

6.2.3 I/V Along the Nanowire 148

6.3 Conclusion 150

7 Metals on 2D Rare Earth Silicide 152

7.1 Manganese on Ultra Thin Rare Earth Silicide 152

7.2 Growth 153

7.2.1 Ultra Thin RE Silicide 154

7.2.2 Manganese 156

7.3 I/V Measurements 159

7.3.1 Mn Islands 160

7.3.2 Mn Film 161

7.4 Conclusion 163

8 Conclusions and Further Work 165

8.1 General Conclusions 165

8.1.1 Development of IV.x, the Fitting Routine 165

8.1.2 Nickel Silicide on Si(111) 166

8.1.3 Erbium Silicide on Si(111) 166

8.1.4 Erbium Silicide Nanowires on Si(001) 167

8.1.5 Manganese on Ultra Thin Erbium Silicide on Si(111) 167

8.2 Further Work 168

8.2.1 Instrument and Technique Development 168

8.2.2 Note After Viva - Peripheral Tunnelling 169

8.2.3 Future Experiments 169

Appendices 171

A Transport to LENNF 171

B The Vick's " Chocolate Stuff " 172

List of Abbreviations 173

List of Symbols 175

Bibliography 178

List of Tables

4.1 Comparison of fitting methods to a 250μm diameter B-type $NiSi_2$ dot . . 99

4.2 Comparison of $NiSi_2$ samples analysed using Plot A. 100

4.3 Comparison of $NiSi_2$ samples analysed using IV.x over the full applied voltage range 110

4.4 Comparison of $NiSi_2$ samples analysed using IV.x over the forward applied voltage range. 115

5.1 Average fit parameters for $ErSi_2$ islands on Si(111). 131

5.2 $ErSi_2$ island temperature variation I/V curves analysed using IV.x. 136

List of Figures

1.1 Schematic representaion of a GMR device using a simple resistor network model. 22

1.2 Ideal Schottky barriers on n-type and p-type semiconductors. 23

1.3 STM scans of the surface reconstructions of Si(111)7 $\times$ 7 and Si(001) 4° offcut 2×1. 25

2.1 Band diagrams showing the formation of a Schottky barrier between a metal and an n-type semiconductor. 31

2.2 Transport mechanisms across an n-type semiconductor Schottky barrier. . 34

2.3 Quasi-Fermi levels in a forward biased Schottky barrier for thermionic emission and diffusion theory. 35

2.4 Image force lowering of a Schottky barrier. 38

2.5 Image force lowering of a Schottky barrier under different biasing conditions. 41

2.6 Field and thermionic field emission under forward bias. 44

2.7 Field and thermionic field emission under reverse bias. 46

2.8 Schematic of a possible back-to-back Schottky barrier circuit. 48

2.9 Bratkovsky's δ-doped barrier. 53

2.10 Graph of the voltage drops for individual Schottky barrier diodes in a back-to-back circuit. 55

2.11 Graph of Schottky Barrier Height ϕ_b variations. 56

2.12 Graphs varying the area of the contact, ideality factor and shunt resistance. 57

2.13 Graphs varying the series resistance, temperature and doping concentration. 58

2.14 Graph of the voltage dropped across a low Schottky barrier height. 60

3.1 LEED Schematic and example 7×7 Si(111) LEED image. 62

3.2 Omicron sample plates, DC heating and e-beam. 67

3.3 Image and schematic of the MBE system. 70

3.4 Image of the mask used on the sample plate in the MBE system and an example sample grown with the mask 71

3.5 Image and schematic of the STM system. 72

3.6 Nanoprobe images. 74

3.7 Image of vacuum suitcase. 75

3.8 Two probe contact geometries for I/V collection. 76

3.9 Two and four probe contact geometry for measuring resistance 77

3.10 Van der Pauw contact measurements. 78

4.1 A-type and B-type $NiSi_2$ structure. 81

4.2 $NiSi_2$ thickness. 82

4.3 LEED and RHEED images of the Si(111)7×7 reconstruction. 83

4.4 LEED and RHEED 1×1 Si(111). 84

4.5 SEM image of 250 μm diameter B-type $NiSi_2$ dot. 86

4.6 Raw I/V data taken from a 250 μm B-type $NiSi_2$ dot. 86

4.7 Forward bias $\ln(I)$ against V data taken from a 250 μm B-type $NiSi_2$ dot. 88

4.8 $\ln(I/(1-\exp(-qV/kT)))$ against V data taken from a 250 μm B-type $NiSi_2$ dot. 89

4.9 Shunt resistance circuit and raw and correct I/V for shunt resistance. . . . 90

4.10 Series resistance circuit schematic. 91

4.11 Plot of $F(V)$ against V. 92

4.12 Plot of $F(V)$ against V for low applied voltage. 93

4.13 Plot of conductance against V. 95

4.14 Plot A, Conductance/Current against Conductance. 96

4.15 Plot B, Differential Resistance against Inverse Current. 97

4.16 Plot C Current/Conductance against Current. 98

4.17 Plot of series resistance against ideality factor for different fits of a 500 μm diameter A-type $NiSi_2$ dot. 102

4.18 Plot of Schottky barrier height against ideality factor for different fits of a 500 μm diameter A-type $NiSi_2$ dot. 102

4.19 Flowchart of IV.x fitting program. 105

4.20 Plot of the turning point in the current when the image force lowering tends to the Schottky barrier height. 107

4.21 Plot of experimental data and program fit of I/V data from the 250 μm diameter B-type $NiSi_2$ dot. 109

4.22 Plot of A-type and B-type 1000 μm dot showing the curve of the turning point. 111

4.23 Plot of the reverse bias of the 250 μm diameter B-type $NiSi_2$ and the difference between experimental data and the fitted model. 113

4.24 Plot of the I/V turning point of the 250 μm diameter B-type $NiSi_2$ dot experimental data fitted using the full voltage range and just the forward bias. 114

5.1 2D RE silicide on silicon cross section structure. 120

5.2 3D RE silicide on silicon cross section structure. 121

5.3 3D $ErSi_2$ $(\sqrt{3} \times \sqrt{3})R30°$ RHEED pattern 123

5.4 Nanoprobe SEM image of the 3D $ErSi_2$ grown through the mask in the MBE 123

5.5 LEED taken at 50 eV of a) Si(111)7×7; b) One ML Er on Si(111) annealed at 650 °C, hint of 3D $ErSi_2$ $(\sqrt{3} \times \sqrt{3})R30°$ spot; c) Hydrogen terminated 1 ML of Er on Si(111),1×1 pattern. 124

5.6 STM scans of 3D $ErSi_2$ islands grown and annealed at 650 °C. 125

5.7 STM scans of 3D $ErSi_2$ islands grown at different temperatures. 126

5.8 Nanoprobe SEM image of the sample previously imaged in the STM in figure 5.7 of the 3D $ErSi_2$ islands. 126

5.9 I/V curve of a 500 μm diameter $ErSi_2$ dot with a separate fit to the up and down sweeps of the applied bias. 128

5.10 I/V curve from $ErSi_2$ island on Si(111), measured from one tip on the island to the back contact of the sample plate. 130

5.11 I/V curve from $ErSi_2$ island on Si(111) with hydrogen passivation, measured from one tip on the island to the back contact of the sample plate. The IV.x fit is plotted alongside. 130

5.12 I/V curve from two neighbouring islands connected only by the substrate. A curve generated from the oxide tunnel expression is plotted alongside. . 132

5.13 SEM image of the four tips during a Van der Pauw measurement. 133

5.14 The ohmic curves measured from the probe tips during a Van der Pauw measurement and linear fits to the data. 134

5.15 SEM image of the $ErSi_2$ island with the tip positioned to measure the I/V at different temperatures. 135

5.16 I/V curves taken at different sample temperatures between an $ErSi_2$ island and the back contact. 137

5.17 SEM image of two $ErSi_2$ islands with the tips positioned to measure the I/V between the islands. 138

5.18 I/V curves taken at different sample temperatures between two $ErSi_2$ islands. 139

6.1 STM scans of $ErSi_2$ nanowires on Si(001) 4° offcut. 143

6.2 SEM image of $ErSi_2$ nanowires with side branches, a possible future sample for I/V measurement. 144

6.3 Oxidised NW sample I/V curve with tunnel plot. 145

6.4 Nanoprobe SEM image of two tips contacted onto a NW ready to take an I/V measurement 146

6.5 I/V curve from the $ErSi_2$ NW shown in figure 6.4, measured from a single tip and the silicon back contact. 147

6.6 I/V curve from an alternative $ErSi_2$ NW measured from a single tip and the silicon back contact. 147

6.7 SEM image of two tips contacted to the NW to measure the I/V along the NW. 148

6.8 Example I/V taken along the NW with a linear fit to obtain the resistance. 149

6.9 SEM image of the remains of four tips and the NW after a catastrophic discharge. 150

7.1 2D Er Silicide on Si(111) LEED and STM images. 154

7.2 2D Er silicide grown at 550 °C LEED and STM images 155

7.3 2 ML of Mn Islands on 2D RE Silicide STM image and LEED image. . . 157

7.4 Nanoprobe SEM image of Mn Islands 158

7.5 10 ML Mn on 2D RE Silicide STM image and LEED image 159

7.6 Nanoprope STM image and I/V curve of oxidised Mn islands. 160

7.7 I/V data from a 10 ML Mn film on 2D Er Silicide on silicon. IV.x fit with optimised oxide tunnel barrier thickness of 1.5 nm. 162

7.8 I/V data from a 10 ML Mn film on 2D Er Silicide on silicon taken with an alternative tip to figure 7.7 but using the same oxide tunnel parameter. . . 162

A.1 Mini Adventure. 171

Acknowledgements

If it's not broken, don't fix it, because it will be broken soon, so then you can mend it. I have enjoyed my four-and-a-bit years of Ph.D, honestly. Thanks to all the people who have made it possible and much more entertaining than it might otherwise have been.

I would like to thank my two supervisors, Steve Tear and Sarah Thompson for all the guidance, advice, support and generally putting up with me. Phil Hasnip has been a legend when it comes to all things programming. Alex Walton at LENNF has humoured most of my crazy ideas about I/V curves; we never did get the hang of guessing the shape correctly.

The Physics department at York is a truly special place, being the most friendly and supportive environment I could ever have wanted. I'm extremely grateful to all the staff and students, especially the Nanophysics group, old and new. It would never have been possible with out Dave, Rich and Neil; thanks for all the support.

To get me out the office and into another dark hole, the caving club and its mad bunch, thanks for dragging me to horrid places, however much I complain, I like caving really! I would like to mention a special place in Wales, the Talyllyn Railway, where I have been able to escape to a place of steam, mud, concrete and fantastic friends.

I finally need to thank my family for their support, and my friends far and wide, especially Cat for always being there, feeding me, and understanding how rubbish I am (and buying me a campervan).

Declaration

The work presented in this thesis is based on my own research except where it is explicitly stated in the text. No part of this work has previously been submitted for any other qualification.

Most of the I/V curves presented within this thesis were obtained at the LENNF facility, with the kind assistance of Dr. Alex Walton. The fitting program was developed in collaboration with Dr. Phil Hasnip.

Andrew J Vick

For Mum

Frances E Vick

(1950-2008)

Chapter 1

Introduction

The world we live in is driven by technology and the ever growing need to automate systems to make our lives easier and processes faster. The underlying technology that makes this possible is semiconductor electronics which has been the corner stone of information technology for many decades. Silicon chips can be found in almost every household appliance from the computer to the toaster.

Present semiconductor electronics uses the manipulation and storage of electric charge, however with the need to improve performance of integrated circuits the use of existing ideas are reaching their limits. Over the last 40 years, the number of transistors per unit area which can be etched onto a silicon chip, which governs the processing power of a computer, has doubled every 18 months, a trend known as Moore's law. 2011 has seen the launch of 22 nm etched transistors which are rapidly approaching the limit of miniaturisation and packing density which these transistors can handle before the heat they generate cannot be dissipated fast enough and unwanted quantum-mechanical effects hinder their function. Nano structures and self assembled nano objects could hold vital properties for the next step. Self assembled nano structures such as nanowires, because of their ordered, defect free crystal structure, can handle high current densities. One further possible avenue to increase the processing power of the chip is spin electronics (spintronics), which uses the magnetic moment or spin of the electron and also its charge. Several reviews on the subject provide an insight into the possibilities and challenges that are to be faced in the development of spintronics.[1–5]

The late 1980's saw the discovery of enhanced magnetoresistance and the development of the spin valve, the first electronic device to exploit the intrinsic spin of the electron. The

magnetoresistance effect stems from the spin dependent transport of the injected current in the ferromagnetic layers of the device. These layers can be engineered to manipulate and detect the spin-polarised current, producing a new family of electronic devices that utilise the spin as well as the charge of the carriers. By combining these metal devices with semiconductor materials, a new group of magnetically controlled devices are hoped to be: non-volatile, versatile, fast, energy efficient and potentially capable of data storage and processing simultaneously: a movement towards a full computer on a chip. Some possible applications of this technology include magnetic memories and data storage (such as magnetic random access memory), spin transistors and even quantum computers.

To integrate these devices with semiconductors there are three main issues to be addressed. These are: successful injection of a spin polarised current, the storage or transport of a spin polarised current and finally the detection of the spin polarised current. Spin transport has been observed in GaAs with spin orientation conserved for up to 4 μm and spin polarisation has been detected by various methods in GaAs.[6] However, the polarised spin injection into a semiconductor remains very challenging. Magnetic semiconductors have shown 90% spin injection efficiency, but only at low temperatures, making them an unrealistic option. This leaves a ferromagnetic layer on a semiconductor as the most promising option with some success shown on GaAs and InAs providing a few percent spin injection efficiencies.

Silicon has been less studied due to the problems of probing the spin injection and spin diffusion length using optical methods which have been successful on GaAs due to the direct band gap. However, silicon is the most important semiconductor in the electronics industry, in a market worth over $300 billion in 2010. The technology of electrical contact fabrication to silicon is very important for the fabrication of microcircuits and has been studied to gain fundamental understanding of metal-semiconductor interfaces. From calculations, silicon has shown long spin diffusion lengths of 30 to 70 μm which could be required for spintronics.[7] Silicon therefore should be an obvious choice of semiconductor for spintronics with the promising steps reported by Jansen.[8,9]

Injecting a spin polarised current into a semiconductor requires an interface between a ferromagnetic material and the semiconductor, which needs to have a spin dependent resistance at the interface of the two materials. This is one of the great challenges for spintronics,[1,2] which could be overcome by using a potential barrier to the polarised carrier flow such as a tunnel barrier or a Schottky barrier. The Schottky barrier occurs naturally

between most metal-semiconductor junctions and needs to be engineered to provide the required properties for spin injection and accumulation. Theoretical studies by Bratkovsky and Osipov have shown engineering the barrier using a δ-doped layer at the interface can produce the right interface properties to achieve approaching 100% spin injection.[10,11]

In engineering the metal-semiconductor interface we need to produce a well ordered structure at the contact as defects can affect the barrier properties. York University's surface physics group have good experience at handling silicon and knowledge of growing well characterised low dimensional rare earth silicide structures.[12–16] This thesis expands the structure work already done within the group on rare earth silicide materials into the new area of Schottky barrier measurements. Initially, low dimensional structures which are routinely grown in the group are studied before moving on to a new study of manganese on erbium silicide on silicon. The challenges of measuring current-voltage (I/V) curves from low dimensional structures and extracting the Schottky barrier height is addressed by way of a new fitting program. This has shown many problems with the existing analysis methods and the problems which need overcoming to extract a reliable Schottky barrier height from an I/V curve. This work provides an insight into the importance of the interface as well as the difficulties of engineering the interface and measuring the interface properties, opening many avenues of research for the future.

1.1 Spintronics and Schottky Barriers

The 2007 Nobel Prize in Physics was awarded to Professors Peter Grünberg and Albert Fert for the discovery of giant magnetoresistance (GMR) in 1988. This opened the way to new ideas of using the spin of an electron, not only its charge. GMR is now very technologically advanced and its contribution to the hard disk drive industry is invaluable: a review is provided by Thompson.[17] A GMR device uses the spin of the electron and a magnetic field which alters the magnetisation of the layers in the device, thus changing the resistance. The layers filter the electron current depending on its spin polarisation because of spin dependent scattering. Figure 1.1 shows a schematic of the simplest GMR device, a bilayer construction, which can be modelled using a resistor chain.

From this idea we can build more complex devices with the common idea of spin manipulation using a ferromagnet to select a spin orientation. Existing electronic devices use a small quantity of charge to differentiate between the logic 0 and 1, for example a

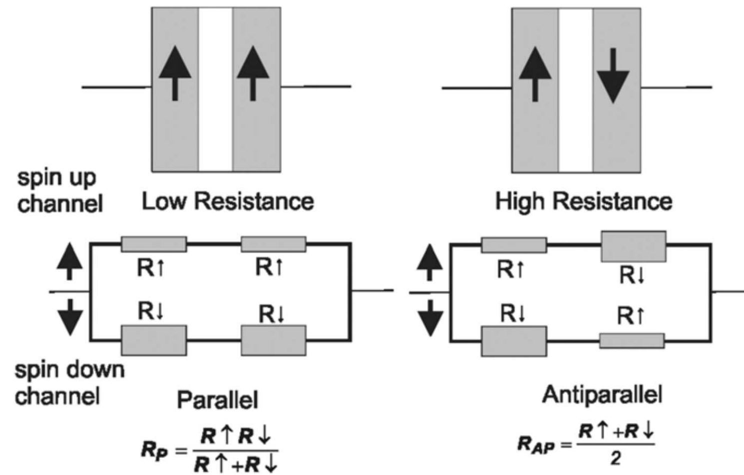

Figure 1.1: Schematic representaion of a GMR device using a simple resistor network model. In the left picture, the spin-up channel is the majority spin channel in both the ferromagnetic layers, experiencing a low resistance (R↑) throughout the structure. In the right-hand picture, the spin-up channel is the majority spin channel (R↑) in the first magnetic layer but the minority-spin channel (R↓) in the second magnetic layer and *vice versa* for the spin-down channel. Neither spin channel is of low resistance throughout the structure and the overall resistance state of the structure is high. GMR occurs when the relative orientation of the magnetic layers is switched, usually by the application of a magnetic field. Image and caption from Thompson.[17]

field effect transistor. This device switches between on and off by the presence of charge encountering high and low resistance. The use of charge as a logic carrier is limited by the speed the device can switch as it is restricted by thermal equilibrium. If the information is encoded in the electron spin orientation rather than the pool of charge the device could switch much faster. Spin-up and spin-down can coexist for up to 10 ns without a barrier between them. It is also easy to switch the logic by applying a magnetic field but all of this needs to take place as part of a semiconductor device.

A spin-polarised current can be generated from a ferromagnetic metal as it will contain excess carriers aligned to the direction of magnetisation of the material. Passing this polarised current into the semiconductor is hard because the resistance of the metal is very much lower than that of the semiconductor; this is known as the conductivity mismatch. The current through the junction will have no spin preference as the semiconductor will dominate the contact and as it is non-magnetic it does not matter what the concentration of accumulated spin is. To overcome this conductivity mismatch a way must be found to inject spin into a semiconductor and accumulate it there. This accumulated spin current will drive the injection and transport of a spin-polarised current through the semiconductor. The injection and extraction is dominated by two factors: the ferromagnetic material

used to spin polarise the current and more importantly the interface between this and the semiconductor.

To overcome the conductivity mismatch problem we need to engineer a spin dependent barrier at the interface between the semiconductor and the ferromagnet. This could take several different forms, for example a tunnel barrier made of a thin insulating layer like an oxide or alternatively in the form of a Schottky barrier. Whatever barrier is engineered it provides a spin dependent resistance similar to that of the silicon, enabling current to be injected into the semiconductor driven by the spin accumulation in the semiconductor. Without this barrier the high electron density and short diffusion length within the ferromagnet would reach a thermal equilibrium across the interface leaving no accumulation within the semiconductor and failed injection.

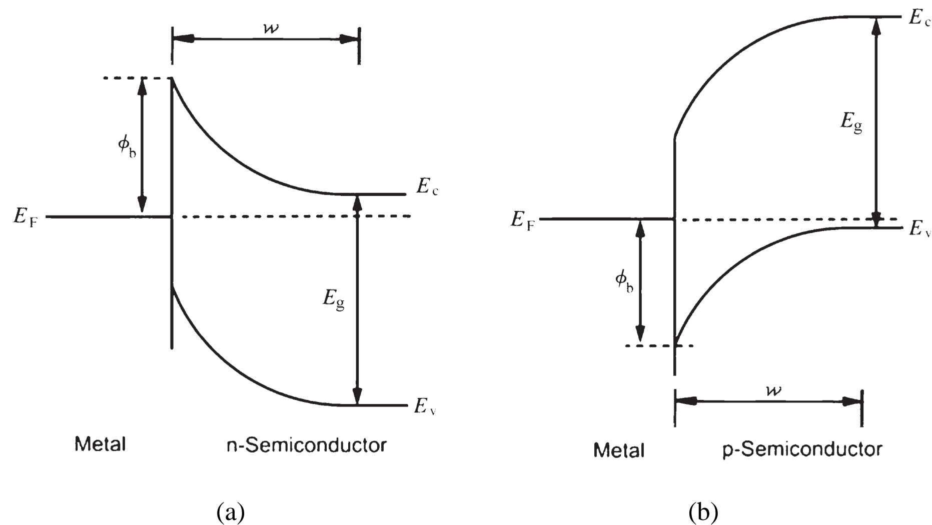

Figure 1.2: Ideal Schottky barriers formed between a metal and a) n-type semiconductor; b) p-type semiconductor.

When a semiconductor and a metal come into contact the junction depends on the materials which are combined. Occasionally an ohmic contact is produced which is not useful for spin injection, however normally a Schottky barrier is formed. Figure 1.2 shows the Schottky barrier formed when a metal comes into contact with either an n-type or p-type doped semiconductor. A Schottky barrier is a rectifying barrier for electrical conduction across the interface, the properties of which need to be engineered for efficient spin injection. When a metal is brought into contact with n-type silicon, the barrier height (ϕ_b) is the difference between the conduction band minimum (E_c) and the Fermi level (E_F). For a p-type it is the difference between the valence band maximum (E_v) and the Fermi level (E_F). The Fermi level of the semiconductor and metal equalise, bending the conduction

and valence bands creating the depletion region (w) where there are no free carriers. E_g is the band gap energy.

The effective height of the Schottky barrier (ϕ_e) and the width of the depletion region (w) can be tuned by altering the amount of doping within the semiconductor bands, moving the Fermi level or changing the Fermi level pinning. The engineering of the Schottky barrier to give the required barrier properties relies on the structure at the interface, even more so if the doping concentration in the very top layer of the semiconductor is to be altered. This is the δ-doped layer, which will theoretically achieve 100% spin injection by reducing the width of the Schottky barrier depletion region and increase the tunnelling transparency.[10,11]

1.2 Material Selection

The materials studied in this thesis have been chosen based on their potential use within spintronics development and the knowledge already in existence within the surface physics group at York. The substrate used throughout is silicon because of its wide use within the commercial industry; any new technology using silicon may have more impact and be more accepted by electronic component manufacturers. When some metals, for example: Fe, Mn, Er or Ho, are deposited onto silicon at an elevated temperature a well ordered metal-silicon compound is formed: a silicide. Silicides have found a wide application in silicon integrated circuits as contacts and gate electrodes. Thin film silicides are produced by the deposition of metal on to a silicon substrate where heat treatment provides the energy for a reaction to take place, ensuring an intimate contact is created. Due to the reaction of metal with silicon to form the silicide any contact formed sits well below the original silicon surface ensuring an intimate contact. This consuming of silicon removes any starting surface reconstructions that may have been present.

1.2.1 Silicon Substrates

Silicon is easy to cut and can be cleaned by heat treatment, producing atomically flat terraces. The diamond structure of silicon is a face centred cubic lattice with a lattice constant of 5.429 Å. The samples grown for this thesis have used both Si(111) and Si(001) 4° offcut substrates both with a light n-type doping giving a resistivity of $\sim 5 - 10$ Ωcm

When the Si(111) surface is heated above 600 °C the 7×7 surface reconstruction is formed. The structure of the 7×7 reconstruction was not fully understood until the real space imaging of the Scanning Tunnelling Microscope (STM) allowed the corner holes of the dimer-adatom-stacking fault model to be identified. Figure 1.3a shows an STM image of the 7×7 reconstructed silicon surface. The reconstruction is several layers of atoms deep, driven by the energy stabilisation of eliminating dangling bonds. The first layer of the reconstruction is the formation of dimer rows pairing up the dangling bonds. The dimer rows form a corner hole and a stacking fault which both cost energy but this is reduced by the addition of adatoms which reduce the number of dangling bonds by three. Duke provides an excellent introduction to surface reconstructions including the various other Si reconstructions.[18]

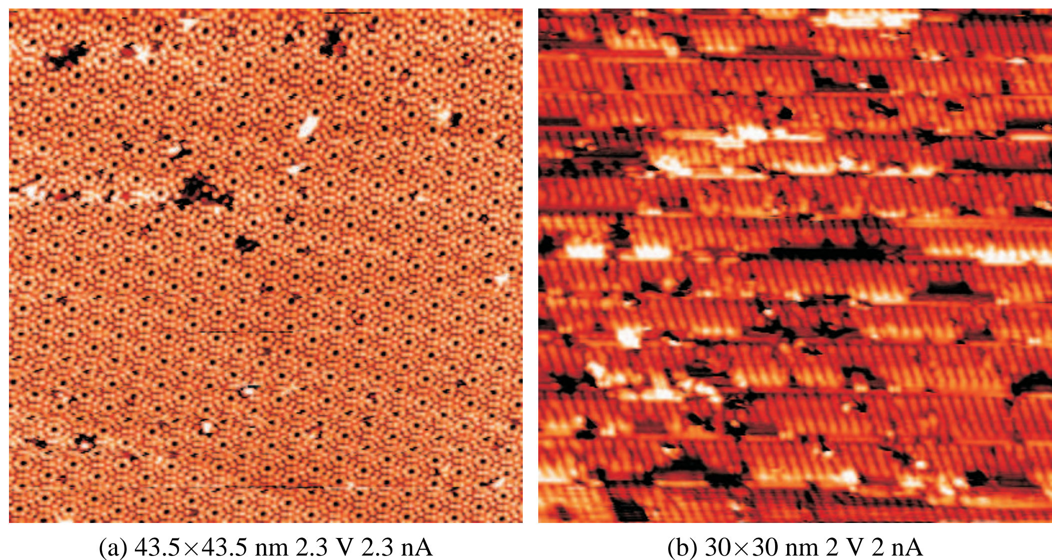

(a) 43.5×43.5 nm 2.3 V 2.3 nA (b) 30×30 nm 2 V 2 nA

Figure 1.3: STM scans of the surface reconstructions of a) Si(111)7×7; b) Si(001)4° offcut 2×1.

The Si(001) surface, once cleaned, gives the 2×1 reconstruction of buckled dimer rows. Each terrace on the surface, steps down half a unit cell and the dimer row orientation changes by 90° on each terrace. This alternating to give perpendicular dimer rows allows nanowire growth in both directions. To remove the alternating dimer rows and encourage parallel nanowire growth, 4° offcut silicon can be used. The angle of the offcut provides the right energy constraints for the terrace steps to drop down a double step height each time, leaving all the terrace dimer rows orientated in the same direction. Figure 1.3b shows an STM image of the Si(001) 4° offcut surface. Using the 4° offcut Si(001) substrate gives terraces which are only a few nanometres wide.

1.2.2 $NiSi_2$: A Test Material

$NiSi_2$ has a similar lattice structure to Si and a very close lattice match producing some of the most defect free silicide silicon interfaces. The fluorite (CaF_2) structure of $NiSi_2$ has a lattice constant of 5.406 Å and the Si lattice constant is 5.429 Å,[19] giving a lattice mismatch between $NiSi_2$ and silicon of ∼0.4%. This small lattice mismatch of Si(111) to $NiSi_2$ promotes epitaxially grown $NiSi_2$ on Si(111) to be atomically abrupt. The Schottky Barrier Height (SBH) of $NiSi_2$ on Si(111) shows a remarkable dependence on the interface structure with a difference of 0.14 eV between two alternative interface terminations.[20] Because epitaxially grown $NiSi_2$ produces very well ordered interfaces which show a well characterised SBH, this material acted as a good test material for our method and analysis techniques.

1.2.3 Rare Earth Silicides

This thesis investigates measuring the Schottky barrier height of low dimensional rare earth silicide structures and the use of a 2D rare earth layer to tune the Schottky barrier. Rare earth metals have low workfunctions of ∼3 eV which produce some of the lowest Schottky barrier heights on n-type silicon of ∼0.4 eV. There has already been some success, by Min, at tuning tunnel barriers using rare earth gadolinium.[21] The structure of the interface is very important to the resulting Schottky barrier hence the use of low dimensional rare earth structures, with which the York group has much experience.[12–16]

The rare earth silicide system was first studied by Baglin,[22] and a more recent review is given by Netzer.[23] Rare earth (RE) silicides have a great technological potential due to their contact on silicon producing low Schottky barrier heights on n-type silicon of ∼0.4 eV, compared with transition metals which have a Schottky barrier in the region of 0.7 eV. The hexagonal rare earth silicide structure has a very good lattice match to the Si(111) surface, meaning almost defect free structures can be achieved. The rare earth silicides have been shown to be metallic with a high thermal and electrical conductivity (2.9×10^4 $(\Omega \mathrm{cm})^{-1}$).[24] For this thesis, erbium (Er) has been used as the rare earth element which is a typical trivalent RE.

1.2.4 Manganese

Manganese is antiferromagnetic in the bulk but is predicted to have a large magnetic moment in low dimensional structures such as thin films and islands grown on noble metals.[25,26] If this magnetic moment is present in low dimensional structures it may have a role to play in spintronics as the spin polarising material. Manganese has been grown on top of 2D rare earth silicides and the evidence indicates the manganese does not react with the silicon. The 2D rare earth structure may also tune the Schottky barrier at the interface allowing possible spin injection and accumulation in the silicon.

1.3 Chapter Summary

This thesis is divided into seven further chapters. Chapter 2 covers the theory of Schottky barriers and the transport mechanisms which may be taking place for electrons to overcome the Schottky barrier. These expressions have been used to simulate current-voltage curves providing an example of how the relevant variables such as Schottky barrier height affect the curve. Chapter 3 introduces the experimental techniques used within the work, providing a brief overview of the equipment and techniques used to grow and take the data. Chapter 4 is concerned with the extraction of a reliable value for the Schottky barrier height from an I/V curve. Several graphical methods are explored incorporating transport mechanisms which take the Schottky barrier away from the ideal thermionic case. A computer fitting routine has been developed to improve the analysis speed and accuracy, using the whole data set and incorporating several transport mechanisms. To test the various analysis methods, $NiSi_2$ interfaces with Si(111) have been grown and analysed. This highlighted several problems with the fitting routine and the assumptions made in the theory enabling improvements to be made. Chapter 5 investigates erbium silicide islands grown on Si(111). These islands have been contacted using an Omicron Nanoprobe measuring the Schottky barrier and using the Van der Pauw method to measure the sheet resistance. Temperature-dependent measurements have been taken from the same $ErSi_2$ island. This chapter starts to address the challenges of measuring nanoscale objects and the process of fitting to an I/V curve from such an object. The I/V curves obtained required additional theory for an oxide tunnel barrier to be included for the program to obtain a satisfactory fit. Following on from this, Chapter 6 studies rare earth silicide nanowires grown on vicinal 4° offcut Si(001). These nanoscale structures have been probed to measure the Schottky

barrier into the silicon and also the conduction along the wires. This chapter highlights the technical difficulty of contacting to such small structures and then measuring the I/V curve, finding the limit of the Nanoprobe. The sensitivity of the samples to oxidation has been shown and possible effects from nanoscale properties of the nanowires encountered, for which the fitting program cannot provide an accurate fit at the time of writing. Chapter 7 explores the use of 2D rare earth silicide as a buffer layer and δ-doped layer to manganese islands and films. The original growth of an erbium buffer layer to manganese is presented and preliminary I/V curves are shown. Finally Chapter 8 provides concluding remarks on the work presented and future directions for the investigation.

Chapter 2

Theory of Schottky Barriers

2.1 Schottky Barriers Historical

One hundred and forty years ago, Braun discovered the asymmetry in electrical conduction through copper contacted to iron sulphide, a phenomena which has underpinned a lot of technology to this day.[27] Early experiments on radio detectors used a variety of point contacts on metal sulphides with little understanding of the rectifying properties being utilised. One of the most famous point contacts was a tungsten tip in contact with a crystal, normally of lead sulphide, this was more commonly known as the 'cat's-whisker' rectifier which played an important role in the boom in broadcasting in the 1920's.

In 1931, Schottky, Störmer and Waibel made the first attempts to explain the rectifying properties of metal-semiconductor contacts by showing a potential drop occurs almost entirely at the contact when a current is applied. This is fundamental to all these contacts as it implies there is a potential barrier at the interface between the metal and the semiconductor; this would later become known as the Schottky barrier (SB). Attempts to explain the rectifying behaviour using quantum mechanical tunnelling of electrons provided unsatisfactory solutions as the easy current flow was in the wrong direction. Schottky and Mott independently pointed out in 1938 that the direction of rectification could be explained by the normal processes of drift and diffusion.[27]

During the Second World War, the use of point contacts on silicon and germanium for microwave radar significantly increased our understanding of rectifying contacts. Most importantly the development in 1942 of Bethe's thermionic-emission theory explained the emission of electrons into a metal. Since 1945 semiconductor physics has driven the devel-

opment with the invention of the first point-contact transistor in 1947 by Bardeen, Brattain and Shockley. The move to thin film deposition in the 1950's with the development of high vacuum systems provided more stable and reproducible contacts.[27] From that point onwards the activity was, and is still, driven by semiconductor technology with the aim to make devices smaller and faster and to obtain a full understanding of the current transport through metal-semiconductor interfaces. There is a need for the theory to evolve to include new developments due to small size effects, spin effects and the introduction of new materials to achieve these advances.

2.2 The Formation of a Schottky Barrier

The contact between a metal and a semiconductor can take on many different electrical properties from strongly rectifying to ohmic, each having its own applications. The barrier formed depends on the two materials being bought into contact, specifically the doping of the semiconductor and the workfunction of the metal (ϕ_m) and semiconductor (ϕ_s). How the two materials contact each other is also very important to the outcome of the barrier, for example whether the interface structure is abrupt and defect free or if there is mixing between the two materials.

The workfuction is the minimum amount of energy needed to excite an electron from the Fermi level to the vacuum level outside the surface of the material. For a semiconductor, the workfunction is a statistical average of energies necessary to remove an electron from the valence and conduction bands as strictly there are no energy levels available in the band gap. The energy band diagrams shown in figure 2.1 are for an n-type semiconductor with a work function less than that of the metal. This type of interface contact is the most important as the majority of contacts are of this form; also this thesis concentrates on n-type silicon interfaces. Silicon has a workfunction of ~ 4.8 eV for a lightly doped n-type substrate, which changes with doping concentration because the Fermi level is altered by the amount and type (n or p) of doping.[28] This workfunction can be compared with nickel, for example, which has a value of ~ 5.15 eV.[29] However this value for the work function is for polycrystalline nickel and it is found that the work function depends on the crystal surface plane. The work function of nickel is now, for each surface plane, as follows: Ni(110)=5.04 eV, Ni(100)=5.22 eV and Ni(111)=5.35 eV hence the surface plane used and the resulting structure at the interface will have an effect on the barrier.[30]

2.2.1 The Schottky-Mott limit

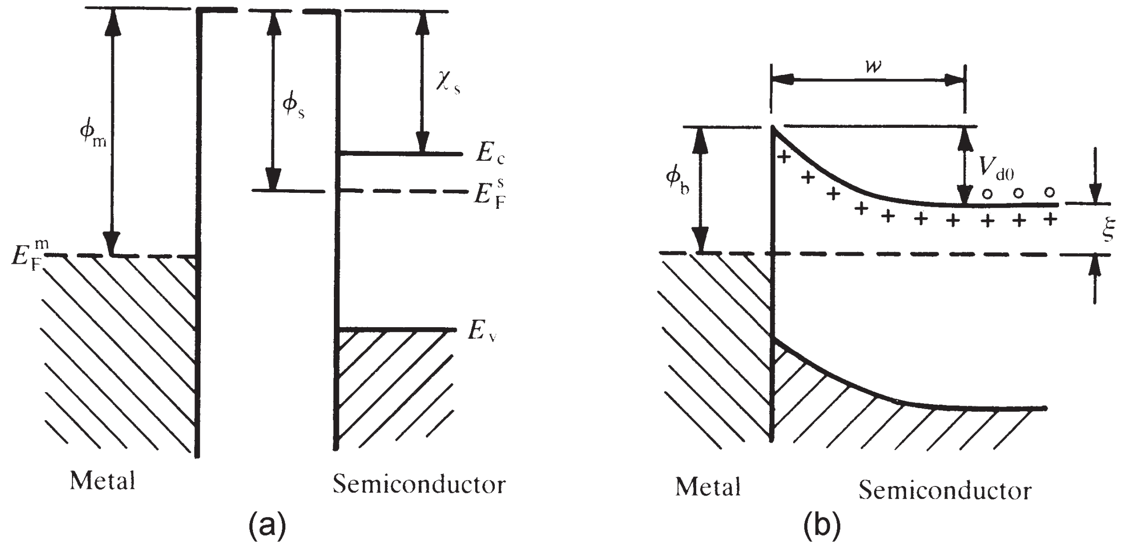

Figure 2.1: Band diagrams showing the formation of a Schottky barrier between a metal and an n-type semiconductor a) neutral and isolated; b) electrically connected in perfect contact. Figure adapted from Rhoderick.[27]

The neutral and isolated materials in figure 2.1a can first be connected electrically by a wire allowing electrons to flow from the conduction band of the semiconductor to the metal forcing the Fermi levels to equalise as seen in figure 2.1b. This leaves a depletion region of width w in the semiconductor as the uncompensated positive donor ions are fixed in the lattice and there are no free carriers, other than thermally generated ones to compensate them. This produces a potential gradient across the depletion region as the bands bend down giving rise to the Schottky barrier ϕ_b. This results in an electric field across the gap from right to left caused by electrons on the metal surface and the uncompensated positive donor ions left in the depletion region of the semiconductor.

When the surfaces are bought into perfect contact (figure 2.1b) the height of the remaining barrier can be measured relative to the Fermi level. Walter Schottky and Sir Neville Mott proposed the barrier height between a metal and a semiconductor could be given by

$$\phi_b = \phi_m - \chi_s. \tag{2.1}$$

This expression is the Schottky-Mott limit, where the workfuction of the metal and the electron affinity χ_s of the semiconductor give the barrier height.[27] The electron affinity of

a semiconductor is taken as the energy difference between the bottom of the conduction band to the vacuum level outside the surface. Equation (2.1) is a first-order approximation for the Schottky barrier height (SBH) and is rarely supported by experimental results. In practice the contact is never as perfect as in figure 2.1b, more commonly there is a thin oxide insulating layer which electrons have to tunnel through so the SBH is not as strongly dependent on ϕ_m. The Schottky-Mott limit also assumes that the surface dipole contributions to ϕ_m and χ_s do not change when the metal and semiconductor come into contact and that there are no localised states on the surface of the semiconductor. Most importantly the Schottky-Mott limit assumes the contact between the metal and the semiconductor is an abrupt juntion, with no intermixing of the two materials and no defects at the interface.

Forward and Reverse Bias

When a voltage is applied to a SB the equilibrium of the barrier changes. When a positive bias is applied to the metal the Fermi level of the semiconductor (E_F^s) is lifted relative to the metal Fermi level (E_F^m) reducing the barrier height (ϕ_b) and the depletion width (w) narrows. This is forward bias where, as the applied voltage is increased, the current flow increases. When a negative voltage is applied to the metal the Fermi level of the semiconductor drops increasing the band bending and therefore the binding energy of the electrons increases. The increase in binding energy means the barrier is higher and the electron requires more energy to overcome it, this is reverse bias where less current flows. The forward and reverse bias give the I/V curve its characteristic rectifying behaviour.

2.2.2 Modelling Theories

These initial ideas from Schottky and Mott were further developed by Bardeen who took into account the effect of interface states.[27] This was then modified by Cowley and Sze who considered the effect of a dipole layer.[31] Since the mid 1980's much effort has been put into finding a theoretical model for a Schottky barrier which does not assume that the SBH is insensitive to the interface structure. Several experiments showed that there was a dramatic dependence of the SBH on the orientation/structure of a single crystal metal-semiconductor interface. The most striking of these was the work done on the interface termination of silicon with nickel silicide by Tung.[20] Further experiments with the spatially resolved technique of Ballistic Electron Emission Microscopy (BEEM) highlighted

the problems with inhomogeneity in polycrystalline SBH and why many experimental results did not fit with theory.[32–34] BEEM uses a Scanning Tunnelling Microscope (STM) to inject electrons with energies considerably higher than the metal Fermi level, some of which will traverse the SB into the semiconductor without being scattered in the metal. This allows the metal-semiconductor interface to be mapped out from the BEEM current. If Ballistic Electron Emission Spectroscopy (BEES) is carried out at a point by sweeping the energies of the ballistic electrons, the onset of emission over the barrier at that point can be found and therefore the local SBH can be determined. This technique shows the change of SBH across the contact area, meaning many previous results are an average of several barrier heights. Small changes in the structure at the interface on the nanoscale affect the SBH, leading to an inhomogeneous contact.

The current theoretical models, in an attempt to correctly predict the SBH for an interface, take account of the metal and semiconductor surface states and the interface dipole due to the chemical bonding between the two materials. A comprehensive review of Schottky barrier concepts by Tung critically covers some of these theoretical models including the metal induced gap states model and the bond-polarization theory model.[35] The remainder of this chapter details the theory of current transport systems across the barrier, which can be used to fit experimental I/V curves to explain the rectifying behaviour and extract the SBH with some confidence.

2.3 Transport Mechanisms Across Schottky Barriers

Once a Schottky barrier has formed there are four main transport mechanisms for an electron to overcome the potential barrier. For an n-type semiconductor in forward bias, figure 2.2 shows the transport mechanisms for an electron to overcome the Schottky barrier. These are:

(a) emission of electrons from the semiconductor to the metal over the barrier;

(b) quantum mechanical tunnelling through the barrier;

(c) recombination in the space charge region;

(d) recombination in the neutral region (‘hole injection’).

Shottky barriers which are dominated by thermionic emission (mechanism (a)) are said to be nearly ideal and any of the other processes in figure 2.2 move away from this ideal behaviour.

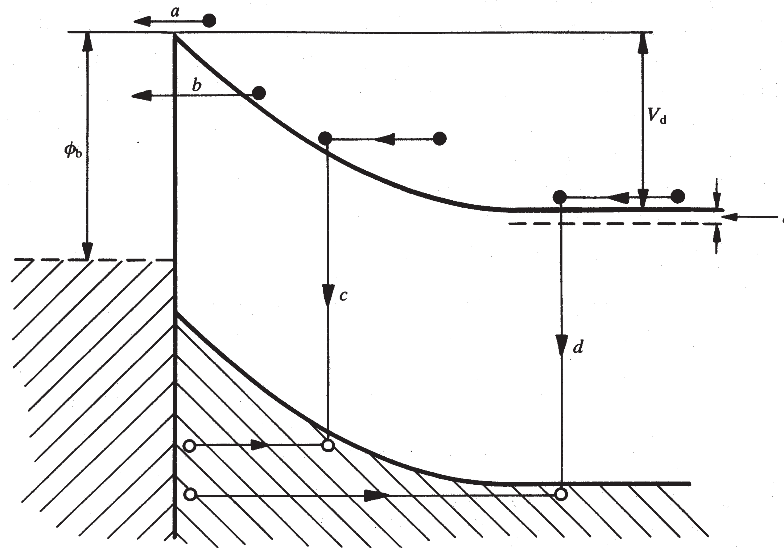

Figure 2.2: Transport mechanisms across a Schottky barrier on n-type semiconductor in forward bias, a) emission over the barrier, b) tunnelling through the barrier, c) recombination in the space charge region, d) recombination in the neutral region. Image from Rhoderick.[27]

2.3.1 Drift and Diffusion

An electron has to travel through the semiconductor depletion region before being emitted over the barrier into the metal. This migration is controlled by the drift and diffusion theory which was first proposed independently by Wagner, Schottky and Spenke.[27] Schottky and Mott initially believed that drift and diffusion in the electric field of the barrier was the rate limiting mechanism for current flow over the barrier. However the thermionic emission theory developed by Bethe was shown to be the dominant process in most cases.

Diffusion theory assumes that the concentration of electrons in the semiconductor at the interface is not altered by the applied bias. This results in a gradient in the quasi-Fermi level as it drops to meet the metal Fermi level when a voltage, V is applied. The quasi-Fermi level is a hypothetical energy level which describes electron behaviour under non equilibrium conditions, as shown in figure 2.3. In the thermionic emission case the electrons are emitted into the metal with energies above the metal Fermi level, therefore the quasi-Fermi level is flat in the semiconductor and through collisions in the metal the emitted electrons lose energy to come into equilibrium with the metal Fermi level. As the gradient of the quasi-Fermi level is the driving force for electrons the main obstacle to current flow in thermionic emission is the process of emission of electrons into the metal whereas in diffusion theory the main obstacle is drift and diffusion in the depletion region.

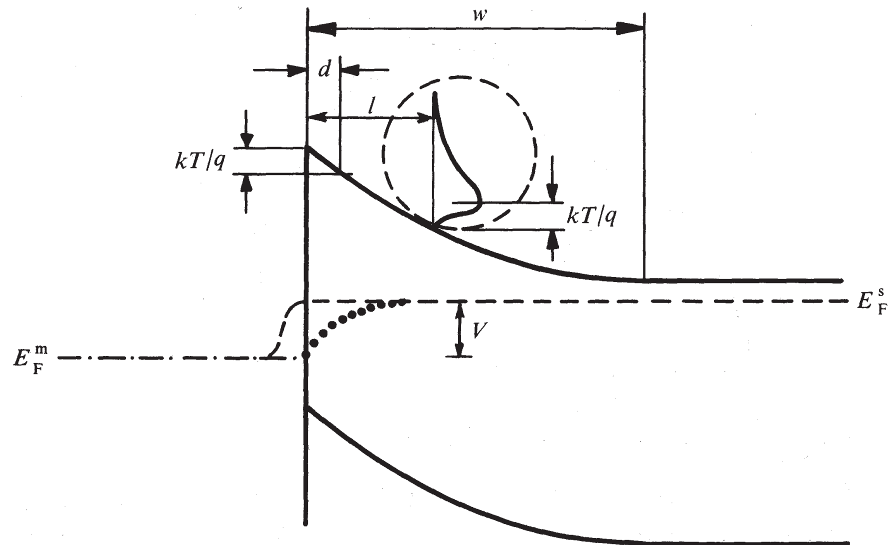

Figure 2.3: Quasi-Fermi levels in a forward biased SB; **......** for diffusion theory and **- - - - -** for thermionic emission. The broken circle shows the Boltzmann distribution of energies which have made their last collision at a distance l from the interface. Image from Rhoderick.[27]

For thermionic emission to dominate, the quantity of electrons arriving at the barrier through drift and diffusion must exceed the number emitted over the barrier by thermionic emission. On average the electrons which pass over the barrier have made their last collision at a distance l from the barrier, making l the mean free path of the electron. The electrons will have a Boltzmann distribution of energies after these final collisions, with the average energy of the distribution above the bottom of the conduction band by $\frac{1}{2}kT$ due to motion normal to the interface. As shown in figure 2.3 only the electrons in the energy distribution with more kinetic energy than the amount the conduction band rises in the remaining distance l will pass into the metal, the rest will be reflected back into the semiconductor. Therefore if $l \gg d$, where d is the distance the conduction band falls an amount kT/q from the maximum of the barrier, only a small fraction of electrons can pass into the metal meaning thermionic emission is the rate limiting factor. If $l \ll d$ then the majority of the electrons arriving at the barrier will be able to pass into the metal and diffusion is the rate limiting mechanism. Hence, thermionic emission assumes infinite mobility through the semiconductor, as it is taken that the mean free path of an electron in the semiconductor is longer than the distance the barrier falls through an amount kT/q, providing a condition which must be satisfied before drift and diffusion can be neglected.[27]

The true behaviour however is somewhere between the two extremes of thermionic

emission and diffusion as the processes are in series. Crowell and Sze have combined thermionic emission and diffusion theory,[31,36] however drift and diffusion mechanisms are still normally neglected at low frequencies.

2.3.2 Thermionic Emission

Thermionic emission is the rate limiting process of electron emission over the barrier when the temperature is high and a non-degenerate semiconductor is used. We must also assume this is a homogeneous SBH which is roughly defined as one who's SBH varies on a lateral length scale much longer than the depletion region width.

The thermionic emission of electrical carriers from a region in thermal equilibrium over an energy barrier ϕ_b in either direction is I_0, the saturation current,

$$I_0 = SA^*T^2 \exp\left(-\frac{q\phi_b}{kT}\right), \tag{2.2}$$

where S is the area of the contact, A^* is the Richardson constant, k is the Boltzmann constant, T is the absolute temperature and q the unit of charge. This current arises from thermally generated carriers in the depletion region and flows all the time in forward and reverse directions over the barrier, even when a bias is applied in one direction.

When a forward bias V is applied to a uniform SB the concentration of electrons on the semiconductor side of the interface is increased by a factor $\exp(qV/kT)$. This increase in electron concentration and the fact that the barrier is lowered by the applied bias means an extra current flows from the n-type semiconductor to a metal. Combining the saturation current, equation (2.2), with the current from the applied bias gives the current in the forward direction as

$$I_f = SA^*T^2 \exp\left(-\frac{q\phi_b - qV}{kT}\right). \tag{2.3}$$

Finally, the net current flow (I) is the difference between the forward and reverse directions,[35]

$$I = I_f - I_0 = SA^*T^2 \exp\left(-\frac{q\phi_b}{kT}\right)\left[\exp\left(\frac{qV}{kT}\right) - 1\right]. \tag{2.4}$$

Richardson Constant

A^* is the Richardson constant for thermionic emission in semiconductors. It has been modified from the Richardson constant for metal thermionic emission by the substitution of the free electron mass m for the semiconductor effective mass m^*, where h is Planck's constant,

$$A^* = 4\pi m^* q k^2/h^3. \tag{2.5}$$

This expression is correct if the semiconductor's conduction band has spherical constant-energy surfaces, this is not the case for silicon which is elliptical. The appropriate values can be calculated for silicon as m^*=2.05m for $\langle 100 \rangle$ directions and m^*=2.15m for $\langle 111 \rangle$ directions.[37]

A^* can be further modified to A^{**} taking into account the quantum mechanical reflection of electrons. These are electrons which have sufficient energy to overcome the barrier but are reflected back into the semiconductor without emission into the metal. Also, phonon scattering of electrons between the top of the barrier and the metal surface are taken into account. Both of these processes will return the electron to the semiconductor. A^{**} is not strictly a constant as it has a slight dependence on bias; however this is masked by the image force lowering. The value of A^{**} can be less than A^* by as much as 50%, however a change in A^{**} by a factor of two has an effect on the current comparable to a change in ϕ_b of less than kT/q as equation (2.4) is dominated by the exponential term. For a diode at room temperature (300 K) $kT/q \sim 0.025$ eV and a factor of two change in A^{**} shows as a change in the SBH of ~ 0.018 eV. All the analysis in this thesis has been done using the accepted average value of $A^{**} = 112 \times 10^4$ A m^{-2} K^{-2} calculated from all the crystal orientations in silicon by Andrews and Lepselter.[38]

2.3.3 Schottky Effect - Image Force Lowering

Thermionic emission theory predicts the current/voltage characteristics to be of the form of an ideal rectifier according to equation (2.4). However this assumes the barrier height to be independent of applied bias which, due to the electric field in the depletion region, is not the case. All interfaces, even perfect ones with no interfacial layer, have a reduced barrier by an amount $\Delta\phi_{bi}$ due to the image-force.

The image force is the attraction of an electron to the metal surface due to an electric

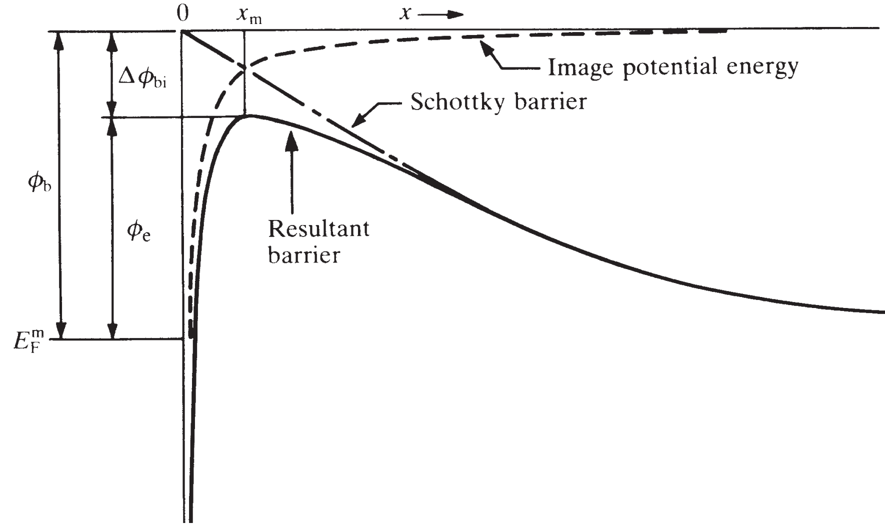

Figure 2.4: Image force lowering of a Schottky barrier. Image adapted from Rhoderick.[27]

field, which changes with applied bias. To calculate the electric field, which must be perpendicular to the surface, an assumption that a positive charge is located at the mirror image position in the metal is used. When an electron is at a distance x from the interface the attractive force, F is

$$F = \frac{-q^2}{16\pi\varepsilon_s x^2}, \tag{2.6}$$

where ε_s ($= \varepsilon_r\varepsilon_0$) is the permittivity of the semiconductor calculated from the permittivity of free space and the relative permittivity of silicon (taken as ε_r=11.68). The work done by the electron in moving from infinity to the point x is the integration of the force, equation (2.6), over this distance.[31] This gives the potential energy of the electron due to the image force at position x as shown in figure 2.4.

When an external field $\mathscr{E}$ is applied to the barrier, the total potential energy PE as a function of distance is given by

$$PE(x) = \frac{q^2}{16\pi\varepsilon_s x} + q\mathscr{E}. \tag{2.7}$$

From this the overall Schottky barrier lowering effect $\Delta\phi_{bi}$ at the maximum barrier height position x_m as seen in figure 2.4 can be given by the condition $\partial PE(x)/\partial x = 0$ as,[31]

$$x_m = \left(\frac{q}{16\pi\varepsilon_s\mathscr{E}}\right)^{1/2}; \qquad \Delta\phi_{bi} = \left(\frac{q\mathscr{E}}{4\pi\varepsilon_s}\right)^{1/2} = 2\mathscr{E}x_m. \tag{2.8}$$

The electric field in the barrier can be expressed in terms of the applied bias voltage and the doping level using the depletion approximation. This assumes the charge density

rises abruptly at the depletion region edge as the majority carrier concentration of the bulk substrate drops immediately to zero. The charge density then stays constant in the depletion region up to the barrier as the donor density N_d is constant. This means the electric field strength will rise linearly from the edge of the depletion region to the interface according to Gauss's theorem, so the field strength at the surface will be given by $\mathscr{E} = qN_d w/\varepsilon_s$, where w is the width of the depletion region.[27] This can be written as $\mathscr{E} = (2qN_d V_d/\varepsilon_s)^{1/2}$ if the depletion width is substituted by a term containing the diffusion potential V_d.

Instead of making the assumption that the electron density falls abruptly by allowing the majority carrier concentration to fall gently to zero by penetrating into the depletion region and considering the effect minority carriers have on the field close to the metal, a more accurate expression for the electric field can be found. The density of electron and holes at a distance x from the interface depends on their respective quasi-Fermi levels (see Section 2.3.1). Assuming a flat quasi-Fermi level for electrons, the electron density in the depletion region, n_e for a non-degenerate semiconductor can be given as,[27]

$$n_e = n_0 \exp\left(\frac{q\psi}{kT}\right), \tag{2.9}$$

where n_0 is the electron concentration in the bulk of the semiconductor (neutral region). ψ is the electrostatic potential in the semiconductor at a distance x from the interface. The assumption that the quasi-Fermi level is flat is a good one for thermionic emission but for diffusion theory in the region close to the metal it may not be. As the electron concentration in this region will however be negligible compared to the donor concentration N_d, no significant error results. The hole quasi-Fermi level is assumed to be flat through the depletion region, coinciding with the metal Fermi level giving the hole concentration as,[27]

$$p = p_s \exp\left(\frac{-q(V_d + \psi)}{kT}\right), \tag{2.10}$$

where p_s is the equilibrium hole density immediately adjacent to the interface. Combining the electron density, equation (2.9) and the hole density, equation (2.10) with the donor concentration the net charge density is given by,

$$\rho = q(N_d + p - n_e). \tag{2.11}$$

Using Poisson's equation, the charge density and the electrostatic potential can be related,

giving the electric field strength in the Schottky barrier as,[27]

$$\mathscr{E}^2 = \frac{2q}{\varepsilon_s}\left\{N_d\left(V_d - \frac{kT}{q}\right) + \frac{p_s kT}{q}\left[1 - \exp\left(\frac{-qV_d}{kT}\right)\right] + \frac{kTN_d}{q}\exp\left(\frac{-qV_d}{kT}\right)\right\}, \quad (2.12)$$

where it has been assumed that there has been complete ionisation of the donors, so for an n-type semiconductor n_0 can be assumed very close to N_d. It has also been assumed that N_d is constant throughout the depletion region.

If we assume that the barrier is not large enough to make the surface strongly p-type, this is more likely on semiconductors with small band gaps, the term involving p_s can be neglected. It is also regularly assumed that $qV_d \gg kT$ meaning the remaining exponential term is negligible. This results in an approximation for the field in the Schottky barrier of,

$$\mathscr{E}^2 = \frac{2qN_d}{\varepsilon_s}\left(V_d - \frac{kT}{q}\right). \quad (2.13)$$

The first term of this expression is identical to the term gained from the depletion approximation where the charge density is assumed to rise abruptly at the start of the depletion region. The second term is a correction to this harsh turn on, forming a transition region where the charge density rises gently. Because of this Debye tail, the depletion region does not have a precisely defined width as the conduction band asymptotically approaches the bulk value.[27]

Equation (2.13) for the electric field in the Schottky barrier can be substituted into equation (2.8) for $\Delta\phi_{bi}$, giving an expression for the barrier lowering due to the image force as,

$$\Delta\phi_{bi} = \left\{\frac{q^3 N_d}{8\pi^2 {\varepsilon_s}^3}\left(\phi_b - V - \xi - \frac{kT}{q}\right)\right\}^{1/4}. \quad (2.14)$$

The diffusion potential V_d has also been substituted for and is defined as $V_d = \phi_b - V - \xi$, the potential difference across the depletion region, where ξ is the energy difference between the Fermi level and the bottom of the conduction band in the semiconductor (as indicated in figure 2.2) and can be calculated from the donor concentration N_d and the effective density of states in the conduction band N_c

$$\xi = -\ln\left(\frac{N_d}{N_c}\right)\frac{kT}{q}; \qquad \text{where,} \;\; N_c = 2\left(\frac{2\pi m^* kT}{h^2}\right)^{3/2}. \quad (2.15)$$

The image force lowering effect would be exaggerated by heavier doping or a thicker interfacial layer as this would increase the field across the Schottky barrier. The effect

of image force lowering on the forward characteristic is considered to be negligible for Schottky barriers with $N_d < 10^{23}$ m^{-3}. Figure 2.5 shows how the energy bands change under different biasing conditions. Under forward bias ($V > 0$) the conduction band moves up and the depletion region narrows, as illustrated by w_1. The effective barrier height is slightly larger than at zero applied bias because the field in the Schottky barrier is reduced meaning the forward barrier lowering $\Delta\phi_F$ is also reduced. Under reverse bias ($V < 0$) the conduction band drops below the Fermi level of the metal, extending the depletion region width as shown by w_3. The effective barrier is lower because the electric field in the Schottky barrier is increased by the applied bias, so the barrier lowering $\Delta\phi_R$ is increased.

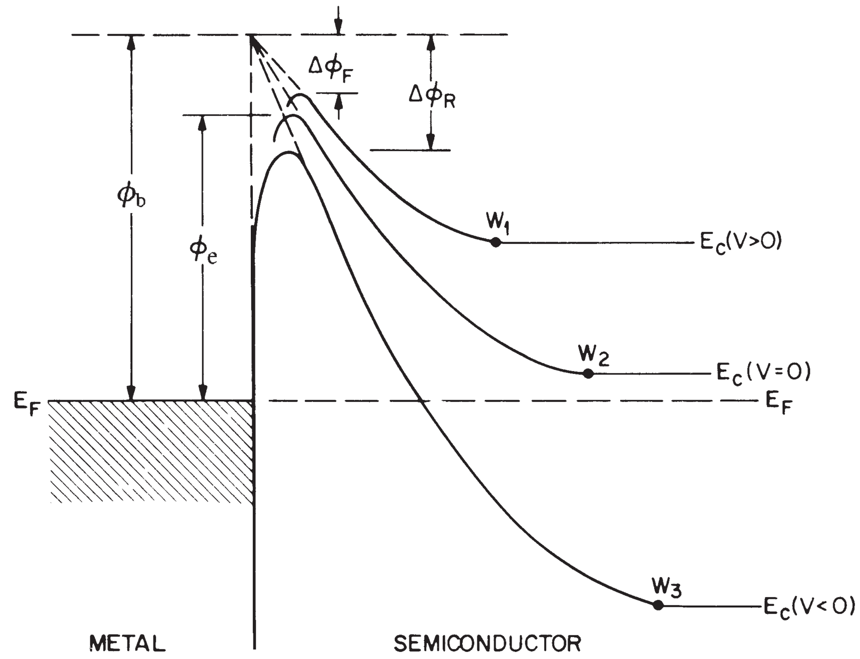

Figure 2.5: Image force lowering of a Schottky barrier under different biasing conditions. The barrier lowering under forward and reverse bias are $\Delta\phi_F$ and $\Delta\phi_R$, respectively. Image adapted from Sze.[31]

The effective barrier ϕ_e which the electrons have to surmount can be written as $\phi_e = \phi_b - \Delta\phi_{bi}$. If we assume the gradient of the effective barrier with voltage ($\partial\phi_e/\partial V = \beta$) is constant we can write

$$\phi_e(V) = \phi_{b0} - (\Delta\phi_{bi})_0 + \beta V, \tag{2.16}$$

where ϕ_{b0} and $(\Delta\phi_{bi})_0$ refer to the zero bias values. Substituting this for ϕ_b into the

thermionic equation (2.4) the net current now becomes

$$I = SA^{**}T^2 \exp\left(-\frac{q(\phi_{b0} - (\Delta\phi_{bi})_0 + \beta V)}{kT}\right)\left[\exp\left(\frac{qV}{kT}\right) - 1\right]. \tag{2.17}$$

Which, using $\beta = 1 - 1/n$ can be rewritten as,

$$I = SA^{**}T^2 \exp\left(-\frac{q\phi_e}{kT}\right)\exp\left(\frac{qV}{nkT}\right)\left[1 - \exp\left(-\frac{qV}{kT}\right)\right], \tag{2.18}$$

where n is the ideality factor.

Ideality Factor

n is the ideality factor which is a dimensionless quantity which parameterizes how the diode deviates from an ideal thermionic barrier. The deviation could result from the presence of image force lowering if its not accounted for by using ϕ_e, an interfacial layer, an inhomogeneous barrier height or other processes like tunnelling across the barrier. The ideality factor gives a good indication as to how close to thermionic emission the I/V curve is and if any new physics should be used to fit the data. Unfortunately n is not always straight forward as it can be a function of bias and often changes with temperature. To be confident the current across a barrier is determined by thermionic emission theory, a value of $n < 1.1$ is required. If it is greater than this then another transport mechanism is allowing electrons to pass over the SB.

2.3.4 Tunnelling Through the Schottky Barrier

Carriers with energies lower than the full barrier height can still overcome the barrier by quantum tunnelling through it. Tunnelling is more likely in heavily doped semiconductors as the depletion region will be narrower due to the more densely packed donors. Tunnelling also becomes more dominant at low temperatures and plays an important role in the reverse bias characteristics. In forward bias, when a positive voltage is applied, the Fermi level in the semiconductor is lifted and more electrons can flow over the barrier. The width of the depletion region is also narrowed, sometimes to a point where electrons can tunnel through the barrier; but at room temperature, on a non degenerate semiconductor, it does not narrow enough before the electrons have enough energy to overcome the barrier thermally. However, in reverse bias, according to the thermionic emission theory the only current flowing is I_0, equation (2.2) the saturation current. As the band bending

increases and the Fermi level in the semiconductor drops below the metal Fermi level, the electrons in the metal see the barrier narrowing due to the applied bias, enabling the possibility of tunnelling. Hence tunnelling is more often apparent in reverse bias as a departure from ideal thermionic emission behaviour.

The analysis in this thesis is concerned only with reverse bias tunnelling as it is expected to have a larger effect at low dimensions and as the measured current flow is in the region of nanoamps. Forward bias tunnelling has been assumed not to be present because we are using a lightly doped semiconductor at room temperature. It would be possible to extend the theory to include the forward tunnelling for low temperatures and high doping concentrations in the future. The following theory for tunnelling is included for completeness and background understanding, the information is gathered from a summary by Rhoderick,[27] further detail can be found in Padovani and Stratton's article.[39]

Forward Bias Tunnelling Characteristics

In degenerate semiconductors at low temperatures, the forward bias current can arise from tunnelling of electrons from the bottom of the semiconductor conduction band, with energies close to the semiconductor Fermi level, this process is known as Field Emission (FE). When the temperature is increased the move into the Thermionic Field Emission (TFE) regime is made. At higher temperatures, electrons are excited and tunnelling probability increases as these electrons see a narrower and lower barrier. However the density of excited electrons decreases rapidly with increasing thermal energy, so there is a maximum contribution from TFE electrons at an energy E_m above the bottom of the conduction band, as schematically shown in figure 2.6. A further increase in temperature would return to thermionic emission dominating, as electrons would have enough energy to surmount the barrier and any contribution from tunnelling would be negligible.

Quantum tunnelling is the phenomenon of an electron with less energy (ΔE) than the top of the barrier penetrating through it. The probability of finding an electron in a certain position from the barrier can be calculated using the Wentzel-Kramers-Brillouin (WKB) approximation. Applying this to the Schottky barrier with a diffusion potential V_d and assuming the top of the barrier is triangular, the probability is

$$P = \exp\left\{ -\frac{2}{3}\frac{(\Delta E)^{3/2}}{E_{00}V_d^{1/2}} \right\}, \tag{2.19}$$

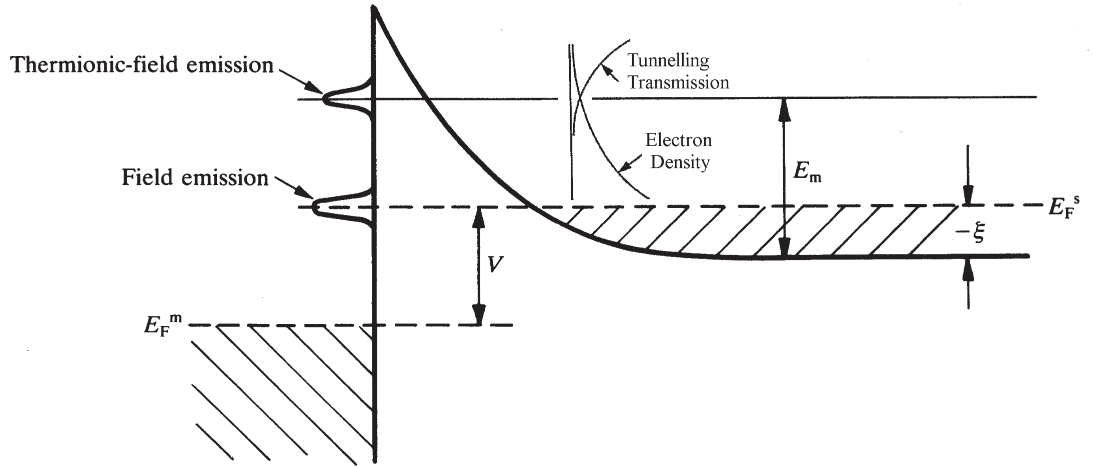

Figure 2.6: Field and thermionic field emission under forward bias. The diagram refers to a degenerate semiconductor to show field emission, this means ξ is negative. Image adapted from Rhoderick.[27]

where E_{00} is a property of the bulk semiconductor which is important to tunnelling theory as it contains the donor concentration and semiconductor permittivity, both of which affect the tunnelling of electrons. E_{00} is given by

$$E_{00} = \frac{\hbar}{2}\left(\frac{N_d}{m^* \varepsilon_s}\right)^{1/2}. \tag{2.20}$$

The onset of thermionic field emission can be thought of as a form of barrier lowering $\Delta\phi$ which works well for silicon with $N_d < 10^{24}$ m^{-3}, giving a value for $E_{00} \approx 10^{-2}$ eV.[27] To extend this tunnelling theory beyond simple barrier lowering Padovani and Stratton,[39] and Crowell and Rideout,[40] have derived current-voltage characteristic expressions.

First we can get a feel for the onset of tunnelling as the ratio kT/qE_{00} is a measure of the relative importance of thermionic emission to tunnelling. As a rough guide we should expect field emission if $kT \ll qE_{00}$, thermionic field emission if $kT \approx qE_{00}$, and thermionic emission if $kT \gg qE_{00}$. For the values of donor concentration $N_d = 5 \times 10^{-21}$ m^{-3} expected for the silicon used in this thesis, TFE will not occur until the temperature drops to 4.5 K; hence, forward tunnelling has been neglected. Increasing the donor density will increase the temperature at which TFE will occur.

If the experimental parameters move into a tunnelling regime, the following current-voltage relationship can be used with the appropriate saturation current density J_s expres-

sion for either FE or TFE,

$$I = SJ_s \exp\left(\frac{V}{E_0}\right)\left[1 - \exp\left(-\frac{qV}{kT}\right)\right], \tag{2.21}$$

where E_0 can be thought of as the amount of band bending for a semiconductor that would yield a tunnelling probability of $\exp(-1)$ (~37%) at the base of the barrier

$$E_0 = E_{00}\coth\left(\frac{qE_{00}}{kT}\right). \tag{2.22}$$

The expression for the saturation current density J_s for TFE is given by Padovani and Stratton as,

$$J_s = \frac{A^{**}Tq\exp(-q\xi/kT)\{\pi E_{00}(\phi_b - V - \xi)\}^{1/2}}{k\cosh(qE_{00}/kT)}\exp\left(-\frac{(\phi_b - \xi)}{E_0}\right). \tag{2.23}$$

This is the most likely form of tunnelling to be encountered if the temperature is lowered and the doping density increased.

Using the current-voltage expression for FE and TFE, equation (2.21) and part of the Taylor expansion of the barrier transparency, Padovani and Stratton give a more exact analysis for the tunnelling temperature regimes taking into account the Schottky barrier properties.[39]

The temperature below which field emission occurs for a degenerate semiconductor where ξ is negative can be given as

$$kT < 2qE_{00}\{\ln(-4\phi_b/\xi) + (-2E_{00}/\xi)^{1/2}\}^{-1}, \tag{2.24}$$

and the temperature above which thermionic field emission occurs as

$$kT > 2qE_{00}\{\ln(-4\phi_b/\xi)\}^{-1}. \tag{2.25}$$

Finally the transition between thermionic field emission and pure thermionic emission depends on applied bias, as the upper temperature limit for thermionic field emission uses the diffusion potential V_d ($= \phi_b - \xi - V$), which is bias dependent. Therefore the tunnelling will become less significant as the applied voltage increases;

$$\cosh^2(qE_{00}/kT)/\sinh^3(qE_{00}/kT) < 2V_d/3E_{00}. \tag{2.26}$$

Using these more exact expressions for the temperature limits for the donor density of $N_d = 5 \times 10^{-21}$ m^{-3} the TFE occurs between 3.3 K and ~50 K at zero applied bias, which is still below the temperature regions investigated in this thesis.

Reverse Bias Tunnelling Characteristics

Thermionic emission theory is used successfully to fit forward bias I/V curves; however it often underestimates the reverse bias. For an ideal SB this current should saturate at a very low current and for a microelectronics system this assumption is fine. However in nanosystems, nanoamps are flowing in the forward bias. This is comparable to that of the reverse bias or leakage currents in a SB meaning the reverse bias can be much more important. If the SBH is dependent on voltage, the reverse bias characteristics will not show saturation. The simplest explanation for the unsaturated characteristics is barrier lowering by the image force. Using equation (2.14) we can see the image lowering $\Delta\phi_{bi}$ is proportional to the applied bias $V^{1/4}$, this is often enough to fit the I/V curve in the reverse bias.

If the image force lowering is not enough to explain the deviation from saturation, tunnelling is often the cause of the 'soft' reverse characteristics. Tunnelling becomes more significant at lower doping levels in reverse bias than forward, with both thermionic field and field emission becoming important as shown in figure 2.7. It can be calculated that departures from thermionic emission begin to occur at donor concentrations of 10^{23} m^{-3} for silicon.[27]

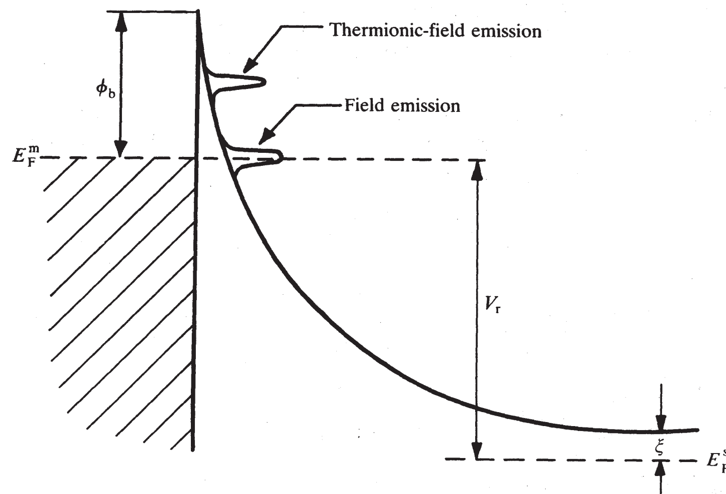

Figure 2.7: Field and thermionic field emission under reverse bias. Image from Rhoderick.[27]

Padovani and Stratton have also derived the current/voltage relationship for thermionic field emission for reverse bias.[39] For reverse bias voltages (V_r) greater than 3kT/q the

current becomes

$$I = SJ_s \exp\left\{V_r\left(\frac{q}{kT} - \frac{1}{E_0}\right)\right\}, \tag{2.27}$$

where J_s is a slowly varying function with reverse bias:

$$J_s = \frac{A^{**}T(\pi q E_{00})^{1/2}}{k}\left\{q(V_r - \xi) + \frac{q\phi_e}{\cosh^2(qE_{00}/kT)}\right\}^{1/2} \exp\left(-\frac{\phi_e}{E_0}\right). \tag{2.28}$$

This expression coincides with that for forward bias tunnelling at small values of V_r and doping density such that $kT \geq qE_{00}$, the condition for thermionic field emission. This means the forward and reverse biases agree at the origin as the characteristic should be continuous.

At higher doping concentrations, field emission can occur but in the reverse bias it does not require the semiconductor to be degenerate as the electrons are tunnelling from the metal which is always degenerate. For field emission to occur at room temperature, donor concentrations in excess of 5×10^{24} m^{-3} are required.[27] As for forward bias the expression for field emission has many terms and as it is not used within this work the reader is referred to Padovani and Stratton's work.[39]

2.3.5 Recombination Effects

Recombination currents can cause apparent deviations of n from unity as they cause departure from thermionic emission. Two kinds of recombination can occur, one in the depletion region (space-charge region) and the other in the neutral region of the semiconductor. Computer curve fitting programs have been developed to obtain more accurate estimates of the SBH using recombination theory by McLean.[41] Recombination in the space charge region generally takes place via localised states within the energy gap. These localised states could be caused by defects at the interface, hence the need to have a well ordered structure. This effect becomes more important with high SB at low temperatures and low forward bias.

If the SBH on an n-type semiconductor is greater than half of the band gap, the region of the semiconductor adjacent to the metal becomes p-type containing a high density of holes. These holes can diffuse into the neutral region under forward bias, giving rise to hole injection.

2.4 Deviation from a Single Schottky Barrier

So far we have assumed that the Schottky barrier is homogeneous and has a continuous height over the whole contact. This is hard to fabricate and normally not achieved as defects and changes in structure lead to an inhomogeneous SBH which is averaged over. Also we have assumed that the Schottky barrier is the only component in a circuit where the voltage can be dropped. This is rarely the case as the semiconductor itself has a resistance which is in series with the barrier. Leakage currents and edge effects may act as parallel resistors. Finally, to measure an I/V curve there must be two contacts to the semiconductor in which case there may be two Schottky barriers or at least a contact resistance. A schematic of a possible circuit of components where the voltage could be dropped is shown in figure 2.8.

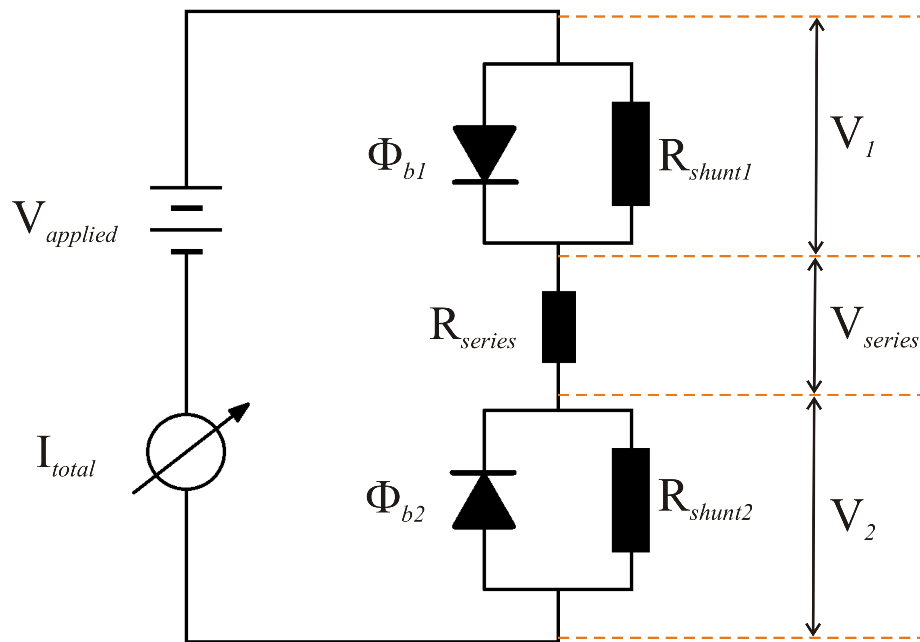

Figure 2.8: Schematic of a possible back-to-back Schottky barrier circuit showing components where voltage drops can occur, ϕ_b Schottky barrier, R_{series} series resistance, R_{shunt} parallel shunt resistance.

In the back-to-back circuit shown in figure 2.8 the forward biased SB current is modelled using thermionic emission, equation (2.18), with the addition of the shunt resistance as shown in equation (2.31). The reverse biased SB uses the saturation current from thermionic emission, again equation (2.18), and similarly the addition of a different shunt resistance. Also the reverse bias SB includes the reverse tunnelling from equation (2.27). The series resistance is applied over both SBs as indicated by equation (2.30).

2.4.1 Inhomogeneous Schottky Barriers

An inhomogeneous barrier is one where the SBH varies over a lateral distance less than the width of the depletion region. This gives areas with different SBH which can be seen as parallel conduction paths. To model such a situation the total current is the linear sum of contributions from every area. Taking equation (2.4), assuming the overall transport mechanism is thermionic and the ideality factor is unity, we can write:

$$I = A^{**}T^2 \left[\exp\left(\frac{qV}{kT}\right) - 1\right] \sum_i S_i \exp\left(-\frac{q\phi_i}{kT}\right), \tag{2.29}$$

where S_i and ϕ_i are the area and SBH of the ith patch.[35] This simple extension to cover inhomogeneous barriers can be applied to any of the other transport mechanisms. The main concern with the parallel conduction model approach to inhomogeneous SB is the assumption that the patches are independent from each other electrically. Tung provides an approach to include the interaction between neighbouring sections of the same interface.[35,42,43]

2.4.2 Series Resistance

In equation (2.18) it has been assumed that the entirety of the applied bias has fallen across the metal-semiconductor (MS) interface. The reality is there are voltage drops across many other components; the ohmic contact, the bulk silicon and the circuit cabling. If we assume the resistance is not bias dependent we can subtract an ohmic drop of IR_{series} from the voltage giving

$$I_d = SA^{**}T^2 \exp\left(-\frac{q\phi_e}{kT}\right) \exp\left(\frac{q(V - IR_{series})}{nkT}\right) \times \left[1 - \exp\left(-\frac{q(V - IR_{series})}{kT}\right)\right]. \tag{2.30}$$

2.4.3 Shunt Resistance

The shunt resistance is the effect of a parallel conduction path, for example, a leakage current around the Schottky barrier. This can be added as a second component to the measured current alongside the diode current. $I = I_d + I_p$ where I_d is the current from

equation (2.30) and

$$I_p = \frac{V - IR_{series}}{R_{shunt}}, \tag{2.31}$$

where R_{shunt} is the shunt resistance which is assumed not to be a function of bias.

2.4.4 Double Barrier

When making connections to a semiconductor to measure an I/V curve, two metal semiconductor interfaces have to be formed. This could lead to two SB being formed as in the circuit schematic in figure 2.8. As one interface is into the semiconductor and one out we have a back-to-back SB situation. While one SB is forward biased the second is reverse biased so both barriers are interlinked, possibly leading to one barrier dominating over the other. If we were to assume both barriers were ideal and follow thermionic emission the reverse bias for each barrier would only allow the saturation current I_0, equation (2.4) to flow. The Metal-Semiconductor-Metal (MSM) structure can be modelled using thermionic emission with barrier lowering as shown by Sze, Colman and Loya on PtSi-Si-PtSi contacts.[44] As we have already seen, thermionic emission underestimates the reverse bias which becomes more important in lower dimensional systems. One solution to this is to combine the forward bias described by thermionic emission in equation (2.18) and the reverse bias described by tunnelling in equation (2.27). These have been successfully combined by Zhang *et al* to model I/V taken from semiconductor ZnO, CdS and Bi_2S_3 nanowires contacted with a two metal tips.[45,46]

2.4.5 Vacuum Tunnel Barriers

We have seen that electrons can tunnel through the SB. However this might not be the only barrier they need to tunnel through. If there is an interfacial insulating layer present between the metal and the semiconductor, the only way an electron can progress is to tunnel through it. This technology is used in microwave tunnel diodes and may have important technological benefits in an alternative avenue of investigation for spintronics.[31] With the MS junctions studied in this thesis, it is more likely that the sample becomes oxidised so the contact to the metal of the MS junction is an oxide tunnel barrier. This can be taken further and a vacuum tunnel barrier added during Scanning Tunnelling Spectroscopy (STS) measurements. Wiesendanger provides a detailed overview of tunnelling and its use

and treatment in Scanning Probe Microscopy (SPM).[47] The original work by Simmons on tunnelling through a thin insulator between similar and dissimilar electrodes is of most interest here.[48,49] Simmons presents a generalised expression for tunnelling through an insulating film between two metal contacts:

$$I = \frac{Sq}{2\pi h w_i^2}\left\{(q\phi_t - \frac{qV}{2})\exp\left[-\frac{4\pi w_i}{h}(2m)^{1/2}(q\phi_t - \frac{qV}{2})^{1/2}\right]\right. \\ \left. -(q\phi_t + \frac{qV}{2})\exp\left[-\frac{4\pi w_i}{h}(2m)^{1/2}(q\phi_t + \frac{qV}{2})^{1/2}\right]\right\}, \quad (2.32)$$

where w_i is the thickness of the insulating layer, ϕ_t is the height of the rectangular tunnel barrier, which will be material specific, S is the tunnelling cross section, m is the mass of the electron, h is Planck's constant and V is the applied voltage. The net current arises from the difference in the current flowing from each metal under an applied bias. The first term is the current flowing from the left to the right metal electrode whereas the second term is from right to left giving a net difference. When the applied voltage is zero the terms are identical, cancelling each other out so there is no net current.

This expression for tunnelling, although across a barrier, is different to the SB tunnelling because this is between two metals, not a metal and a semiconductor of the SB. This expression could be used to describe a vacuum tunnel gap between a scanning tunnelling microscope (STM) tip and the metal thin film. It has been used in this work to fit an I/V curve taken from an $ErSi_2$ nanowire which was transferred in atmosphere, therefore coating the nanowire in an insulating oxide layer.

2.5 Schottky Barriers of Nanostructures

Downscaling the dimensions of a Schottky barrier has an effect on the electrical properties which the theory discussed so far cannot describe as it assumes an infinitely extending interface. Smit *et al* have measured nanoscale $CoSi_2$ islands on Si(111) using an STM tip and report an increase in conductance with a decrease in island size.[50] They propose a model which predicts a narrower barrier for nanoscale diodes which has a increase in tunnelling due to the narrowing.[51] This effect starts affecting the depletion region width when the diameter of the island becomes less than the distance the depletion region extends into the semiconductor. A similar effect has been reported on gold nanoclusters with a measured increase in SBH with an increase in cluster size.[52]

One dimensional structures have shown improved current transport characteristics because of the reduced phase space for scattering events, reducing the probability of backscattering. Although this increased conduction is excellent for efficient current transport, the process is dominated by the contact which has different properties at the nanoscale. Tunnelling has been shown to be more important on 1D semiconductor structures which have been connected with a 3D metal contact.[53] $ErSi_2$ nanowires on Si(001) have shown an increase in current density with a decrease in the nanowire width but no change is noted with a change in length.[54] The increase in current density is attributed to an increase in tunnelling probability with decreasing nanowire width.

The growth of nanostructures leaves much of the substrate surface uncovered, this allows different conduction paths between two islands; perpendicular to the surface into the semiconductor bulk or parallel along the surface. Erbium silicide islands on Si(111) have been investigated by Dupont-Ferrier showing the transport between two similar islands is mainly parallel to the 7×7 surface and is the more active channel. This can be switched to transport through the semiconductor by oxygen absorption passivating the surface reconstruction.[55,56] Similar effects of barrier lowering and parallel surface transport are found on $ErSi_2$ islands on Si(001).[57]

2.6 Engineering the Barrier

The I/V curve measured from a Schottky diode can be affected by several of the processes already discussed, hence the importance of careful analysis. Osvald shows that a MS contact which was believed to be an Ohmic contact could be a low SB.[58] The majority of these processes arise because of the interface structure, therefore the SBH has a critical dependence on the local structure; this is most prominent with an inhomogeneous barrier.[59,60] The amount of silicon in a silicide has been shown through calculations to affect the SBH, an increase in the ratio of Si in the silicide causes a decrease in the SBH.[61] It has also been shown that different clean silicon surfaces produce different SBH with the same metal. Iridium silicides have shown a difference in SBH with different phases of the silicide.[62] The importance of the interface structure has been shown by Tung with the $NiSi_2$ system which shows a 0.14 eV difference in the SBH between two interfaces.[20]

The interface is essential to the understanding of the SBH and can lead to incorrect analysis if defects and inhomogeneities are not considered. Bratkovsky and Osipov pro-

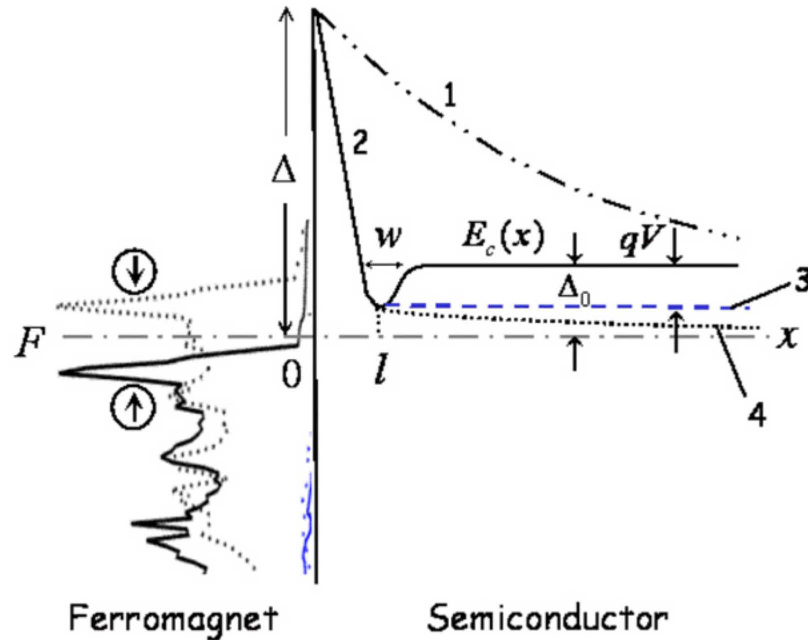

Figure 2.9: Bratkovsky's δ-doped barrier. Energy diagrams of ferromagnet semiconductor heterostructure with a δ-doped layer (F is the Fermi level, Δ the height and l the thickness of an interface potential barrier, Δ_0 the height of the thermionic barrier in the n-semiconductor). The standard Schottky barrier (curve 1); $E_c(x)$ the bottom of the conduction band in the n-semiconductor in equilibrium (curve 2), under small (curve 3) and large (curve 4) bias voltage. The spin-polarized density of states in Ni is shown at $x < 0$. Image and caption from Bratkovsky.[10]

posed engineering the barrier to provide the properties required for spin injection by selecting an advantageous interface structure.[10,11] Spintronics has a need to pass a current from a metal into a semiconductor this is the reverse bias scenario, to do this, the barrier needs to allow electrons to tunnel into the semiconductor. As shown in figure 2.9, when using a δ-doped interface the barrier can be tuned to the required width using additional doping at the interface, narrowing the tunnel barrier which increases its transparency.

2.7 Simulating Schottky Barrier I/V Curves

A MATLAB simulation script was written to observe how the variable parameters affect the overall I/V curve for a back-to-back SB. This enables us to see how the I/V curve is altered by the parameters of the two SBs and reveals a limitation with the theory in the low voltage/SBH region.

2.7.1 MATLAB Simulation Script

Based on the ideas used by Zhang,[45] the program uses a modified Newton Raphson method to find values for the voltage dropped across each component in the circuit in figure 2.8. In an iterative loop, the program first corrects the SBH for the image force lowering using equation (2.14), then uses Kirchoff's laws, equations (2.33) and (2.34) to combine the voltage and current for each component:

$$V_{applied} = V_1 + V_2 + V_{series}, \tag{2.33}$$

$$I_{total} = I_1 = I_2 = I_{series}, \tag{2.34}$$

where V_1 is the voltage dropped across and I_1 the current through, the first SB (ϕ_{b1}) and corresponding shunt resistance (R_{shunt1}). V_2 is the voltage dropped over and I_2 the current through the second SB (ϕ_{b2}) and corresponding shunt resistance (R_{shunt2}). Finally V_{series} is the voltage dropped over R_{series} and I_{series} is the current through R_{series}.

I_1 and I_2 are the currents though ϕ_{b1} and its paired shunt resistor R_{shunt1} and ϕ_{b2} and its paired shunt resistor R_{shunt2} respectively. Depending on the applied bias (forward or reverse) these currents have to swap over to describe the barriers' behaviour. With the circuit in a configuration such that ϕ_{b1} is forward biased and ϕ_{b2} is reverse biased the current is:

$$\begin{aligned} I_1 &= I_{1forward} + \frac{V_1}{R_{shunt1}}, \\ I_2 &= I_{2reverse} + \frac{V_2}{R_{shunt2}}, \end{aligned} \tag{2.35}$$

where $I_{1forward}$ is the forward bias current which comes from the thermionic emission equation (2.18) with the voltage taken as V_1. The reverse bias current, $I_{2reverse}$, is taken from the reverse tunnelling equation (2.27) with V_2 as the input voltage. However, $I_{2reverse}$ is not zero at zero applied voltage due to the equilibrium probability tunnelling current of:

$$I = \frac{SA^{**}T(\pi q E_{00})^{1/2}}{k} \left\{ -q\xi + \frac{q\phi_e}{\cosh^2(qE_{00}/kT)} \right\}^{1/2} \exp\left(-\frac{\phi_e}{E_0} \right). \tag{2.36}$$

This would normally be cancelled out by a similar current from the forward tunnelling current expression but as we are not using this we have to subtract it from equation (2.27).

Utilising $V = IR$ and equation (2.34), as the current through each section of the circuit is equal, we get the identity,

$$V_{series} = I_{series} R_{series} = I_1 R_{series} = I_2 R_{series} \tag{2.37}$$

Substituting these into the equation (2.33) we can write down two simultaneous equations which can be solved using a Newton-Raphson method to get a value for V_1 and V_2:

$$0 = V_1 + V_2 + I_1 R_{series} - V_{applied},$$
$$0 = V_1 + V_2 + I_2 R_{series} - V_{applied}. \tag{2.38}$$

Once a value for V_1 and V_2 has been found, the total current can be calculated from,

$$I_{total} = \frac{V_{applied} - V_1 - V_2}{R_{series}}. \tag{2.39}$$

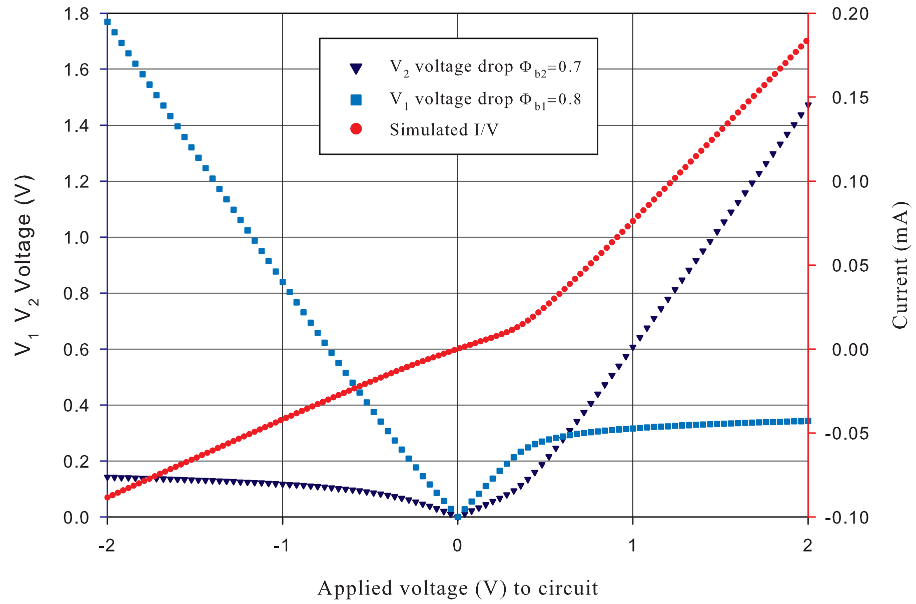

Figure 2.10: Graph of the voltage drops for individual SB diodes in a back-to-back circuit and the final simulated I/V curve.

Using this MATLAB simulation script the voltage across each diode can be simulated and the corresponding I/V curve calculated. The simulated I/V curve for back-to-back SBs with values for the first barrier of $\phi_{b1} = 0.8$ eV, $R_{shunt1} = 20$ kΩ, area $S = 5 \times 10^{-8}$ m^2 and the second barrier of $\phi_{b2} = 0.7$ eV, $R_{shunt1} = 8$ kΩ, area $S = 1 \times 10^{-6}$ m^2, with a series resistance $R_{series} = 1$ kΩ and a temperature of 298 K is shown in figure 2.10. Alongside the I/V curve, the voltage drop over ϕ_{b1} and the parallel shunt resistor R_{shunt1} is shown as it moves from forward bias $(+V)$ to reverse bias $(-V)$ and for ϕ_{b2} and the parallel shunt resistor R_{shunt2} moving from reverse bias $(+V)$ to forward bias $(-V)$.

2.7.2 Parameter Trends

Using the MATLAB simulation script described above sets of curves have been produced giving an idea of how one parameter could alter the curve. The starting base set of values for the simulation are, $T = 298$ K, doping concentration $N_d = 5\times10^{21}$ m^{-3}, $R_{series} = 500$ Ω and for both barriers, $\phi_b = 0.8$ eV, $R_{shunt} = 20$ kΩ, Area $S = 10^{-10}$ m^2 and ideality factor $n = 1$.

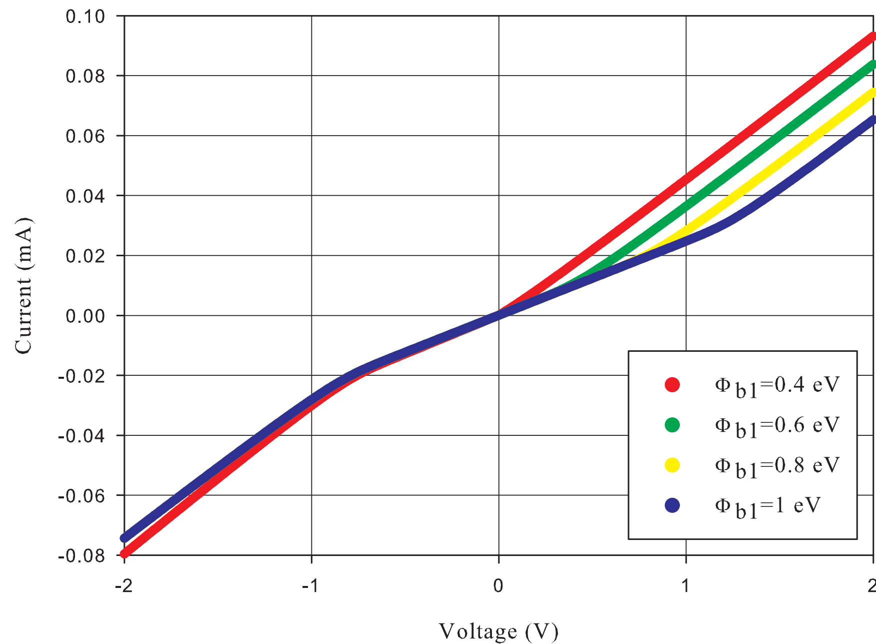

Figure 2.11: Graph of Schottky Barrier Height, ϕ_{b1} variations and the effect on the I/V curve.

Figure 2.11 shows that changing the SBH effects the position of the knee of the forward bias curve, moving it higher in voltage with a higher SBH. This is due to the turn on voltage, the point where the majority of electrons can overcome the barrier by thermionic emission. This has little effect in reverse bias until you reach low barrier heights where more current flows at high applied bias. This is the effect of tunnelling through the barrier combined with the image force lowering in the reverse bias, causing the barrier to be narrower at lower energies. Figure 2.12a shows the area of the junction variation on the I/V curve. This has a very similar effect on the curve as the SBH, as the area is a scaling term and the exponential term containing the SBH is also a constant scaling term. As these two variables have a similar effect on the I/V curve it is difficult to separate the two from each other in fitting.

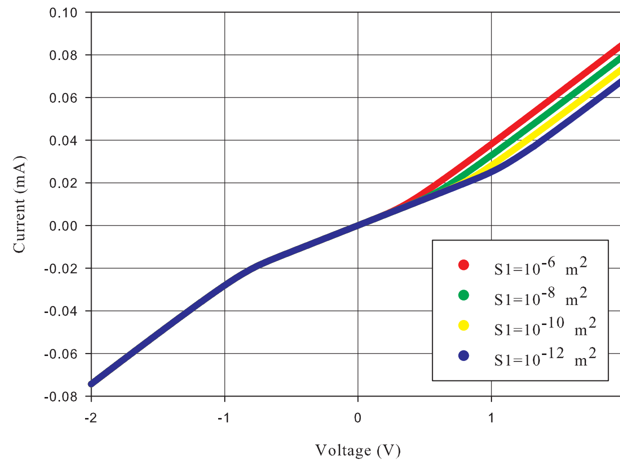

(a) Area S

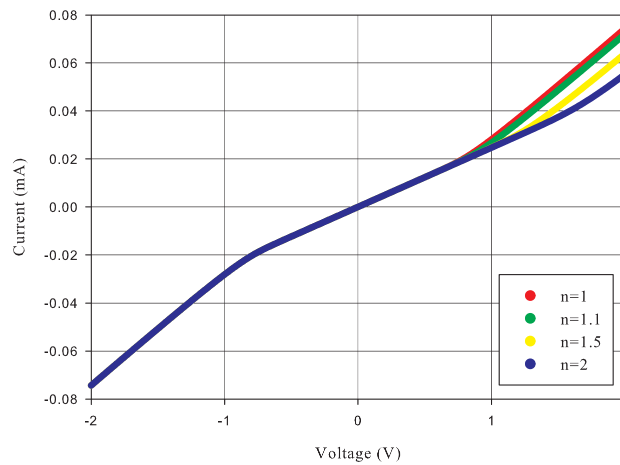

(b) Ideality Factor n

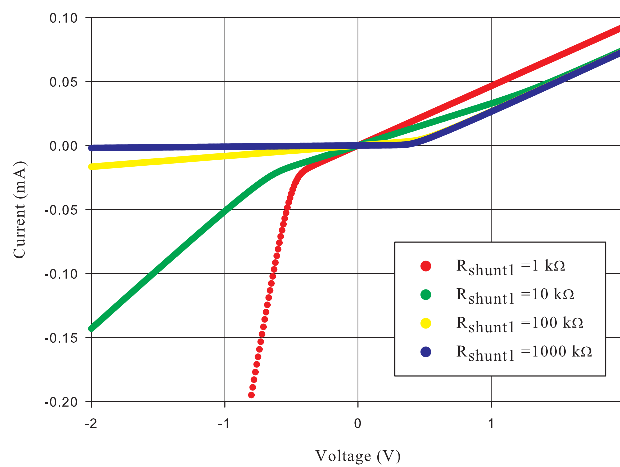

(c) Shunt Resistance R_{shunt}

Figure 2.12: Graphs varying the area of the contact, ideality factor and shunt resistance for the first SB in the circuit.

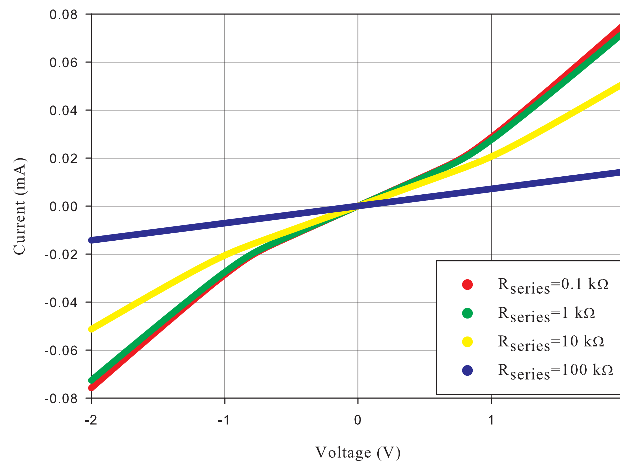

(a) Series Resistance R_{series}

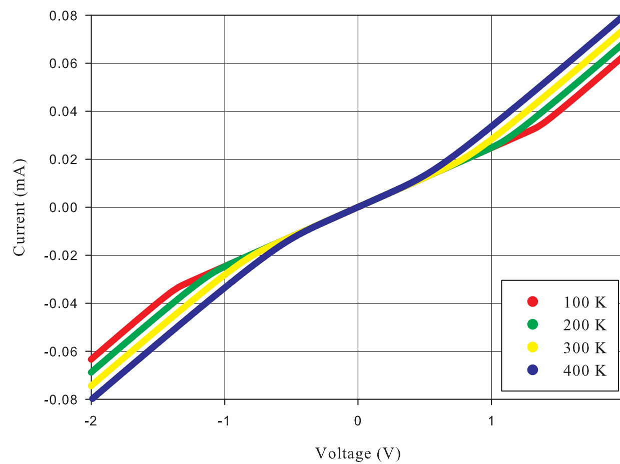

(b) Temperature T

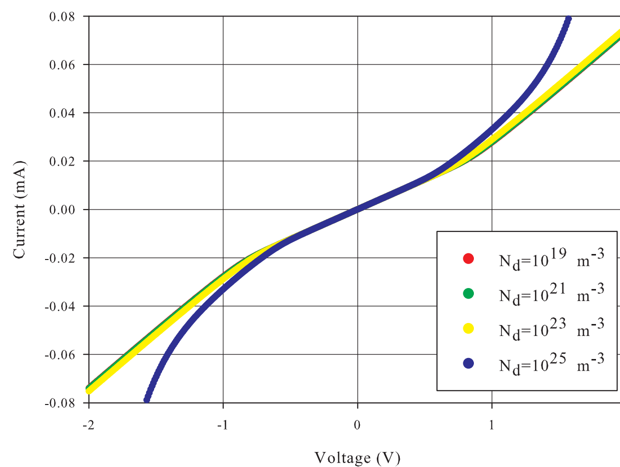

(c) Doping Concentration N_d

Figure 2.13: Graphs varying the series resistance, temperature and doping concentration, variables which effect the whole circuit.

The ideality factor variation is shown in figure 2.12b and affects the curve by moving the knee to a higher voltage but also altering the gradient of the curve as the value of n increases. This is because the exponential term involving n is dependent on applied voltage altering the gradient at high vales of n. Although the shunt resistance is linked with one barrier it has a significant effect on both biases as can be seen in figure 2.12c. With very high shunt resistance the reverse bias characteristic is almost purely thermionic, as the large resistance dominates the voltage drop.

The effects of series resistance, temperature and doping concentration affect the whole circuit and therefore the whole I/V curve as can be seen in figure 2.13. Figure 2.13a shows the series resistance variation, which softens the knee as the curve starts to look ohmic with high resistance values. This is because as the series resistance increases the voltage dropped across the series resistor increases so the effect of the SB becomes negligible. The temperature variation curve, shown in figure 2.13b, shows that changing the temperature affects the curve in a similar way to area but on both ends of the I/V curve. This is because the energy of the electrons has been increased so they can overcome the barrier at lower applied bias; this affects both barriers in the circuit, hence the effect on both ends. This provides an opportunity to extract a more reliable area measurement from the data by varying the temperature. The doping concentration has a very small effect until the image force lowering and tunnelling become more significant, at around 10^{24} m^{-3}. Above this doping concentration the I/V curve shows a steady change in gradient with applied bias as shown in figure 2.13c, as the extra doping causes the barrier to be more transparent to tunnelling.

2.7.3 Low Voltage and Low Schottky Barrier Height

Figure 2.14 shows the simulated curves for the voltage dropped across two back-to-back SBs. The simulation used ϕ_{b1}=0.2 eV and ϕ_{b2}=0.8 eV and all the other parameters are equal to the base parameters used in the previous trends simulation. It was observed that the voltage dropped across the low SBH in the reverse bias was negative. This result would be unphysical as this SB would not provide a voltage.

As the negative voltage drop is in the reverse bias, equation (2.27) for reverse bias tunnelling was considered. More specifically, the function for J_s, equation (2.28), which

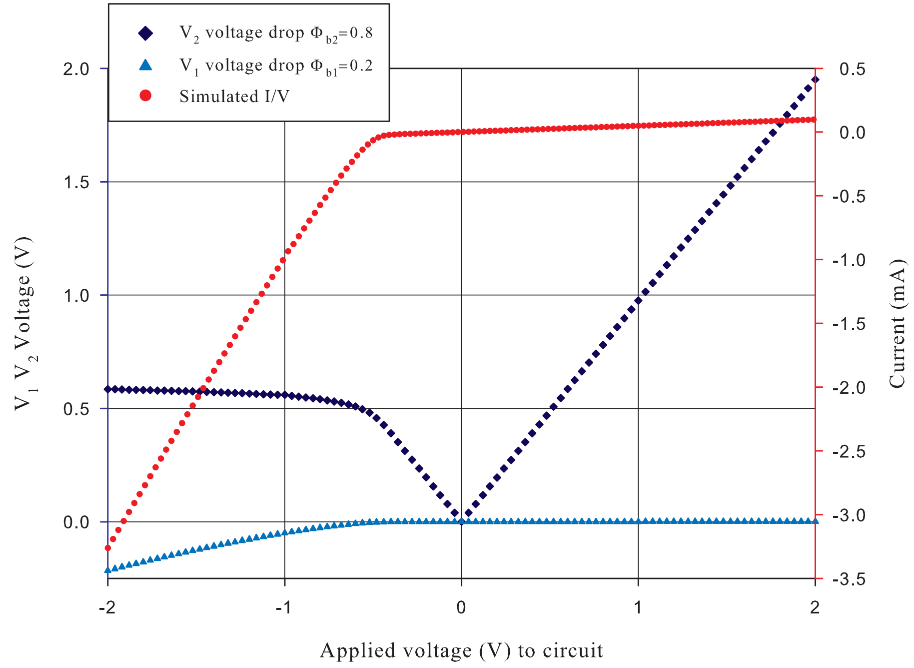

Figure 2.14: Graph of the voltage dropped across a low SBH and the resulting I/V curve. Note the negative voltage drop over the reverse biased ϕ_{b1}=0.2 eV SB.

contains the expression for the electron kinetic energy:

$$E^{1/2} = \left\{ q(V_r - \xi) + \frac{q\phi_e}{\cosh^2(qE_{00}/kT)} \right\}^{1/2}, \tag{2.40}$$

where $q(V_r - \xi)$ is the ballistic electron expression. When the voltage is less than ξ the first bracket, $q(V_r - \xi)$, is negative. If the SBH is small, of the same order as ξ, then the second term is too small to make the square root positive resulting in the negative voltage drop. ξ has a value of $\sim$0.2 eV under the temperature and doping conditions used here hence the problem arises with a simulation of ϕ_b=0.2 eV.

This problem therefore only occurs at low voltages and low barrier heights. In this case, the voltage can be set to zero when it is equal to or less than ξ. This has been incorporated in the next generation of fitting programs developed in FORTRAN in Section 4.3.2.

The ballistic electron expression, $q(V_r - \xi)$, is the energy an electron has in the conduction band after being excited into the conduction band from the Fermi level (see figure 2.7). If the voltage is less than ξ then the electron does not have enough energy to reach the conduction band, so according to this expression would be left in the band gap. This would not be a physical situation, as if the electron does not have enough energy to get into the conduction band it should not be able to tunnel.

Chapter 3

Experimental Techniques

This chapter introduces the techniques used to prepare and analyse the samples studied in this thesis. Several different vacuum systems have been used, including a Balzers molecular beam epitaxy growth chamber for fast material deposition, and an Omicron scanning tunnelling microscope with growth chamber. These systems have been used to prepare samples and verify the surface reconstructions with techniques such as scanning tunnelling microscopy and low energy electron diffraction. The electrical interface properties have been studied using probes both in and out of vacuum by making contact with the surface and measuring a current-voltage curve, from which the Schottky barrier height can be extracted. The Omicron Nanoprobe system available at Leeds through the Leeds EPSRC Nanoscience and Nanotechnology Facility (LENNF) has been the main system for in-vacuum contact electrical measurements.

3.1 Surface Characterisation

The reconstruction of the surface is very important to this work, as it gives an indication of the surface homogeneity and provides a check against previous structural determination work, providing confidence in the sample structure. Several of the rare earth silicides have been studied previously in the York group and the silicide structure has been determined using Medium Energy Ion Scattering (MEIS),[12,63] so the growth of these structures is well characterised. The following techniques have been used to check the sample surface reconstruction during sample preparation: Low Energy Electron Diffraction (LEED), Reflection High Energy Electron Diffraction (RHEED), and Scanning Tunnelling Microscopy (STM). An introduction to surface physics and relevant techniques is given by Prutton and

Woodruff respectively.[64,65] Scanning Electron Microscopy (SEM) has also been utilised to study the surface island coverage and topography.

3.1.1 Electron Diffraction

Low Energy Electron Diffraction

To study the surface structure and reconstruction, the technique of LEED has been utilised. Electrons with energies between 10 and 200 eV are used as they do not penetrate far into the surface, making this a very surface sensitive technique.[64,65] Davisson and Germer first demonstrated the wave nature of the electron in 1927 using low energy electrons scattered from a single crystal of nickel,[66] this was then developed into this powerful analytical tool.

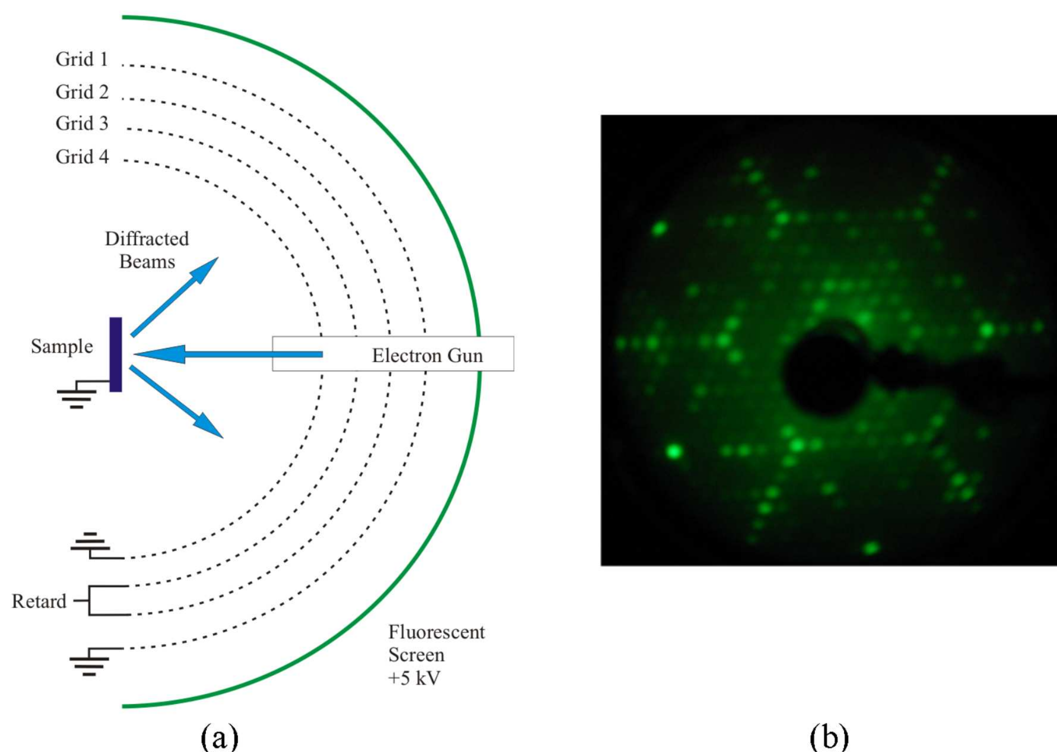

Figure 3.1: a) Schematic of an Omicron Spectra LEED system; b) Example LEED pattern of the silicon (111) surface 7×7 reconstruction.

An electron gun focuses low energy electrons onto the sample surface where the beam is diffracted by the surface crystal structure. The incident beam is focused to a spot on the sample with a diameter between 0.1 mm and 1 mm, with a maximum current of about 2 μA and an energy between 10 and 200 eV. A series of grids with a common centre on the sample allows a small window of electron energies through, by being biased close to

the primary beam energy. The outer grids (1 and 4) are grounded with the retarding grids (2 and 3) biased $\sim$20 V less than the incident electron beam energy. The grids cut out the majority of inelastically scattered electrons leaving the elastically scattered electrons to pass through onto a fluorescent screen, which is biased at +5 kV, where the diffraction pattern is seen. Figure 3.1 gives a schematic cut through of a LEED system and an example pattern from the 7×7 reconstructed Si(111) surface.

The pattern maxima show the surface reciprocal lattice, hence knowledge of the surface mesh can be gained. The LEED pattern of 7×7 reconstructed Si(111) in figure 3.1 indicates that the surface lattice is seven times bigger than the underlying bulk silicon lattice because of the six extra spots between the more intense primary spots. If the spots are sharp we can be confident the majority of the surface is well ordered whereas double or stretched spots indicate a heavily stepped surface.

Quantitative structural information can be gained from LEED by measuring the intensity of the diffracted spots as a function of incident beam energy. This is very powerful, not only to gain surface structure, but also to indicate subtle sub-surface differences a few monolayers deep. This can identify between two different orientations of a silicide on Si(111) by the rotational symmetry in the intensity of the diffraction spots. This technique is very time consuming and some prior knowledge of the structure is required for complex surface fitting to the LEED-I/V curves.

Reflection High Energy Electron Diffraction

RHEED is a technique akin to LEED but using a grazing angle of incidence and higher energy electrons ($\sim$6 kV). These scatter off the crystalline surface creating a diffraction pattern indicating the surface structure. Higher energy electrons can be used in this technique because of the grazing angle which keeps the technique surface sensitive. The advantage of this geometry is you can use RHEED while growing a thin film, giving information about the quality of growth and an indication of when a monolayer is complete. The grazing angle also means that by rotating the sample, different crystal orientations can be accessed.[64,65]

3.1.2 Scanning Tunnelling Microscopy

Binnig and Rohrer invented the STM in 1982 from experiments on vacuum tunnelling.[67] Using their STM they were the first to image the 7×7 reconstruction of the Si(111) surface.[68] This great leap forward in surface imaging at the atomic scale earned Binnig and Rohrer the 1986 Nobel Prize in Physics. The technique is now widely used within the surface science community and indeed beyond surface science, being one of the few techniques which can image individual atoms on a surface.

The technique uses an atomically sharp tungsten tip which is moved close to the surface using piezoelectric crystals. The conducting tip is at a potential of $\sim$2 V relative to the sample therefore a tunnelling current of $\sim$2 nA can flow. In constant current mode this tunnelling current is kept constant by a feedback loop which alters the sample-tip distance via the piezoelectric crystals. Rastering the tip over the surface builds up contours of constant charge density across the surface, giving an indication of atomic positions and surface structure. The contrast in this image is produced from the change in voltage applied to the piezoelectric crystals in keeping the tip current the same.

The physics department at York has an Omicron room temperature STM which is used to analyse surface structures alongside MEIS and LEED. The STM is controlled by the Omicron SCALA software which is also capable of image analysis. Spectroscopy measurements, current-voltage (I/V) curves or, with the addition of a lock-in amplifier, dI/dV curves, can be taken during scanning on a grid pattern or at a single point. During a spectroscopy curve measurement the feedback loop controlling the height of the tip is turned off allowing a voltage sweep to take place. This requires the system to be very stable so the tip does not drift into, away from, or laterally to the sample surface. Although it is possible to take spectroscopy data during scanning in this system, it suffers from having in-vacuum amplifiers which are limited to 50 nA. This provides a problem with trying to take I/V curves in contact mode as this saturates the in-vacuum amplifier at very low voltages. Measurement of I/V curves over a meaningful voltage range can only be done in tunnelling, with the extra vacuum tunnel gap added onto the I/V curve, giving an extra level of complication to the SBH extraction.

3.1.3 Scanning Electron Microscope

SEM uses high energy electrons ($\sim$ 0.5-30 keV) as a probe of the sample to produce surface topography on the scale of tens of nanometres, chemical analysis can also be gained from emitted x-rays. Initially electrons are produced by thermionic or field emission and accelerated towards the sample, passing through several magnetic lenses to focus and manipulate the beam. This control allows the focused beam (0.4 to 5 nm diameter spot) to be raster-scanned over the surface allowing an image to be produced. When the beam of electrons hits the surface, secondary electrons are liberated from the top few nanometres. These inelastically scattered electrons are detected using an Everhart-Thornley detector with an energy cut-off accepting only secondary electrons generally with energies of $<$ 50 eV. This energy cut-off removes other signals such as elastically scattered (backscattered electrons) or x-rays, all signals that can be utilised in other ways.[69] The signal detected from the secondary electrons depends upon both the surface electronic characteristics and the sample-beam interaction angle. This technique was originally developed by Knoll in 1935 and now routinely reaches nanometre resolution at magnifications of 1×10^6 times with field emission electron sources.

The York JEOL Nanocentre has an FEI Sirion SEM which has been use to test samples for feasibility before taking similar samples to LENNF. The commercial FEI instrument does not use a vacuum sample chamber which is compatible to the UHV growth chambers so any samples are transferred in air to the instrument. Transferring samples in air and the fact the chamber is not UHV can lead to carbon contamination while scanning the surface with the electron beam.

3.2 Sample Growth

The samples studied in this thesis have been grown on different crystal planes and with different deposition metals. To be able to reproduce an almost identical sample for repeat measurements, careful controls are followed during preparation and growth to ensure the best probability of producing the same surface and interface each time. Careful control of cleaning procedures, temperatures, deposition rates, annealing times and vacuum conditions all play a part in engineering reproducible samples.

3.2.1 Ultra-High Vacuum

The rate at which a surface becomes coated with adsorbed atoms depends on the pressure of the residual gas in the chamber. In atmosphere the surface would be fully coated (one monolayer, $\sim 2 \times 10^{15}$ atoms cm^{-2}) in roughly 10^{-9} seconds whereas in Ultra High Vacuum (UHV) ($\sim 10^{-10}$ mbar) it takes several hours, for this reason all the samples studied in this thesis are grown in UHV.[70] This means once the majority of adsorbed atoms have been removed from the substrate in vacuum the surface stays clean long enough to achieve a pure epitaxial growth with the least amount of contamination on the surface, at the interface, or in the metal film.

3.2.2 Substrate and Sample Heating

As samples are generally loaded into the UHV system from atmosphere via an entry lock it is expected that the substrate surface is contaminated with hydrocarbons and silicon oxide. The substrate is initially outgassed overnight at a temperature of ∼600 °C. The next process is to produce a clean well ordered surface reconstruction, this is done by flash cleaning where the silicon is raised to a temperature of ∼1200 °C for 30 s. The surface reconstruction and cleanliness can be checked using LEED and STM.

Direct Current Heating and E-beam Heating

We can use two types of heating plates as shown in figure 3.2, each one designed for a different heating method either direct current or e-beam. Direct current (DC) heating uses the resistive properties of silicon. A current of about 10 A is passed through silicon using a current limited power supply (Delta power supply SM 7020 or equivalent). E-beam heating bombards the back of the sample with electrons thermally emitted from a hot tungsten or thoriated tungsten filament floated at 1kV, and the emission current from the filament to the sample is controlled by a current limited power supply. Temperatures of ∼1200 °C can be reached by both methods. DC heating is the preferred heating method as only the silicon is heated not the whole sample plate. It also produces a more uniform temperature across the sample compared to e-beam heating.

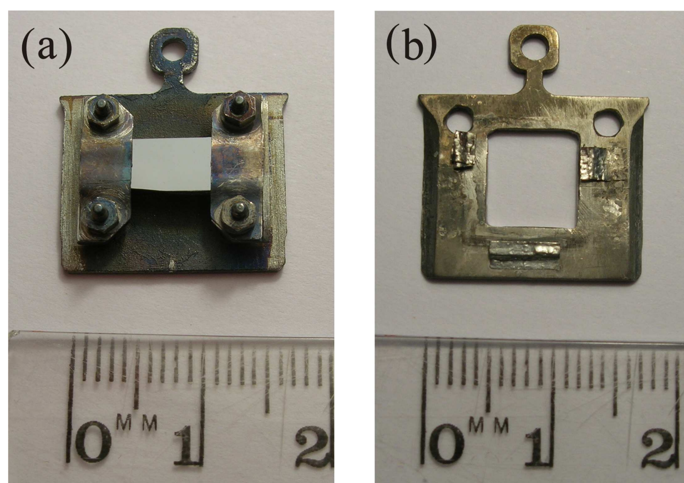

Figure 3.2: a) Direct current heating sample plate, b) E-beam heating sample plate.

Substrate Sample Plates

All the samples are mounted on Omicron molybdenum room temperature sample plates allowing possible transfer between UHV systems. The silicon substrates are cut to size using a diamond scribe, for DC heating samples are ∼10 mm by ∼4 mm whereas the e-beam samples are ∼10 mm square. The orientation of the silicon wafer is kept the same for repeat samples by always keeping the wafer flat at the top and marking the left side as you look at the polished face. This marked left side is mounted into the sample plate to the left side when the plate's tag is uppermost. This is crucial for using LEED to identify a difference in the interface orientation between samples of $NiSi_2$. Keeping the substrate alignment the same is also very important for the work on vicinal 4° Si(001) as the step direction dictates the growth direction of the nanowires. The direction of the nanowires must be known so the width of the nanowire is cross sectioned for transmission electron microscopy. All substrates are kept as clean as possible, wiped with iso-propanol and only ceramic tools e.g. tweezers are used to avoid nickel contamination from stainless steel.

Pyrometer

To measure the temperature of the silicon an Impac infrared pyrometer, model IS 50 Si-LO plus, has been used. This instrument is designed specifically for use on silicon. The focal length is adjustable, allowing the temperature to be measured from the small sample area through a window in the UHV chamber. The emissivity is set to 0.7 for silicon and the temperature range accessible is 400 °C to 1300 °C.

3.2.3 Film Thickness Monitoring

Once a clean substrate surface has been achieved, thin films of metals can be deposited using molecular beam epitaxy. The careful control of pure metal atoms being laid down layer by layer allows the engineering of new interfaces and surfaces. To control the film growth the metal sources are calibrated using a quartz crystal microbalance (QCM) which is positioned in the same place or as close to the sample substrate as possible. The QCM measures the rate of frequency change as the source deposits material on to the crystal, as a change in mass of the crystal causes a change in the oscillation frequency. By calculating the mass of material required to form a unit cell of silicide on Si(111), the frequency change required for a monolayer (ML) coverage can be calculated. This enables a ML rate to be calculated from the rate of change of frequency for the material being deposited, assuming the rate is constant.

3.2.4 Types of Deposition Sources

A variety of deposition sources have been used to grow different materials in the various vacuum systems.

Basic Metal Sublimation Source

Designed and built in the department, this is a very simple source where a piece of material is held in a tantalum boat through which a high current is passed, typically up to 25 A. The source is water cooled by two hollow copper feedthroughs, which also carry the current and inside these are plastic water return tubes. These cool a copper shroud which is enough to protect the surrounding chamber from heating up; the shroud also helps to collimate the material beam. Obviously this method only works for metals which sublime and have a vapour pressure at temperatures lower than that of tantalum. These types of sources have been utilised for erbium and manganese. Typically a deposition rate of 0.1 ML per minute for a rare earth metal and a rate of 1 ML per minute for Manganese has been used. This source can also take filaments of material, and has been used with titanium to cap samples for Transmission Electron Microscope (TEM) preparation by Jeremy Mitchell.

E-beam Sources

Two types of e-beam source have been used, an Omicron EFM3 and a Mantis Quad source. These can accept crucibles or rods and have been used for gold and nickel primarily. These sources work by bombarding the material, or crucible containing the material, with high energy electrons which are thermally emitted from a hot thoriated filament and accelerated with a voltage onto the material in the region of 1 kV. The Ni rod EFM3 source was able to achieve a deposition rate of up to $\sim$1.5 Å/min.

Balzers Source

The Balzers source is a larger e-beam source, so can deliver a fast deposition rate of angstroms per second. Two large cooled crucibles hold targets of material to be evaporated; an electron beam accelerated by 6 kV from a tungsten filament is steered towards the material. Careful control of the emission current enables the material to evaporate at a steady rate.

Atomic Hydrogen Source

Designed and built for my undergraduate final year project, the atomic hydrogen cracker works by heating a tungsten capillary by e-beam heating to $\sim$2000 °C, through which molecular hydrogen is passed. The high temperature tungsten enables the dissociation of hydrogen molecules to form a collimated beam of atomic hydrogen. This source is used to hydrogen-terminate samples, passivating the surface.

3.3 Vacuum Systems

3.3.1 The Molecular Beam Epitaxy System

The MBE system is able to deliver a fast deposition rate from the Balzers source, which was essential for the growth of $NiSi_2$. The system is pumped by a Varian V-550 turbomolecular pump with a base pressure of 1×10^{-9} mbar. During deposition, liquid nitrogen cryopumping is enabled which helps to maintain the pressure around 1×10^{-7} mbar. The system has a fast entry lock for easy transfer of samples and a RHEED system for surface

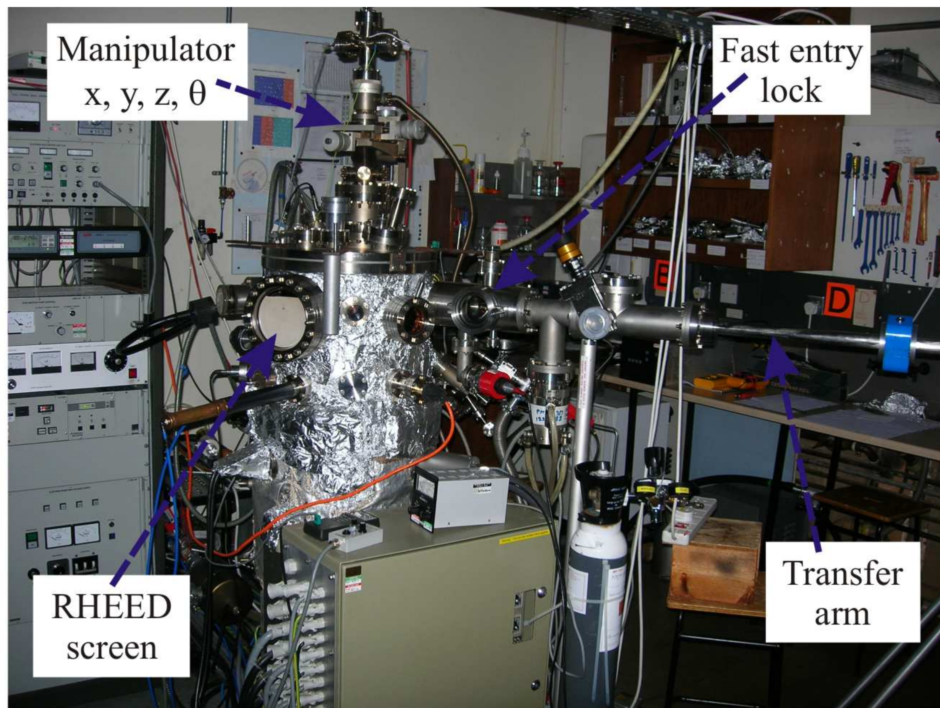

(a)

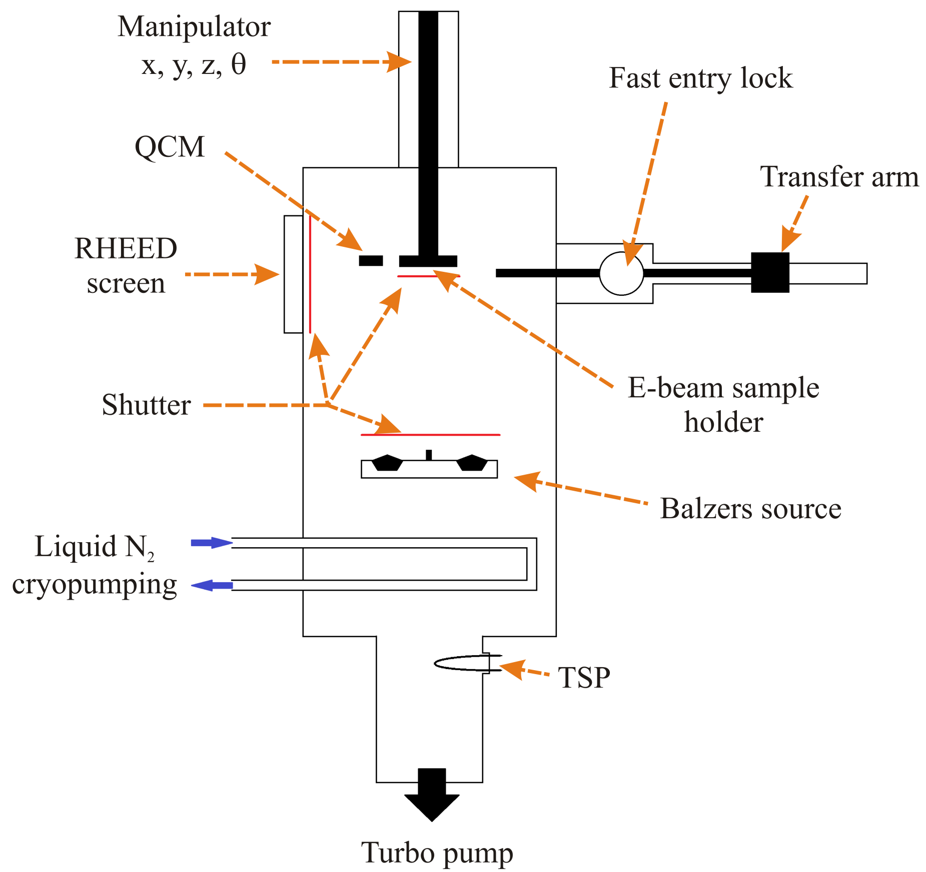

(b) SIDE VIEW

Figure 3.3: Images of the MBE system. a) Image of the MBE chamber, b) Schematic of the MBE system from the side.

characterisation. However, the only sample heating method able to reach a high enough temperature to flash clean silicon is e-beam. The system schematic is shown in figure 3.3.

The MBE system was used for the growth of $NiSi_2$ on Si(111). Deposition sources on the MBE could deliver a fast deposition rate of the order of 0.5 Å/s which was required to form the different interface terminations of $NiSi_2$ on Si(111). The higher deposition rate was required to reproduce the reaction dynamics reported by Tung.[71] The deposition rate was measured using a quartz crystal microbalance which is mounted next to the sample manipulator at the same distance from the source. The sample plate could easily be adapted to hold a mask with holes of different diameter.

Masking the sample

To control the contact area of the Schottky barrier, a mask with varying hole sizes ranging from 1 mm to 0.25 mm in diameter was developed as seen in figure 3.4. The mask had to be set away from the sample to allow the silicon to outgas and not recontaminate during flashing which was done by e-beam heating the back of the silicon.

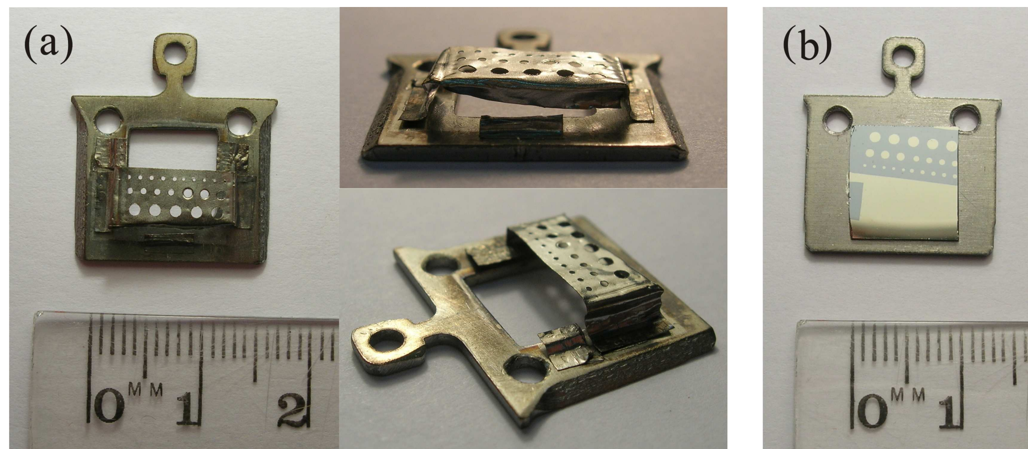

Figure 3.4: a) Image of the mask attached to a sample plate from 3 angles to show the raised mask and clips to secure the silicon substrate, b) Image of a sample grown with the mask now mounted on a blank sample plate for transport to Leeds.

3.3.2 The York Omicron STM System

The York Omicron STM system shown in figure 3.5 provides a very flexible growth chamber combined with several analysis options, providing a powerful tool. The STM is bolted to a preparation chamber which has a large variety of material sources allowing the growth

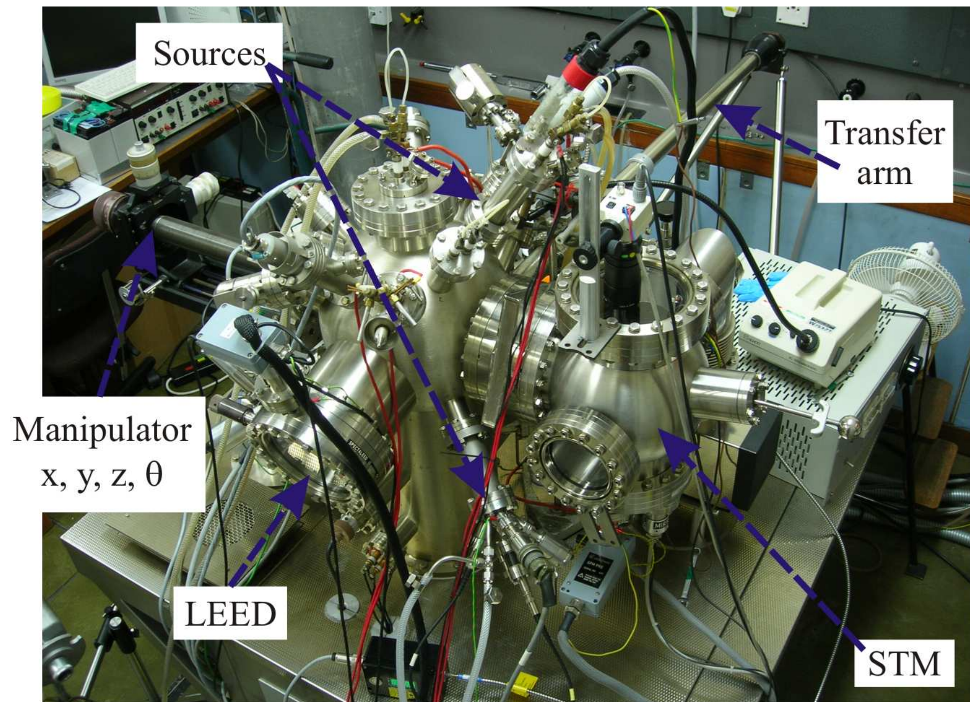

(a)

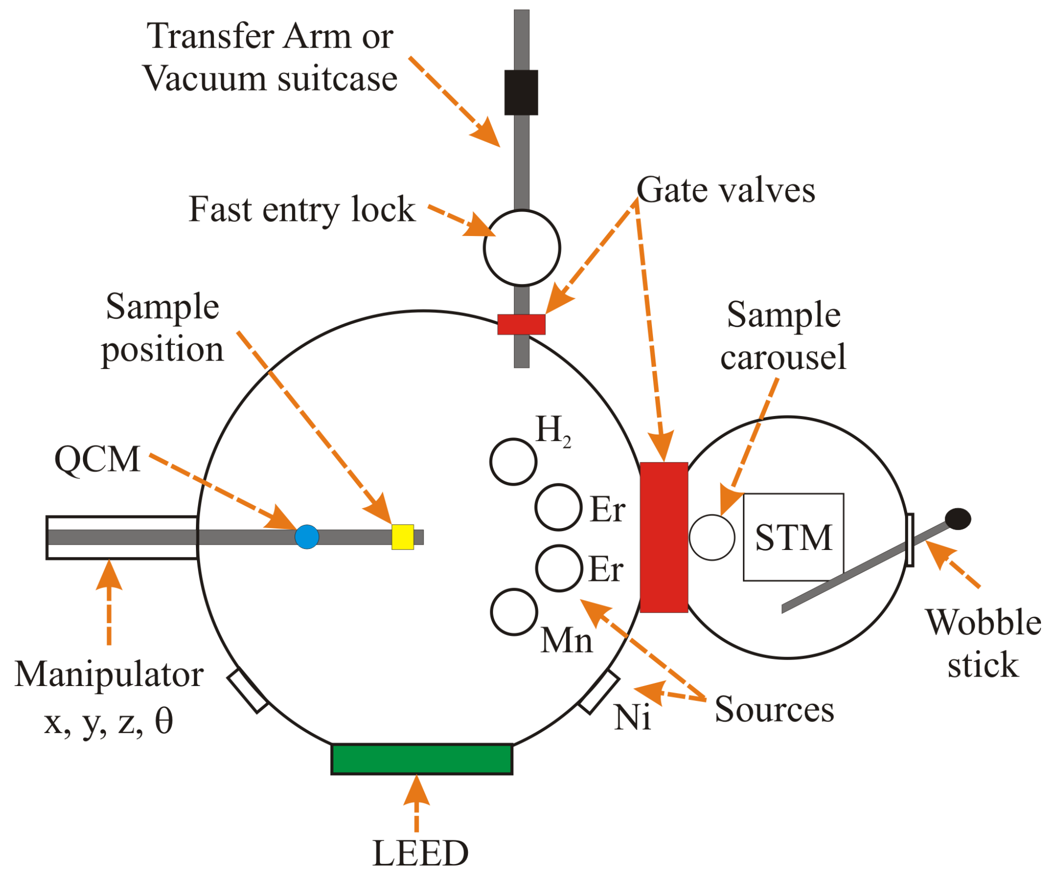

(b) PLAN VIEW

Figure 3.5: a) Image of the STM system, b) Schematic of the STM chamber, plan view.

of a wide range of materials in a vacuum of 1×10^{-10} mbar, which is maintained by two Varian ion pumps and a Titanium Sublimation Pump (TSP). The manipulator allows both direct heating and e-beam heating of the sample. The QCM is mounted on the manipulator 55 mm from the sample position allowing calibration of the source at the exact sample position before the sample is moved into position. The manipulator is also equipped to provide cooling *via* nitrogen gas cooled by liquid nitrogen. This can achieve temperatures down to 100 K for the growth of manganese islands on a rare earth 2D layer. To check all the stages of growth, LEED is available for sample characterisation as well as the STM itself. A fast entry lock enables the easy transfer of samples and can be replaced to allow the coupling of a vacuum suitcase for sample transport to other systems, especially the Omicron Nanoprobe in Leeds.

3.4 Interface Characterisation

3.4.1 Omicron Nanoprobe

LENNF provide access to an Omicron Nanoprobe *via* application for time. Substantial use of this facility has been made to allow contact probe measurements in UHV on nanoisland surface features. The Nanoprobe consists of a fast entry lock which will accept the coupling of the vacuum suitcase and the analysis chamber as can be seen in figure 3.6. The Nanoprobe is four STM tips, two of which are capable of imaging; these are all controlled by piezoelectric crystals for fine movement. The sample stage temperature can be varied by liquid helium using a flow cryostat and a heater, allowing measurements to be taken at several temperatures within the range of 25-450 K.

To guide the tips, the Nanoprobe is fitted with a Zeiss Gemini FEGSEM column which is in UHV so provides a much cleaner environment than the FEI SEM in York. The Gemini column does not achieve the few nanometre resolution seen in other instruments because the working distance of the microscope is longer than normal as it is hindered by the space needed for the STM tips to fit under the SEM column. This means the resolution is tens of nanometres and contrast can be lost due to the presence of the STM tips under the SEM column. The Gemini SEM column provides real time imaging which allows the tips to be manoeuvred into place over a nano structure; even with the SEM it is still very challenging to position a tip let alone four tips on a nano island. A normal

automatic tunnelling approach is performed before manual control is taken for the final approach to contact. This is possible because the amplifiers are not in-vacuum so can be easily bypassed. The I/V curves are taken using a Keithley 2400 sourcemeter to provide the voltage bias and a Keithley 6514 electrometer to measure the current. The Keithley instruments are controlled by in-house software to acquire I/V curves.

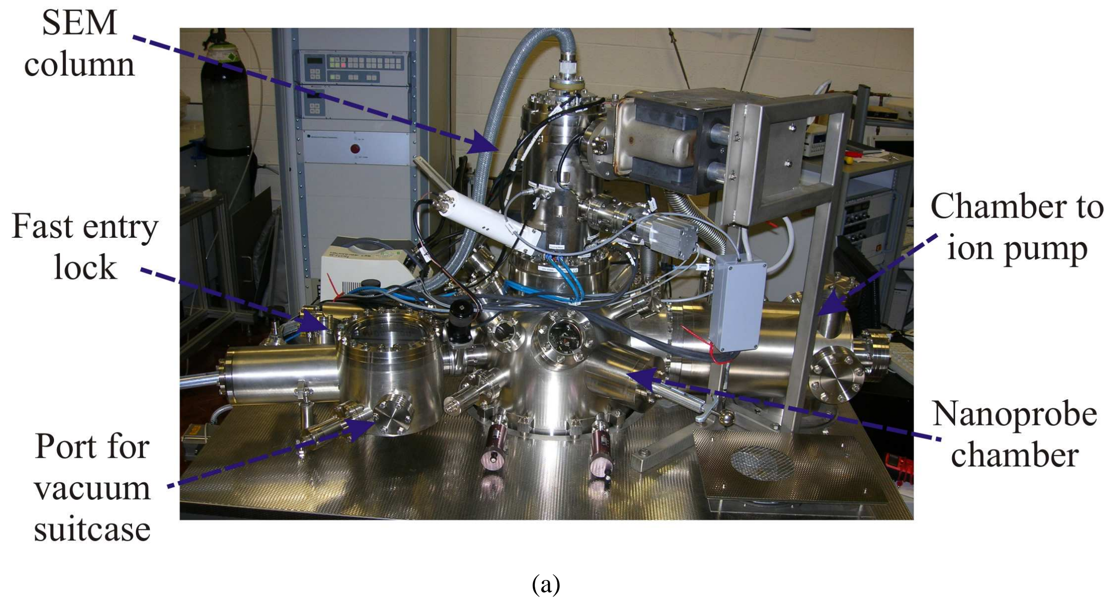

(a)

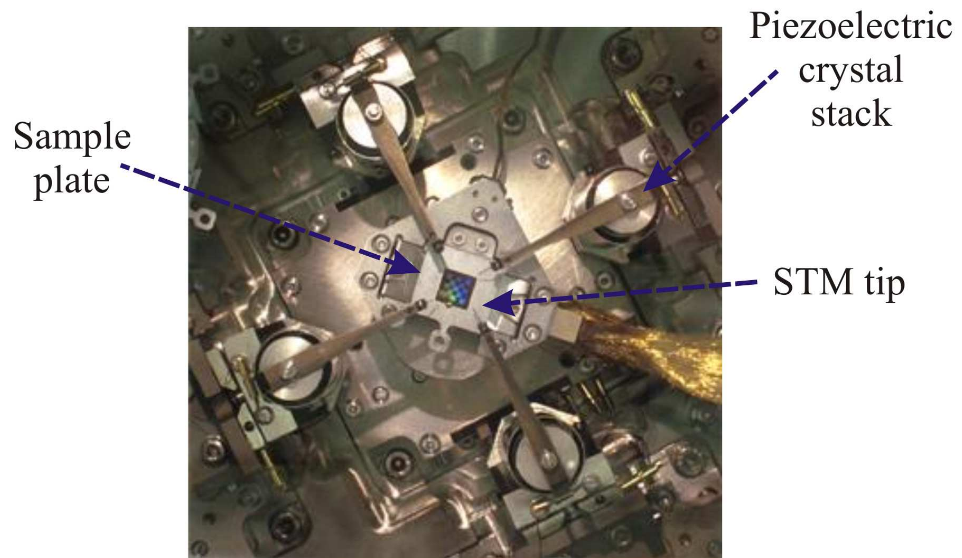

(b)

Figure 3.6: a) Nanoprobe vacuum chamber, b) Four piezoelectric crystal stacks holding the STM tips above the sample.

Vacuum suitcase

A vacuum suitcase is crucial to the transport of samples from York to Leeds in what is believed the first vacuum sample transport between the two universities. The vacuum suitcase shown in figure 3.7 was bought off the shelf from Omicron with the Leeds Nanoprobe system. It consists of a small chamber containing a grab arm which is pumped by a 24 V battery operated ion pump, keeping the pressure in the region of 5×10^{-8} mbar. This allows careful transport by car of one sample at a time in near UHV from the York STM instrument to the Leeds Nanoprobe.

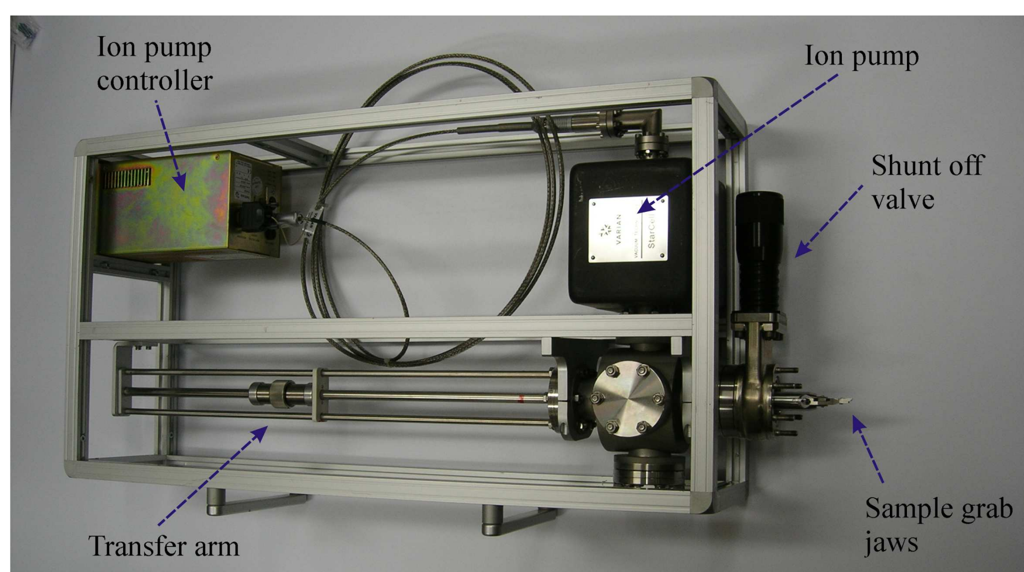

Figure 3.7: Image of vacuum suitcase, 24 V battery not included.

3.4.2 I/V Measurements

The majority of I/V measurements for this project have been taken in the Nanoprobe in Leeds with some testing done in York with an on the bench set up. The Nanoprobe uses tungsten STM tips to make contact to structures on the sample surface. A measurement can be taken between two tips or between one tip and the back contact on the silicon substrate. This back contact is either a silver dag connection between the silicon and the sample plate or a tantalum clip on a DC heating plate.

The Nanoprobe uses a Keithley 2400 sourcemeter to provide the voltage bias and a Keithley 6514 electrometer to measure the current or two electrometers if a 4 point measurement is required. The in-house software controls the sweep parameters including volt-

age range, point density and compliance. The sweep runs from 0 V up to the maximum positive voltage, down to negative voltage then returns to zero, completing the loop. Most I/V sweeps are taken from a maximum voltage range of 3 volts with 100 data points per quadrant, which takes approximately 20 sec. A 500 data points per quadrant scan over a ± 1 V range has also been taken for some samples. The compliance (maximum supplied current) is set as low as possible according to each sample to allow the most precision for the measurement. The error in the individual data points is minimal, at 0.0005% error in the current measurement and very smooth curves are produced if a good contact is made to the surface. There is a systematic error in the data which means at 0 V there is a small amount of current recorded, this is corrected for by subtracting this current off the whole data range.

In York a Keithley 2601A sourcemeter with the provided software, TSP express, was used to take I/V curves across the contacts on a DC plate while in the STM vacuum system. This was used to find the electrical properties of the back contact before transport of the sample to LENNF. Here, the sweep went from negative to positive voltage only using 200 data points to keep the data density the same as from the Nanoprobe.

Two Point Probe Measurements

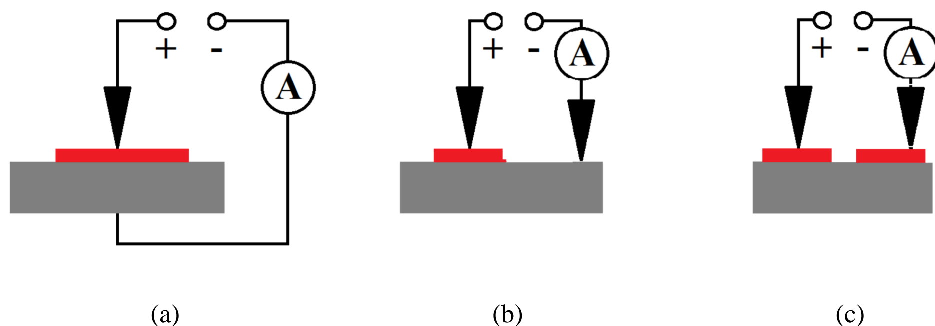

Figure 3.8: Two probe contact geometries for I/V collection, a) Tip on surface feature to back of substrate, b) Tip on surface feature to tip on silicon substrate, c) Two tips on different surface features, only connected by the substrate.

The majority of I/V data was taken from a two contact geometry. Figure 3.8 shows the possible contact geometries of, one tip on a surface feature and the second contact the sample plate, one tip on the surface feature and a second tip on the silicon substrate within a few microns of the feature and two tips on different surface features, only connected by

the substrate. This could be, for example, two self ordered islands close to one another.

Four Point Probe Measurements

By placing two tips onto the same surface feature, as shown in figure 3.9a, the resistance can be found. However, the resistance in this geometry also includes the contact resistance of the tips, which will be different for each new contact made. By using a four probe geometry, as shown in figure 3.9b, and supplying the current to the outside two tips and measuring the voltage from the middle two, the I/V can be taken without the problems of contact resistance. It is assumed that any substrate conductivity contribution is negligible due to the high resistivity of the silicon substrate and any potential barrier formed between the island and the substrate.

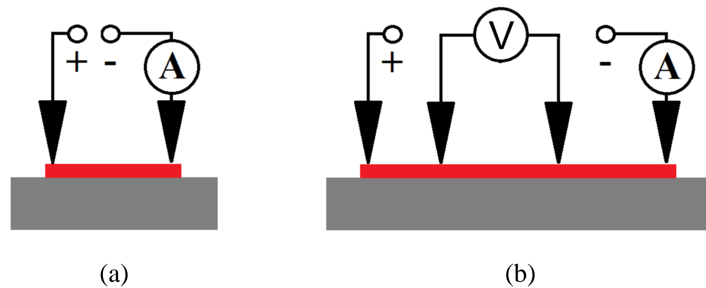

Figure 3.9: Two and four probe contact geometry for measuring resistance a) Two probes connected to the same surface feature, b) Four probe geometry for I/V measurement, current supplied to outer two tips and voltage measured from the centre tips.

Van der Pauw Measurements

In 1958 L. J. van der Pauw proposed a method to measure the sheet resistance of a thin film of arbitrary shape.[72] This method allows the sheet resistance and resistivity to be gained from four contacts made onto the edge of an arbitrary shaped thin film which contains no holes.

Setting up the four contacts as shown in figure 3.10, two resistances can be defined as:

$$R_{14,23} = \frac{V_{14}}{I_{23}}, \qquad R_{43,12} = \frac{V_{43}}{I_{12}}, \tag{3.1}$$

where V_{ij} is the potential difference between contacts i and j. Likewise, I_{ij} is the magnitude of current driven from contact i to j. The sheet resistance R_s can be calculated

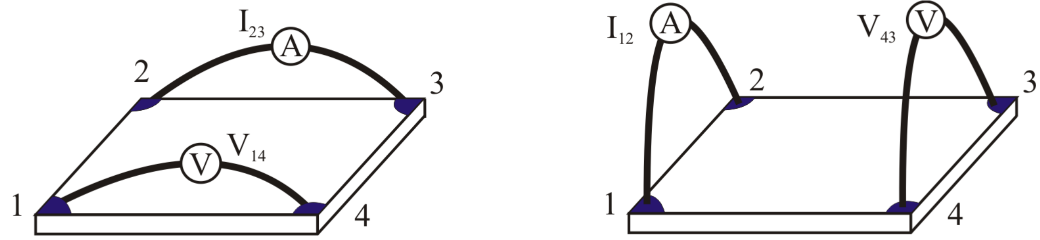

Figure 3.10: Van der Pauw contact measurements to acquire two resistances.

iteratively by solving the following formula,

$$\exp\left(-\frac{\pi R_{14,23}}{R_s}\right) + \exp\left(-\frac{\pi R_{43,12}}{R_s}\right) = 1. \tag{3.2}$$

The resistivity ρ can then be calculated if the thickness d of the film is known using,

$$\rho = R_s d. \tag{3.3}$$

3.4.3 Transmission Electron Microscope

The structures presented in this thesis have been studied using TEM in collaboration with Jeremy Mitchell. After I had grown and taken I/V data at LENNF, the samples were passed to Jeremy, further repeat samples for TEM were grown in collaboration. TEM uses higher energy electrons (typically $\sim$200 keV) than SEM to pass a parallel beam of electrons directly through a thinned sample allowing diffraction patterns and columns of atoms to be imaged.[73] Using the York JEOL Nanocentre's aberration-corrected scanning TEM, the interface structure has been imaged by Jeremy. This requires a cross section sample to be prepared which means the sample has to be painstakingly thinned to a few tens of nanometres.

Chapter 4

Application of Analysis Methods to Nickel Silicide-Silicon Interfaces

Once an I/V curve has been collected, the task of extracting the Schottky barrier height (SBH) can begin. As we have seen in chapter two there are many things which can alter the I/V curve from the rectifying behaviour of thermionic emission, including series resistance, shunt resistance and tunnelling in the reverse bias. This chapter sets out to show some methods to analyse experimental I/V curves, starting with the very simple assumption that the only transport mechanism is thermionic, then developing the methods further to include series and shunt resistance, extracting the SBH with some plots designed to give a large linear section from the plotted data. Finally we have used a fitting routine to fit a more complex arrangement to include back to back SBs and various resistances. These different methods are applied to the test system of $NiSi_2$ on n-type Si(111) as a way of comparing the methods and testing the fitting program to be used in later studies.

4.1 The $NiSi_2$-Si Interface

As a material which has been studied extensively over the years, $NiSi_2$ is well documented in the literature making it ideal for a test material. With good control over epitaxial growth, single crystal homogeneous $NiSi_2$ - Si interfaces can be grown providing reliable, reproducible SBH measurements. The fluorite (CaF_2) structure of $NiSi_2$ can be grown epitaxially on Si(111) producing an atomically abrupt interface. This is possible because of the 0.4% lattice mismatch between the silicon substrate and the $NiSi_2$. The lattice constant of Si is 5.429 Å and the $NiSi_2$ is 5.406 Å producing the very low lattice mismatch and

structurally ordered, defect free interfaces.[19] One of the most attractive reasons, beside the low lattice mismatch, for us to use the $NiSi_2$ - n-type Si(111) interface is a difference in SBH of 0.14 eV between two interface orientations.

4.1.1 Background

The importance of the interface structure on the SBH was first realised with the $NiSi_2$ n-type Si(111) interface by Tung in 1984.[20] The $NiSi_2$-Si(111) interface can form two different interface structures which differ by a 180° rotation producing the A or B-type interface. Experiments showed the difference in SBH between type A and type B interface to be 0.14 eV as the measured SBH are 0.65 eV and 0.79 eV for A type and B type respectively. It is also interesting to note that $NiSi_2$ on Si(100) has shown barriers 0.25 eV lower than the A type $NiSi_2$ Si(111) interface.[74] This striking result of SBH for a very simple 180° interface rotation lead to some heated debate. Liehr et al argued that there is no difference between SBH for A and B type showing repeated measurements with both interfaces yielding SBH of 0.78 eV.[75] Liehr claimed that the difference seen by Tung was due to defects or other disorders at the interfaces.

The difference has been experimentally confirmed by Tung,[76] and others,[77–79] but some doubt about the perfection of the interfaces still arose. It was theoretical calculations which solved the debate, as they showed there was a difference in SBH between the two interface terminations. This was done by using experimentally determined structures in ab initio calculations to provide a difference in SBH between the B type and A type $NiSi_2$ interfaces of 0.15-0.17 eV.[80,81] These calculations do not provide accurate absolute SBH probably due to the local density approximation assumed in the calculations. The calculations are however able to provide an accurate difference between A and B type as the same unit cell was used in both cases cancelling out any systematic errors. The difference seen between the SBH of A or B type on Si(111) and the SBH of $NiSi_2$ on Si(100) has not been reproduced by these calculations because of the inaccurate absolute SBH. Many groups have tried to find a solution to the absolute SBH and have put the difference between experimental and theoretical values down to defects not present in the model,[82–84] and the fact the structural lattice relaxation is a crucial part of density functional theory (DFT).[19]

$NiSi_2$ is a material of interest due to its close lattice match with silicon providing

well ordered interfaces. Recent work, see Woodruff,[85] use it as a Schottky contact to Si nanowires to determine the SBH of nanoscale contacts. Also $NiSi_2$, with the addition of platinum and sulphur, is allowing the engineering of very low SBH of the order of 0.1 eV on n-type silicon.[86]

4.1.2 Interface Structure of $NiSi_2$-Si(111)

The atomic structure of high quality A-type and B-type $NiSi_2$ - Si interfaces have been studied by several different experimental techniques.[77,87–90] The work by Vrijmoeth,[77] using medium energy ion scattering (MEIS) was critical in showing that the difference in SBH between the two interface orientations was not due to defects but to the interface geometry. An azimuthal rotation of 180° is the only difference between the two forms of interface. A-type silicide has the same orientation as the underlying Si substrate whereas B-type is rotated 180° about the Si(111) surface normal, see figure 4.1.

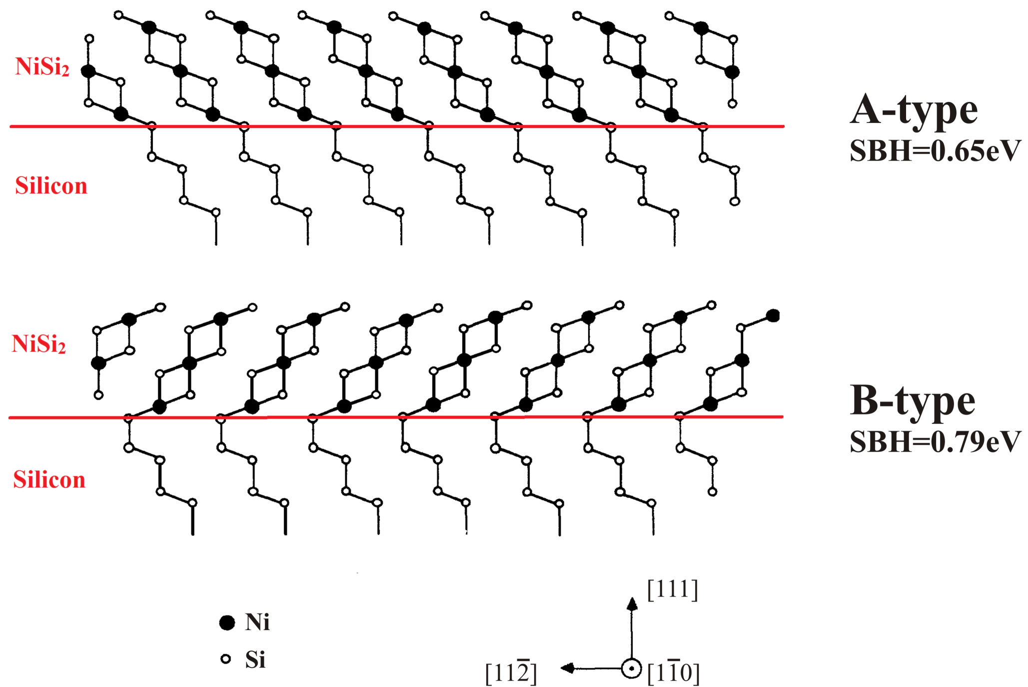

Figure 4.1: A-type and B-type $NiSi_2$ structure showing the 180° rotation at the interface.

This subtle interface difference would not be observable with STM, a technique such as TEM would be required to image the interface.[91] However LEED can provide some clues as to the interface termination. The 1×1 LEED image shows a 3 fold rotation seen in figure 4.4a which would alter with the 180° interface rotation. This fingerprint could

be taken using LEED-IV to give an idea about the interface termination and the amount of A and B type mixing.[90] The difference in the geometry of the bonds at the $NiSi_2$ - Si interface leads to a difference in charge density distribution which causes the difference in SBH between the two interfaces.

4.1.3 Growth

Tung has published many papers and reviews on the subject of $NiSi_2$ growth.[92,93] Tung initially showed the difference in SBH between the two interfaces of $NiSi_2$ after refining the growth technique in the preceding years.[71,94] The interface orientation is dependent on the amount of nickel deposited onto the surface as summarised in figure 4.2 taken from Tung.[71] Tung's work is the accepted growth method with most groups citing his work and following a very similar process to achieve the interface termination required. Tung uses a Ni deposition rate in the region of 0.7-1.5 Å/s with a subsequent annealing at 450 °C to 500 °C for ∼1 minute to form the silicide with the termination dependent on the original Ni thickness.

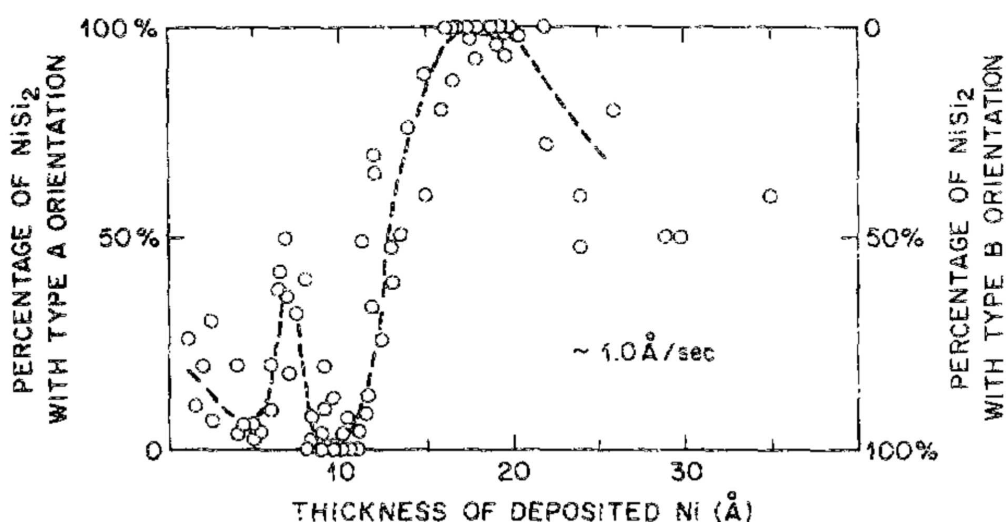

Figure 4.2: The variation of $NiSi_2$ orientation as a function of deposited nickel thickness. Nickel depositions are maintained at 0.7-1.5 Å/s with a subsequent annealing at 450 °C to 500 °C for ∼1 minute. Image and caption taken from Tung.[71]

In our work to achieve different samples with different interface terminations we altered the thickness of nickel according to Tung's method using 10 Å for B-type and 18 Å for A-type. Initially the growth of $NiSi_2$ was done in the growth chamber of the STM system but the deposition rate of the Ni source was low, around 0.026 Å/s. The interface

produced was assumed to be B-type as this is the most favourable but there was no indication of a change using the thicker A-type growth from the LEED observations, so the move to the MBE system was made to make use of the higher rate deposition sources. Although growth was at a higher chamber pressure and the Si could only be cleaned using e-beam, the growth rate could reach 0.5 Å/s. The use of the MBE system also allowed the adaption of the plates to add the mask controlling the area of the contacts.

Silicon Substrate

Cleaning the n-type Si substrate surface was achieved by flashing the silicon using DC heating in the STM growth system and e-beam heating in the MBE system. After outgassing the silicon overnight at 600 °C the temperature is cycled three times between 1200 °C for 30 s and 900 °C for a minute. Then to form the 7×7 reconstruction a slow cool down to 700 °C of ∼10 °C every 15 s was performed. The quality of the reconstruction is indicated by LEED in the STM system and RHEED in the MBE system as shown in figure 4.3. The LEED and RHEED images were judged by the quality of the pattern, how focused and sharp the diffraction spots are, that the contrast is sharp with minimal background from scattered electrons, if the primary spots are more intense than the secondary spots and that there is no streaking of the spots. The indication that a 7×7 surface is achieved is the presence of six extra spots between each primary spot, showing the surface reconstruction is seven times larger than the bulk silicon substrate. Once a clean surface is achieved the deposition is carried out as soon as possible to reduce contamination.

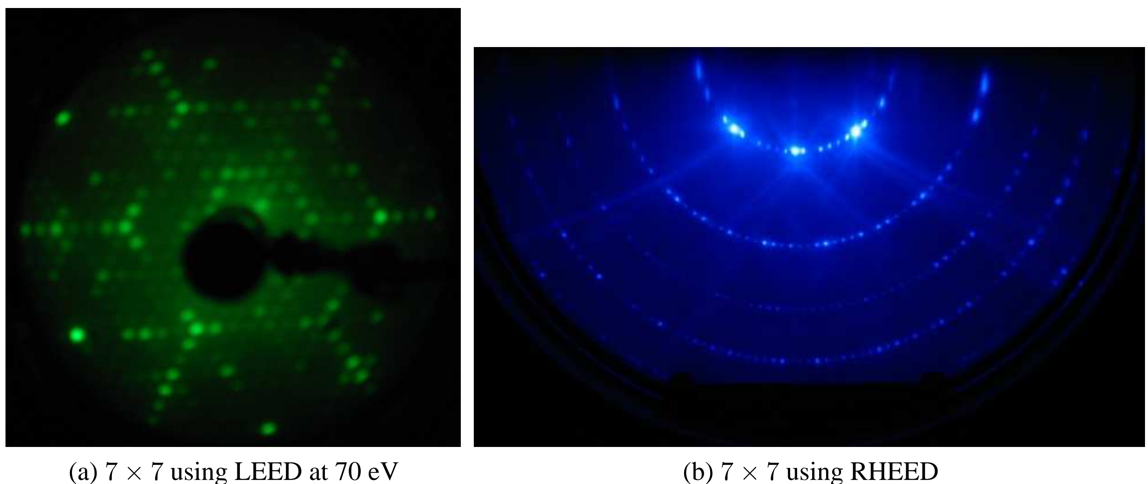

(a) 7×7 using LEED at 70 eV (b) 7×7 using RHEED

Figure 4.3: LEED and RHEED images of the Si(111) 7×7 reconstruction, showing the extra 6 diffraction spots between each brighter primary spot.

B-Type Interface

To create a B-type interface termination, 10 Å of nickel was deposited onto clean Si(111) at a rate of 0.5 Å/s. This was then annealed for 10 mins at 650 °C producing a 1×1 LEED or RHEED pattern as seen in figure 4.4 with no fractional spots observed. The quality of the surface reconstruction was judged by the quality of the LEED/RHEED image as it was for the silicon substrate. The $NiSi_2$ has almost the same size lattice as the bulk silicon, therefore the LEED/RHEED diffraction patterns should only show the 1×1 spots, any extra spots mean that a different reconstruction is present. The LEED image 4.4a shows the 3-fold rotation in the primary spots as three of the primary spots are more intense than the other three. This difference in intensity between primary spots changes with the electron beam energy; this is what is used in LEED-IV to fingerprint the surface.

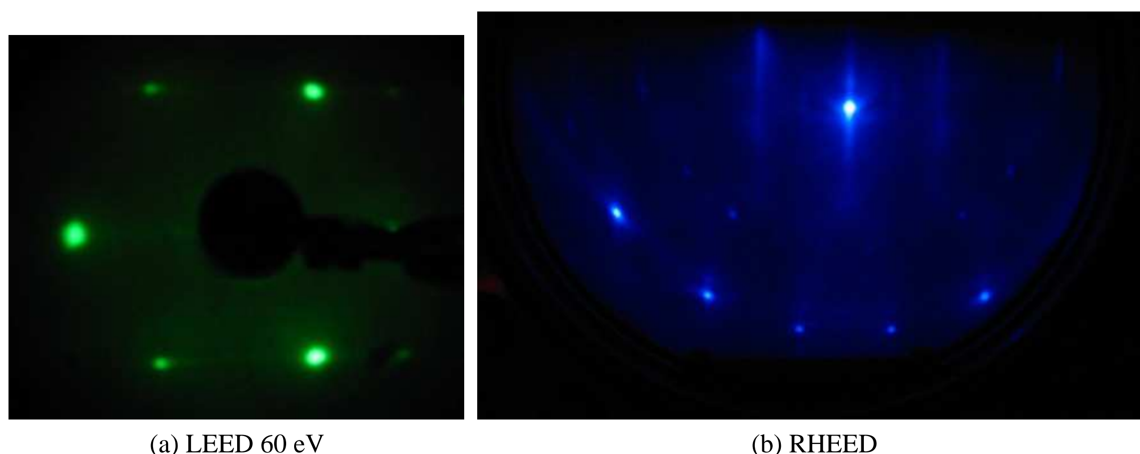

(a) LEED 60 eV (b) RHEED

Figure 4.4: LEED and RHEED 1×1 $NiSi_2$ - Si(111).

A-Type Interface

To create an A-type interface termination 18 Å of Nickel was deposited onto clean Si(111) at a rate of 0.5 Å/s. As for B-type, this was also annealed for 10mins at 650 °C also producing a 1×1 RHEED pattern. At the same beam energy the A-type 1×1 LEED pattern should show the opposite three spots to the B-type being more intense. The Si substrate was loaded into the system in the same orientation for both samples to observe this change. The comparison between the intensity of spots not only tells us the interface orientation but indicates the interface mixing. If all six spots are the same intensity at a beam energy known previously to give a 3 fold pattern, both interface terminations can be assumed to be present in equal amounts of area.

Capping and Nickel

In an attempt to protect the $NiSi_2$ layer from contamination which may affect the interface structure and to make the film thick enough that the Nanoprobe tips did not puncture through to the interface, some samples were further capped with 500 Å of Ni. This was deposited at a rate between 0.5 Å/s and 1 Å/s producing a polycrystalline covering layer. Also samples of polycrystalline nickel were grown by deposition of 10 Å onto the clean Si surface without any annealing. This Ni sample was grown to find the SBH of a polycrystalline interface enabling a comparison to the ordered interface types. It could also indicate if the capping layer of polycrystalline Ni had affected the underlying contact.

These different samples based on Tung's work on $NiSi_2$ were produced to test the Nanoprobe's I/V collection and analysis techniques. We also aimed to produce the SBH's Tung reported for A-type (0.65 eV) and B-type (0.79 eV).[20,95]

4.1.4 I/V Measurement

Five different samples were grown in the MBE system and taken over to LENNF in atmosphere. These were, B-type capped and uncapped, A-type capped and uncapped and Ni on Si(111) with no anneal. These were mounted on Omicron sample plates with silver dag. All the samples were grown with the mask giving known contact diameters of 250 μm, 500 μm and 1000 μm. These could clearly be seen in the SEM as shown for a 250 μm diameter dot in figure 4.5. This shows the masked growth of the $NiSi_2$ which confines the area but does not produce a necessarily clean edge as you can see an extra ring on the SEM image of this spot.

I/V data were taken from a selection of contacts using a tungsten tip in contact with the $NiSi_2$ dot. The geometry of the measurement is shown in the inset of figure 4.6 showing the second connection is to the back side of the silicon substrate. The I/V curve for a 250 μm diameter B-type dot is shown in figure 4.6 and this data will be used in the following discussion comparing analysis methods. The I/V curve shows characteristic rectifying behaviour of a single Schottky barrier but the reverse bias clearly does not saturate.

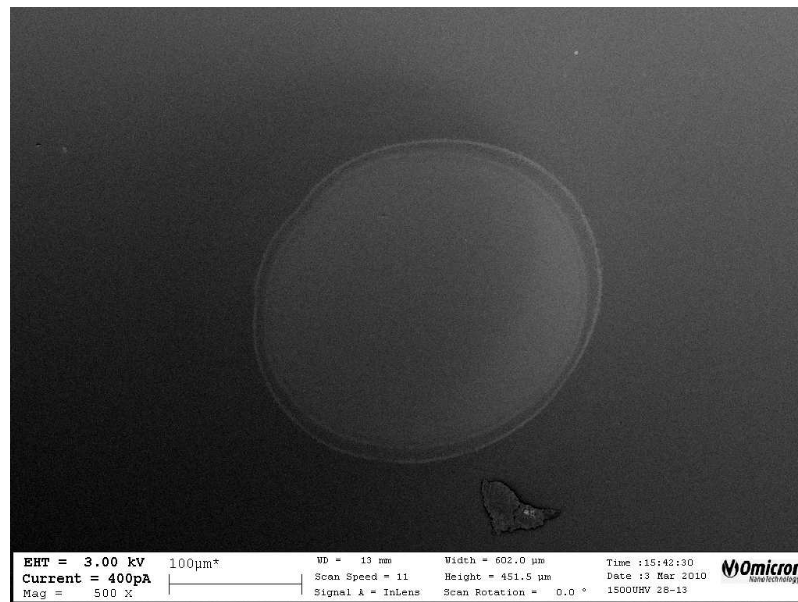

Figure 4.5: SEM image of 250 μm diameter B-type $NiSi_2$ - Si(111) contact, taken in the Nanoprobe.

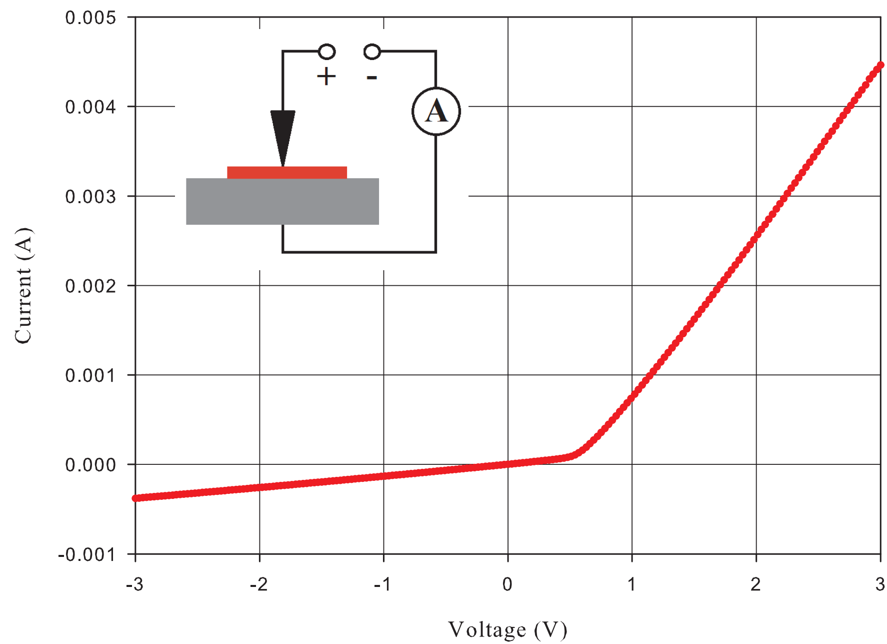

Figure 4.6: Raw I/V data taken from a 250 μm diameter B-type $NiSi_2$ dot. Inset measurement geometry of tungsten tip contacting $NiSi_2$ and out the back of the silicon substrate.

4.2 Graphical Fitting Methods

Graphical fitting methods involve finding ways to plot the data to give access to a linear fit which can provide the SBH. If the SB is well behaved and follows pure thermionic emission this is a straight forward task as a log-linear plot will provide a straight line. As more deviations from thermionic emission are added to the theory, access to the SBH becomes more challenging as any linear region is reduced. Some of these plotting techniques are described in the following sections taking into account series and shunt resistance.

4.2.1 Logarithmic I/V Plots

As thermionic emission is governed by an exponential term, by far the easiest route to SBH extraction is to plot the data on a log-linear scale. This does assume the data has been taken from a pure thermionic emission SB diode which is rarely the case.

Ln(I) against V

Taking the equation for thermionic emission including the ideality factor, equation (2.18), and simplifying it for values of V greater than $3kT/q$, it can be written as:

$$I = SA^{**}T^2 \exp\left(-\frac{q\phi_e}{kT}\right) \exp\left(\frac{qV}{nkT}\right), \tag{4.1}$$

then taking the log of both sides and putting in the form of $y = mx + c$ we can obtain values for n and ϕ_e,

$$\ln(I) = \frac{q}{nkT}V + \ln\left\{SA^{**}T^2 \exp\left(-\frac{q\phi_e}{kT}\right)\right\}, \tag{4.2}$$

this means a plot of $\ln(I)$ against V should give a straight line for forward bias but as can be seen from figure 4.7 it is far from linear for this 250 μm B-type $NiSi_2$ contact. The plot is not linear because not all the applied voltage is dropped across the SB but over some other components in the circuit like a shunt or series resistance. There may also be other transport mechanisms for electrons to overcome the barrier other than thermionic emission for example tunnelling through the barrier or recombination effects.

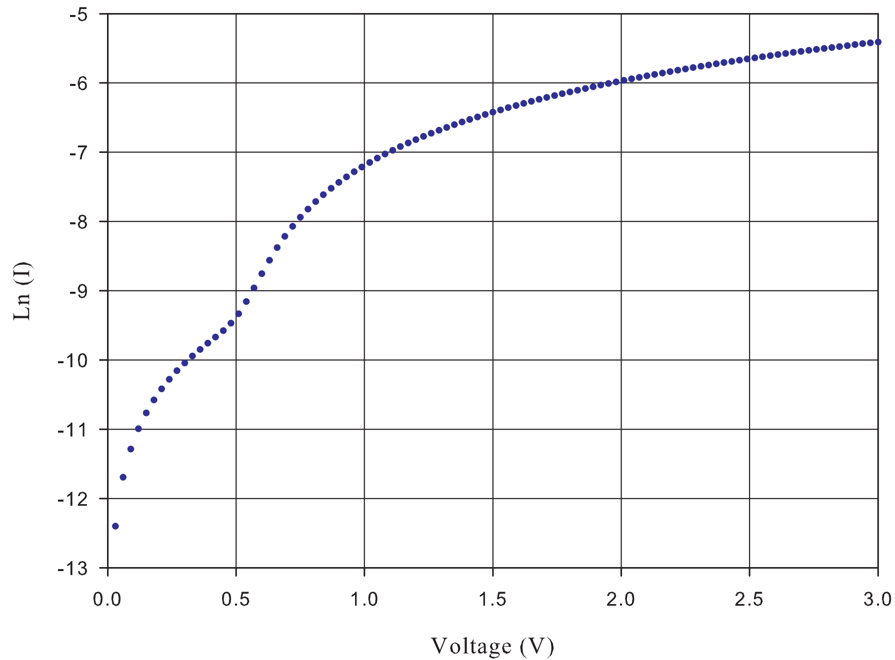

Figure 4.7: Forward bias $\ln(I)$ against V data taken from a 250 μm B-type $NiSi_2$ dot.

Ln(I/(1-exp(-qV/kT))) against V

The simplification above only allows the forward bias to be plotted where V is greater than $3kT/q$. If equation (2.18) is not simplified as above a graph of $\ln(I/(1-\exp(-qV/kT)))$ against V can be plotted. This should give a straight line for all values of V including reverse bias for a thermionic diode. However, a plot for the 250 μm B-type $NiSi_2$ dot shown in figure 4.8 highlights the fact even more that the forward bias data is not from a thermionic diode.

Although there seems to be a straight section in reverse bias this does not continue into the forward bias regime indicating that the whole of the applied bias is not dropped across the SB. When the reverse bias is fitted with a linear least squares fit the gradient and intercept give values of 1.016 ± 0.001 for n and 0.464 ± 0.001 eV for the SBH. Although the ideality factor is good as it is less than 1.1, the SBH is much lower than expected. Taking a small section of forward applied bias between 0 V and 0.6 V and taking a linear least squares fit, a SBH of 0.517 ± 0.002 eV and 8.2 ± 0.5 for n can be obtained. The errors on these values are taken from the mean variance of the fit and are small due to the low noise on the data. Clearly the ideality factor for the forward bias is indicating that this is not pure thermionic emission. The fact that the graph is not a straight line over the

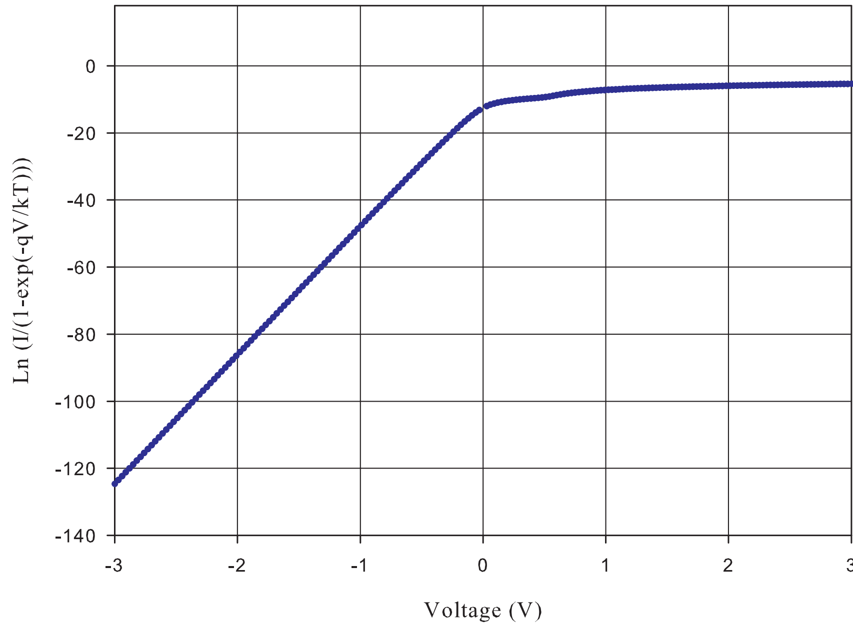

Figure 4.8: $\ln(I/(1-\exp(-qV/kT)))$ against V data taken from a 250 μm B-type $NiSi_2$ dot.

whole voltage range is an indication that this is not a convincing analysis. So there must be another transport mechanism in place, the most likely is a resistance.

4.2.2 Shunt Resistance

The assumption that the only transport mechanism is thermionic emission is clearly insufficient as both log plots produce non-linear curves. The most obvious feature of the I/V graph indicating deviation from pure thermionic emission is the unsaturated reverse bias current. This could be due to shunt resistance. Assuming a single Schottky barrier and a parallel shunt resistance as shown in the inset of figure 4.9 the current is now $I = I_d + I_p$ and a simple correction can be made to the current to obtain only the current through the diode, I_d. Finding a value for the shunt resistance is done by assuming that at high reverse bias all the current is flowing through the shunt resistor, therefore the gradient of the I/V curve is simply $1/R_{shunt} = I/V$. For our 250 μm B-type $NiSi_2$ dot the shunt resistance is found to be 8372 ± 5 Ω. However, depending on which section of the reverse bias is used to fit for the gradient, this value could alter by as much as 500 Ω. This is due to the data from the reverse bias regime not being completely linear possibly because the shunt resistance is dependent on the applied voltage, which could arise from the current causing

heating and therefore a change in the shunt resistance with applied voltage. The data may also not be linear in the reverse bias because there is reverse bias tunnelling or a second SB.

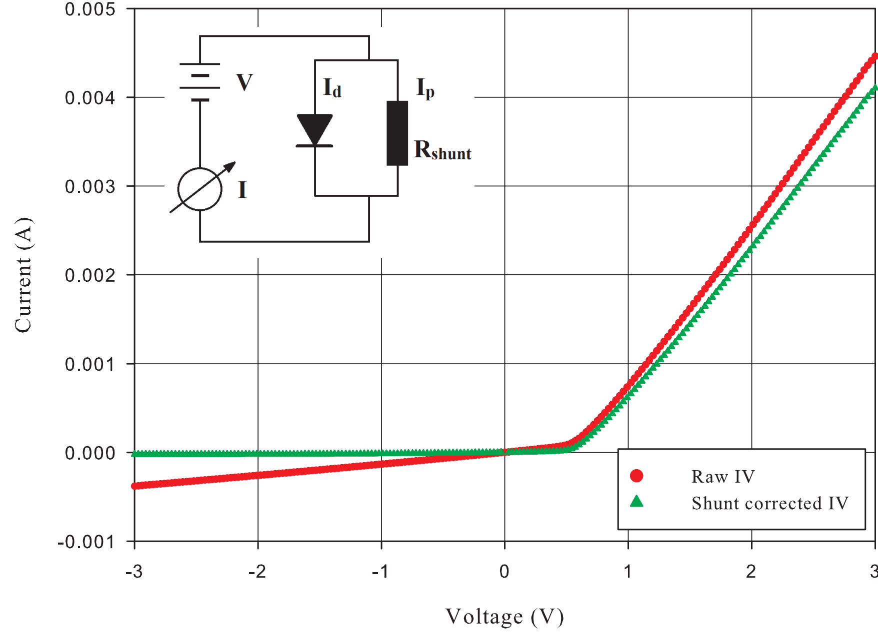

Figure 4.9: Raw I/V data taken from a 250 μm B-type $NiSi_2$ dot, and the corrected I/V data for a shunt resistance of 8372 Ω. The inset is a schematic of the circuit with the SB and shunt resistor.

The current through the shunt resistor, I_p, can be calculated using the applied voltage and the extracted shunt resistance, then the current through the diode, I_d, can be calculated from the measured current $I - I_p = I_d$. The current through the SB diode can now be plotted against applied voltage as shown in figure 4.9. Taking this corrected I/V data and repeating the plot of $\ln(I/(1 - \exp(-qV/kT)))$ against V still does not yield a straight line over the whole voltage range. For the corrected reverse bias a value for the ideality factor of 1.008 ± 0.001 and the SBH of 0.506 ± 0.001 eV can be obtained. However taking the small section of forward applied voltage between 0 to 0.6 V, n can be calculated to be 8.1 ± 0.3 and the SBH to be 0.517 ± 0.002 eV. Although the shunt correction has lowered the ideality factor, making it almost perfect in reverse bias, which is to be expected as the current is saturated, the plot is still not linear over the whole voltage range indicating there are still other mechanisms causing the data to be curved. This is further highlighted by the exceptionally large ideality factor obtained from the forward bias region. The shunt resistance correction has brought the value of the SBH for forward and reverse bias closer

to each other, however, the SBH still does not agree with the expected value.

4.2.3 Series Resistance - Norde Plots

Norde presented a method for the extraction of the series resistance alongside the SBH from an I/V curve.[96] The series resistance will arise from the silicon substrate and provides a second voltage drop, meaning not all the applied voltage is dropped across the SB. Figure 4.10 shows a schematic for the circuit components including the SB, the series resistor, R_{series}, and the shunt resistor, R_{shunt}, which is greyed out as this has been corrected for in the previous section.

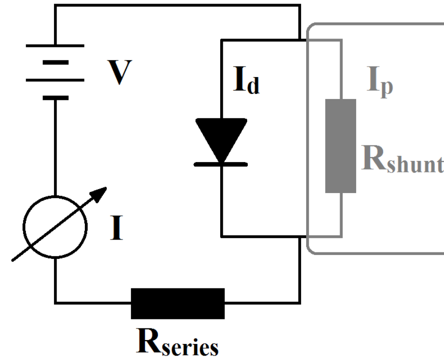

Figure 4.10: Series resistance circuit schematic, the shunt resistance is greyed out as it has been corrected for.

With a series resistance present the straight line part of the logarithmic plot will be confined to a voltage of $kT/q \ll V \ll IR_{series}$ which can prove too small an interval to extrapolate from to gain the SBH. Norde makes use of a plot of the function $F(V)$,[96] equation (4.3) which when plotted shows the turning point between these two voltage regimes:

$$F(V) = \frac{V}{2} - \frac{kT}{q} \ln \left[\frac{I}{SA^{**}T^2} \right]. \tag{4.3}$$

If we assume the SB is not voltage dependent (i.e. $n = 1$) we can write the pure thermionic current from equation (2.4) with the addition of series resistance as,

$$I = SA^{*}T^2 \exp\left(-\frac{q\phi_b}{kT} \right) \left[\exp\left(\frac{q}{kT}(V - IR_{series}) \right) - 1 \right]. \tag{4.4}$$

By combining equations (4.3) and (4.4) when the applied voltage is greater than $3kT/q$ we get,

$$F(V) = \phi_b + IR_{series} - \frac{V}{2}. \tag{4.5}$$

At low applied voltages only a very small current flows, which makes the term IR_{series} negligible, therefore a plot of $F(V)$ against V will have a slope of -1/2. If there is a sufficiently large linear region, ϕ_b could be obtained from the intercept of the extrapolated fit but this is rarely the case. When the series resistance is dominant at high applied voltages, the current is determined by $I = V/R_{series}$ and we can write the function $F(V)$, equation (4.3) as,

$$F_R(V) = \frac{V}{2} - \frac{kT}{q}\ln\left[\frac{V}{R_{series}SA^{**}T^2}\right]. \quad (4.6)$$

This would give a straight line with gradient of +1/2 for high applied bias where the resistance is dominating the current. From these two limits a plot of $F(V)$ against V should give a minimum at the point the gradient changes from -1/2 to +1/2. Plotting the data from the shunt resistance corrected I/V curve in figure 4.9 from our 250 μm B-type $NiSi_2$ dot we find the high voltage gradient is $+0.477 \pm 0.001$ as can be seen in figure 4.11.

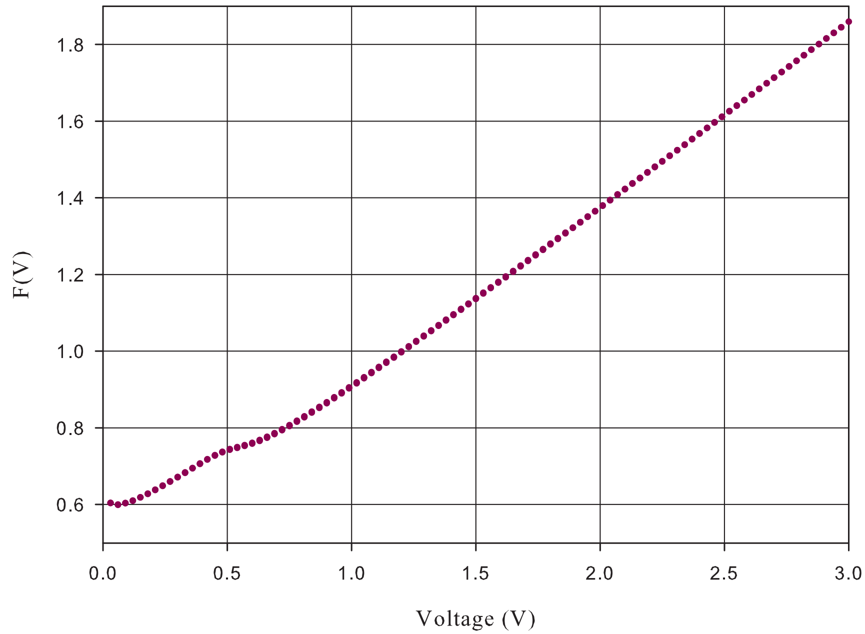

Figure 4.11: Plot of $F(V)$ against V showing the series resistance dominating at high applied bias giving a slope of approximately +1/2.

The turning point can just be seen in figure 4.11 at the very low voltages (~ 0.1 V) but there are not enough data points in this region. Figure 4.12 shows a high density point scan taken over low voltage to show the detail at the turning point, this data was taken immediately after the previous scan. This allows the voltage at the minimum (V_{min})

and the $F(V)$ value at the minimum ($F(V_{min})$) to be determined and the current at the minimum (I_{min}) to be found.

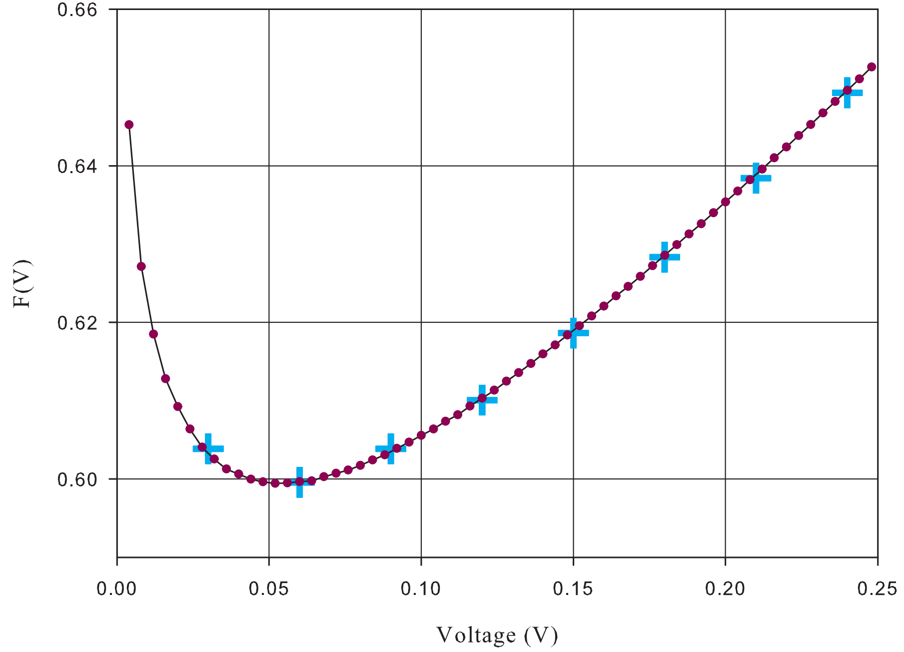

Figure 4.12: Plot of $F(V)$ against V for low applied voltage showing the turning point. The light blue crosses are the original scan with the repeat high density scan in purple circles.

These values acquired from the minimum at the turning point allow the calculation of the SBH and the series resistance using,

$$\phi_b = F(V_{min}) + \frac{V_{min}}{2} - \frac{kT}{q}, \tag{4.7}$$

$$R_{series} = \frac{kT}{qI_{min}}. \tag{4.8}$$

From the turning point on the graph of $F(V)$ against V for the B-type $NiSi_2$ dot in figure 4.12, a value of 0.599 ± 0.001 eV for $F(V_{min})$ and 0.052 ± 0.001 V for V_{min} are found giving a value of 980 ± 40 nA for the current. This in turn gives the calculated SBH as 0.599 ± 0.001 eV and the series resistance as 26 ± 2 kΩ.

This analysis produces a very high series resistance which is much higher than expected as a value for the series resistance less than the shunt resistance is normally observed and expected. The turning point measured from the graph is at 0.052 ± 0.001 V

which is below $3kT/q$ which at room temperature (298 K) is ∼0.077 V. This means that this analysis is not theoretically valid for this data set and could explain the high series resistance. Although the SBH found using the Norde plot is higher than for the logarithmic plot methods it still does not agree with expected values. In addition the Norde method does not include voltage dependence of the barrier or recombination effects, both of which have been shown to reduce the accuracy of this method by McLean.[97] Recombination current becomes apparent at low bias voltages potentially in a very similar region to the Norde turning point evaluation. Also it should be noted this method only uses a very small number of data points around the minimum and the rest are ignored. It has been shown however that this method does have some success when applied to two I/V curves taken at different temperatures.[98] If the minimum values from two $F(V)$ curves at different temperatures are used, four simultaneous equations can be solved producing a more reliable value for the SBH and the ideality factor.

4.2.4 Series Resistance - Small Signal Evaluation

The effect of series resistance can be deconvolved from the experimental I/V by use of plots designed to give the maximum linear section, if the incremental conductance can be calculated. The series resistance can be taken from the slope of the I/V curve at high applied bias but the conductance $G = \partial I_d/\partial V$ does not always saturate as the changing slope of the I/V curve in figure 4.13 shows. Also, increasing the applied current may bring on joule heating and a resistance change with temperature variation.

The following analysis method proposed by Werner,[99] avoids using the high voltage region and therefore the high current regime by working in the mid range which is also away from the effects of recombination currents at low voltage. In this intermediate voltage range the voltage drop across the diode and the series resistance are comparable. By simplifying equation (2.30) for the series resistance by working only in forward bias and assuming the voltage dropped over the diode V_d is very much greater than $3kT/q$ we can write,

$$I_d = SA^{**}T^2 \exp\left(-\frac{q\phi_e}{kT}\right) \exp\left(\frac{q}{nkT}(V - IR_{series})\right). \tag{4.9}$$

This assumes that any deviations from ideal behaviour are hidden in the ideality factor n, that the series resistance is voltage independent and that the contact is homogeneous. The numerical determination of the small signal conductance $G = \partial I_d/\partial V$ from the I/V curve

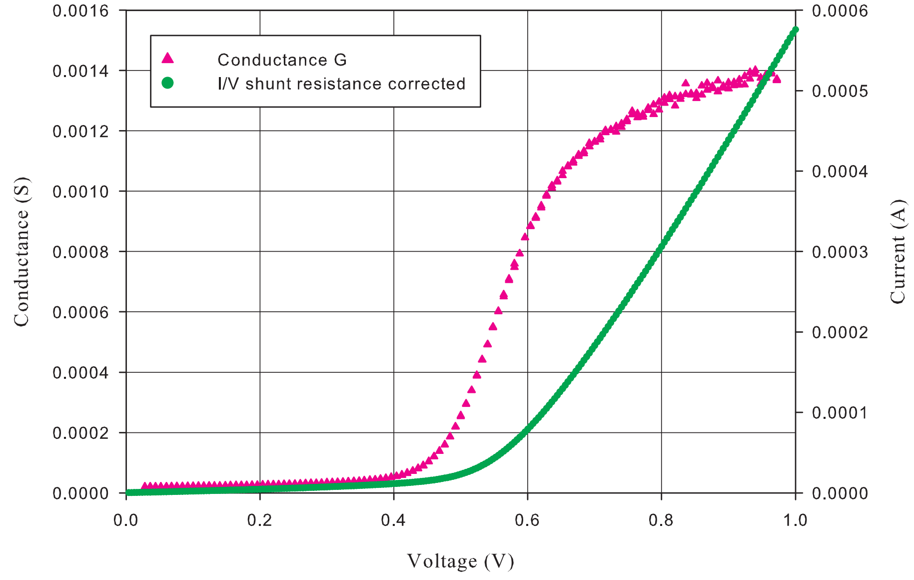

Figure 4.13: Plot of conductance $G = \partial I_d/\partial V$ against V in triangles and the corresponding I/V curve after shunt resistance correction in circles.

demands voltage steps of 1 mV to give a good approximation to the curve. Instead, if the identity $G = I_d\partial(\ln I_d)/\partial V$ is used, bigger voltage steps of 10 mV are adequate as the logarithmic current curve is less steep. This gives rise to three possible plots to extract the SB, ideality factor and series resistance. Werner has labelled the plots A,B and C the naming of which has been followed here.[99]

Plot A

Using the identity for the small signal conductance $G = \partial I_d/\partial V$ equation (4.9) yields,

$$\frac{G}{I_d} = \frac{q}{nkT}(1 - GR_{series}). \tag{4.10}$$

Plot A is a plot of G/I_d versus G in which the linear section, when fitted, provides a gradient of $-qR_{series}/nkT$ with an x-axis intercept of $1/R_{series}$ and y-axis intercept of q/nkT.

From our B-type $NiSi_2$ dot, Plot A, when fitted using a least squares linear fit to the straight section indicated by the arrows in figure 4.14 gives a value of $645 \pm 1\ \Omega$ and ideality of 1.54 ± 0.01. The linear section of this data is over a small number of points as indicated, the high voltage data gives a conductance over 1.2 mS and is increasingly

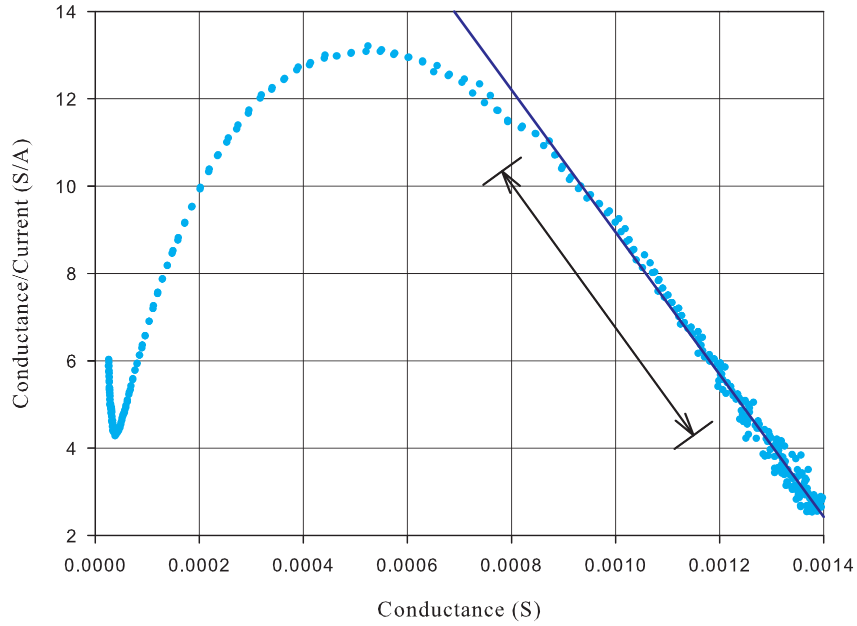

Figure 4.14: Plot A conductance/current against conductance, equation (4.10).

noisy therefore the linear fit has not used this data. Using the extracted series resistance the voltage dropped over the series resistance can be subtracted from the applied voltage to leave only the voltage dropped over the SB as $V_d = V - IR_{series}$. Using the obtained voltage drop over the SB the SBH can be extracted using the normal logarithmic plot. This produces a value of 0.806 ± 0.002 eV for the SBH and an ideality of 1.588 ± 0.008.

Plot B

Plot B is derived using the identity $1/G = R_{dr}$, where R_{dr} is the differential resistance, which is substituted into equation (4.10) to give,

$$R_{dr} = \frac{nkT}{qI_d} + R_{series}. \tag{4.11}$$

Using equation (4.11), a plot of the differential resistance ($1/G$) against the inverse current ($1/I_d$) provides a graph with slope nkT/q and an intercept of R_{series}. A value of $653 \pm 2\ \Omega$ for the series resistance and 1.46 ± 0.04 for the ideality factor is obtained from Plot B in figure 4.15. Using this series resistance to correct the voltage for the log plot to enable the extraction of values of 0.824 ± 0.003 eV for the SBH and 1.51 ± 0.01 for the ideality factor. This plot, because it uses $1/I_d$ has the disadvantage that the high voltage

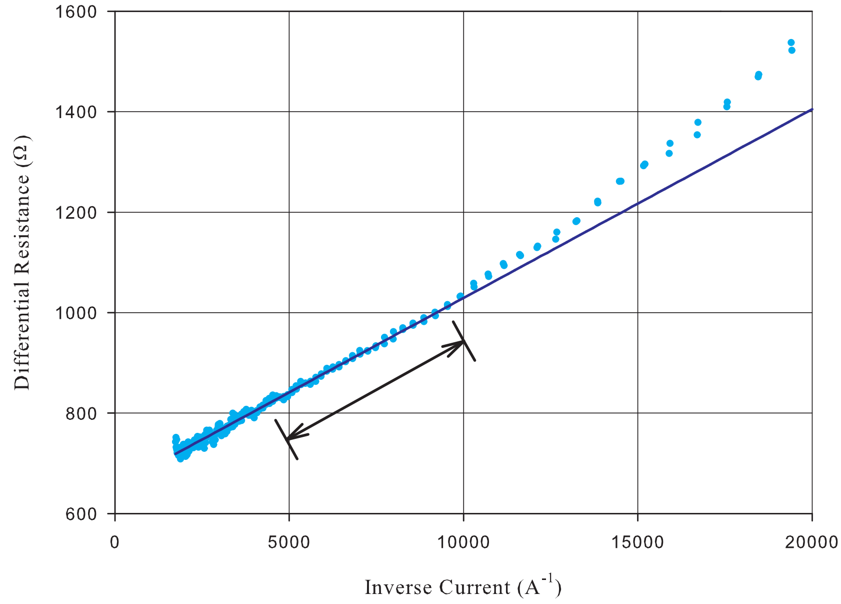

Figure 4.15: Plot B, Differential Resistance against Inverse Current, equation (4.11).

data is compressed. A large proportion of the low voltage data has been removed from this plot so the used linear region can be seen.

Plot C

Finally, plot C uses the identity for the differential resistance $R_{dr} = (1/I_d)\partial V/\partial(\ln I_d)$ substituted into equation (4.11) to give,

$$\frac{\partial V}{\partial(\ln I_d)} = R_{series} I_d + \frac{nkT}{q}. \tag{4.12}$$

Where the gradient of the resulting plot is R_{series} and the intercept nkT/q. Note that the left hand side of equation (4.12) is equal to I_d/G.

This plot gives a large linear region and a fit provides the series resistance to be $655 \pm 5\ \Omega$ and the ideality calculated from the intercept of 1.44 ± 0.04. The uncertainty on the series resistance is higher than for the other plots due to the series resistance being obtained directly from the gradient of the graph so the slight noise on the data which can be seen in figure 4.16 effects this measurement directly. Using this value for series resistance the SBH is 0.828 ± 0.003 eV and the ideality factor is 1.49 ± 0.01.

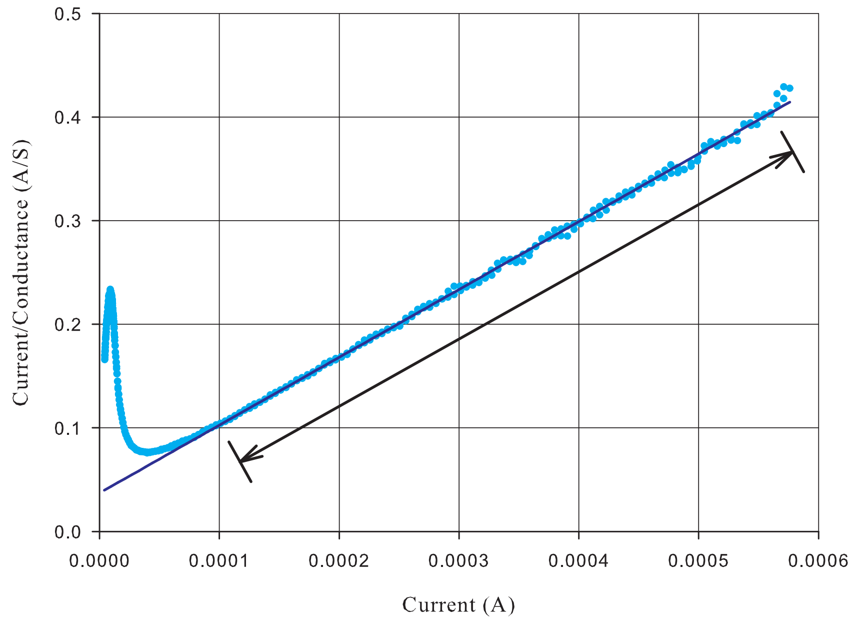

Figure 4.16: Plot C Current/Conductance against Current, equation 4.12.

4.2.5 Comparing Graphical Fitting Methods

The analysis of the 250μm diameter B-type $NiSi_2$ dot using the methods introduced in the previous sections, is summarised in table 4.1. As the graphical fitting method has evolved to include extra circuit components such as the shunt and series resistance the extracted SBH moves towards the excepted value of 0.79eV. The shunt resistance was calculated from the reverse bias section of the I/V curve and used to correct the current for some of the fitting methods as indicated in table 4.1. The initial use of the logarithmic plots without the series resistance produced a low SBH and a very bad ideality factor of ~ 8 for the forward bias, a clear indication that the fitted theory is not complete. The Norde plot unfortunately is not appropriate for this data set as the turning point is at a voltage less than 3kT/q, producing a very high value for the series resistance compared to the shunt resistance. The small signal conductance plots each provide very similar values for the series resistance and SBH with the values being deduced from the corrected forward bias regime.

Although not very significant, plot A has the lowest uncertainties for the values from the small signal conductance fitting, something Werner also concludes, stating this analysis 'yields the most reliable and accurate values for the SBH, the ideality n and series resistance'.[99] It is worth noting however that the uncertainties are based on the goodness

Analysis Method	R_{shunt} (Ω)	R_{series}	SBH (eV)	Ideality Factor
$\ln(I)$	-	*NA*	-	-
Reverse bias of $\ln(I/(1-\exp(-qV/kT)))$	- 8372 ± 5	*NA* *NA*	0.464 ± 0.001 0.506 ± 0.001	1.016 ± 0.001 1.008 ± 0.001
Forward bias of $\ln(I/(1-\exp(-qV/kT)))$	- 8372 ± 5	*NA* *NA*	0.517 ± 0.002 0.517 ± 0.002	8.2 ± 0.5 8.1 ± 0.3
Norde Plot	8372 ± 5	$26 \pm 2k\Omega$	0.599 ± 0.002	*NA*
Plot A Plot B Plot C	8372 ± 5 8372 ± 5 8372 ± 5	$645 \pm 1\Omega$ $653 \pm 2\Omega$ $655 \pm 5\Omega$	0.806 ± 0.002 0.824 ± 0.003 0.828 ± 0.003	1.588 ± 0.008 1.51 ± 0.01 1.49 ± 0.01
Fitting program	6816	596 Ω	0.823	1.36

Table 4.1: Comparison of fitting methods to a 250μm diameter B-type $NiSi_2$ dot.

of fit of the straight line only and are not a realistic error. For plot A the straight section is sometimes only a handful (10 to 20) of data points long, which as there are so few points produces a better linear fit, whereas Plot B and C have larger straights region using more data points but with more noise increasing the uncertainty. All of these plots suffer from human error in deciding which data points to include in the least squares linear fit. This will be further discussed in section 4.2.7 to obtain more realistic uncertainties. Plot A will be used to analyse all the $NiSi_2$ sample I/V curves, as it has the lowest fitting uncertainty and also the tests on the accuracy of the plots by Werner conclude that plot A is the most reliable.[99]

4.2.6 $NiSi_2$ Sample Comparison

The five different samples: B-type $NiSi_2$ on n-type silicon, capped and uncapped, A-type $NiSi_2$ on n-type silicon capped and uncapped and nickel have been analysed for 250μm and a 500μm dots. This has been done first by removing the effect of the shunt resistance by taking the gradient of the reverse bias, before deducing the series resistance using Plot A from the small signal conductance fitting method. Once the current and voltage across only the diode are known, the SBH and ideality factor are extracted using the $\ln(I/(1-\exp(-qV/kT)))$ plot. The results from the ten analysed I/V curves are shown in table 4.2.

For each type of sample the resistances, both shunt and series are very similar for both

Sample	Diameter (μm)	R_{shunt} (Ω)	R_{series} (Ω)	SBH (eV)	Ideality
B Type	250	8372 ± 5	645 ± 1	0.806 ± 0.002	1.59 ± 0.01
	500	8789 ± 5	543 ± 1	0.699 ± 0.002	2.33 ± 0.01
B Type Capped	250	3126 ± 5	1154 ± 1	0.887 ± 0.008	1.62 ± 0.03
	500	3118 ± 5	1037 ± 1	0.694 ± 0.008	3.0 ± 0.1
A Type	250	7754 ± 5	604 ± 1	0.831 ± 0.002	1.42 ± 0.01
	500	6833 ± 5	557 ± 1	0.837 ± 0.003	1.42 ± 0.01
A Type Capped	250	6475 ± 5	252 ± 1	0.897 ± 0.002	1.15 ± 0.01
	500	13095 ± 5	221 ± 3	0.800 ± 0.003	1.40 ± 0.01
Nickel	250	4554 ± 5	227 ± 3	0.75 ± 0.02	1.7 ± 0.1
	500	5091 ± 5	154 ± 3	0.879 ± 0.002	1.19 ± 0.01

Table 4.2: Comparison of $NiSi_2$ and Nickel samples of 250μm and 500μm diameter analysed using Plot A.

diameter dots. The A type capped sample being the odd one out with a comparatively high shunt resistance of $\sim 13k\Omega$. The spread in SBH is quite large from 0.694 ± 0.008 to 0.897 ± 0.002. The 500μm dots tend to have a lower SBH for the silicide compared to its 250 μm pair, this however is coupled with a larger ideality factor. The A-type samples have produced a larger SBH in general to the B-type and nothing close to the expected 0.65eV SBH for the A-type termination. From this it can be assumed that the A-type termination has not been achieved, supported by the fact that no change in the rotation of the LEED or RHEED patterns has been seen. A-type is the harder termination to grow as it is not the preferred orientation energetically and a mix of both types is more likely to be formed. The average SBH for the four B-type samples is 0.772 ± 0.004 eV and for the A-type 0.841 ± 0.003 eV the average for the two polycrystalline nickel samples is 0.82 ± 0.01 eV. The B-type average is close to the expected value of 0.79eV.

4.2.7 Fitting Tolerance of the Small Signal Evaluation

The spread of SBH and resistances shown in table 4.2 can partly be accounted for by the human decision of which data points to fit to. To study this effect one data set has been analysed many times by taking a different set of points to include in the linear fit each time. To test how much the value can alter by choosing different numbers of data points, the 500 μm diameter A-type $NiSi_2$ dot has been analysed using all three small signal plots with

different linear regions fitted. This will provide a more realistic error for the judgement of the number of points to include in the linear fit. This will also help to show if a lower SBH for the A-type can be deduced making it closer to B-type.

Firstly the reverse bias fitting to find the shunt resistance can alter from $7004 \pm 5\Omega$ if fitted to -2V to -1.9V to $6527 \pm 5\Omega$ if the entire straight section is used. A mid range value of $6833 \pm 5\Omega$ from -2 V to -0.8 V is also compared. The difference in these comes from the fact the reverse bias is slightly curved. The smallest value of $6527 \pm 5\Omega$ is actually an over correction as the current begins to rise at high applied bias.

For each of these shunt resistances the three small signal plots A, B and C have been used to deduce the series resistance which varies from $554.6 \pm 0.5\Omega$ to $564.9 \pm 0.5\Omega$. Figure 4.17 shows a plot of the series resistance against the ideality factor found from the logarithmic fit. The three shunt resistances $6527 \pm 5\Omega$, $6833 \pm 5\Omega$ and $7004 \pm 5\Omega$ are shown in red, blue and yellow respectively, and the plots A, B or C used to find the series resistance are indicated by squares, circles and triangles respectively.

The three shunt resistances are separated into three linear regions with lowest resistance of $6527 \pm 5\Omega$ giving some of the highest series resistances. There is also a trend for the lower series resistances to lead to a higher ideality factor. The values extracted using plot C are concentrated at the high series resistance, low ideality factor region of the graph, where as plot B gives a wide scatter of values over the whole region. The values extracted using plot A all seem to fall in the mid region of the graph, an indication that this method possibly gives a more averaged value.

The SBH for each set of shunt and series resistance has been found using the $\ln(I/(1-\exp(-qV/kT)))$ plot and these values are shown in figure 4.18 using the same marking as in the previous figure. The plot of SBH and ideality gives a very good linear trend with increasing SBH and decreasing ideality factor. This is because the SBH and ideality factor are in different exponential terms, as seen in equation (4.9) so to fit the same curve they play off against each other. The high values of ideality are an indication of a poor interface, which for the A-type $NiSi_2$ might be expected. Several published works use the idea to extrapolate the trend in figure 4.18 to find a value for the SBH at $n = 1$.[100,101] This idea would not be a very satisfactory solution as for this data we would obtain a value for the SBH higher than the band gap of silicon of 1.1 eV.

The difference in fitting the shunt resistance from the reverse bias of the A-type $NiSi_2$

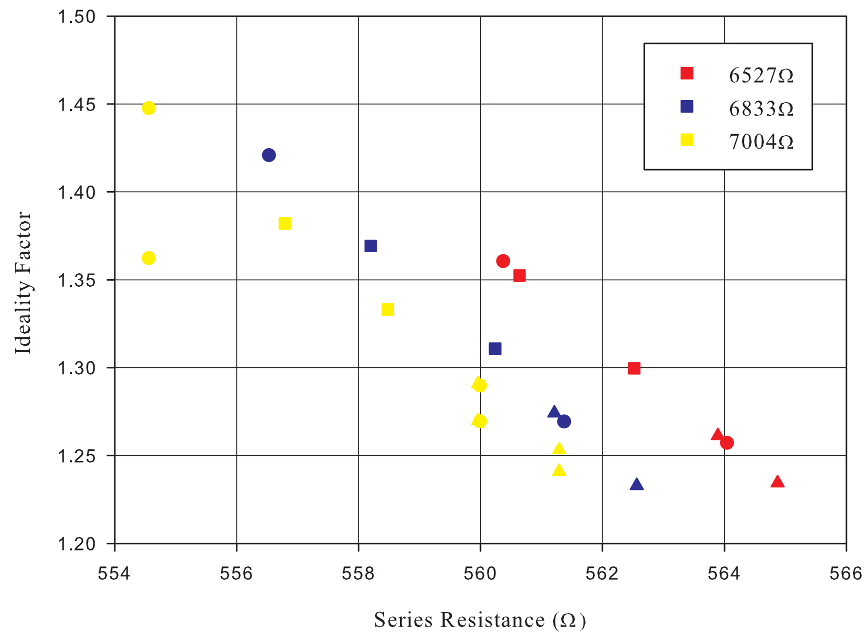

Figure 4.17: Plot of series resistance against ideality factor for different fits of a 500 μm diameter A-type $NiSi_2$ dot. The three shunt resistances used are $6527 \pm 5\Omega$, $6833 \pm 5\Omega$ and $7004 \pm 5\Omega$ shown in red, blue and yellow respectively. Plot A, B and C are indicated by squares, circles and triangles respectively.

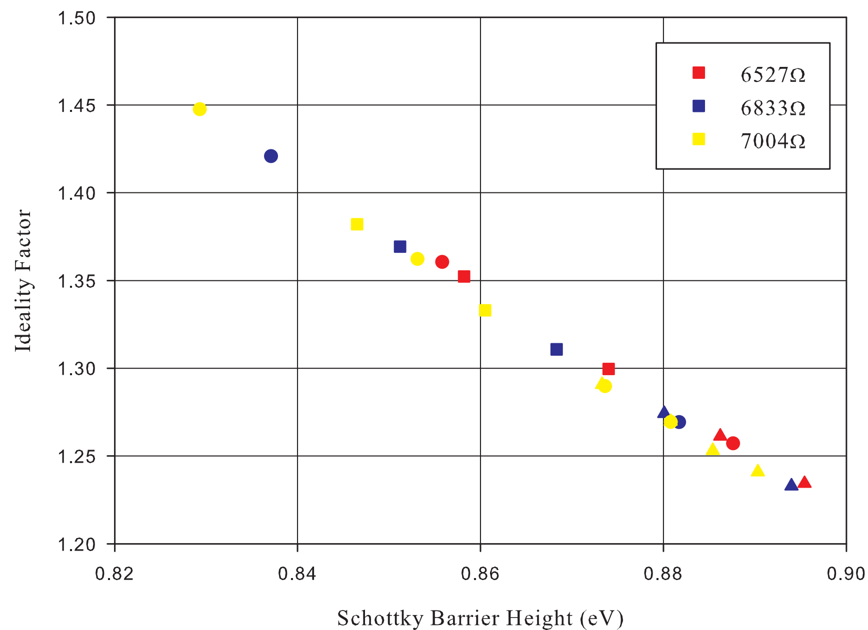

Figure 4.18: Plot of SBH against ideality factor for different fits of a 500 μm diameter A-type $NiSi_2$ dot. The three shunt resistances used are $6527 \pm 5\Omega$, $6833 \pm 5\Omega$ and $7004 \pm 5\Omega$ shown in red, blue and yellow respectively. Plot A, B and C are indicated by squares, circles and triangles respectively.

dot being examined is $\sim 480\Omega$ ($\pm 3.7\%$) leading to a potential spread in the series resistance from the fitting of $\sim 10.3\Omega$ ($\pm 0.9\%$). This in turn leads to an uncertainty in the SBH of ± 0.03 eV from the uncertainty in fitting to the linear sections in all the stages of the analysis. From these observations we can obtain a more realistic error for the small signal graphical fitting method. This alters the error on the SBH's in table 4.2 and the average B-type value of 0.772 ± 0.03 eV now fits the expected value of 0.79 eV within error.

The use of graphical fitting methods to extract the SBH is a very time consuming process. This is because several plots are required to recover the current and voltage across the SB by removing the shunt and series resistance contributions. The method suffers from human judgement of which data points to include in the least squares straight line fit and the use of a small area of data points from the whole I/V sweep. This leads to quite a high uncertainty in the extracted SBH of ± 0.03eV which is 20% of the difference between the A-type and B-type $NiSi_2$ interface terminations of 0.14eV. Using a graphical method only allows certain theory to be included for the extraction of the SBH.

4.3 Fitting Routine for Back-to-Back Barriers

A better approach to the graphical fitting method is to fit the theory to the whole experimental I/V curve using a numerical fitting program. This would not only reduce the uncertainty in the extracted SBH but the theory could also be expanded to include for example: back to back SB's, image force lowering, tunnelling in the reverse bias, tunnelling through an oxide layer, tunnelling in the forward bias and potentially inhomogeneous SB's.

4.3.1 MATLAB

A fitting routine was written by the author using the expressions from the MATLAB simulation script discussed in section 2.7. These were used with a least squares non linear fitting routine within MATLAB to solve the voltage dropped across each component within the circuit. This routine was adapted from a program written by Zhang *et al*,[45,46] which attempted to fit back-to-back SB to semiconductor nanowires.

This program worked very well for test data produced from the simulation unless one of the shunt resistances was very large or there was only one SB. It sometimes did manage

a sensible fit on experimental data but this was very sensitive to starting parameters and could not always be repeated. In the process of trying to improve the program's capabilities the under lying problem that MATLAB calculated complex numbers for the current, sometimes leading to unrealistic negative resistances was revealed. On seeking the support and guidance of Phil Hasnip the decision was made to rewrite the fitting program in FORTRAN where more control could be taken of the basic routines.

4.3.2 IV.x - I/V Fitting Program

The collaboration with Phil Hasnip lead to the design and programming of the program IV.x, which fits experimental I/V curves to extract the SBH and resistance values. Developing from the MATLAB script I had already written we started with the same theory as used in the simulation program in section 2.7. The theory included thermionic emission over the barrier in forward bias and tunnelling in the reverse bias. The circuit included two back-to back SB with individual shunt resistances and a combined series resistance as shown in figure 2.8. The SBH was also modified by the image force lowering to give the effective barrier. As already discussed in section 2.7.3 the ballistic electron expression was removed when $V_r < \xi$. The coding of IV.x was undertaken by P. Hasnip, in collaboration with the author.

Unlike the MATLAB program which solved the voltage dropped across the individual SB the new program took the approach to equalise the current through each part of the circuit. For the MATLAB program when a resistance became small, a small change in voltage gave a big change in current therefore finding a good solution became very difficult, by equalising the currents we hoped to avoid this problem.

To calculate the I/V curve a chi squared (χ_I^2) value for the current is calculated and optimised. The objective function to be minimised is,

$$\chi_I^2 = \frac{1}{3}\left[(I_1 - \mu_I)^2 + (I_2 - \mu_I)^2 + (I_{series} - \mu_I)^2\right], \tag{4.13}$$

where μ_I is the mean of the currents,

$$\mu_I = \frac{1}{3}(I_1 + I_2 + I_{series}), \tag{4.14}$$

Once the I/V curve has been calculated it is compared to the experimental I/V curve

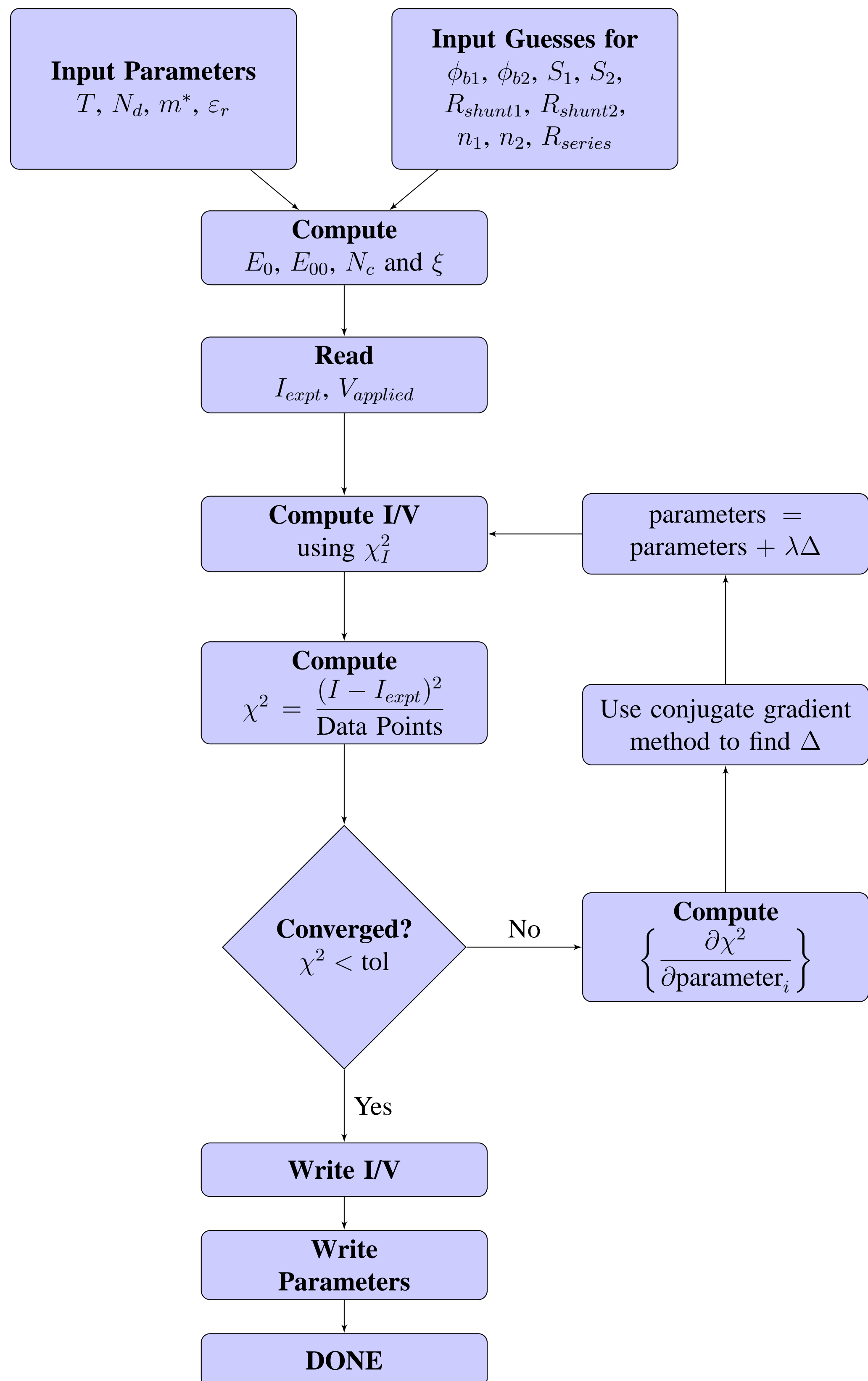

Figure 4.19: Flowchart of IV.x fitting program.

by calculating the goodness of fit using,

$$\chi^2 = \sum \frac{(I_{model} - I_{expt})^2}{\text{Data points} \times \mu A^2}. \tag{4.15}$$

This is the χ^2 value reported from the fitting program expressed in its normalised form. A future alteration to the program would be to include the current normalisation making χ^2 dimensionless. The program was written to optimise the fitting by using the preconditioned Fletcher-Reeves conjugate gradient method. The differential of χ^2 for each of the variables gives the gradient to follow to minimise the χ^2 value and hence get closer to a good fit for the experimental I/V curve. The flowchart for the program is shown in figure 4.19. This approach gave more flexibility to add in extra variables like area and ideality factor and using FORTRAN meant we had more idea what caused the fitting routine to fail. To fit the I/V curve the program varied two SBH, two shunt resistances, two areas, two ideality factors and the series resistance.

Image Force Lowering - A More Exact Expression

The program did not manage to fit some curves very well, in some cases failing completely, returning a large χ^2 value. This was found to be caused by a slight problem with the theory which produced a double turning point. The fitting program found this because of a high density in data points which meant one data point fell near the turning point, where normally with a lower data point density the fitting program would not notice the turning point. The turning point arose from the image force lowering in forward bias. The barrier lowering ($\Delta\phi_{bi}$) decreases with forward bias (see figure 2.5) and therefore the effective barrier ϕ_e tends towards ϕ_b. It was found at a certain applied voltage that $\Delta\phi_{bi}$ decreases faster than the thermionic emission over the barrier increases, therefore the current decreased with increasing voltage producing the double turning point shown in figure 4.20.

The electric field in the SB used in the image force lowering, equation (2.14), had several assumptions associated with it: that there were no p-type donors at the interface and that $qV_d \gg kT$ allowing the exponential term to be neglected. For our samples with low SB and the large band gap of silicon, neglecting the p_s term is still valid. However the exponential term should be left in for completeness. The resulting electric field in the

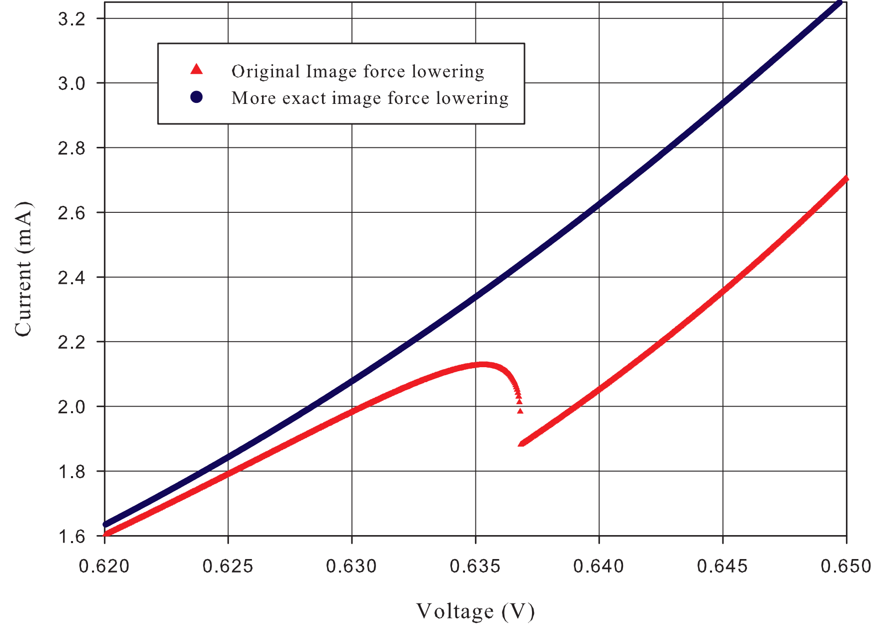

Figure 4.20: Plot of the turning point in the current when the image force lowering tends to the SBH.

barrier is,

$$\mathscr{E}^2 = \frac{2q}{\varepsilon_s}\left\{N_d\left(V_d - \frac{kT}{q}\right) + \frac{kTN_d}{q}\exp\left(\frac{-qV_d}{kT}\right)\right\}, \tag{4.16}$$

and the new expression for the image force lowering is,

$$\Delta\phi_{bi} = \left\{\frac{q^3 N_d}{8\pi^2{\varepsilon_s}^3}\left[\phi_b - V - \xi + \frac{kT}{q}\left(\exp\left(\frac{-qV_d}{kT}\right) - 1\right)\right]\right\}^{1/4}. \tag{4.17}$$

Using this new expression for the image force lowering removed the double turning point as shown in figure 4.20 and meant the fitting routine did not get stuck in the local minimum. This is because the effective barrier tends towards ϕ_b more gently.

4.4 IV.x Analysis of $NiSi_2$

The fitting routine IV.x was used to analyse the five different sample types which were B-type capped and uncapped, A-type capped and uncapped and polycrystalline Ni. I/V curves have been taken in the Nanoprobe from these samples from three different diameter contacts 250 μm 500 μm and 1000 μm of which there are multiple contacts which repeat measurements were taken from. The total number of I/V curves came to over one hundred

hence the use of the fitting program for analysis. Although data was taken from a large set of dots only the data sets which were converging well, indicated by a χ^2 value less than 1000, at the start were continued with, this was to speed up the process. Many of the curves which were not fitting well at the start were also ones which had lost contact during the I/V sweep or exhibited hysteresis effects from the out and return of the sweep. The data presented is, where possible, an average of several fits with the mean variance reported as an error. If a single curve is the only data available then the χ^2 value is a gauge of the goodness of fit. For the $NiSi_2$ data set a χ^2 of less than ten is an excellent fit by eye. A χ^2 of 10 is an average difference in the fit of 3 μA. If a χ^2 value less than 1 is reported the fit is excellent and any improvement adjusts the SBH by hundredths of an eV.

4.4.1 Analysis of Full Applied Voltage Range

The I/V curves were analysed across the whole applied voltage range initially taking into account the reverse bias voltage. The temperature was fixed at 291 K and the doping concentration at 5×10^{21} m^{-3}. The program was allowed to fit to two back-to-back SB but the fit only used the first forward biased barrier under positive voltage, removing the second barrier. The parameters SBH, ideality factor, area, shunt and series resistance were allowed to vary during the fitting process.

Analysis of the 250 μm Diameter B-type $NiSi_2$ dot

The data from the 250 μm diameter B-type $NiSi_2$ dot which has been used throughout this chapter to compare the fitting methods is presented here for comparison. Figure 4.21 shows the experimental data and the fit from IV.x which has a χ^2 value of 1.556.

The program obtained values for the SBH of 0.844 eV and the effective barrier at zero applied bias as 0.823 eV. The ideality was fitted as 1.361, the area as 6.68×10^{-2} mm^2 which is a dot diameter of 292 μm. The series resistance obtained was 596 Ω and the shunt resistance 6816 Ω. These values can be compared with the graphical fitting methods in table 4.1 where it can be noted that the resistances have been reduced. The effective SBH falls within the small signal conductance plots. The ideality has been reduced compared to the graphical fitting methods, which is expected as the image force lowering is now taken into account in the fitting program. The area is fitted slightly larger than the nominal circular dot diameter would produce. The nominal dot areas if assumed to be circular are

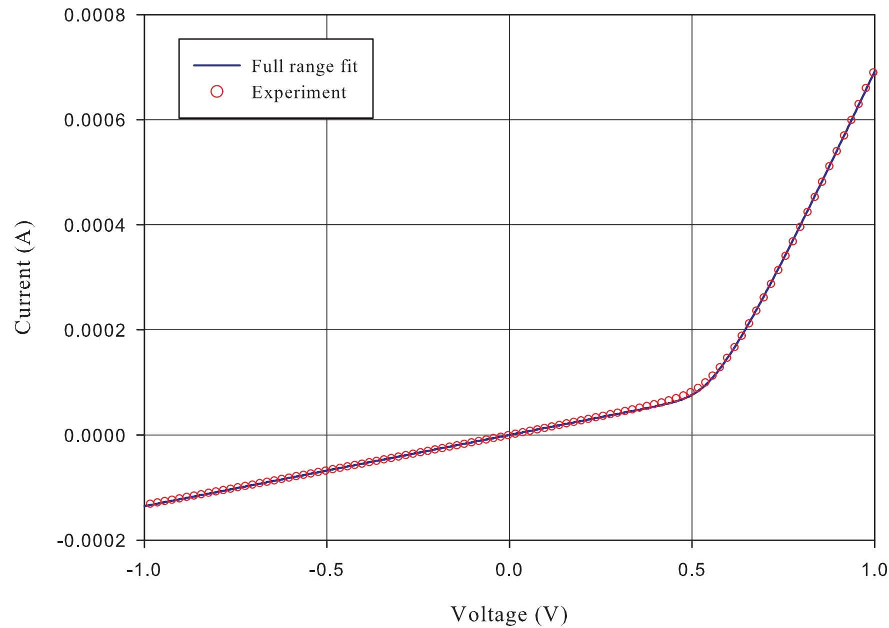

Figure 4.21: Plot of experimental data and program fit of I/V data from the 250 μm diameter B-type $NiSi_2$ dot.

calculated to be 0.049 mm^2, 0.196 mm^2, 0.785 mm^2 for 250 μm, 500 μm and 1000 μm diameter dots respectively. However as the mask is made by mechanical drilling of holes in a thin tantalum sheet there is an error in the size and if the hole is elliptical further error in the area could be introduced. Therefore we expect the fitted areas to be greater than the nominal hole size.

Results from the Analysis of the $NiSi_2$ Samples

The complete set of $NiSi_2$ samples has been analysed using IV.x in the same manner as for the 250 μm diameter B-type $NiSi_2$ dot. The average values obtained from the fits are presented in table 4.3. The presented error values are obtained from the mean variance of the fitted parameters hence where there is only one sample no error can be presented, in this case the χ^2 value should be used as a guide.

The values in table 4.3 can be compared with the graphical fitting analysis in table 4.2. The resistances, series and shunt from the program fit are very similar values to the ones obtained from the graphical fitting methods and have similar values for each sample type. The capped samples provide the least variance in the resistances across the dot sizes for each sample from the program fit, possibly indicating a more stable contact to the dot as

Sample	Dot Diameter (μm)	Fitted Area (mm^2)	R_{shunt} (Ω)	R_{series} (Ω)	SBH (eV)	Effective SBH (eV)	Ideality	χ^2
B	250	0.239 ± 0.034	6934 ± 527	610.7 ± 7.6	0.874 ± 0.019	0.854 ± 0.019	1.342 ± 0.101	1.43 ± 1.06
	500	0.347 ± 0.091	9261 ± 1287	601.3 ± 6.3	0.816 ± 0.016	0.797 ± 0.016	1.522 ± 0.096	5.04 ± 4.02
	1000	4.51 ± 3.32	5020 ± 2290	736.6 ± 29.7	0.679 ± 0.012	0.661 ± 0.012	2.397 ± 0.178	19.93 ± 7.06
B Cap	250	0.691 ± 1.36	1988 ± 430	834.9 ± 64.8	0.799 ± 0.034	0.780 ± 0.034	1.440 ± 0.168	4.99 ± 2.78
	500	816.7	2280	830.9	0.878	0.858	2.534	8.25
	1000	2.15 ± 1.53	1213 ± 137	1056.8 ± 8.6	0.663 ± 0.026	0.645 ± 0.025	1.980 ± 0.088	9.29 ± 1.43
A	250	0.175 ± 0.038	6877 ± 320	218.2 ± 24.2	0.874 ± 0.006	0.855 ± 0.006	1.301 ± 0.045	5.49 ± 2.08
	500	0.231 ± 0.061	5743 ± 281	509.1 ± 11.3	0.846 ± 0.026	0.827 ± 0.026	1.333 ± 0.067	7.36 ± 4.15
	1000	0.754	4487	504.3	0.785	0.766	1.605	10.17
A Cap	250	0.314	5641	235.0	0.922	0.902	1.198	7.93
	500	0.362 ± 0.119	8776 ± 1520	237.5 ± 9.2	0.864 ± 0.020	0.845 ± 0.020	1.253 ± 0.040	26.52 ± 12.26
Ni	250	0.305 ± 0.303	4144 ± 129	195.9 ± 2.3	0.947 ± 0.024	0.926 ± 0.024	1.017 ± 0.093	90.47 ± 0.71

Table 4.3: Comparison of $NiSi_2$ samples analysed using IV.x over the full applied voltage range. The errors are obtained from the mean variance of the fitted parameters; hence no value can be calculated when only one curve is available.

the capping layer increases the thickness of the contact. The SBH between the A-type and the B-type are similar values around 0.85 eV, supporting the previous outcome that the growth of A-type was unsuccessful. The SBH for the 1000 μm are all lower than the other dot sizes but this comes with a higher average χ^2 value, a high ideality and in some cases an unrealistic area. The 1000 μm dots are possibly inhomogeneous SB which could be the cause of the inconsistent values. Since the χ^2 values are insensitive to changes in area, the fitting program has been shown to struggle when fitting to the area parameter. An area change from 0.1 mm^2 to 1×10^{-3} mm^2 only affects the χ^2 in the 6th decimal place. The high χ^2 values indicate that the fitted parameters for the Ni samples are not particularly accurate, suggesting there are extra features in the data that the theory cannot describe.

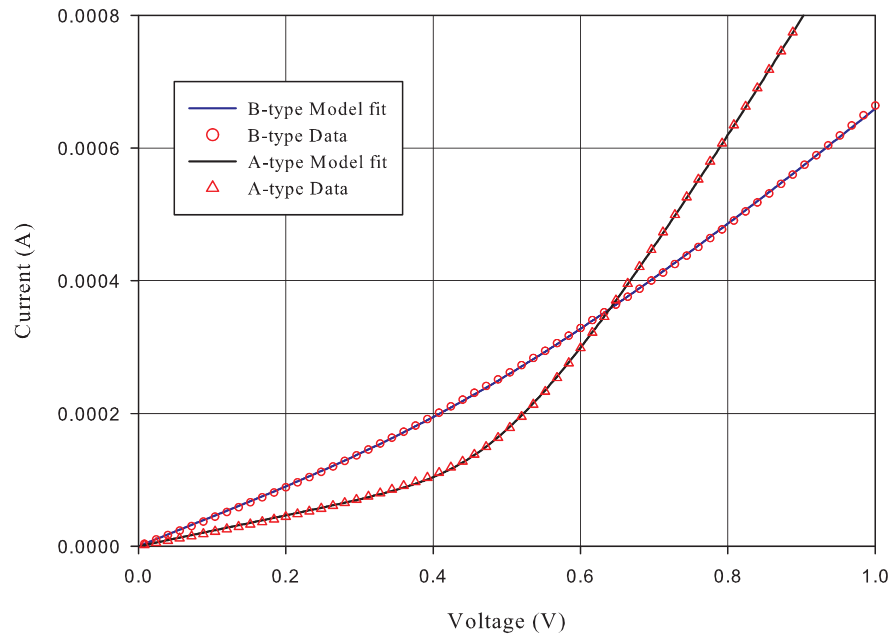

Figure 4.22: Plot of A-type and B-type 1000 μm dot showing the different curves of the turning point.

The large spread and most unrealistic values in area are linked with high ideality factors and high χ^2 values. This is because the program has used ideality and area to fit curves with a very slow turn-on of the emission over the SB. This slow turn-on is not described by the thermionic emission expression but ideality and area can be used to improve the fit, this can be seen starting to happen in the simulations especially for the ideality in figure 2.12b. Figure 4.22 shows two curves from 1000 μm dots, an A-type with a sharp turn on and a B-type with a very gentle turn-on. The B-type has fitted parameters of R_{shunt}=1402 Ω, R_{series}=968 Ω, SBH=0.700 eV, n=2.55, area=11.5 mm^2 and an overall χ^2=2.96 where

as the A-type has fitted parameters of R_{shunt}=3819 Ω, R_{series}=302 Ω, SBH=0.811 eV, n=1.49, area=0.74 mm^2 and an overall χ^2=2.21. The gentle B-type curve has been fitted with a very high unrealistic area and a very high ideality factor also the two resistances are very similar in magnitude. The A-type has an area that is correct for 1000 μm dot and a more sensible ideality, although high enough to indicate there is some transport mechanism missing. The gentle turn-on which requires the fitting program to increase the area and the ideality is most likely due to an inhomogeneous SB, where different areas turn on at different applied voltages. The large area dots may encourage the development of the dot to be inhomogeneous, hence the fits to any of the 1000 μm dots obtaining high χ^2 values. The gentle turn-on curve could also be an indication that there is an oxide tunnel barrier present, which would not be unexpected with these samples as they were transferred in air to LENNF. However the reverse bias shows no evidence of tunnelling in the form of a symmetric ‘s’ shape curve.

Although the fitting program may produce a good fit indicated by the χ^2 value, the parameters should be scrutinised and compared to the I/V curve and fit. A high value of ideality factor or an unrealistic area is a clear indication that the experimental I/V curve has another transport process involved. The resistances should be different with the shunt resistance being an order of magnitude larger than the series; if they are similar the SB is a poor one with a high leakage past it. Using these observations the use of the fitting program will allow more informed decisions about the quality of the I/V curve under investigation and the accuracy of the extracted values.

Note After Viva

The external examiner expressed the opinion that the area should have been measured from the SEM images and fixed in the fitting program. The area was fixed in a test run of this data, however this was not reported in this thesis as the variation in other parameters was still present. This will be done for any publications which require the inclusion of this work. The area was allowed to vary in this experiment to investigate the capabilities of IV.x. Part of the theory missing in the program is forward tunnelling or more specifically peripheral edge tunnelling. This idea is discussed further in section 8.2.2.

4.4.2 Analysis of Forward Bias Range

The fit of the I/V curve in figure 4.21 would appear to be an excellent fit however on closer inspection the reverse bias and the turning point have more variance. The position of the turning point of the I/V curve is crucial as this contains the information about the SBH as this is when thermionic emission turns on and the current increases as more electrons are emitted over the barrier. The reverse part of the I/V curve is shown in figure 4.23 alongside the difference between the model and the experimental data. The reverse bias has a gentle curve on the data which, as the fitting program is minimising the χ^2 is fitted through the middle, this in turn means the program does not fit the turning point as well. To attempt to get a better fit at the turning point only the forward bias data was fitted to. The graphical fitting methods also only fit to the forward bias once a shunt resistance has been established.

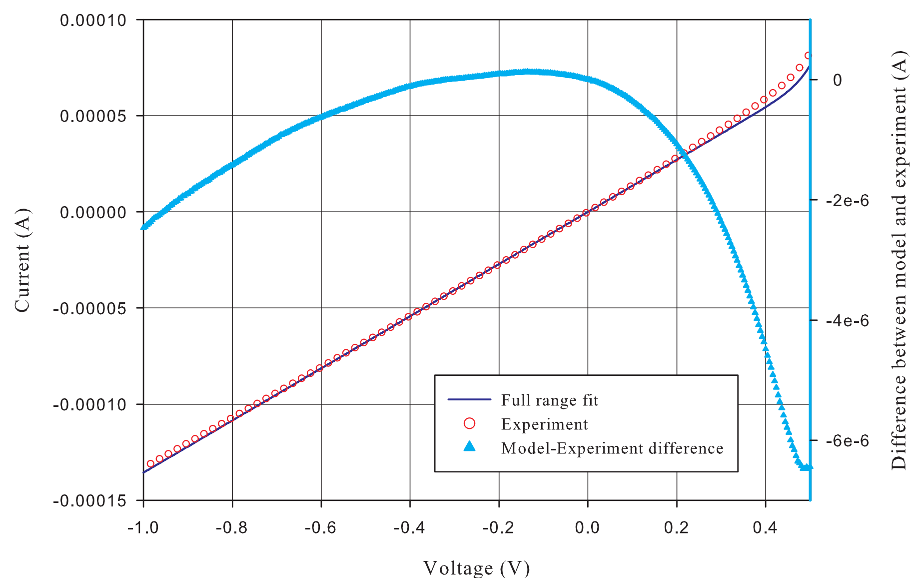

Figure 4.23: Plot of the reverse bias of the 250 μm diameter B-type $NiSi_2$ and the difference between experimental data and the fitted model.

Separating Area from Schottky Barrier Height

The area and SBH are equivalent in the expression for thermionic emission in forward bias because they both scale the current. This means if only the forward bias data is used the program cannot find a unique solution to the area and the SBH. However because of the

image force lowering there is a very small dependence on voltage in the forward bias for the SBH. To enable the fitting program to fit to the forward bias only the program searches along the contour of equivalent area and SBH to find the solution pair with the lowest χ^2 from the image force lowering. This is not a problem when the reverse bias data is present due to the area and SBH having a different relationship to each other.

Analysis of the 250 μm Diameter B-type $NiSi_2$ dot

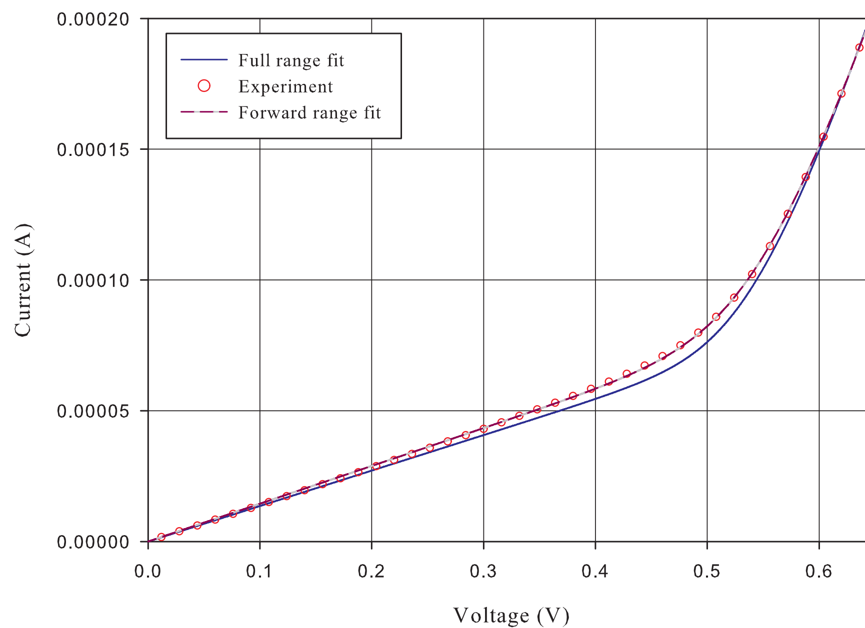

Figure 4.24: Plot of the I/V turning point of the 250 μm diameter B-type $NiSi_2$ dot experimental data fitted using the full voltage range and just the forward bias.

Again the 250 μm diameter B-type $NiSi_2$ dot has been used as a comparison example. Fitting only to the forward bias regime reduced the χ^2 value by an order of magnitude to 0.176. The rest of the values obtained by the fitting program were a SBH of 0.893 eV and the effective barrier at zero applied bias of 0.874 eV, ideality of 1.223 and an area of 8.00×10^{-2} mm^2 which is a dot diameter of 319 μm. The series resistance obtained was 609 Ω and the shunt resistance was 6312 Ω. The resistances have not changed much from the full voltage range fit but there has been a slight increase in area and decrease in ideality. The biggest change is the move from a SBH of 0.844 eV to 0.893 eV as the turning point is fitted better. The effect these fitted values have on the fitted curve is shown in figure 4.24 and it can be clearly seen that fitting the forward bias only puts the fitted curve on top of the experimental data.

Sample	Dot Diameter (μm)	Fitted Area (mm^2)	R_{shunt} (Ω)	R_{series} (Ω)	SBH (eV)	Effective SBH (eV)	Ideality	χ^2
B	250	0.362 ± 0.119	6497 ± 227	620.2 ± 7.3	0.890 ± 0.012	0.870 ± 0.012	1.224 ± 0.039	0.275 ± 0.099
	500	0.079 ± 0.008	7871 ± 1236	604.4 ± 5.2	0.856 ± 0.027	0.836 ± 0.026	1.416 ± 0.183	1.28 ± 0.89
	1000	31.6 ± 16.6	3994 ± 2345	653.5 ± 27.8	0.751 ± 0.029	0.732 ± 0.028	2.567 ± 0.253	9.99 ± 5.59
B Cap	250	2.58 ± 2.59	1948 ± 377	821.8 ± 55.2	0.870 ± 0.036	0.850 ± 0.036	1.577 ± 0.090	1.60 ± 1.91
	500	0.047	2175	744.3	0.982	0.962	2.541	1.97
	1000	17.4 ± 5.9	1256 ± 146	979.5 ± 12.3	0.716 ± 0.016	0.697 ± 0.016	2.420 ± 0.128	3.56 ± 0.60
A	250	0.093 ± 0.005	5937 ± 147	528.4 ± 29.8	0.928 ± 0.006	0.908 ± 0.006	1.114 ± 0.016	0.426 ± 0.331
	500	0.282 ± 0.164	5019 ± 169	514.3 ± 15.7	0.881 ± 0.045	0.862 ± 0.045	1.185 ± 0.085	2.87 ± 3.57
	1000	0.739	3819	501.8	0.811	0.791	1.494	2.21
A Cap	250	0.124	4989	238.6	0.950	0.930	1.075	1.63
	500	0.451 ± 0.040	6533 ± 1081	240.5 ± 8.6	0.923 ± 0.015	0.903 ± 0.015	1.112 ± 0.050	22.56 ± 15.94
Ni	250	12.7 ± 12.7	3659 ± 136	196.4 ± 1.4	0.987 ± 0.145	0.967 ± 0.144	1.000 ± 0.144	130.3 ± 41.7

Table 4.4: Comparison of $NiSi_2$ samples analysed using IV.x over the forward applied voltage range. The errors are obtained from the mean variance of the fitted parameters; hence no value can be calculated when only one curve is avaliable.

Results from the Analysis of the Forward Bias Data of the $NiSi_2$ Samples

Running the analysis on just the forward bias gives an excellent result for the 250 μm diameter B-type $NiSi_2$ dot so this approach was extended to the whole data set to obtain the averages in table 4.4. As before the error values are obtained from the mean variance of the fitted parameters hence where there is only one sample no error can be presented.

Only fitting to the forward bias has dropped the χ^2 value on all the samples except Ni where it has increased. The resistances have altered a small amount but generally stayed around the same value. The area is still a problem especially for the 1000 μm case which gives unrealistic areas. The A-type uncapped sample has produced the closest set of areas to the spot diameters but with larger χ^2 for the 500 μm and 1000 μm cases. Generally the SBH has increased with an improved χ^2.

4.4.3 Inhomogeneous A-type $NiSi_2$

The A-type dots have not produced a lower SBH as expected indicating that the growth did not produce an A-type interface termination. It is likely that the A-type dots are actually mixtures of B-type and A-type making an inhomogeneous SB. Although the fitting program could not fit two parallel SB it was easy to run two SB in the same direction in series. This would not be the correct geometry for the patch inhomogeneous model but could be seen as barriers between layers in the structure. Using this fitting model the χ^2 value was marginally reduced however the two SBH obtained were similar in magnitude as it uses one barrier turning on after another to broaden the curve at the turning point. This effect could also be achieved using tunnelling through the barrier to broaden the turning point.

4.5 Conclusion

The growth of $NiSi_2$ has not been as straightforward as expected with the requirement of the fast deposition rate, which was achieved using the MBE system. During the growth no evidence of the formation of an alternative interface orientation was observed with LEED or RHEED, it is assumed the orientation which was achieved was B-type or a mixture, as pure A-type is more difficult to achieve. The evidence from the I/V analysis supports the assumption of B-type orientation with a B-type SBH of 0.816 ± 0.016 eV with

an effective SBH of 0.797$\pm$0.016 eV which agrees with the value of 0.79 eV previously reported.[20] The A-type SBH extracted from the I/V curves is not lower as expected but marginally higher than the B-type indicating an unsatisfactory growth of an A-type diode. The growth of the 1000 μm dots does not seem to have achieved one type of interface contact orientation, with the fitting program reporting unrealistic values for the area and high χ^2 values for the fits indicating the modelled theory is not complete for these dots. The most likely missing theory is that for inhomogeneous SB.

The use of the Nanoprobe to collect I/V curves has proved very successful on these large scale contacts. The Nanoprobe I/V collection produces high quality data which is very reproducible. The I/V curves can be taken with many data points with very low noise on the data points enabling the fitting routine to get a better fit with a lower χ^2. The $NiSi_2$ dots have not tested the nanoscale capabilities of the Nanoprobe but the procedure of I/V collection enables the confidence to move to smaller scale structures.

The analysis of the curves using the graphical fitting methods shows that it is essential to include the series and shunt resistance as the raw data does not have the correct shape for pure thermionic emission. Including the resistances gives a more realistic value for the SBH. The small signal plots and the fitting program provide values which are comparable to each other; however both have a large spread in values. The fitting program has fitted a high proportion of the I/V curves speeding up the process of analysis and producing very good χ^2 values for the majority of curves. The advantage of the fitting program is it uses the whole data range whereas the small signal plots only use a very small fraction of the forward bias data points. The spread in values indicates that not all the samples have grown as intended with the indication that the 1000 μm diameter dots are inhomogeneous. The graphical fitting method does not include image force lowering or area fitting and will only work if the back contact is ohmic whereas the fitting program addresses all of these issues. Using the fitting routine program the whole data set can be considered including image force lowering and tunnelling in the reverse bias. This allows a more accurate fit to the whole curve and more confidence in the extracted values.

The fitting program has not solved all the problems but the analysis of the $NiSi_2$ samples has identified several issues with the fitting algorithm and theory. The most troublesome problems were the image force lowering and the double turning point which was caused by the image force lowering in positive applied bias as it tends to the actual SBH. This was overcome by the addition of an extra term in the image force lowering. The very

small change in χ^2 due to the area means fitting to area is very slow and ideally requires forward and reverse bias and at the very least the image force lowering to provide a voltage dependence on the SBH. The fitting program is very robust and can produce excellent fits to the majority of I/V curves. However sometimes the fitting program produces unrealistic parameters which suggest there is theory missing from the model. The ideality factor is very important in gauging how reliable the extracted values are however, the shape of the fit to the experimental curves should still be visually inspected. The turning point of the I/V curve is crucial to indicating if theory is missing from the model as tunnelling through the barrier, an oxide tunnel barrier and inhomogeneous barrier will all affect this region. Using the $NiSi_2$ samples as a test of the Nanoprobe and the new fitting routine has allowed an understanding of how the program works and when the extracted parameters should be questioned. This is crucial for reliable SBH extraction and we will go on to use it on low dimensional $ErSi_2$ structures in the following chapters.

Chapter 5

Rare Earth Silicide on Si(111)

This chapter focuses on the low-dimensional self-assembled rare earth (RE) silicides on n-type silicon(111). The self assembled growth of 3D RE islands on silicon provides a small contact area of a known structure, which can be measured using the Nanoprobe. I/V curves have been collected from a variety of island sizes through several different geometries. A variation of temperature I/V measurements have been achieved allowing the effect of temperature on the SB properties to be studied. Finally the islands were large enough for a four probe contact enabling the Van der Pauw measurement of sheet resistance to be obtained.

5.1 Rare Earth Silicides

The interest in RE silicides within the electronics industry is growing due to the very low SBH of 0.3-0.4 eV formed between a RE silicide and n-type silicon.[102] RE silicides on p-type silicon produce SBH of ∼0.7 eV,[103] which added to the 0.4 eV from n-type give the silicon band gap value of ∼1.1 eV. RE silicide growth on Si(111) is also attractive due to the small lattice mismatch between the Si(111) substrate and the hexagonal RE bulk silicide (0001) plane of -2.55% for Lu to 0.83% for Gd.[104] This small mismatch means there is minimal strain at the interface between the two materials enabling the growth of large epitaxial areas. The growth of RE silicides was initially conducted by Baglin,[22] and the structure and conductivity measurements by Thompson;[105] a more recent review from 1995 on the RE silicides is provided by Netzer.[23]

5.1.1 Structure

The structure of RE silicides has been extensively studied using a variety of techniques such as LEED,[106,107] medium energy ion scattering (MEIS),[12,16,63] and STM.[108,109] These techniques have revealed the detailed structural models presented here and that the trivalent RE (such as Dy, Ho and Er) form very similar silicides with common electrical properties.

2D RE Silicide

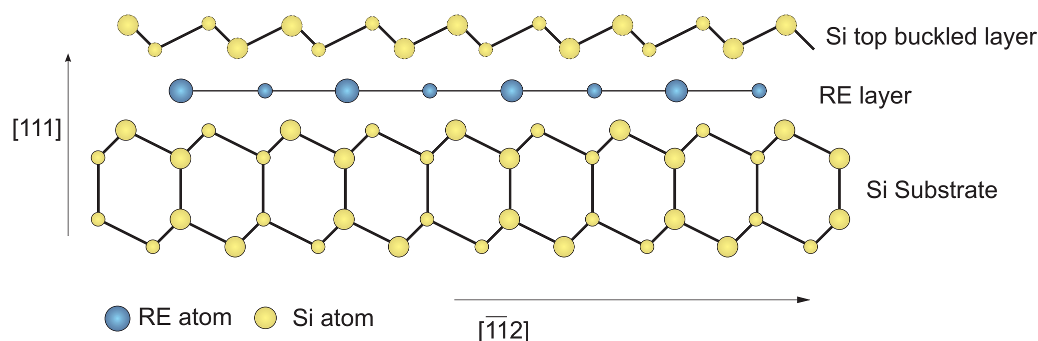

Figure 5.1: Cross section of the 2D RE silicide on silicon B-type buckled structure. Atoms out of plane of the cross section are indicated by smaller circles.

When one monolayer (ML) of trivalent RE is deposited onto a silicon (111) surface and annealed at ~500°C, a two dimensional (2D) hexagonal RE disilicide with a 1×1 periodicity is formed. One ML coverage is defined as 7.88×10^{18} atoms per m^2 for the Si(111) 1×1 surface; this is enough RE to react with the silicon to produce a complete single layer of $RESi_2$ unit cells. This can be seen as a change in the LEED pattern from the substrate Si(111) 7×7 reconstruction to a 1×1 pattern. The RE silicide forms with a stoichiometry of two Si atoms per RE atom to give $RESi_{2-x}$ where $x = 0$. Figure 5.1 shows the RE silicide structure with the RE atoms sitting just under a buckled bi-layer of Si. The Si bilayer is buckled in the reverse direction to the underlying bulk silicon, known as B-type buckling. The subsurface RE atoms sit at the T_4 sites of the Si(111) surface, i.e. above the second layer of substrate Si atoms.[110] This position, with the reverse buckled bilayer above, gives the RE atom the maximum number of nearest neighbours, stabilising the structure. This passivation of the surface leads to a stable bulk-like terminated silicon structure which may allow for further deposition of material without silicide formation. The use of a 2D Er silicide buffer layer is investigated in Chapter 7 with the deposition of manganese.

3D RE Silicide

If the two-dimensional RE silicide surface is annealed at a higher temperature (∼700°C) the 2D silicide diffuses into islands. This structure can also be formed by the deposition of more than one ML of RE onto silicon followed by an anneal at ∼600°C. This forms a three dimensional RE silicide where alternating layers of RE atoms and Si atoms sit above the bulk silicon substrate. The final RE atom layer before the surface, like the 2D RE silicide, sits under a bilayer of silicon. The bilayer can take the B-type buckling as in the 2D or alternatively the A-type, where the bilayer has the same buckling direction as the bulk silicon. However it is more likely that a mixture of A and B type buckling is produced.[63]

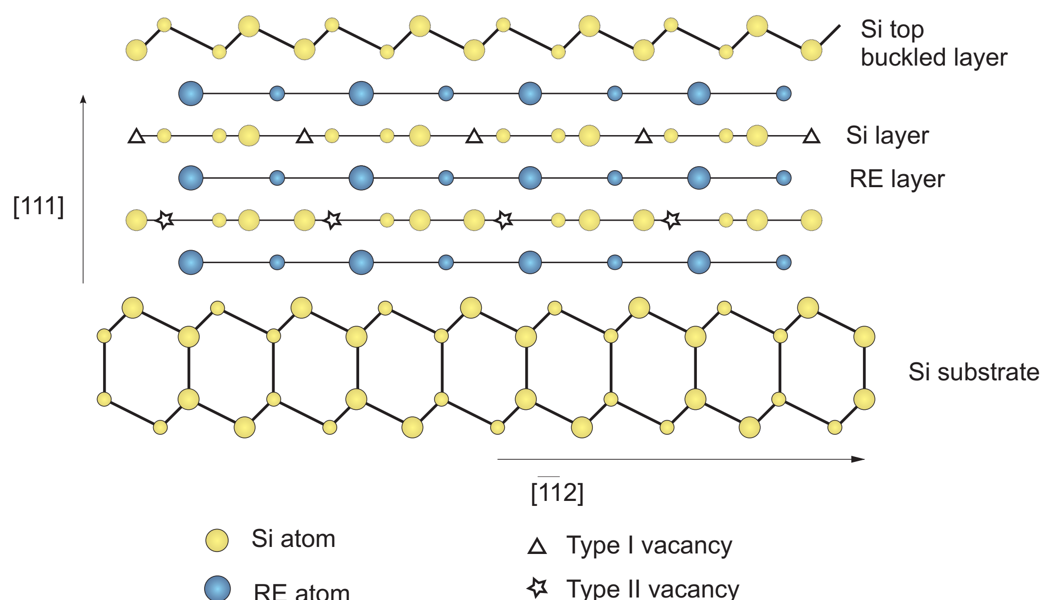

Figure 5.2: Cross section of the 3D RE silicide on silicon showing the vacancies in the Si graphitic layers with an A-type buckled termination structure. The two types of vacancies differ in position relative to their neighbouring layers. Atoms out of plane of the cross section are indicated by smaller circles.

This structure for the 3D RE silicide shown in figure 5.2, although very similar to the 2D, differs by the existence of vacancies in the Si layers where every sixth Si atom is missing. This has the effect of changing the stoichiometry for the 3D silicide to RESi_{2-x} where $x \approx 0.3$. The vacancies exist to relieve the slight strain in the structure from the lattice mismatch and because they are in an ordered array of vacancies they give rise to a $(\sqrt{3} \times \sqrt{3})R30°$ periodicity which shows in the LEED pattern.

Hydrogen Termination of the RE Silicide and Silicon Surfaces

When an islanded surface is produced, the remaining substrate area around the silicide islands is formed from silicon reconstructions. These can take the form of the original Si 7×7 reconstruction or the metastable reconstructions of 5×2 or $(2\sqrt{3} \times 2\sqrt{3})R30°$.[14] These reconstructions can be passivated by hydrogen absorption. This process was carried out for one of the samples to reduce any lateral conduction across the surface through reconstructions with metallic like behaviour, for example 7×7.

Hydrogen termination of the sample also has an effect on the RE silicide Si bilayer. When the surface is passivated, a hydrogen atom is absorbed to a site in the layer of rare earth atoms,[111] this causes the bilayer buckling to reverse.[112,113] The switch from A-type to B-type or vice versa can be observed by a change in the 3 fold LEED pattern.

5.1.2 Growth

The reaction of RE atoms with silicon takes place at an optimum temperature of 550 °C to form a rare earth silicide. This temperature is optimum as it allows all the RE to react with the silicon producing a uniform coverage. If this temperature is increased, the RE silicide diffuses into islands, an effect that can be made use of. Samples of 3D silicide in both thin film and island form have both been grown and investigated as part of this study.

Masked Growth

Using the mask developed for the $NiSi_2$, it was possible to grow known area dots of $ErSi_2$ 3D silicide on n-type Si(111). The Si substrate was prepared as for the $NiSi_2$ using the e-beam heating on the MBE system. The Si was outgassed overnight at 600 °C then flash cleaned at 1200 °C producing a good 7×7 RHEED pattern. The deposition of Er was done from the Balzers source on the MBE, during deposition the pressure of the system was $\sim 2 \times 10^{-8}$ mBar. 10 ML of Er were deposited onto the Si(111) substrate, held at 550 °C, in approximately 40 minutes. This was then post-annealed for a further 30 minutes at 400 °C. A 30 ML sample was also grown under the same conditions except at a higher rate of deposition, so the deposition time was constant at ~40 minutes.

Figure 5.3 shows an example of the $(\sqrt{3} \times \sqrt{3})R30°$ RHEED pattern produced by

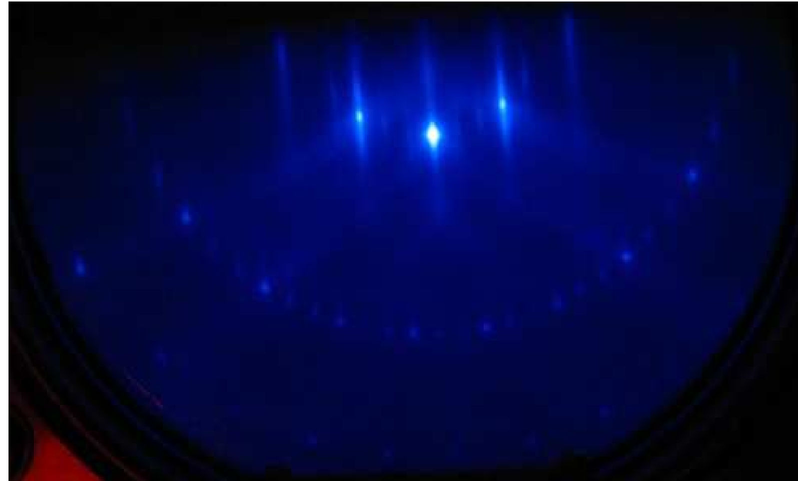

Figure 5.3: 3D $ErSi_2$ $(\sqrt{3}\times\sqrt{3})R30°$ RHEED pattern from 10ML Er deposited on Si(111).

both the 10 ML and 30 ML $ErSi_2$ depositions. The $(\sqrt{3}\times\sqrt{3})R30°$ reconstruction shown by the RHEED is a good indication that $ErSi_2$ has been formed. These samples were removed from the MBE system and silver-dagged onto plain Omicron sample plates to be transported to LENNF in atmosphere.

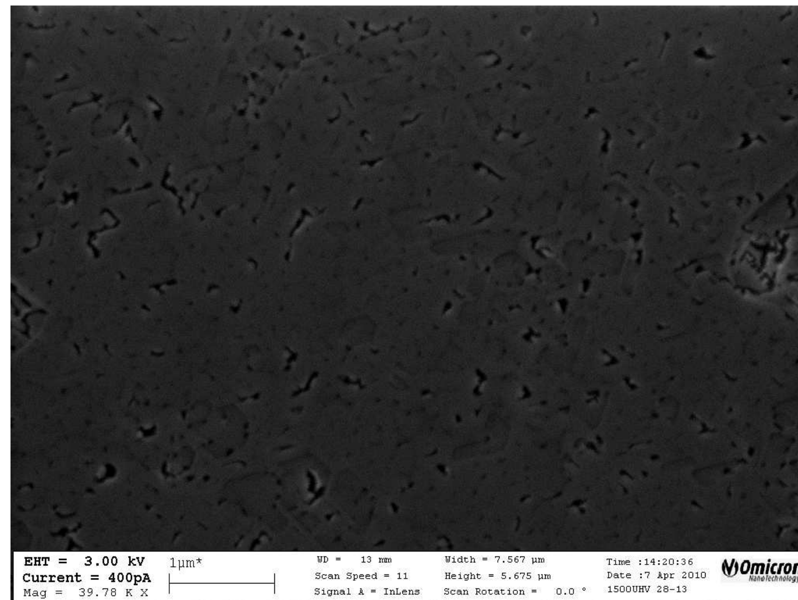

Figure 5.4: Nanoprobe SEM image of 10 ML of 3D $ErSi_2$ grown through the mask in the MBE; defects in the surface show as dark areas.

The growth of the 3D $ErSi_2$ samples in the MBE system did not produce a uniform thin film as seen for the $NiSi_2$. Figure 5.4 shows the crazed surface imaged with the Nanoprobe SEM. This pinhole defected surface of the thin film may be due to the strain in the lattice between Si(111) and $ErSi_2$ not completely removed by the temperature during the annealing process. This could also be aggravated by the high system pressure during deposition,

leading to possible contamination. As these samples were removed from vacuum to transport to LENNF, the pinholes may allow contamination i.e. oxidation to occur through the film down to the silicon substrate, affecting the structure and potentially the SBH.

Self Assembled Growth

The second way to control the size of the $ErSi_2$ contact to the Si requires the exploitation of the self-assembly properties of the silicide. Ostwald ripening allows small islands of $ErSi_2$ to coalesce into larger ones or in this case the 2D silicide to form islands of 3D $ErSi_2$. These samples were prepared in the STM system using the DC heating to outgas the Si substrate overnight at 600 °C, then flash cleaned by cycling to 1200 °C three times before cooling slowly from 900 °C to 700 °C to form the 7×7 reconstruction.

When one ML of Er is deposited onto clean Si(111) at 650 °C over 20 minutes and then post annealed for a further 20 mins at the same temperature, islands of 3D form on the surface. This gives a subtle change in the 7×7 LEED pattern (figure 5.5b) from the original clean Si(111) 7×7 reconstructed surface pattern (figure 5.5a). The first change in the LEED pattern is the weaker intensity of the six extra spots of the 7×7 pattern. The second is the appearance of the $\sqrt{3}$ spots in the centre of each triangle of the hexagonal primary spots, this is an indication of the 3D silicide formation.

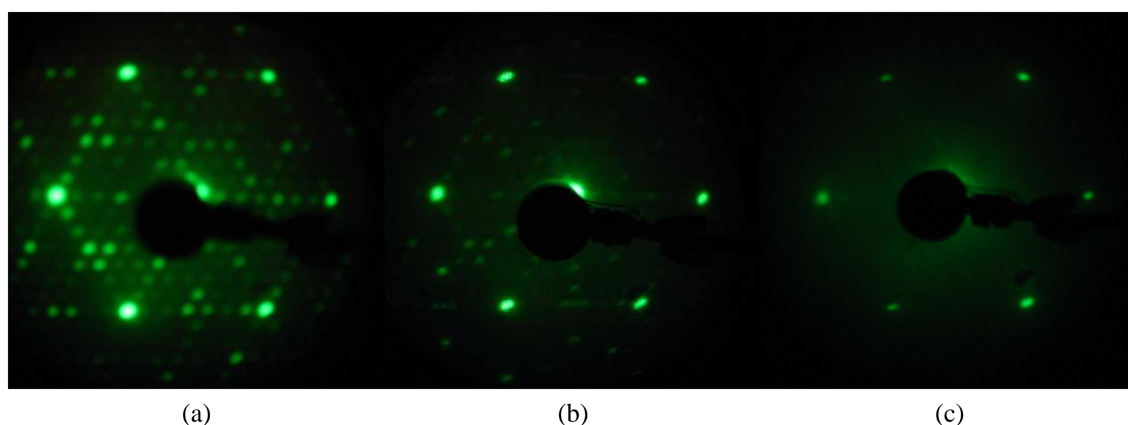

(a) (b) (c)

Figure 5.5: LEED taken at 50 eV of a) Si(111)7×7; b) One ML Er on Si(111) annealed at 650 °C, hint of 3D $ErSi_2$ $(\sqrt{3} \times \sqrt{3})R30°$ spot; c) Hydrogen terminated 1 ML of Er on Si(111),1×1 pattern.

Before the samples were transported to LENNF, an indication of the surface structure and quality was gained from imaging the surface with STM. These samples were hard to scan in the STM because of the height of the 3D $ErSi_2$ islands compared to the surface

reconstructions. The height of the islands could vary from 0.8 nm to 2 nm. Figure 5.6a is a 500 nm scan with three distinct regions, the bright white flat regions of the 3D islands, the lower grey reconstructed 7×7 regions and the dark holes of a metastable reconstruction probably $(2\sqrt{3} \times 2\sqrt{3})R30^{\circ}$ with unreacted Er as bright flecks on the surface. Figure 5.6b is a zoomed scan, 73 nm of the top corner of the middle island in image 5.6a, again showing the three areas in more detail. Defects in the 3D island surface are present as darker pinhole spots on the island surface. The 3D islands are not always surrounded entirely by the 7×7 reconstruction, some areas are adjacent to the $(2\sqrt{3} \times 2\sqrt{3})R30^{\circ}$.

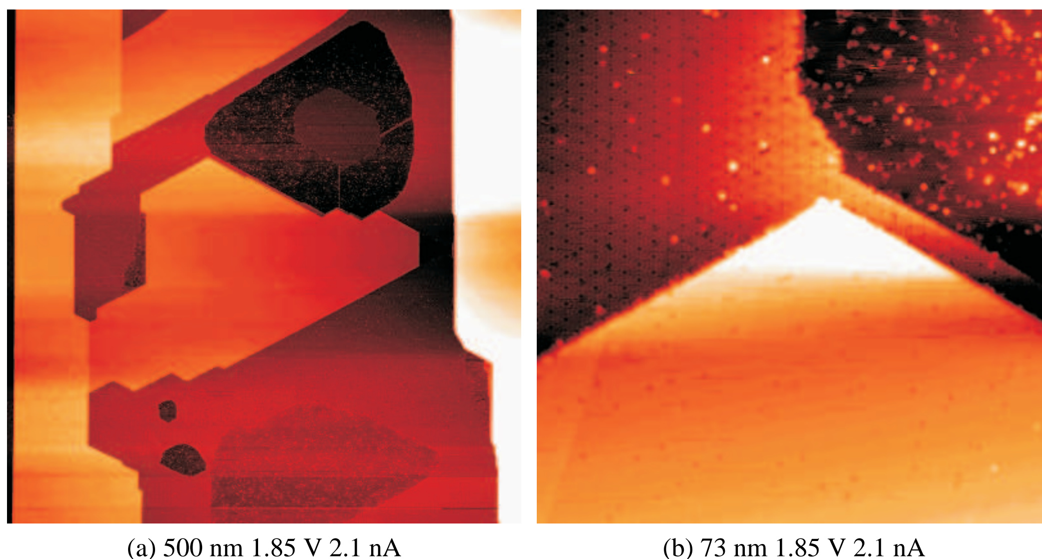

(a) 500 nm 1.85 V 2.1 nA (b) 73 nm 1.85 V 2.1 nA

Figure 5.6: STM scans of 3D $ErSi_2$ islands grown from 1 ML of Er and annealed at 650 °C. a) 500 nm×500 nm, b) 73 nm×73 nm close up showing the surface structure of the three reconstructions.

Although this growth produces 3D $ErSi_2$ islands on the Si(111) surface, as shown in figure 5.7a the surface can be a bit crowded in places. To reduce the density of islands on the surface the Er coverage was reduced to 0.8 ML. This would mean it would be easier to contact only one island with the Nanoprobe tip and that the islands were not connected to each other. To further enlarge the islands, the deposition temperature was increased to 800 °C, again depositing 0.8 ML in approximately 20 minutes continuing with an anneal for 10 minutes at the same temperature before reducing to 650 °C for the final 10 minutes. The resulting surface had almost no impact on the clean silicon 7×7 LEED pattern because the 3D islands were now spread so sparsely.

In an attempt to reduce any effect on the I/V curves that the different surface reconstructions around the 3D islands might have as shown in figure 5.6, the surface was passivated with atomic hydrogen. By hydrogen terminating any dangling bonds and removing

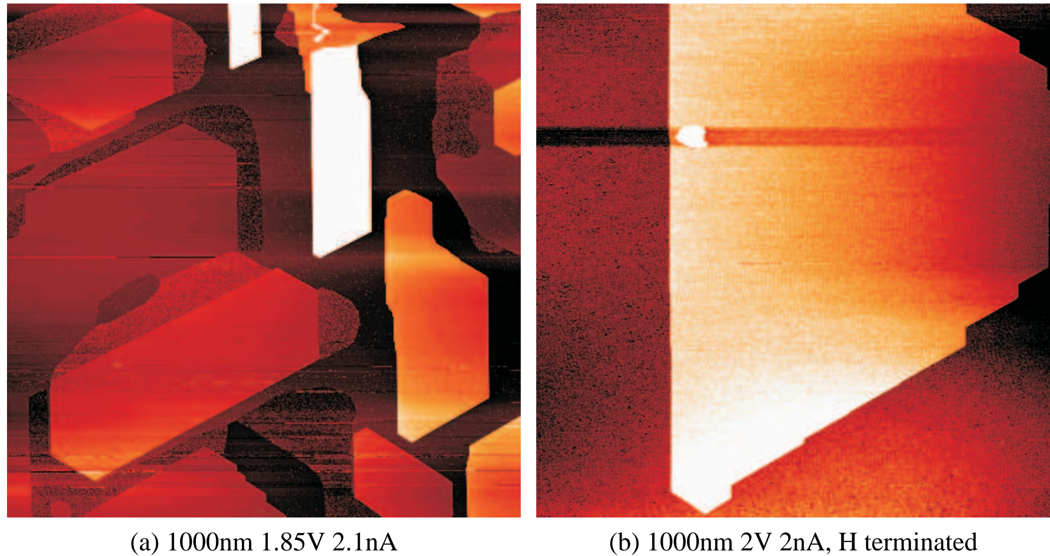

(a) 1000nm 1.85V 2.1nA (b) 1000nm 2V 2nA, H terminated

Figure 5.7: STM scans of 3D $ErSi_2$ islands grown at different temperatures a) 1 ML at 650 °C, b) 0.8 ML at 800 °C and hydrogen terminated.

the reconstructions of the silicon substrate, the surface can be returned to the bulk properties of silicon. To do this hydrogen was leaked into the system until the pressure was 5×10^{-8} mbar, then the tungsten capillary in the hydrogen cracking source was raised to a temperature of 1950 °C. After the sample was exposed to the beam of atomic hydrogen for 15 minutes a 1×1 LEED pattern was achieved as shown in figure 5.5c, this indicates a passivated surface has been achieved. If the exposure is for an shorter length of time the LEED pattern still shows the $(\sqrt{3} \times \sqrt{3})R30°$ spots.

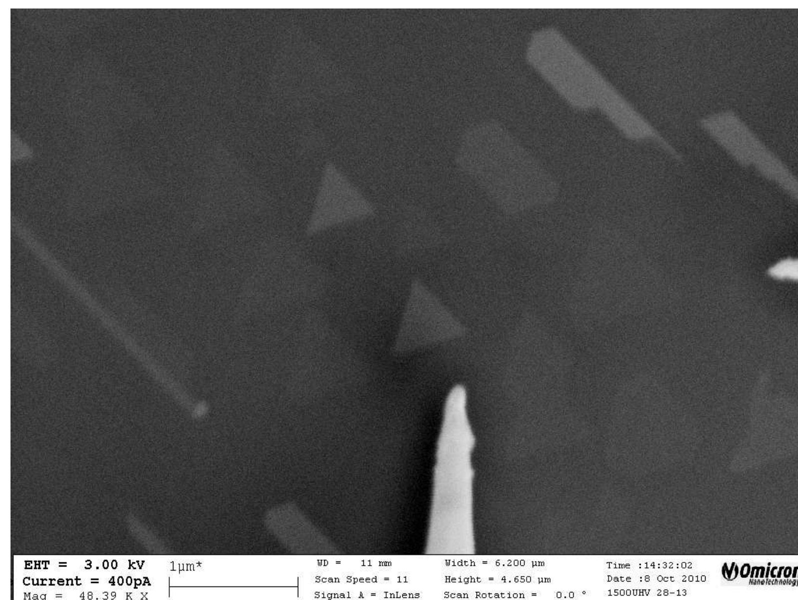

Figure 5.8: Nanoprobe SEM image of the sample previously imaged in the STM in figure 5.7 of the 3D $ErSi_2$ islands.

The final surface is shown in figure 5.7b where a large 1000 nm sided equilateral triangular island is shown after hydrogen termination, with no surface reconstructions around the island. The samples were transferred to LENNF in the vacuum suitcase to reduce contamination and oxidation of the samples, enabling contact to the silicide rather than an oxide layer during I/V collection. These hundreds of nanometre diameter islands are visible in the Nanoprobe SEM as shown in figure 5.8.

5.2 I/V Measurements

The samples were transferred to LENNF where the Nanoprobe was used to take a variety of I/V measurements from different geometries using one or two tips, and Van der Pauw measurements were taken using four tips.

5.2.1 I/V from Masked Dots

The first $ErSi_2$ samples were grown in the MBE through the same mask that was used for the $NiSi_2$ dots. This produced the granular film with pinhole defects, shown in figure 5.4, which after transporting to LENNF in air was probed using a single STM tip and the back contact. The granular film of a 500 μm diameter dot produced the I/V curve shown in figure 5.9 with a hysteresis between the up and down sweep of the applied positive bias. This hysteresis was reproducible out to an applied voltage of $\sim$5 V and a current of $\sim$4 mA at the maximum applied positive bias. The position of the up sweep knee stayed constant for each repeat measurement sweeping to a higher applied bias.

Fitting to the two sides of the hysteresis produced the fits shown in figure 5.9. The following values were obtained from the up and down sweeps respectively from the fits: χ^2 of 196.8 and 82.8, SBHs of 1.437 eV and 1.127eV with effective SBHs of 1.414 eV and 1.106 eV. Series resistances of 5645 Ω and 5759 Ω and shunt resistances of 2.2 MΩ and 3611 Ω. The areas were 1.9×10^{-3} mm^2 and 9.9×10^{-4} mm^2 with idealities of 1.079 and 1.093. The main difference between the up sweep and the down sweep is a drop in fitted SBH and the dramatic drop in the shunt resistance indicating that the SB is much leakier as the applied voltage is decreased. These effects could be caused by a change in the field across the interface of the two materials.

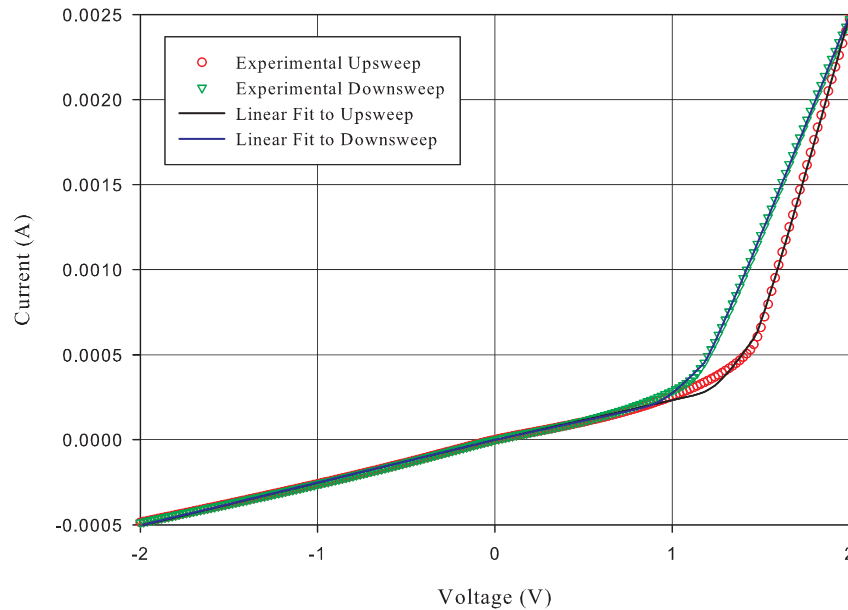

Figure 5.9: I/V curve of a 500 μm diameter $ErSi_2$ dot with a separate fit to the up and down sweeps of the applied bias.

These samples were transferred in air so oxidation may have occurred between the grains of the $ErSi_2$. This additional oxide may act as an insulating layer causing parts of the surface to act as a capacitor which charges up as the bias is applied. This accumulated charge then affects the SB characteristics on the return sweep. The SBHs are unrealistic for one direction as it is larger than the band gap of silicon, although the field altering due to the oxide between the inhomogeneous surface could be the cause. The hysteresis of these samples is reproducible and has been seen on samples grown with different thickness deposits of Er. Sweeping to a higher voltage obtains the same curve on the up sweep however the down sweep gradient has to alter to align the return knee. Altering the maximum applied voltage also alters the sweep rate, which seemed to indicate no time dependence. However a time dependence would be expected if it was a capacitor. A further measurement would be to hold the voltage steady and measure the current over time to look for an RC decay. These samples have an unknown structure due to the many pinholes observed on the surface, because of this the SB properties have an extra level of complexity for which the fitting routine presently contains no theory for. However, the program fits show that a significant change in the shunt resistance and the SBH begin to describe the differences in the two sides of the sweep.

5.2.2 I/V of the Self Assembled Island-Silicon Interface

The self-assembled $ErSi_2$ islands were transferred to LENNF in the vacuum suitcase. The I/V curves were taken with the bias applied to one tip on an island and the second contact was taken as the sample plate substrate contact. Figure 5.10 shows a curve from a sample which has not been hydrogen-passivated. The back contact, which is the back of the silicon substrate to the sample plate contact, seems to be dominating as a larger current flows in the reverse bias compared with the forward. Using the back-to-back fitting program IV.x to fit the data the program removed the forward biased SB and only fitted the back contact, the reverse SB. The fit obtained values of 0.95 eV for the SBH with an area of 3.35 mm^2, an ideality of 1.01, shunt resistance of 473 MΩ and a series resistance of 84 kΩ. The fit returns a χ^2 value of 9.9×10^{-4} which is a good fit. This means the back contact is dominating and any SB under the high reverse shunt current of this back contact cannot be extracted. To be able to extract good parameters from I/V curves, the back contact should be ohmic or very leaky with a low shunt resistance. In an attempt to improve the back contact, the back face of the silicon was further roughened using a diamond file, and to improve the front contact and reduce oxidation the surface was hydrogen passivated.

The $ErSi_2$ islands grown and then passivated with hydrogen produced I/V curves which could be fitted to extract the forward SBH. Figure 5.11 shows one of the experimental I/V curves from island 1 with the corresponding fit from IV.x. The fit obtained values of 0.288 eV for the SBH and 0.277 eV for the effective barrier at zero applied bias. The shunt resistance fitted at 70.9 kΩ indicating a very low leakage current with a series resistance of 1673 Ω. The ideality was fitted as 1.01 and the area of 0.562 μm^2 compared to the area measured from the SEM image of 9.46 μm^2. Although this is a seemingly large difference in area, the fitting program will make very little change to the χ^2 if the SEM value was used. The fitting program is not going to be able to improve the area quickly due to the large χ^2 value of 20.95 which, although high, is due to the slight hysteresis in the forward bias from the voltage sweep which can just be seen in figure 5.11 as a splitting of the circular data points. This hysteresis is due to the contact of the tip on the island changing due to drift or changes in any oxidation of the surface. Hysteresis of this type is often seen when the first contact is made to an island; the contact is improved by pressing the tip into the surface slightly more to make a stable contact.

I/V curves were collected from five different $ErSi_2$ islands and analysed, the results

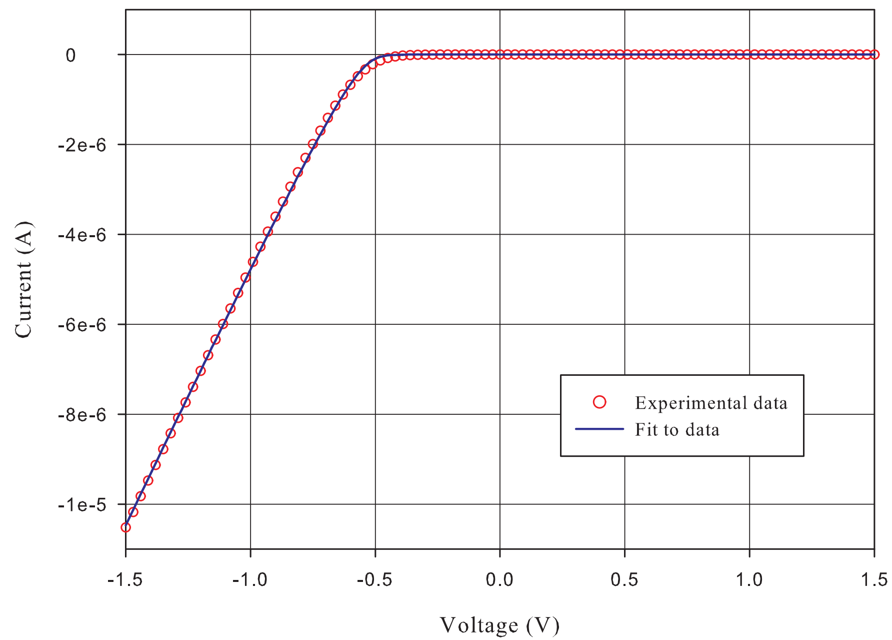

Figure 5.10: I/V curve from $ErSi_2$ island on Si(111), measured from one tip on the island to the back contact of the sample plate. The fit to the data from IV.x is also plotted.

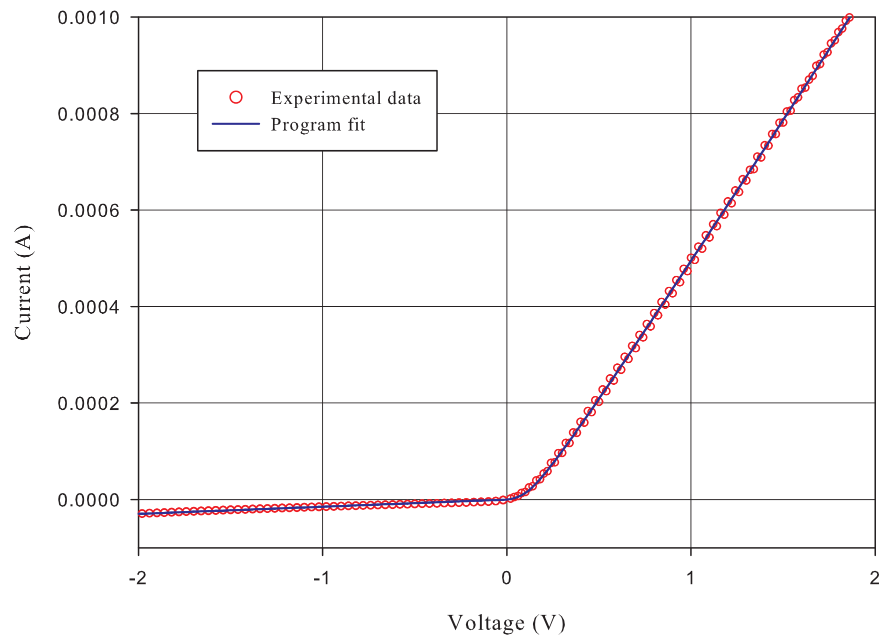

Figure 5.11: I/V curve from $ErSi_2$ island on Si(111) with hydrogen passivation, measured from one tip on the island to back contact of the sample plate. The IV.x fit is plotted alongside.

are presented in table 5.1. The presented data are averages of several experimental data fits and the errors are obtained from the mean variance of the fit parameters. From the

	Island 1	Island 2	Island 3	Island 4	Island 5
SBH (eV)	0.300 $\pm$0.016	0.548 $\pm$0.046	0.382 $\pm$0.077	0.501 $\pm$0.008	0.511 $\pm$0.001
Effective SBH (eV)	0.289 $\pm$0.015	0.532 $\pm$0.045	0.369 $\pm$0.075	0.485 $\pm$0.008	0.496 $\pm$0.001
Shunt (kΩ)	67.1 $\pm$7.5	31377.8 $\pm$1585.1	315.7 $\pm$29.8	1178.9 $\pm$132.7	558.9 $\pm$8.2
Ideality	1.052 $\pm$0.022	1.022 $\pm$0.015	1.00 $\pm$0.01	1.00 $\pm$0.01	1.019 $\pm$0.003
Measured Area (μm^2)	9.46 $\pm$0.01	0.69 $\pm$0.01	1.47 $\pm$0.01	0.58 $\pm$0.01	0.45 $\pm$0.01
Fitted Area (μm^2)	0.945 $\pm$0.822	0.111 $\pm$0.04	0.765 $\pm$0.509	0.202 $\pm$0.004	0.185 $\pm$0.002
Series (Ω)	1845.9 $\pm$168.6	9935.8 $\pm$878.2	7223.2 $\pm$534.8	9486.3 $\pm$526.8	6436.2 $\pm$115.6
χ^2	13.4 $\pm$8.3	4.3 $\pm$1.6	6.77 $\pm$0.30	0.75 $\pm$0.35	0.51 $\pm$0.04

Table 5.1: Average fit parameters for $ErSi_2$ islands on Si(111).

five islands measured, the fitted SBH has a large spread of 0.30 eV to 0.55 eV with the two best χ^2 fits giving similar SBH of 0.5 eV. All the shunt resistances are large indicating very little leakage past the SB, therefore a good contact. The area fits are smaller than the measured areas from the SEM images with the closest match between SEM and fitted area being the islands with the best χ^2 fits. These values are close to reported $ErSi_2$ island SBH which have been shown to vary with annealing temperature between 0.28 eV and 0.43 eV.[114]

5.2.3 I/V Between Self Assembled Islands

By measuring between two $ErSi_2$ islands separated only by the substrate, it was hoped to use the back-to-back fitting routine to fit and extract both SBH at the same time. Unfortunately, this geometry produced I/V curves which were largely dominated by tunnelling as

shown in figure 5.12. The data has been plotted alongside an oxide tunnel curve simulated using equation (2.32) with parameters of oxide layer thickness 1.0 nm, barrier 2.22 eV and area of 0.04 μm^2 which would be reasonable values for the tip contacting to an oxide layer. The experimental data is not totally from a tunnel barrier due to the slight unsymmetrical shape of the experimental curve. This means the tunnel curve does not follow the data exactly. The fitting program IV.x cannot fit an oxide tunnel barrier on top of a back-to-back SB at the time of writing as the code can only handle two barriers. The addition of further barriers in series unfortunately requires rewriting parts of the code in the future.

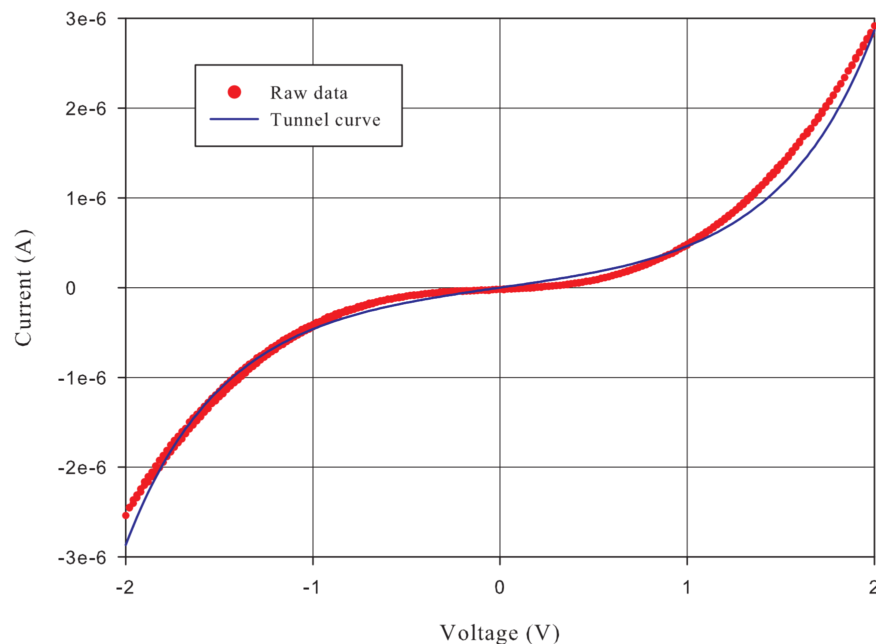

Figure 5.12: I/V curve from two neighbouring islands connected only by the substrate. A curve generated from the oxide tunnel expression is plotted alongside.

Note After Viva

Peripheral edge tunnelling caused by the crowding of field lines may be the cause of the slow turn-on seen in the I/V curves and not an oxide tunnel barrier. This idea is discussed further in section 8.2.2.

5.2.4 Van der Pauw

Several two-probe measurements were taken with both tips on the same island. Although this produced some excellent ohmic curves with two point contacts, this includes the contact resistances of the tips. The sample which was transferred after erbium growth has an average resistance of 8212 Ω whereas the hydrogen terminated sample has an average of 1133 Ω. The hydrogen termination has enabled a lower contact resistance between the island and the tip because the hydrogen has passivated the surface reducing the oxidation.

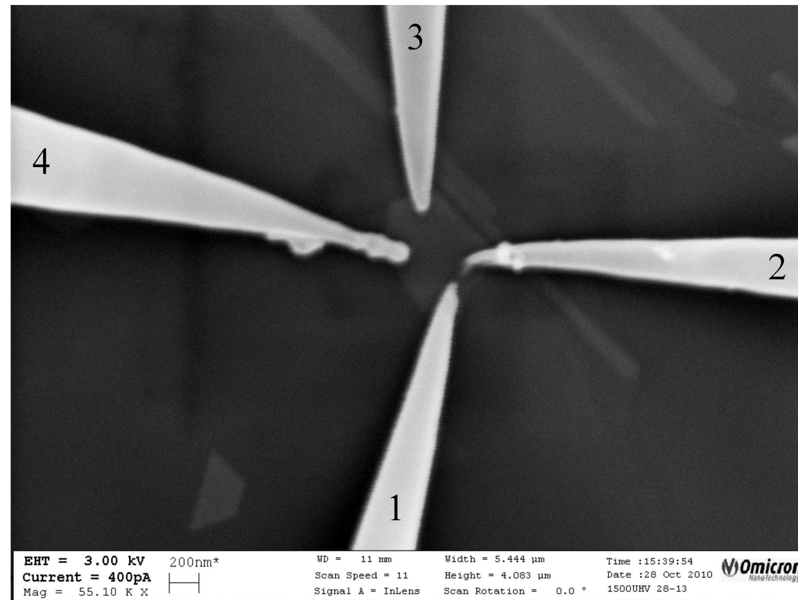

Figure 5.13: SEM image of the four tips during a Van der Pauw measurement.

To take a resistance measurement of the $ErSi_2$ island without the contact resistance, a Van der Pauw measure was taken as described in section 3.4.2. The four tips were bought into contact with the island as shown in the SEM image in figure 5.13. Two resistances were obtained by sourcing a current to two adjacent tips and measuring the voltage across the opposite two probe tips, then swapping the pairs of tips by 90° and repeating the measurement. This provides two ohmic curves which are shown in figure 5.14. The resistance measured from the gradient of the plots of V against I in figure 5.14 from using tips 4 to 1 to source and tips 2 to 3 to probe was $1185 \pm 5\ \Omega$ and for source tips 3 to 4 and probe tips 1 to 2 a resistance of $286 \pm 5\ \Omega$. Solving the expression in section 3.4.2 using numerical methods results in a sheet resistance of $2874 \pm 21\ \Omega$/sq and a resistivity of between $2.87 - 5.75 \times 10^{-4}\ \Omega$cm assuming the thickness of the island is between 1 and 2 nm respectively. The bulk value for the resistivity of $ErSi_2$ is $3.4 \times 10^{-5}\ \Omega$cm, as expected the value for a low dimensional island is higher due to the increased scattering.

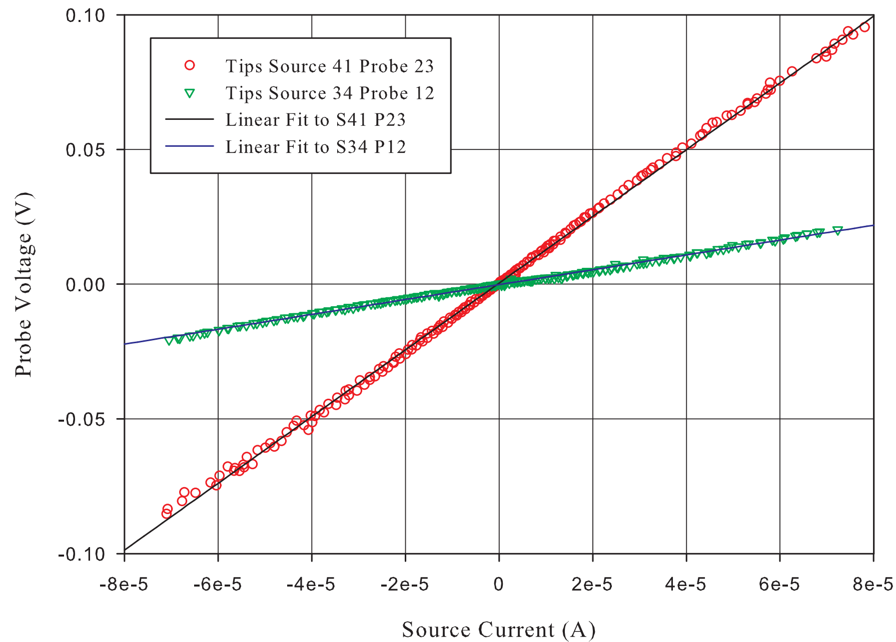

Figure 5.14: The ohmic curves measured during a Van der Pauw measurement and linear fits to the data. The voltage from the probe tips and current from the source tips.

5.3 Temperature variation of I/V Measurements

The hydrogen passivated $ErSi_2$ island sample used to obtain the I/V curves in section 5.2.2 was cooled using the Nanoprobe helium cryostat to take I/V at different temperatures between 179 K and 321 K. The use of the SEM allowed the location and tracking of an island which was measured at each temperature. The tip had to be withdrawn between each temperature change to avoid the tip crashing due to thermal drift.

5.3.1 Temperature I/V Through the Self Assembled Islands

The I/V curves taken from the same island shown in figure 5.15 are presented in figure 5.16a. The high temperature (321 K) I/V curve was the most difficult to take due to thermal drift and this is shown in the sweep of the I/V curve not following the same path on the up sweep compared to the down sweep.

In the high positive applied bias the current decreases with increasing temperature which is not as expected from thermionic emission theory. This is probably due to a change in the resistance with the change in temperature. The change in temperature follows this

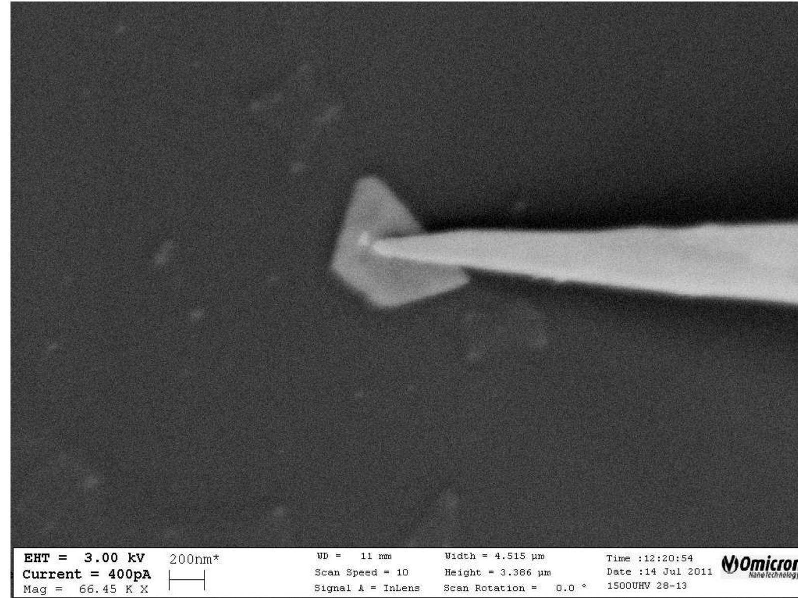

Figure 5.15: SEM image of the $ErSi_2$ island with the tip positioned to measure the I/V at different temperatures.

decreasing trend except for 299 K and 262 K in this high voltage region where they fall very close to each other and in the wrong order. In the negative applied bias region shown in figure 5.16b, the current flowing increases with temperature and all the I/V curves fit this trend. The turning point of the I/V curves shown in figure 5.16c is very important to obtain the SBH, although there is some hysteresis on the I/V sweeps the curves follow the trend of decreasing temperature, increasing SB turn on voltage. This is as expected and shown with the simulated I/V curves shown in figure 2.13b.

The I/V curves were fitted using IV.x by setting the temperature for each I/V curve to the value measured during the experiment. The oxide tunnel barrier has been set at 1.5 nm thickness, this may not be correct as the measurements were taken over the course of a day in which time the oxide thickness may have changed by a few Å. The area of the tunnel barrier has stayed approximately constant with the tunnel barrier increasing with temperature. The first fit was allowed to vary the area of the SB, the second run we fixed the area of the SB at 3.20×10^{-7} mm^2 which is the area of the island measured from the SEM image in figure 5.15. The final fit was run at a smaller fixed area of 8.0×10^{-8} mm^2 to see if a smaller area improved the χ^2 of the fit. All the parameters obtained from these fits are shown in table 5.2. The fits for the fixed area of 3.20×10^{-7} mm^2 are plotted on the I/V curves in figure 5.16. The fit has worked well at the high positive bias and this can be seen from the increase in series resistance with the increase in temperature shown in table 5.2.

Temperature (K)	SBH (eV)	Effective SBH (eV)	R_{series} $(k\Omega)$	R_{shunt} $(M\Omega)$	Ideality	Area (mm^2)	Tunnel Barrier (eV)	Tunnel Area (mm^2)	χ^2
179.0	0.498	0.481	9.8	22.3	1.038	1.56×10^{-8}	0.430	1.35×10^{-6}	1.2232
231.3	0.438	0.422	10.5	22.3	1.017	3.85×10^{-8}	0.513	1.36×10^{-6}	0.3288
262.2	0.419	0.404	11.5	20.3	1.007	1.76×10^{-7}	0.570	1.20×10^{-6}	0.2629
299.2	0.438	0.423	10.7	22.3	1.017	6.71×10^{-8}	0.592	1.32×10^{-6}	1.6337
321.2	0.438	0.423	12.0	22.3	1.017	3.74×10^{-7}	0.606	1.36×10^{-6}	5.9063
179.0	0.541	0.524	10.0	22.3	1.046	3.20×10^{-7}	0.396	1.35×10^{-6}	1.3615
231.3	0.461	0.445	10.7	22.3	1.009	3.20×10^{-7}	0.507	1.36×10^{-6}	0.5766
262.2	0.427	0.412	11.5	20.3	1.000	3.20×10^{-7}	0.572	1.20×10^{-6}	0.2456
299.2	0.421	0.407	10.7	22.3	1.078	3.20×10^{-7}	0.615	1.32×10^{-6}	1.8118
321.2	0.437	0.422	12.0	22.3	1.017	3.20×10^{-7}	0.606	1.36×10^{-6}	5.9032
179.0	0.526	0.508	9.8	22.3	1.041	8.0×10^{-8}	0.418	1.35×10^{-6}	1.2752
231.3	0.439	0.423	10.2	22.2	1.008	8.0×10^{-8}	0.537	1.36×10^{-6}	0.1948
262.2	0.407	0.393	11.8	20.3	1.000	8.0×10^{-8}	0.557	1.20×10^{-6}	0.1986
299.2	0.428	0.413	10.7	22.3	1.088	8.0×10^{-8}	0.591	1.32×10^{-6}	1.6303
321.2	0.243	0.240	12.4	22.3	1.000	8.0×10^{-8}	0.682	1.36×10^{-6}	2.8019

Table 5.2: $ErSi_2$ island temperature variation I/V curves analysed using IV.x. Top part of table is the parameters from a fit where area is allowed to vary, middle block of the table are fits from a fixed area of 3.20×10^{-7} mm^2 and the bottom block are fits from a fixed area of 8.0×10^{-8} mm^2.

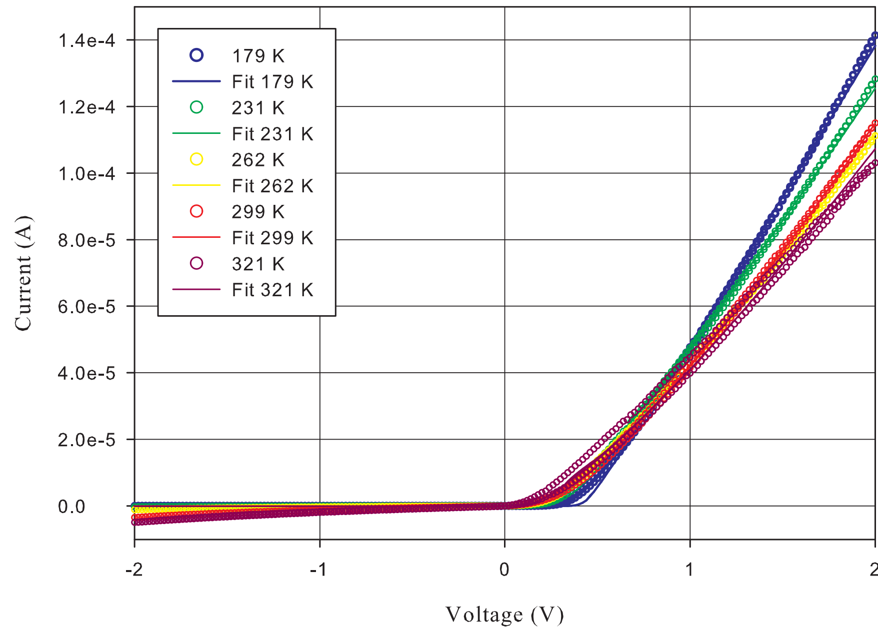

(a) Full bias range

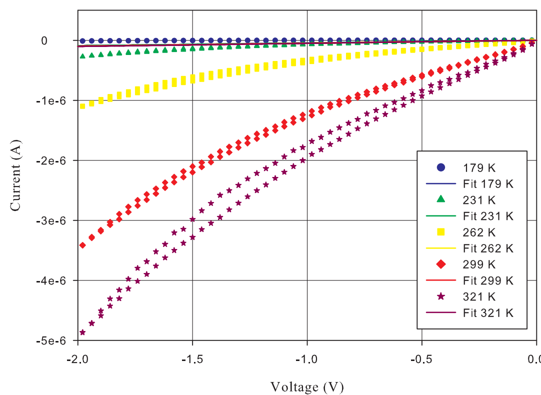

(b) Reverse bias

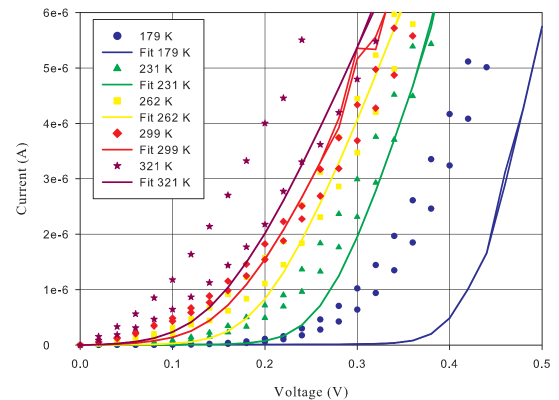

(c) Turning point

Figure 5.16: I/V curves taken at different sample temperatures between an $ErSi_2$ island and the back contact. a) Full I/V curve, b) Negative applied bias regime, c) Turning point of the I/V curve.

The increase in series resistance with temperature is unexpected as the series resistance arises from the silicon resistance and the contact resistance. The silicon resistance would be decreasing with increasing temperature due to more electrons being excited into the conduction band whereas the increase in electron scattering in the metal tip contact to the island would increase the resistance. The 262 K curve which is out of order according to the trend at the high applied bias is matched by the series resistance for this being higher than that for the 299 K fit. The reverse bias has not fitted very well, with the shunt

resistance staying almost constant across all the temperatures. The fit at the turning point shown in figure 5.16c has not fitted the curve very well; however, the fits do lie in the correct order for the increase in temperature.

The values for SBH lie in the region of 0.42 to 0.54 eV with the majority of values at 0.44 eV. The 321 K fit at the smaller fixed area shows a SBH of 0.24 eV; however, the fit of this curve has jumped to fit the reverse bias and does not fit the turning point very well at all, for this reason this value should be ignored.

5.3.2 Temperature I/V Between Self Assembled Islands

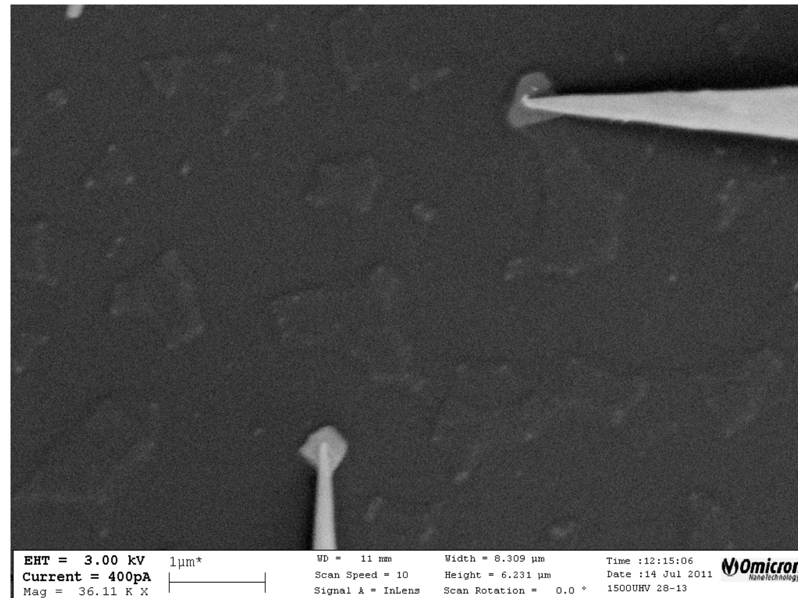

Figure 5.17: SEM image of two $ErSi_2$ islands with the tips positioned to measure the I/V between the islands.

An I/V curve was taken between two islands at different temperatures, these are shown in figure 5.17. The I/V curves are shown in figure 5.18 and follow the trend of increasing current with increasing temperature, which is expected as more electrons will be excited into the conduction band at a higher temperature, thus reducing the series resistance. The curves are influenced by tunnelling to give the very gradual curved turn-on as the temperature is reduced. The curves resemble oxide tunnel curves which cannot be fitted with a back-to-back SB using our fitting program. The highest temperature curve at 299 K has what looks like a SB turn on at low negative applied bias before the gradual tunnelling curve takes over, this odd shape is not possible to describe with the theory used in the fitting program. The strange shape at this low bias could be due to a change in the tip

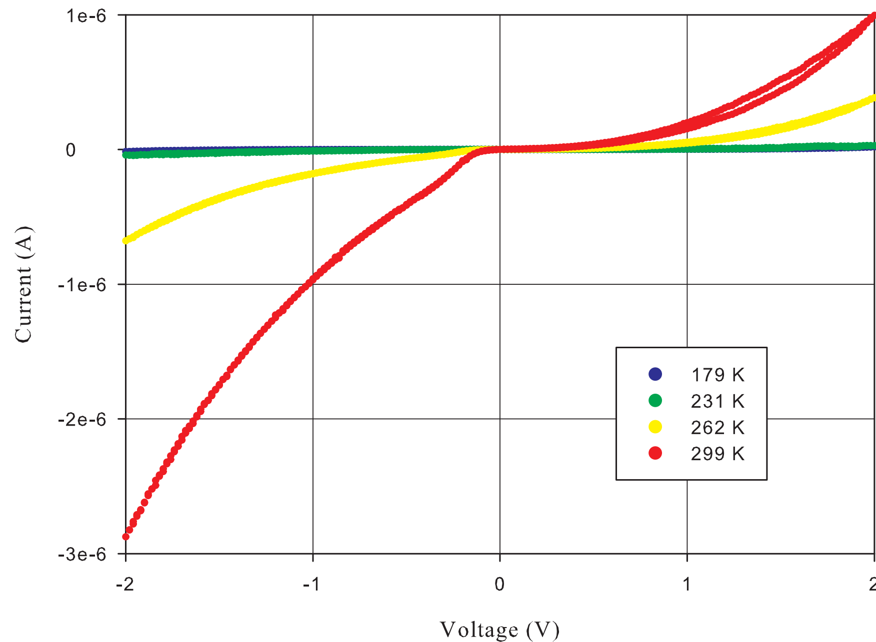

Figure 5.18: I/V curves taken at different sample temperatures between two $ErSi_2$ islands.

contact during the I/V sweep.

5.4 Conclusion

The growth of the masked $ErSi_2$ dots did not produce the well-ordered structure that had been hoped for; instead, a pinhole crazed surface was shown from the SEM image. This unknown structure of a phase of erbium silicide produced an interesting reproducible hysteresis which the fitting program successfully fitted to either side of the sweep. The fit showed that the main difference between the two sides was a big change in the shunt resistance and a change in the SBH. These could be due to a charging effect between grains of the crazed surface structure altering the field across the silicide-silicon interface.

The self-ordered $ErSi_2$ islands produced a more ordered structure and the islands have provided low dimensional contacts to probe with the Nanoprobe. The Nanoprobe has been very successful at probing these types of sample. The hydrogen terminated sample reduced the oxide layer and made it possible to extract the SBH for the correct MS interface. If the back contact to the silicon substrate has a high shunt resistance this can dominate the I/V measurement; the more ohmic the back contact can be made, the more reliably the

island-silicon contact can be measured. The measurement between two similar islands to avoid the back contact and use the back-to-back fitting routine was unable to be fitted with the program because the I/V curve was dominated by tunnelling. The sheet resistance of an $ErSi_2$ was measured by a four point Van der Pauw measurement obtaining a value of 2874 ± 21 Ω/sq. Assuming an island thickness of 1 nm to 2 nm, the resistivity is calculated as $2.87 - 5.75 \times 10^{-4}$ Ωcm compared with the bulk value of 3.4×10^{-5} Ωcm. The experimental value is higher than the bulk value due to the low dimensional size of our islands.

The room temperature measurements gave an average value from the different islands of 0.45 ± 0.09 eV for the SBH, whereas the temperature variation gave an average over the temperatures of 0.45 ± 0.03 eV; this is within error of the previously reported value of 0.43 eV. However, this is reported for an unannealed sample which was seen to drop to a SBH of 0.28 eV with annealing.[114] Another report puts the SBH for $ErSi_2$ at a value of ~0.39 eV, which would mean the room temperature measurements are within error.[102] The temperature variation has shown that the cooling method with the Nanoprobe is successful and some reproducible trends were obtained from the I/V curves. The fitting program has successfully fitted to the curves with the addition of the oxide tunnel barrier. However, the oxide tunnel barrier thickness has to be varied manually and therefore may not be the value which obtains the lowest χ^2 value for each I/V curve.

Note After Viva

The addition of peripheral edge tunnelling to the model may improve the temperature variation fits as tunnelling becomes more dominant at low temperatures.

Chapter 6

Rare Earth Silicide Nanowires on Si(001)

When a sub-monolayer coverage of RE is deposited onto Si(001) at an elevated temperature, RE silicide nanowires (NWs) form across the substrate surface, an observation first noted with Dy by Preinesberger *et al* in 1998.[115] At higher coverages and under different growth conditions, square and elongated islands can be grown.[13] Self-assembled NWs have a possible future in nano electronics as nanometre scale wires and electronic components;[116] however there is little control over where they form on the surface. This chapter looks at measuring the electrical properties along the nanowire (NW) and through the contact to the silicon surface into the bulk, to begin to understand the transport properties of NWs.

6.1 Rare Earth Silicide Nanowires

The growth of RE silicides on the Si(001) surface is of particular interest due to the lattice mismatch between the RE silicide and the Si substrate. The fact the mismatch is small in some directions leading to epitaxial growth but high in others restraining growth plays a key role in NW formation. Depending on the mismatch, NWs can grow up to several microns long but are constrained generally to between 1.5 and 10 nm in width. This variation in size can be achieved by the use of different RE metals with correspondingly different lattice mismatches of their silicides and is dependent on the growth conditions such as deposition temperature and coverage. NW have been reported with RE metals of Dy, Er, Gd, Ho, Sc, Sm,[117,118] but the silicides of Nd and Yb form islands. With appropriate

conditions the NWs can form into bundles of wires increasing their width towards 100 nm.

Quasi-1D systems such as NW are of fundamental interest because their electronic properties are different to 2D and 3D systems. The self assembly nature of the NW means they can be smaller than anything currently achievable by nanolithography techniques and form single crystal structures. The defect free, crystalline structure allows NW to handle high current densities making their use as nanointerconnects between components a viable option. NWs could also be envisaged as switches,[119] memory storage devices,[120] and elements in logic devices.[121] This has yet to be realised due to the readiness of the silicon surface and the RE metals to react with oxygen and the difficulties of mass manufacturing as currently these silicides are produced under UHV conditions.

RE NW have been shown to exhibit metallic properties,[122,123] and some unusual quantum effects.[124,125] One such effect is that of the Peierls distortion where a change in the width of the NW along its length shows a move from metallic to semiconducting behaviour of the NW. This has the potential of a SB junction at the change in the NW properties.[125]

6.1.1 Growth

The lattice mismatch between the Si(001) surface and the RE silicide is thought to be the key factor in NW formation. The hexagonal RE silicide c-axis has a much larger mismatch to the Si(001) lattice than the RE silicide a-axis. The lattice constant for silicon is 3.845 Å where as for $ErSi_2$ the a-axis is 3.798 Å giving a mismatch of -1.22%. However the c-axis for $ErSi_2$ is 4.088 Å yielding a lattice mismatch of +6.3% hence the strained growth in the [110] direction.[15,122]

NWs form by Stranski-Krastanov growth where a wetting layer is created first on the deposition of RE before the growth of NW.[126] NWs consume silicon to form the silicide and therefore are not completely on top of the substrate surface but are partly sub-surface. Studies into the surface reconstructions around a NW is thought to be the precursor to NW growth; Gd, Dy and Ho show 2×4 and 2×7 wetting layers,[15,127] where as Er forms 2×3, 5×2 and $c(5 \times 4)$.[128]

Although the precise structure of the NW is not known due to the small proportion of the surface covered by the NW structure, there is evidence showing that NWs are hexagonal. Cai presents evidence from STM heights of the NW which have been measured

as 0.33 Å which corresponds to the hexagonal phase of $ErSi_2$.[129] Further work shows the square islands to be 1.2-1.4 nm high consistent with the tetragonal silicide phase but there is much contention over this with both tetragonal and hexagonal structures being proposed.[13,130,131]

The growth of NW is very sensitive to the deposition conditions such as temperature, rate of deposition, coverage and annealing time and temperature. The NW were grown onto a substrate of n-type Si(001) 4° offcut to promote NW growth in one direction. This is due to the Si terraces all having perpendicular dimmer rows because of the 4° offcut. This was essential to be able to locate stand-alone NW in the Nanoprobe to be able to make contact to and ensure that there were no connections to other NW. The substrate was cleaned by DC flashing after an outgas overnight at 600 °C. The silicon was flashed up to 1200 °C once and then slow cooled from 900 °C to 700 °C. If the substrate is cycled as it is for Si(111), the surface becomes more rough with terrace edges becoming more undefined. The NW samples were required to be ∼50 nm wide so the Nanoprobe could contact to them, meaning that the wires were bundles of NWs rather than a single NW. To achieve this, 0.4 ML of Er was deposited onto a substrate at 640 °C in approximately 10 minutes. This was then further annealed at the same temperature for 15 mins.

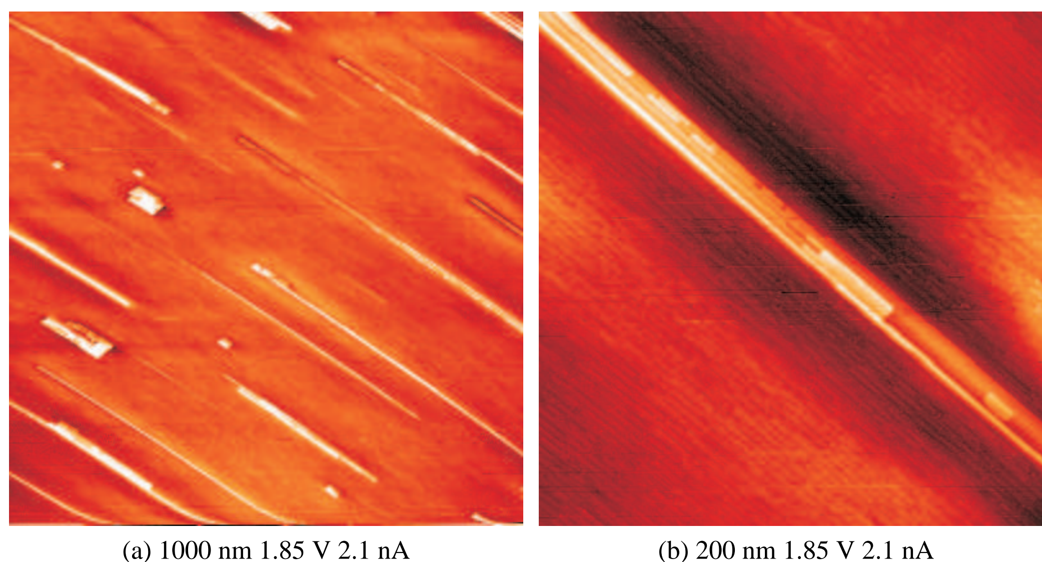

(a) 1000 nm 1.85 V 2.1 nA (b) 200 nm 1.85 V 2.1 nA

Figure 6.1: STM scans of $ErSi_2$ nanowires on Si(001) 4° offcut. a) 1000 nm×1000 nm overview showing isolated NW and islands, b) 200 nm×200 nm close up showing the bundle of NW and the terraced surface of the 4° offcut Si.

This sample preparation produced NW less than a micron long but ∼20 nm wide as shown in figure 6.1a. These NW are up to ∼4 nm in height, but seem to sit in a dip on

the surface of consumed Si. The surface does have some islands present but the majority of NW are unconnected. Figure 6.1b shows that the wide NW is made up from several smaller ones.

Further Nanowire Samples of Interest

Under certain growth conditions 'T' shape NW are formed on Si(001) as shown in figure 6.2. The 'T' shape NW may have a junction at the 'T' allowing a simple transistor mechanism to occur. Controlling the current flow along the NW by the use of the side branch would be an exciting development. The mechanism for this growth is not fully investigated and the structure of the side 'T' is not known.

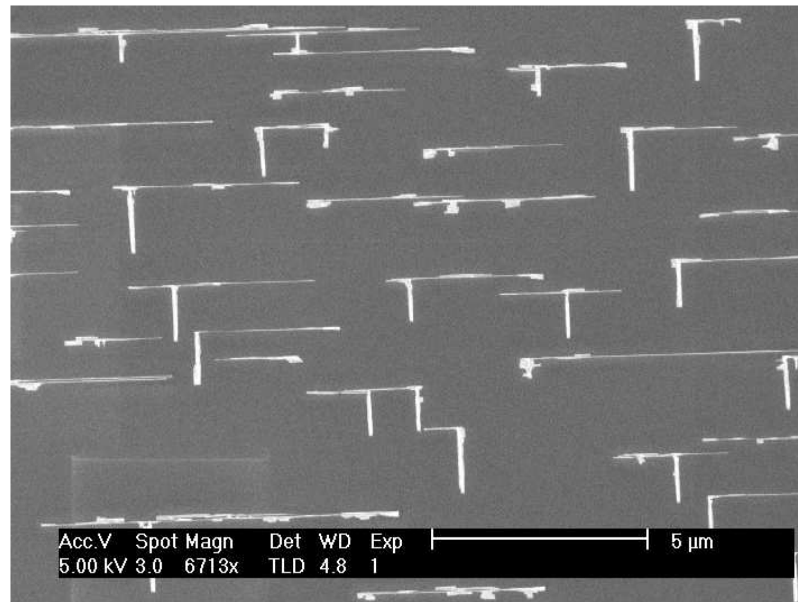

Figure 6.2: SEM image of $ErSi_2$ nanowires with side branches, a possible future sample for I/V measurement.

6.2 I/V Measurements

6.2.1 Tunnelling

Initially we found that the transport of NW in air was producing a very strong oxide layer. We measured some very distinct tunnel I/V curves, characterised by the sweeping 's' shape and the nA magnitude of the measured current. Using a theoretical tunnelling

curve discussed in section 2.4.5, we were able to match this with appropriate parameters showing a good fit by eye to tunnelling conditions. Figure 6.3 shows the experimental data and the tunnel expression plot using parameters of 1.37 nm for the oxide layer thickness, a barrier of 1.81 eV and an area of 9677 nm^2, which is a tip diameter of 111 nm. These values are very realistic for a tip contacting to an oxide layer. To overcome this problem, we developed vacuum transfer between York and Leeds using the vacuum suitcase.

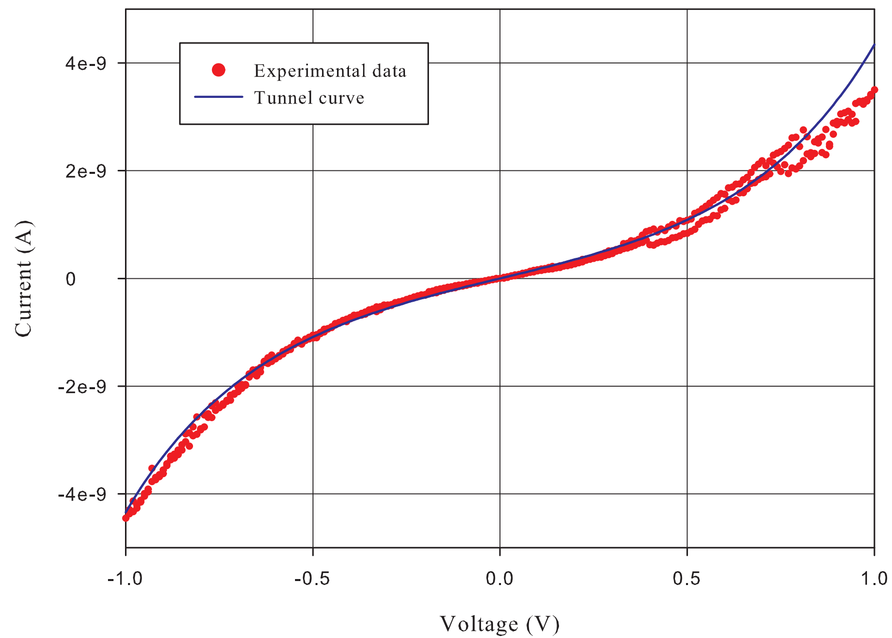

Figure 6.3: Oxidised NW sample I/V curve with tunnel plot.

6.2.2 I/V of the Nanowire-Silicon Interface

With the transfer now in vacuum, the contacts to the NW were much easier to maintain and repeatable I/V curves were produced. Making contact to the thin NW required sharp tips and careful control of the tip. The tips were approached onto the silicon surface where, with a small voltage applied, a few nAs flowed. Then by gently moving the tip over the NW, a jump in current to tens of nAs indicated a contact to the semimetal $ErSi_2$ NW. By taking an I/V curve between two tips, an idea of the tip contact to the NW could be obtained. Once a satisfactory ohmic contact had been achieved, an I/V measurement to the back of the substrate through the interface could then be made. Figure 6.4 shows the two tips positioned on a NW ready for I/V measurement.

The I/V curves obtained still have very gentle curves as shown in figures 6.5 and 6.6

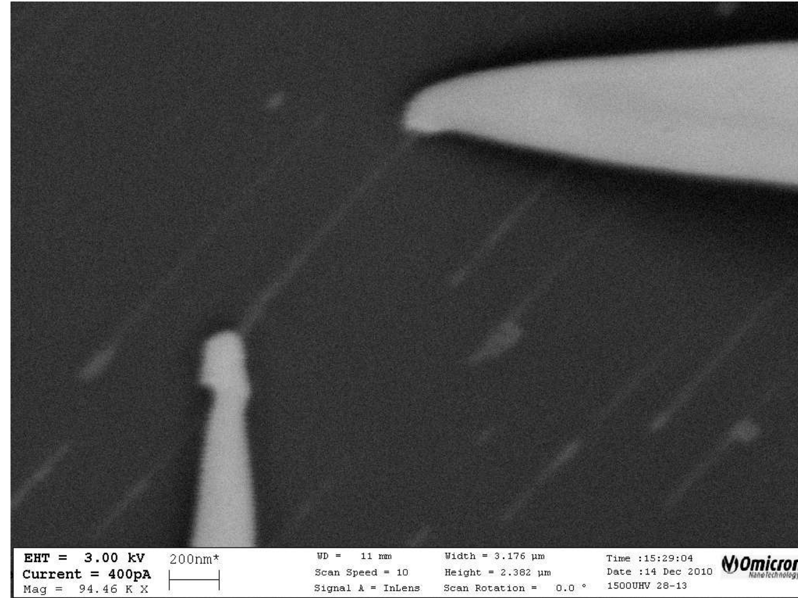

Figure 6.4: Nanoprobe SEM image of two tips contacted onto a NW ready to take an I/V measurement

which stems from tunnelling. This gentle curve is asymmetric with more current flowing with positive applied bias indicating there is a SB curve in addition to the tunnelling. These I/V curves are much more difficult to fit to due to the gentle curve from the tunnelling. By using a single SB and an oxide tunnel barrier in series it was possible to obtain a fit. The I/V curve in figure 6.5 produced a reasonable fit with a χ^2 value of 6.79$\times10^{-6}$ using an oxide tunnel barrier of 0.68 eV, a thickness of 1.5 nm and an area of 3.9$\times10^{-9}$ mm^2. The fitted SB gave values of 0.735 eV for the SBH, 0.716 eV for the effective SBH, with an area of 5.59$\times10^{-7}$ mm^2, series resistance of 4796 Ω and a shunt resistance of 111 MΩ.

The second NW produced the I/V curve in figure 6.6 where the ‘s’ shape is much more pronounced. This means the oxide tunnel barrier is dominating more with the voltage dropped over the SB very small. A fit was obtained with a χ^2 value of 1.44$\times10^{-6}$ using an oxide tunnel barrier of 0.61 eV, a thickness of 1.4 nm and an area of 3.4$\times10^{-11}$ mm^2. The SB gave values for the SBH of 0.621 eV, the effective SBH of 0.603 eV with an area of 5.48$\times10^{-7}$ mm^2, series resistance of 2 MΩ and a shunt resistance of 5 MΩ.

These two curves from different NW give SBH in the region of 0.62 to 0.73 eV which is higher than expected. SBH have been reported for $ErSi_2$ islands on n-Si(001) of 0.38 eV and on p-Si(001) of 0.67 eV,[132] for our NW on n-Si(001) a similar value was expected. The high SBH could be due to the contact not being completely on the NW and the SBH measured could be the tungsten tip-silicon SBH; however any test measurements taken

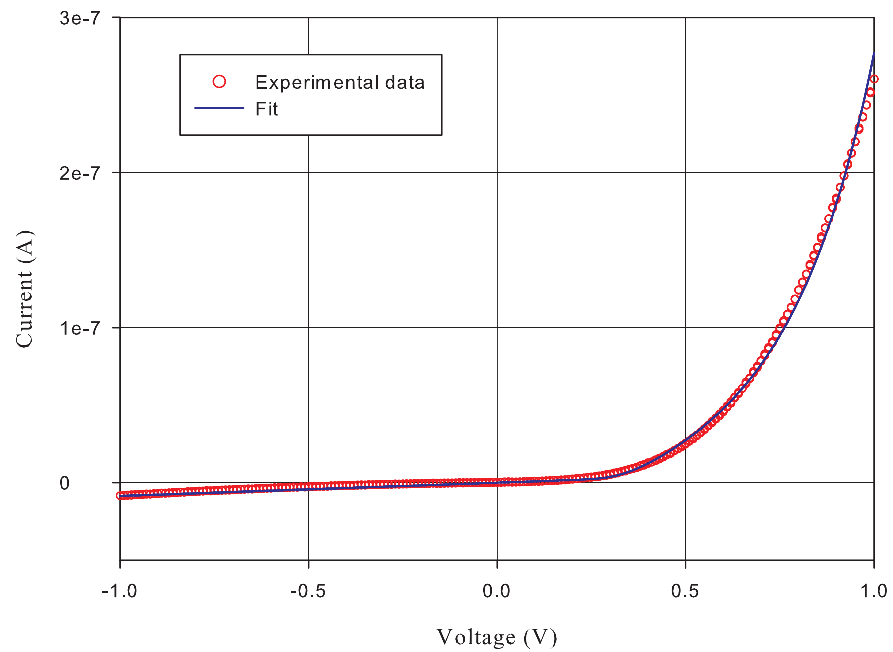

Figure 6.5: I/V curve from the $ErSi_2$ NW shown in figure 6.4, measured from a single tip and the silicon back contact.

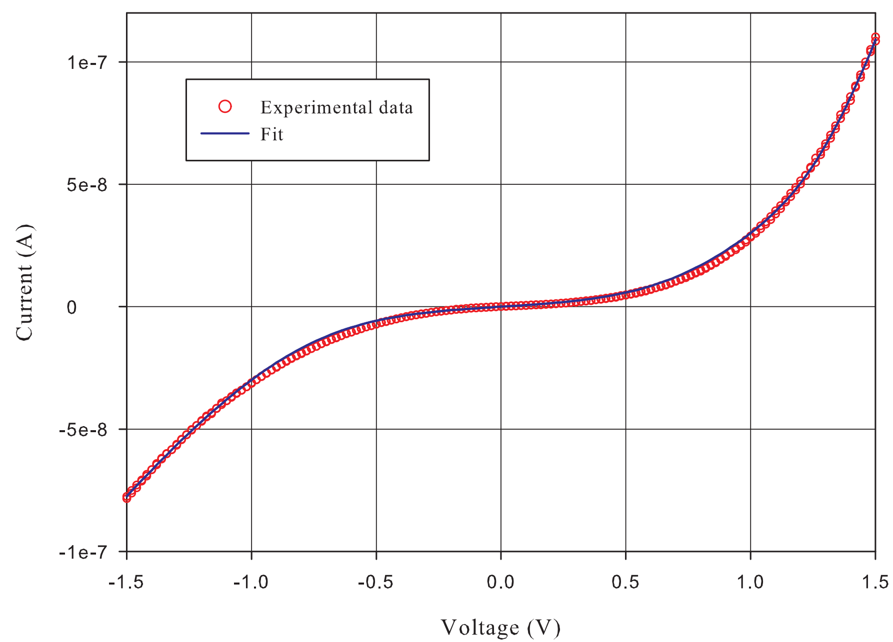

Figure 6.6: I/V curve from an alternative $ErSi_2$ NW measured from a single tip and the silicon back contact.

with a tip on the silicon surface produce very low currents in the order of nA and tend to have no current flowing in the forward bias regime. The SBH extracted using the fitting technique could be incorrect due to the tunnel barrier dominating the I/V curve. Although there is an asymmetry in the I/V curve, it is very difficult to fit a SB to this over the tunnel barrier. The model which we are using to fit to the data does not include tunnelling through the SB which for nanoscale objects has been seen to be more important, as discussed in Section 2.5. This could be a further reason why the fitting routine is struggling to find a solution with the expected SBH of $\sim$0.38 eV.

Note After Viva

Peripheral edge tunnelling caused by the crowding of field lines may be the cause of the slow turn on seen in the I/V curves and not an oxide tunnel barrier. This idea is discussed further in section 8.2.2.

6.2.3 I/V Along the Nanowire

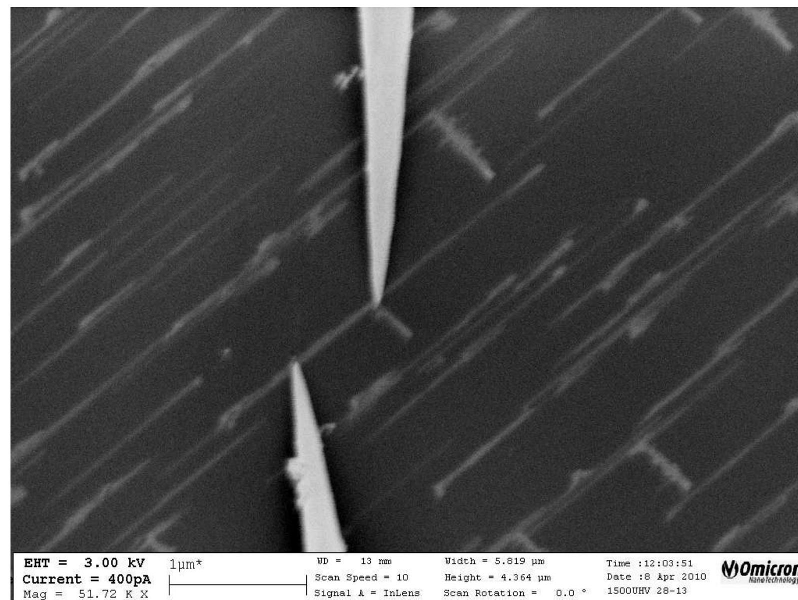

Figure 6.7: SEM image of two tips contacted to the NW to measure the I/V along the NW.

When two tips are contacted onto the same NW as shown in figure 6.7 an I/V curve can be taken along the NW. If there is a good contact, the NW gives an ohmic linear plot from which a resistance can be obtained. Due to the contacts being different for each tip contacted to each different NW, a range of resistances were measured from 16 MΩ to 24

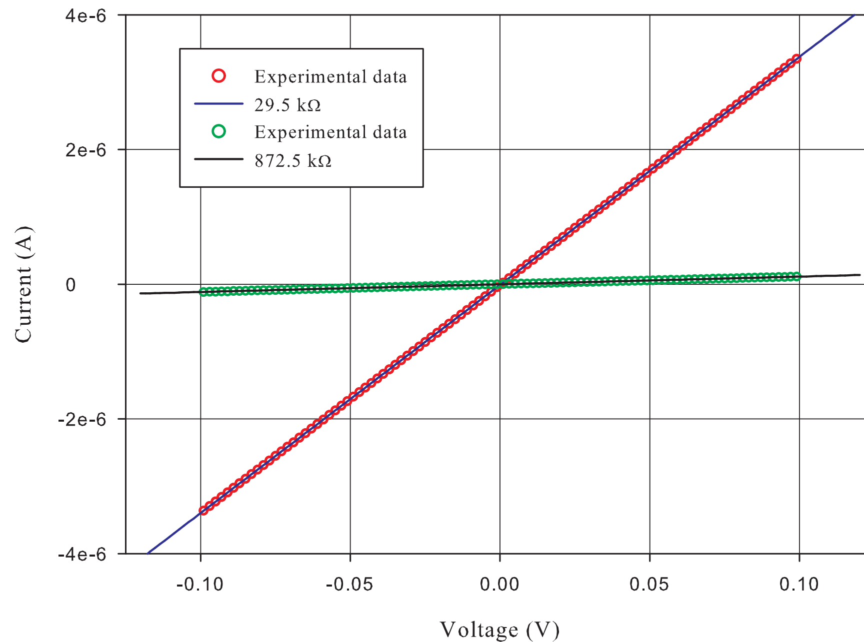

Figure 6.8: Example I/V taken along the NW with a linear fit to obtain the resistance.

kΩ. Figure 6.8 shows two I/V curves taken in this measurement geometry along the NW with the relevant resistances obtained from the least squares linear fit to the data.

Such a large difference in resistance cannot be explained by the difference in the cross sectional area or length between the individual NW's. It is expected the resistivity will be the same for each NW and for this to be the case the cross sectional area or length would need to be a factor of a thousand different to provide the range in resistance observed. Therefore the contact resistance must be affecting these results creating a very large spread in resistances along the wire. Comparing the two probe resistances along the NW to the previous series resistances of 4796 Ω and 2 MΩ, which were obtained from the fit to the SB measurement of the NW, it can be seen that the spread in resistance is similar. The large spread in both of these resistance values must also be related to the contact resistance. The large spread in the contact resistance could be due to an oxide layer or the fact many of these NW are bundles of individual wires. This means one tip could be in contact with a different wire compared to the second tip. The use of the 4° offcut silicon for the orientation of the NW causes the surface to be heavily stepped, meaning that a clear contact to the NW may be hindered by the terrace surface which the tip could be partially contacting. The use of a very sharp tip and a STM capable of high resolution scanning would enable a better positioning of the tip on the nanostructure.

To remove the contact resistance, a four-point probe method was attempted. This required locating four tips onto the NW and sourcing a current to the outer pair and measuring the voltage across the centre two tips. Unfortunately we could never keep all four tips in contact with the NW at the same time due to drift. Finally an unfortunate discharge from the external vacuum circuit ended the session rather catastrophically as shown in figure 6.9.

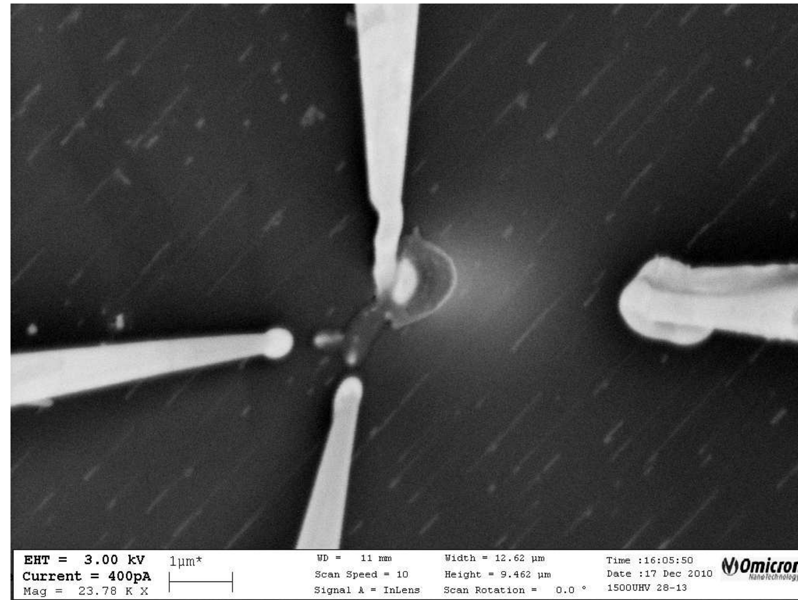

Figure 6.9: SEM image of the remains of four tips and the NW after a catastrophic discharge.

The result of this failed four-point probe measurement was the development at LENNF of a switch box to change the connections between the sourcemeter and the tips. Unfortunately this was not developed in time for a repeat of this very challenging measurement. This type of measurement requires the four tips to be as sharp as possible, less than 50 nm in diameter. The four tips all need to manoeuvred with as little drift as possible to contact to an object nm in width and almost flush with the surface, something which was very technically challenging.

6.3 Conclusion

These small dimension structures are more sensitive to oxidation than the previous $ErSi_2$ islands. Taking I/V measurements from nanowires has proved to be very challenging, with the following SBH extraction not straight forward. Any sample to be measured must be

kept in the best vacuum possible and the time between NW growth and I/V measurement minimised to reduce any oxidation effects. The extracted values from the fitting program and for the resistance measurements along the wire show that the contact resistance plays a big part in the I/V characteristics. The I/V curves required the addition of an oxide tunnel barrier to be able to achieve a reasonable fit, however this requires manually varying the oxide thickness to find the lowest χ^2 value. This is apparent from the two I/V curves which have quite different shapes and require a different thickness to get the best χ^2 value. The extracted SBH of 0.62 eV and 0.74 eV are higher than expected as a value around 0.4 eV would be comparable with the $ErSi_2$ island measurements.

The fitting routine handled these challenging samples very well after the addition of an oxide tunnel barrier. However the fitting routine does not contain any theory for nanoscale effects, such as enhanced tunnelling through the SB, which might be starting to occur in these samples, something for further development of the fitting program. Now improvements to the equipment at LENNF have been made, which it is hoped will stop any discharge, a repeat four-point probe measurement could be attempted to determine the resistivity of the NW. A sample such as this may benefit from hydrogen termination. Once the I/V measurement and SBH extraction is further developed the 'T' sample shown in figure 6.2 can be investigated. These NW samples can be grown much thinner, which would require a new approach to I/V collection utilising a Nanoprobe capable of high resolution STM and better stability.

Chapter 7

Metals on 2D Rare Earth Silicide

This chapter explores the use of a 2D RE silicide grown on n-type Si(111) as a buffer layer to transition metal growth, specifically manganese. A new growth study using erbium is presented, building on previous work done in the group at York using holmium. Preliminary I/V measurements have been taken from 10 ML of Mn deposited on the 2D Er silicide. Mn islands on the 2D Er silicide have been grown but could not be measured in the Nanoprobe as they proved too small to contact with a tip.

The requirement to inject a spin-polarised current into silicon for spintronics and create the appropriate spin-accumulation properties requires careful engineering of the metal semiconductor interface. To create a spin-polarised current, a ferromagnetic layer is required, for example iron. However, iron does not epitaxially grow on silicon as a pure metal because the interface forms iron-silicide, of which the majority of phases are non-magnetic. Iron growth on silicon can also form islands of iron silicide. One method to stop this silicide formation is a buffer layer between the silicon and the metal. It is also possible that this buffer layer can be used as a delta doped layer as proposed by Bratkovsky to modify the SB at the interface for spin accumulation to occur.[10]

7.1 Manganese on Ultra Thin Rare Earth Silicide

Although iron would seem the best ferromagnetic material to spin polarise electrons, it does not epitaxially grow on silicon. The growth of iron on silicon normally concludes in iron silicide formation, an area which has been extensively studied. Good epitaxial growth of Fe silicide can be achieved with the co-deposition of Fe and Si, producing a SBH of

~0.62 eV.[133] Manganese metal, on the other hand, has a closer lattice match to silicon, and therefore 2D RE silicide, compared to Fe, making manganese growth more preferable on a 2D RE silicide. Manganese is antiferromagnetic in the bulk; however, it is predicted to have a large magnetic moment in low dimensional structures such as thin films and islands grown on noble metals.[25,26] This large magnetic moment makes Mn an interesting possible material for spintronics.

Interest in Mn silicide is growing; theoretical studies in 2009 into Mn silicide on Si(001) show possible 50% spin polarisation,[134] and the idea of Mn growth on Si(111) for spintronics applications is being pursued.[135] Manganese clusters have been shown to self-order on Si(111) surface,[136] and when annealed above ~260 °C they form silicide islands.[137] An almost complete film of Mn silicide can be formed at coverages of 4 ML and annealing at 350 °C.[135,138] However, this study aims to grow pure Mn on a 2D Er silicide thin film to eradicate MnSi; this could possibly be extended to other transition metals enabling the Schottky barrier to be engineered.

Growing a well ordered Mn layer on Si(111) without annealing has not yet been achieved and any annealing will cause the silicide reaction to take place. The use of an ultra thin layer of 2D RE silicide as a buffer layer and the deposition of Mn at low temperatures has been shown to reduce the reaction of the Mn with the silicon.[139] Michael Reakes provides evidence in his thesis from MEIS depth profiling that the Mn layer is unreacted with silicon and sits on top of the Si bilayer of the 2D RE silicide layer.[140] The structure of the Mn layer and its magnetic properties are unknown at present but the process of growing Mn metal on top of silicon could have potential in spintronics. The use of the 2D RE silicide provides an important structural barrier between the Mn and silicon and also has the possibility of producing a SB interface suitable for spin injection.

7.2 Growth

To grow a sample of Mn on 2D RE silicide on silicon, several stages with different anneal temperatures encourage the best interface to form, reducing the Mn diffusion and reaction with the silicon substrate. This sample growth was developed by Michael Reakes and Chris Eames using the RE holmium,[139] whereas this study has shown that the more prominent RE, erbium, can also be used as the RE buffer layer. Holmium and erbium are almost identical, producing the same silicide structure with similar properties. There is a

slight difference in lattice constant at 298 K between $HoSi_2$ (3.8081 Å) and $ErSi_2$ (3.7971 Å) hence there is a difference in strain between the two silicides to the silicon substrate. Therefore some of the annealing temperatures had to be altered to allow for the change in strain and the different expansion coefficients.

7.2.1 Ultra Thin RE Silicide

After the n-type Si(111) substrate has been cleaned by outgassing and DC flashing to 1200 °C as described previously, achieving a 7×7 LEED pattern, the next stage is the growth of the 2D RE silicide, the structure of which was discussed in Section 5.1.1. The 2D RE silicide consists of 1 ML of RE sitting under a reverse buckled bilayer of silicon. The formation of a high quality epitaxial 2D RE silicide (one without defects or 3D islands) is vital to prevent Mn silicide formation, as the amount of exposed substrate Si is at a minimum.

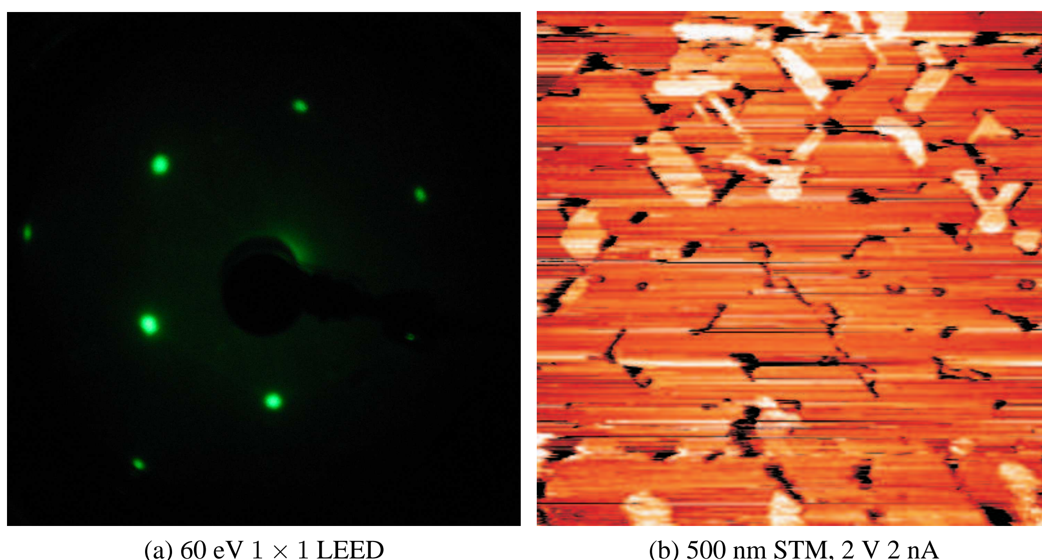

(a) 60 eV 1×1 LEED (b) 500 nm STM, 2 V 2 nA

Figure 7.1: 2D Er silicide on Si(111) a) 1×1 LEED image, b)500 nm STM scan at 2 V 2 nA.

The 2D Er silicide layer was formed by depositing 1 ML of Er in ∼12 minutes under RDE conditions of ∼520 °C. A further 10 minutes anneal at ∼520 °C before reducing to ∼400 °C for a final 10 minutes. The surface reconstruction was checked using LEED and showed a clear 1×1 pattern, shown in figure 7.1a. The sample was then scanned in the STM to assess how large an area was defect free. A 500 nm STM scan is shown in figure 7.1b, where the dark areas are holes in the 2D silicide surface and the bright islands are

the start of a 3D structure. The sample presented is not as defect free as originally aimed for due to the 3D islanding and the pinhole defects in the 2D silicide layer. Further growth studies maybe able to reduce the defect density; however, for this initial study this sample was taken to the next preparation stage.

Normally, 550 °C is considered the optimum temperature for the RE silicide formation, however the reduction in temperature to ∼520 °C was used to reduce the 3D island formation. At higher temperatures, as already seen in chapter 5, the RE silicide diffuses into islands of 3D which cannot be reversed. Figure 7.2 shows a sample of $ErSi_2$ grown at ∼550 °C where 3D islands are clearly present in the STM image, again as brighter islands. The darker holes in the STM image can be a reconstruction of the Si substrate, often 7×7. An indication of 3D island formation can be seen in the LEED pattern with the presence of extra $(\sqrt{3} \times \sqrt{3})R30^\circ$ spots to the expected 1×1 pattern, as shown in figure 7.2b.

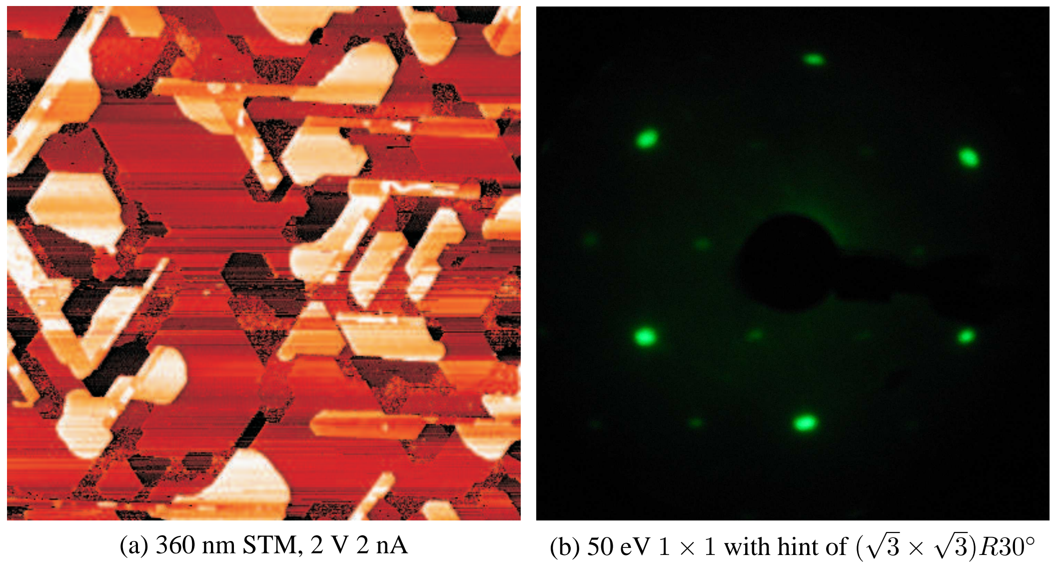

(a) 360 nm STM, 2 V 2 nA

(b) 50 eV 1×1 with hint of $(\sqrt{3} \times \sqrt{3})R30^\circ$

Figure 7.2: 2D Er silicide grown at 550 °C a) 360 nm STM scan at 2 V 2 nA showing in bright the formation of 3D islands, b) LEED image of the sample 1×1 with hint of $(\sqrt{3} \times \sqrt{3})R30^\circ$ indicating the presence of 3D growth.

The first hotter anneal is crucial to allow the Er to react with the Si, annealing at a lower temperature results in unreacted Er left on the surface. The final anneal at ∼400 °C is intended to reduce the lattice mismatch between the $ErSi_2$ and the Si(111) by exploiting their different thermal expansion coefficients. Once all the Er has reacted in the first stage, optimisation of the structure is done with this lower temperature anneal; by lowering the temperature, the two lattices can be made the same size because the thermal expansion of the disilicide is roughly three times that of the Si substrate.[141] The temperature of the final anneal was altered from the 350 °C used by Michael Reakes for the Ho silicide formation

due to the different thermal expansion coefficient of erbium silicide.

7.2.2 Manganese

Once a 2D Er silicide film has been achieved with as few defects as possible, as shown by LEED and STM, Mn can be deposited on top. The sample is first cooled using liquid nitrogen, stabilising over 2 hours at -185 °C, measured by the thermocouple on the manipulator arm a centimetre away from the sample. Depositing onto a cold surface reduces the mobility of the Mn prohibiting the reaction with Si. The deposition time of the Mn is kept as fast as possible to reduce any heating of the sample from the source. Finally, the sample is annealed at a low temperature (∼300 °C) for a short period of time (1 minute) to allow the Mn to order into a crystalline structure. The work by Reakes *et al* produced islands of Mn on the 2D Ho silicide with an average area of 42.8±1.95 nm^2 and with an average diameter of 7.6±0.34 nm.[139] For the measurement of I/V curves using the Nanoprobe, the islands of Mn need to be as large as possible, over 100 nm in diameter, so they can be seen in the SEM and the tips can make contact to them.

Mn Islands on RE Silicide

To try to increase the island size, the length or the temperature of the final anneal could be increased. Depositing 2 ML of Mn in ∼5 minutes onto the 2D $ErSi_2$ held at -185 °C with different annealing conditions produced the STM images in figure 7.3. Both of these samples produced a clear $(\sqrt{3} \times \sqrt{3})R30°$ LEED pattern shown in figure 7.3a.

Figure 7.3b shows the STM image of the sample with a post anneal of 300°C for 5 minutes. The Mn has formed into connected islands mainly along the edges of the 2D Er silicide which seems to have diminished in size. The holes in the 2D seem to be covered with small islands, possibly of Mn, which may have reacted with the surrounding Si hence the 2D decreasing in size.

Figure 7.3c shows the STM image of the sample with a post anneal of ∼400 °C for 2 minutes. This hotter anneal has caused the Mn to pull together into larger islands and again the underlying 2D silicide seems to have been affected with small islands of material. The hotter anneal and the disturbance of the 2D layer mean that the islands of Mn probably have undergone a reaction with the silicon and are now a mixture of Mn and Er silicides.

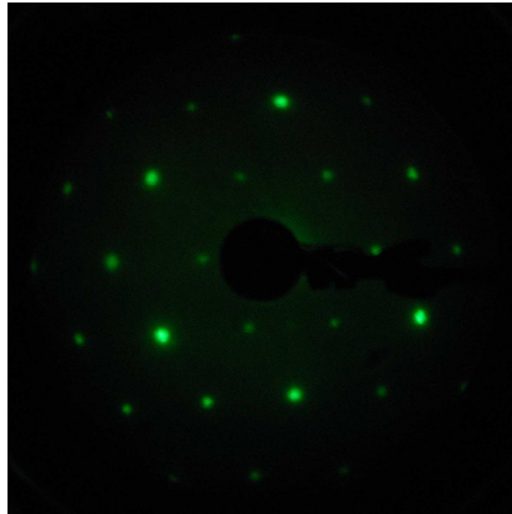

(a) 60 eV LEED $(\sqrt{3} \times \sqrt{3})R30^{\circ}$

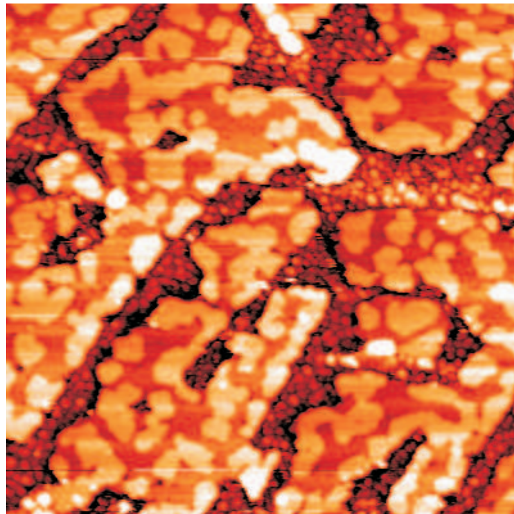

(b) 200 nm STM, 2 V 2 nA 2 ML Mn annealed at 300 °C for 5 minutes

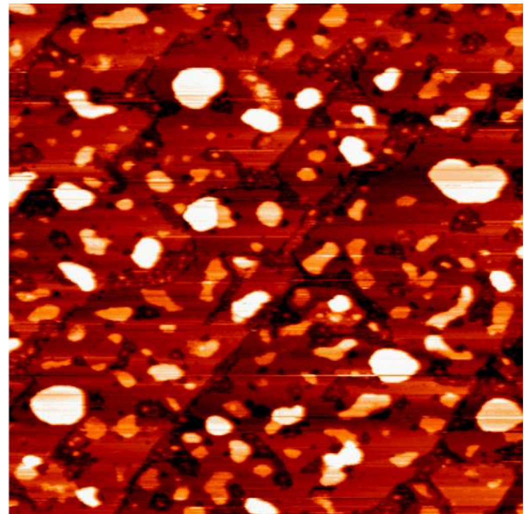

(c) 250 nm STM, 2 V 2 nA 2 ML Mn annealed at 400 °C for 2 minutes

Figure 7.3: Mn Islands on 2D RE Silicide. a) LEED image showing clear $(\sqrt{3} \times \sqrt{3})R30^{\circ}$, b) STM image 200 nm×200 nm of 2 ML Mn annealed at 300 °C for 5 minutes, c) STM image 250 nm×250 nm of 2 ML Mn annealed at 400 °C for 2 minutes.

The sample grown with the final anneal of 400 °C produced the biggest islands in the region of ∼20 nm diameter and 1 nm high. This sample was removed from vacuum and taken to LENNF to see if the surface could be imaged in the SEM. Because this sample was removed from vacuum, the Mn islands will have oxidised. The SEM image shown in figure 7.4 was obtained from the Nanoprobe, the ‘fuzzy blobs’ are assumed to be the oxidised Mn islands. Dr Walton from the LENNF facility expressed concern that the islands would be very challenging to see when the tips were in position and very hard to make contact to with a tip.

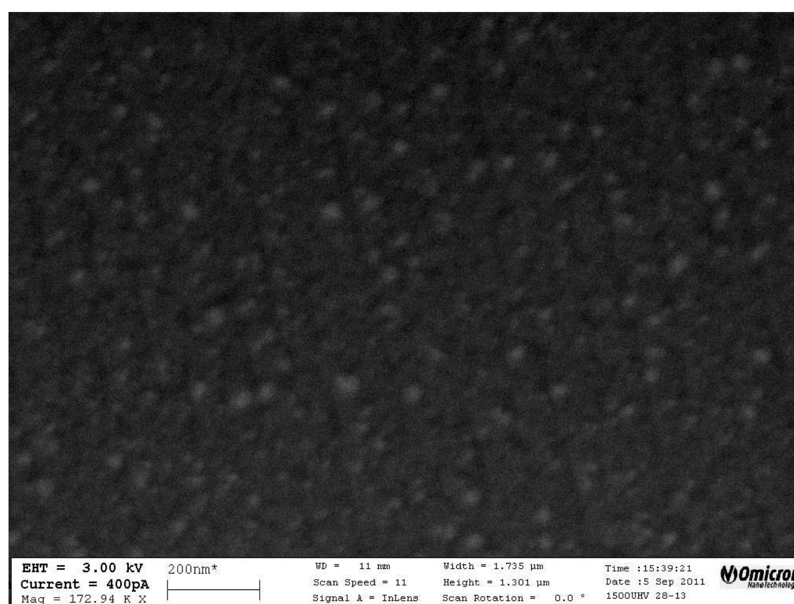

Figure 7.4: Nanoprobe SEM image of Mn Islands, the 20 nm ’fuzzy blobs’ are presumed to be the oxidised Mn islands.

Mn Film on RE Silicide

Due to the concerns of being able to probe the very small islands produced in the previous section, a second sample with a film of Mn on the 2D $ErSi_2$ was prepared.

10 ML of Mn were deposited in ∼10 minutes on to the 2D $ErSi_2$ at -185 °C before a post anneal at 300 °C for 2 minutes. This produced a fuzzy $(\sqrt{3} \times \sqrt{3})R30°$ LEED pattern shown in figure 7.5a indicating some order of the new surface. The STM image in figure 7.5b shows a flat terraced surface through the rather poor STM scanning due to contamination of the tip. The flat terraces are consistent with a higher coverage and what is expected. This sample was transferred to LENNF in the vacuum suitcase for I/V data collection.

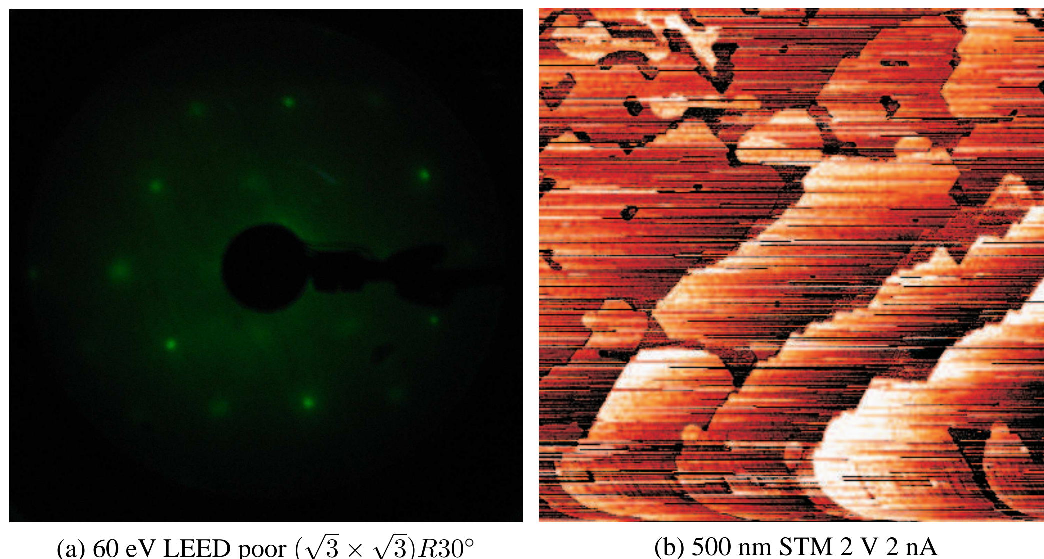

(a) 60 eV LEED poor $(\sqrt{3} \times \sqrt{3})R30°$ (b) 500 nm STM 2 V 2 nA

Figure 7.5: 10 ML Mn on 2D RE Silicide annealed at 300 °C for 2 minutes. a) LEED image showing the poor $(\sqrt{3} \times \sqrt{3})R30°$ from the Mn film surface, b) STM image 500 nm×500 nm of the Mn film.

After I/V data collection the Mn film on 2D $ErSi_2$ sample was returned in the vacuum suitcase to the STM chamber where it was capped with titanium. The sample was then prepared for TEM imaging by Jeremy Mitchell. TEM imaging of this showed the thin films to be heavily oxidised. This oxidation could have arisen from the time involved to transport the sample to LENNF and collect data and some of the oxidation could be due to the titanium capping process; however the harsh cross section preparation probably introduced a high proportion of the oxide damage.

7.3 I/V Measurements

The next challenge for these samples was to obtain an I/V curve and extract the SBH. The Mn island sample was used as a feasibility study for the Nanoprobe to find out if it could take data from such small structures even though the sample will have been oxidised by air during transport. The Mn film was straightforward to take I/V data from but presents some difficulties for the analysis as the inclusion of an oxide tunnel barrier was required.

7.3.1 Mn Islands

The manganese islands which were transported in air to be imaged in the Nanoprobe SEM shown in figure 7.4 could not be seen with an STM tip present under the SEM column. This meant the tip could not be positioned over a nanoisland. In an attempt to find an alternative way to contact a nanostructure, we took an STM image of the islands using the Nanoprobe. The image quality was poor as shown in figure 7.6a due to the sample being oxidised from transport in atmosphere, the quality of the tungsten tips and the stability of the system. Using the STM image, it was hoped that an island could be positioned in the bottom left hand corner where the tip returns to at the end of a scan, then the manual approach of the tip could continue as normal. To locate an island and then position the tip over the island requires minimal drift, which was not the case as drift of 200 nm or more was seen over a scan time of 15 minutes.

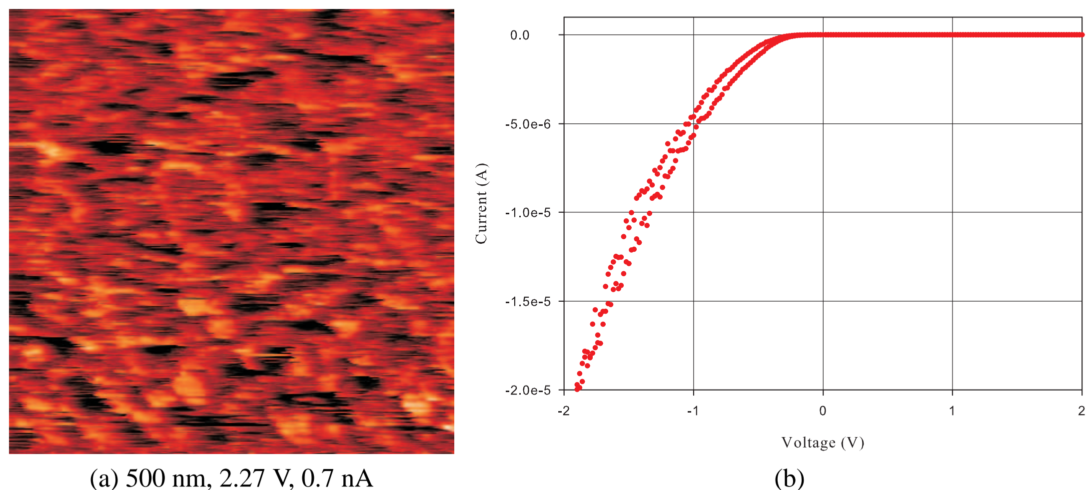

(a) 500 nm, 2.27 V, 0.7 nA (b)

Figure 7.6: Nanoprope data of oxidised Mn islands, a) 500 nm STM image taken using the Nanoprobe, b) I/V curve.

This approach to contact to the Mn islands was tried on a few islands with the same shape of I/V curve measured as shown in figure 7.6b for each attempt. This shape of I/V curve has been seen when the tungsten tip is in contact with silicon oxide. The contact is dominated by the back contact which has a very high shunt resistance so almost no current flows in the positive applied bias. It is not currently possible to fit to this type of curve using IV.x and due to the strong shunt resistance of the back contact, it is doubtful that the curve will contain any useful information about the SB, assuming contact to the Mn island has been achieved.

7.3.2 Mn Film

The manganese film deposited onto a 2D Er-silicide film was transported to LENNF in the vacuum suitcase. I/V data was taken from this sample at a few different locations on the surface with two different tips. Figure 7.7 shows an I/V curve taken from the Mn film. The forward bias of this curve is curved which is an indication of tunnelling. By adapting the fitting program IV.x to include one SB and one oxide tunnel barrier we were able to improve the χ^2 of the fit. We were only able to fit to the parameters for the oxide tunnel barrier of area and barrier height, so we conducted a search across oxide thickness values, finding that a realistic value of 1.5 nm gave the lowest χ^2 fit.

The fit using an oxide tunnel thickness of 1.5 nm is shown in figure 7.7, obtaining values of 1.095 eV for the SBH and 1.074 for the effective SBH over an area of 2.11 mm^2. The series resistance obtained was 117 kΩ, and a shunt resistance of 27 MΩ and an ideality factor of 1.01. The oxide tunnel barrier had a fixed thickness of 1.5 nm, an area of 9.56×10^{-7} mm^2 and a height of 1.05 eV. The fit has a χ^2 value of 5.37×10^{-4}. The tunnel barrier thickness parameter from this excellent fit was applied to the other I/V curves. The I/V curves taken using the same tip produced similar fits; however, the second tip data did not fit as well as shown in figure 7.8 and indicated by a χ^2 value of 0.104 compared to 5.37×10^{-4}. The experimental data obtained is a higher current and the fit does not fit very well at the turning point and at high reverse bias. The fit has increased the current flowing by decreasing the series resistance and increasing the area of the tunnel barrier, which has reduced the curve on the fit in forward bias. The fit is now almost straight in the forward bias which makes the turning point too sharp in the fit and in the wrong place, this in turn makes the reverse bias not fit closely to the experimental data.

The fit in figure 7.8 has fitted parameters with a χ^2 value of 0.104. The SBH is slightly reduced to 1.082 eV and 1.061 for the effective SBH over an almost identical area of 2.12 mm^2. The series resistance has been reduced to 79 kΩ and a shunt is identical at 27 MΩ and an ideality of 1.00. The oxide tunnel barrier area has altered a significant amount from 9.56×10^{-7} mm^2 to 5.01×10^{-2} mm^2, with only a slight change in height from 1.05 eV to 1.04 eV. The thickness cannot be fitted and is fixed at 1.5 nm. This significant change in the tunnel barrier area and the poor fit is an indication that for a different tip the oxide tunnel barrier is different. The oxide tunnel barrier between the tip and the Mn is likely to be different because of the individual shape of each tip. Each time a contact is made to

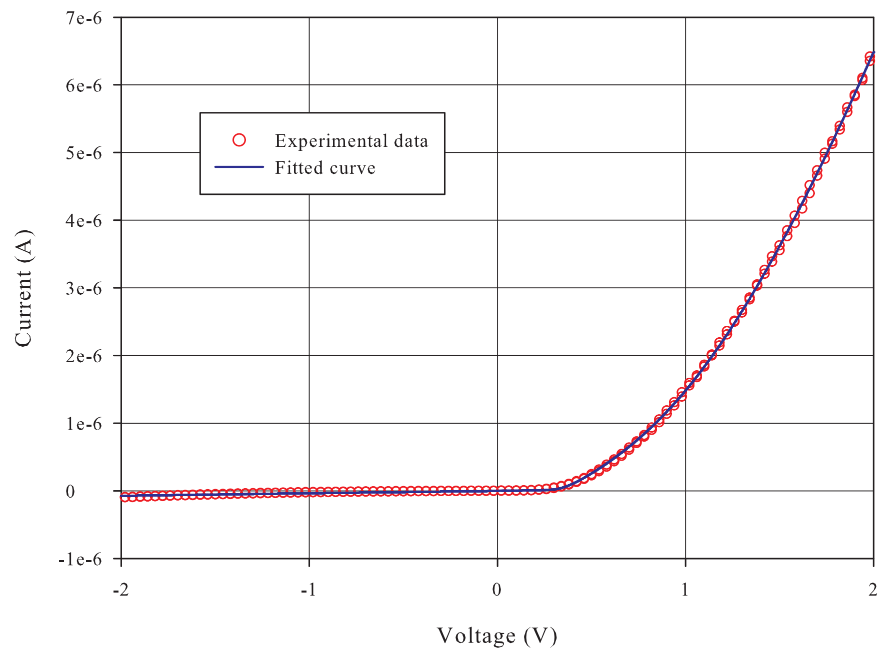

Figure 7.7: I/V data from a 10 ML Mn film on 2D Er Silicide on silicon. IV.x fit with optimised oxide tunnel barrier thickness of 1.5 nm.

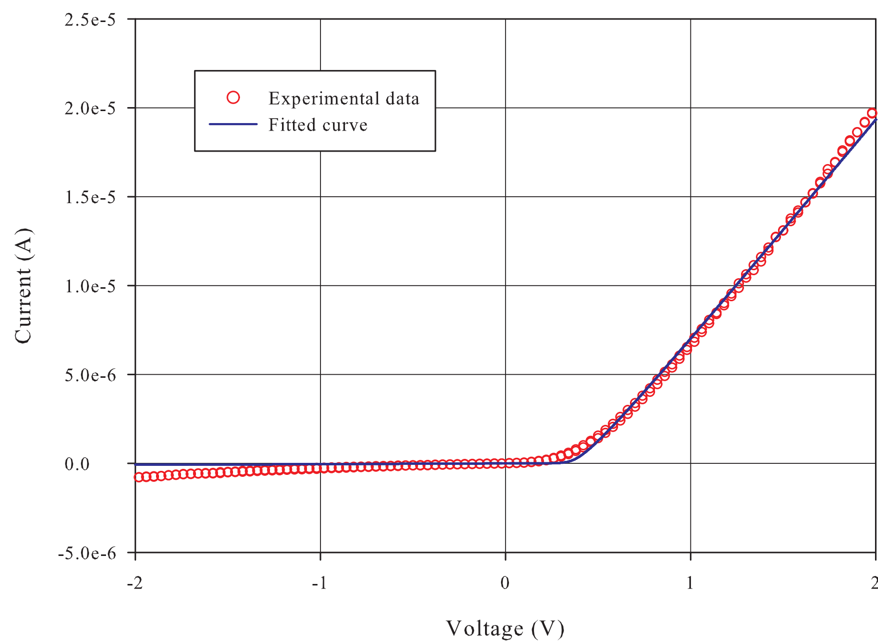

Figure 7.8: I/V data from a 10 ML Mn film on 2D Er Silicide on silicon taken with an alternative tip to figure 7.7 but using the same oxide tunnel parameter.

the surface, the amount of pressure applied by the tip may alter the thickness of the oxide layer, in turn altering the tunnel barrier and the contact resistance.

Altering Doping Concentration

As this sample was designed to use the 2D RE silicide layer to act as a delta doped layer, the doping concentration may not be that of the silicon (5×10^{21} m^{-3}). We ran several fits at different doping concentrations with no significant change in the χ^2 value. A change in the doping concentration from 10^{22} m^{-3} to 10^{24} m^{-3} only produced a decrease in the χ^2 of 1×10^{-6} and no noticeable change in the fitted curve. A concentration of 10^{25} m^{-3} obtained a slightly worse fit with an order of magnitude increase in the χ^2 value. The increase in doping concentration is expected to have little effect on the I/V curve as this only effects the image force lowering; however, if the doping concentration is high then tunnelling through the barrier has a higher probability, as the higher doping narrows the barrier. Altering the doping maybe more important if tunnelling through the barrier was included in the model.

7.4 Conclusion

The manganese samples were very challenging samples not only to grow, due to the extra steps in the growth procedure and careful control required of the temperature, but also to take I/V data from due to the island structure size and the oxidation of Mn. The growth of Mn on 2D erbium silicide has been shown to work in a similar manner to previous work done on $HoSi_2$ with slight alterations to the annealing temperatures. The Mn island size has successfully been increased to 20 nm diameter; however, the quality of the Mn islands is unknown at present.

These initial feasibility studies have shown that taking data from islands less than 100 nm in diameter using the Nanoprobe is very challenging because they cannot be imaged in the SEM or imaged with the STM. This is because the SEM resolution is limited by the long working distance of the column to allow access for the tips. Imaging is also hindered by the presence of the grounded tips, affecting the contrast of the image. To have more success at measuring islands on this scale, a more stable Nanoprobe would be required with higher resolution STM abilities to enable scanning of the islands. These Mn samples

are susceptible to oxidation over the course of transport to LENNF and a 24 hour delay between growth and I/V measurement. Ideally, to improve this the samples should be grown *in situ*. This has been shown by the requirement of an oxide tunnel barrier to fit the curve in the forward bias. Further evidence for the tunnel barrier has been gained from TEM imaging, showing that the sample is heavily oxidised. The analysis has shown the SBH of the manganese on 2D RE silicide to be $\sim$1.1 eV. This is a high value for the 2D RE silicide, which we would expect to be 0.4 eV and for the Mn where we would expect 0.67 eV.[142] This could be due to the oxide altering the structure or the growth, produced Mn and Er silicide. The program has very successfully fitted to these curves with the addition of an oxide tunnel barrier, however this assumption of the gentle curve being all from the oxide layer maybe altering the extracted SBH. The very gentle turn-on of the curve means it is hard to pin point the turn-on of the SB which may lead to a large error in the extracted SBH.

Chapter 8

Conclusions and Further Work

8.1 General Conclusions

This work sets out to measure the Schottky barriers of low dimensional structures to further the development of spintronics. This work has demonstrated that the quality of the interface affects the Schottky barrier and more so, the contacts to the sample affect the measured I/V curve. The effect of the contacts plays a key role in the shape of the I/V curve and ultimately how well the parameters can be extracted. Combining already existing standard SB theory in the development of a new fitting routine allowed the I/V curves to be fitted with confidence. The fitting routine was tested using $NiSi_2$-silicon(111) samples and then modified in the light of findings. This allowed us to learn how the fitting program operated and when to realise the outcomes were not realistic. This gave confidence in the program before work on $ErSi_2$ low dimensional structures was undertaken.

8.1.1 Development of IV.x, the Fitting Routine

The graphical fitting methods developed by Norde and Werner and used in this thesis, have shown that series and shunt resistances are important in the extraction of the SBH. These methods although producing an acceptable result for the SBH are confined to only using a handful of data points on the I/V curve, this is where the strength of a computational fitting routine shows. Although for the test case, the newly developed fitting routine, IV.x gave very similar results to the Werner graphical plots, we can have much more confidence in the computational fitted values because the whole curve is utilised. The new fitting routine IV.x includes, the series and shunt resistances, image force lowering of the barrier and

tunnelling through the barrier, when it is under reverse bias. The latter two are additional theory to what is used in the graphical fitting methods. The program can fit to two SBH, two areas, two ideality factors, two shunt resistances and the series resistance. The routine is capable of handling two barriers and has been used with two back-to-back SBs and also in the configuration of one SB and an oxide tunnel barrier. When the oxide tunnel barrier replaces one of the SB the area and tunnel barrier are fitted instead, the oxide thickness cannot be varied by the fitting program. This addition of the oxide tunnel barrier enabled much of the fitting to contacts where the I/V curve had been affected by the tip contact oxide layer. The fitting routine has proved to be very robust and produces fitted parameters for the majority of curves. However, the tests taught us how to interpret these results and recognise that not all I/V curves are from a well ordered contact. For example, when a large ideality factor or an unrealistic area are obtained these values should be questioned, as this identifies a possible poorly formed interface. The fitting routine does not remove the need to inspect the experimental I/V curve and the obtained fit to this data.

8.1.2 Nickel Silicide on Si(111)

The growth of $NiSi_2$ as a test material for the fitting routine required the fast deposition rate of the MBE system. However, no evidence for the growth of the A-type interface orientation was seen, it is assumed that these samples were either B-type or a mixture of both orientations. This is supported by the extracted SBH for these samples being more consistent with the expected B-type value. The samples grown to be B-type orientations were more successful, with the fitting routine obtaining values for the SBH of 0.816 ± 0.016 eV with an effective SBH of 0.797 ± 0.016 eV which agrees with the value of 0.79 eV previously reported by Tung.[20]

8.1.3 Erbium Silicide on Si(111)

The growth of thick, 10 ML $ErSi_2$ masked dots produced a pinhole crazed surface. This inhomogeneous surface produced some striking results in the form of a reproducible hysteresis, with the shunt resistance and the SBH being the main changes between the curves. This sample highlights the difficulties of understanding the properties of the interface when the structure is not well ordered.

Self assembled islands of $ErSi_2$ were grown on Si(111) producing a better structure. These demonstrated the Nanoprobe technique of collecting I/V from low dimensional structures. These samples also highlighted the importance of the back contact to the sample. This needs to be an ohmic contact or a very leaky Schottky barrier if the SBH of the island-silicon interface is to be extracted. The islands of $ErSi_2$ gave an average SBH of 0.45 ± 0.09 eV. The temperature variation provided a very successful test not only for the Nanoprobe but for the fitting routine as well. The fitting program does not fit to temperature but allows the measured temperature from the experiment to be input. This set of data taken over a temperature range of 179 K to 321 K showed an almost constant SBH with an average of 0.45 ± 0.03 eV which corresponds closely to previously reported values of 0.39 eV. The Van der Pauw sheet resistance measurement for the $ErSi_2$ island obtained a value of 2874 ± 21 Ω/sq and a resistivity of between $2.87 - 5.75 \times 10^{-4}$ Ωcm assuming the thickness of the island is between 1 and 2 nm respectively. As expected for a low dimensional structure this is a higher value than that for bulk $ErSi_2$ of 3.4×10^{-5} Ωcm.

8.1.4 Erbium Silicide Nanowires on Si(001)

The smaller the structure to be probed, the more sensitive to oxidation it becomes. This caused a big problem for the NW samples and the I/V curves were only fitted using an oxide tunnel barrier in addition to a SB. These samples tested the Nanoprobe to its limit, to achieve four sharp tips in contact with the same NW. The SBHs extracted from the I/V curves for these NW samples were 0.62 eV and 0.74 eV, although not unreasonable for a transition metal, the SBH of these NW were expected to be similar to the $ErSi_2$ islands of 0.39 eV. These SBHs maybe higher than expected due to the oxide tunnel barrier smearing out the position of the SB turn-on. These NW are also made up from bundles of wires which might be having an effect on the SBH.

8.1.5 Manganese on Ultra Thin Erbium Silicide on Si(111)

The growth of manganese on a 2D layer of $ErSi_2$ has been shown to be possible with an average island diameter of $\sim$20 nm. These however, require a new technique to obtain I/V curves from as the Nanoprobe was unsuccessful in imaging the islands in the SEM. This is because the working distance of the Nanoprobe SEM is long to allow space for the tips underneath the column; the tips also alter the contrast reducing the resolution of the

instrument. The use of a film of Mn on 2D $ErSi_2$ could be used as a buffer layer, however, preliminary results show the SBH to be surprisingly high at 1.1 eV indicating that the sample is not as well ordered as intended and possible tunnelling effects are altering the extracted SBH measurement.

Using an oxide tunnel barrier to fit to the gentle turn-on of these and previous I/V curves has enabled a better fit judged by the χ^2 value. However it should be noted that for the manganese samples and the NW samples the SBH has been larger than expected. This could be due to the fitting program not finding the real turn-on of the SB, because it has been smeared out by the tunnel characteristics. This could be exaggerated by the fact the program can not fit to the oxide tunnel thickness.

8.2 Further Work

8.2.1 Instrument and Technique Development

The fitting program IV.x has proved to be very robust with the I/V curves that we have fitted. However allowing the fitting program to fit to the thickness of the oxide tunnel barrier would enable us to investigate if the SBHs are high due to the incorrect choice of oxide thickness or because the information is not accessible from the I/V curve. If this can be answered and an oxide tunnel barrier is not a hindrance to the fitting process, the next steps would be to expand the program to fit a back-to-back SB and a oxide tunnel barrier. The next major addition to the fitting program would be the ability to handle inhomogeneous SB. This would allow us to revisit some of the data that we suspect is from an inhomogeneous interface. The transport mechanism of tunnelling though the SB has not been included for the forward bias regime; this would be another future addition. To be able to achieve this the theory would need to be revisited to ensure that the different sections of theory mesh together and double turning points do not arise, as did for the image force lowering. This tunnelling behaviour would be necessary for the inclusion of nanoscale theories, to deal with the enhanced tunnelling through the SB in low dimensional structures. The addition of other nanoscale effects, such as barrier lowering, would enable a better interpretation of the NW samples.

The Nanoprobe has been a very successful tool in collecting high quality I/V data and the vacuum transfer has been invaluable. However some of the samples have still shown

oxidation which might be reduced further if the samples were prepared in situ, minimising the time between growth and measurement. The Nanoprobe struggles with very small structures, especially when the SEM cannot image them satisfactorily because there are four tips under the lens. One option is to develop a new system where an atomic resolution STM was able to image a sample and then be taken into contact. This currently cannot be done in one of the systems in York due to the in-vacuum amplifiers which limit the current that can be supplied to the tip.

8.2.2 Note After Viva - Peripheral Tunnelling

Steve Wilks the external examiner bought to the attention of the author the idea of enhanced peripheral edge tunnelling which could explain the soft turn on of the SB. A brief mention of tunnelling being more prominent in nanostructures was mentioned in section 2.5. At the edge of a metal contact on a semiconductor the field lines become more crowded enabling tunnelling to become an easier transport channel. As the diode contact is shrunk the edge has a higher contributing factor compared to the inside area, hence this effect becomes noticeable. This effect could explain the characteristics seen in the majority of curves taken from low dimensional islands and nanowires in this thesis. It was felt that edge tunnelling is more important than the oxide tunnelling already used. The idea to include forward tunnelling into the fitting program with the addition to allow enhanced peripheral tunnelling should now be a priority for the development of the program.

8.2.3 Future Experiments

This project has opened up the area of research at York into low dimensional Schottky barrier measurement tackling the instruments and techniques needed to obtain high quality I/V measurements. The SBH extraction from the obtained I/V curves is also a challenge but the consolidation of several theories into a new fitting routine has provided a reliable way to analysis the curves.

If the model was capable of fitting to I/V curves from inhomogeneous samples, the analysis could be redone on the $NiSi_2$ samples, to obtain a more satisfactory solution to the A-type samples and the 1000 μm dots. To satisfactorily complete the $NiSi_2$ further growth of A-type samples would be required to obtain samples of pure A-type orientation.

This could be identified by the use of LEED-IV, to look at the structural fingerprint of the $NiSi_2$-Si interface. This would be possible to further validate with some cross sectional TEM work on the samples. All the work presented on $NiSi_2$ has been on Si(111), whereas there is published work on Si(100) which reports a difference of 0.25eV between the SBH of $NiSi_2$ on Si(100) and A-type orientation $NiSi_2$ on Si(111), this could be another test experiment for the fitting routine.

The work on $ErSi_2$ islands could be extended to other RE metals. If a technique to measure small structures using an STM is developed and the islands are grown with smaller dimensions the size effects maybe observable. The size effects might include the lowering of the SBH as the diameter of the island decreases below the distance the depletion region extends into the silicon or enhanced tunnelling though the barrier. Further temperature measurements could be also be carried out.

The Si(001) NW samples have a large promise for further work as little is known about their conductivity and if any junctions exist between different section widths. Again, different RE metals could be tried and then the NW could be reduced in size to remove the possible bundling. This would increase the chances of knowing what the structure of the NW is. Now the Nanoprobe has the addition of the switch box which should remove the risk of electrical discharge at the tips, a return to take a four point probe measurement along the NW would be possible. This would measure the resistance of the wire without the presence of the contact resistance. Finally the 'T' shaped NW could hold some interesting physics if there is a SB between the main NW and the side arm. The side arm may enable the conductance of the main nanowire to be changed by the application of an electric field.

The islands of Mn on 2D $ErSi_2$ on Si(111) require a technique to measure such small objects. If the successful measurement of the I/V can be made from these structures the idea of using the 2D RE layer as a delta doped layer can be assessed. Not only could this type of structure alter the SB of the contact and be engineered for spintronic applications but the prevention of the transition metal reacting with the silicon could have other technological applications. To see if the RE has worked as a buffer layer, TEM imaging of the interface would identify if any mixing has occurred between the silicon and the manganese. If this was possible the growth investigation could be extended to other transition metals on ultra thin RE layers.

Appendix A

Transport to LENNF

Figure A.1: Mini Adventure - Transport for the vacuum suitcase with the samples studied in this thesis.

Appendix B

The Vick's " Chocolate Stuff "

Ingredients

4 oz	Hard margarine
1.5 tbsp	Golden syrup
1 dsp	Sugar
1 dsp	Cocoa powder
2 dsp	Drinking chocolate
2 oz	Raisins
0.5 lb	Rich tea biscuits

Chocolate to cover

Method

- Melt margarine, golden syrup and sugar in a large saucepan
- Add cocoa powder and drinking chocolate to the pan
- Crush rich tea biscuits
- Add biscuits and raisins to the pan; stir well
- Put mixture into a pre-greased dish and squash to form a flat surface
- Allow to cool then pour melted chocolate over the top
- Allow to cool then cut into squares
- Enjoy

List of Abbreviations

BEEM . . . . . . Ballistic Electron Emission Microscopy
BEES . . . . . . Ballistic Electron Emission Spectroscopy
DC . . . . . . Direct Current
DFT . . . . . . Density Functional Theory
FE . . . . . . Field Emission
GMR . . . . . . Giant Magnetoresistance
I/V . . . . . . Current-Voltage
LEED . . . . . . Low Energy Electron Diffraction
LENNF . . . . . . Leeds Nanoscience and Technology facility
MBE . . . . . . Molecular Beam Epitaxy
MEIS . . . . . . Medium Energy Ion Scattering
ML . . . . . . Monolayer
MS . . . . . . Metal-Semiconductor
MSM . . . . . . Metal-Semiconductor-Metal
NW . . . . . . Nanowire
QCM . . . . . . Quartz Crystal Microbalance
RDE . . . . . . Reactive Deposition Epitaxy
RE . . . . . . Rare Earth
RHEED . . . . . . Reflection High Energy Electron Diffraction
SB . . . . . . Schottky Barrier
SBH . . . . . . Schottky Barrier Height
SEM . . . . . . Scanning Electron Microscopy
SPM . . . . . . Scanning Probe Microscopy
STM . . . . . . Scanning Tunnelling Microscope
STS . . . . . . Scanning Tunnelling Spectroscopy

TEM . . . . Transmission Electron Microscope

TFE . . . . Thermionic Field Emission

TSP . . . . Titanium Sublimation Pump

UHV . . . . Ultra High Vacuum

WKB . . . . Wentzel Kramers Brillouin

List of Symbols

A^* .... Richardson constant for semiconductors
A^{**} ...... Modified Richardson constant
d .... Distance over which the conduction band drops kT/q
E .... Energy
E_0 .... Defined by equation 2.22
E_{00} ...... Defined by equation 2.20 property of bulk semiconductor for tunnelling
E_c .... Bottom of conduction band energy in a semiconductor
E_F .... Fermi level energy
E_F^m ...... Fermi level energy of a metal
E_F^s .... Fermi level energy of a semiconductor
E_g .... Band gap energy
E_m .... Energy at which there is a maximum contribution from TFE electrons
E_v .... Top of valence band energy in a semiconductor
$\mathscr{E}$ .... Electric field in a Schottky barrier
F .... Attractive force
h .... Planck's constant 6.62617×10^{-34} J-s
$\hbar$ .... Planck's constant divided by 2π
I .... Electrical current
I_0 .... Saturation current
I_d .... Current through the Schottky barrier (Diode)
I_f .... Thermionic emission forward current
I_p .... Current through the shunt resistor R_{shunt}
J_s .... Saturation current density
k .... Boltzmann constant 1.38066×10^{-23} J/K
l .... Mean free path of an electron

m .... Electron rest mass 9.1095×10^{-31} kg

m^* .... Effective mass

n .... Ideality factor

n_0 .... Equilibrium density of electrons in the interior of the semiconductor

n_e .... Density of electons in the depletion region of the semiconductor

N_c .... Effective density of states in the conduction band

N_d .... Donor density

p .... Density of holes in the valence band of the semiconductor

p_s .... Equilibrium density of holes immediately adjacent to the interface

P .... Probability

PE ...... Potential energy

q .... Unit of charge 1.60218×10^{-19} C

R_{series} .... Series resistance

R_{shunt} .... Shunt resistance

S .... Area of Schottky barrier contact

S_i .... Area of the ith patch of the Schottky barrier contact

T .... Temperature, K

V .... Applied voltage

V_d .... Diffusion potential

V_{d0} .... Diffusion potential at zero applied bias

V_r .... Reverse bias applied voltage

w .... Width of the depletion region

w_i .... Thickness of insulating layer

x .... Distance from interface

x_m .... Maximum Schottky barrier height position

β .... $= \partial\phi_e/\partial V = 1 - 1/n$

ΔE ...... Energy less than the top of the barrier

$\Delta\phi_{bi}$ ..... Image force lowering of the Schottky barrier

$(\Delta\phi_{bi})_0$ ... Image force lowering of the Schottky barrier at zero applied bias

$\Delta\phi_F$ ..... Image force lowering under forward bias

$\Delta\phi_R$ ..... Image force lowering under reverse bias

ε_0 .... Permittivity in vacuum 8.85418×10^{-14} F/cm

ε_r .... Relative permittivity (For Si taken as 11.68)

ε_s .... Semiconductor permittivity ($\varepsilon_r\varepsilon_0$)

ξ .... Energy difference between E_F^s and E_c

ρ .... Net charge density

ϕ_b .... Schottky barrier height

ϕ_{b0} .... Schottky barrier height at zero applied voltage

ϕ_e .... Effective Schottky barrier height

ϕ_i .... Schottky barrier height of the ith patch

ϕ_m .... Metal work function

ϕ_s .... Semiconductor work function

ϕ_t .... Tunnel barrier height

χ_s .... Semiconductor electron affinity

ψ .... Electrostatic potential

Bibliography

1. Bland, T., Lee, K., and Steinmuller, S. *Physics World* **21**(January), 24–28 (2008).

2. Awschalom, D. D. and Flatté, M. E. *Nature Physics* **3**, 153–159 March (2007).

3. Žutić, I., Fabian, J., and Das Sarma, S. *Reviews of Modern Physics* **76**(2), 323–410 April (2004).

4. Gregg, J. F., Petej, I., Jouguelet, E., and Dennis, C. *Journal of Physics D: Applied Physics* **35**(18), R121–R155 September (2002).

5. Gregg, J., Allen, W., Viart, N., and Kirschman, R. *J. Magn. Magn.* **175**, 1–9 (1997).

6. Hagele, D., Oestreich, M., Ruhle, W. W., Nestle, N., and Eberl, K. *Applied Physics Letters* **73**(11), 1580 (1998).

7. Xu, Y. and Thompson, S., editors. *Spintronic materials and technology*. Taylor and Francis, (2007).

8. Jansen, R. *Nature physics* **3**, 521 August (2007).

9. Dash, S. P., Sharma, S., Patel, R. S., de Jong, M. P., and Jansen, R. *Nature* **462**(7272), 491–4 November (2009).

10. Bratkovsky, A. M. *Reports on Progress in Physics* **71**(2), 026502 February (2008).

11. Osipov, V. and Bratkovsky, A. M. *Physical Review B* **70**(20), 1–6 November (2004).

12. Bonet, C., Scott, I. M., Spence, D. J., Wood, T. J., Noakes, T. C. Q., Bailey, P., and Tear, S. P. *Physical Review B* **72**(16) (2005).

13. Eames, C., Reakes, M., Tear, S., Noakes, T., and Bailey, P. *Physical Review B* **82**(17), 1–9 November (2010).

14. Perkins, E. W., Scott, I. M., and Tear, S. P. *Surface Science* **578**(1-3), 80–87 (2005).

15. Pratt, A., Woffinden, C., Bonet, C., and Tear, S. *Physical Review B* **78**(15), 155430 October (2008).

16. Wood, T., Bonet, C., Noakes, T., Bailey, P., and Tear, S. *Surface Science* **598**(1-3), 120–127 December (2005).

17. Thompson, S. *Journal of Physics D: Applied Physics* **41**(9), 093001 May (2008).

18. Duke, C. *Chemical Reviews* **96**(4), 1237–1260 (1996).

19. Fujitani, H. and Asano, S. *Physical Review B* **51**(24), 18019 (1995).

20. Tung, R. T. *Physical Review Letters* **52**(6), 461–464 (1984).

21. Min, B.-C., Motohashi, K., Lodder, C., and Jansen, R. *Nature Materials* **5**(10), 817–822 October (2006).

22. Baglin, J., DHeurle, F., and Petersson, C. *Applied Physics Letters* **36**(7), 594–596 (1980).

23. Netzer, F. *Journal of Physics: Condensed Matter* **7**, 991 (1995).

24. Chen, Y., Ohlberg, D., Medeiros-Ribeiro, G., Chang, Y. A., and Williams, R. S. *Applied Physics Letters* **76**(26), 4004 (2000).

25. Blugel, S. *Physical Review Letters* **68**(6), 851–854 (1992).

26. Wuttig, M., Gauthier, Y., and Blugel, S. *Physical Review Letters* **70**(23), 3619–3622 (1993).

27. Rhoderick, E. and Williams, R. *Metal-Semiconductor Contacts*. Clarendon Press, 2nd edition, (1988).

28. Zangwill, A. *Physics at Surfaces*. Cambridge University Press, (1988).

29. Kaye, G. and Laby, T. *Tables of Physical and Chemical Constants*. Longman, 15th edition, (1986).

30. Baker, B., Johnson, B., and Maire, G. *Surface Science* **24**(2), 572–586 (1971).

31. Sze, S. *Physics of Semiconductor Devices*. John Wiley and Sons, 2nd edition, (1981).

32. Kaiser, W. and Bell, L. *Physical Review Letters* **60**(14), 1406 September (1988).

33. Palm, H., Arbes, M., and Schulz, M. *Physical Review Letters* **71**(14), 2224–2227 (1993).

34. Sirringhaus, H., Meyer, T., Lee, E., and von Känel, H. *Physical Review B* **53**(23), 15944–15950 June (1996).

35. Tung, R. T. *Materials Science and Engineering Reports* **35**(1-3), 1–138 (2001).

36. Crowell, C. and Sze, S. *Solid-State Electronics* **9**(11-12), 1035–1048 November (1966).

37. Crowell, C. *Solid-State Electronics* **8**(4), 395–399 (1965).

38. Andrews, J. and Lepselter, M. *Solid-State Electronics* **13**(7), 1011–1023 (1970).

39. Padovani, F. and Stratton, R. *Solid-State Electronics* **9**(7), 695–707 (1966).

40. Crowell, C. and Rideout, V. L. *Solid-State Electronics* **12**(2), 89–105 February (1969).

41. McLean, A., Dharmadasa, I., and Williams, R. *Semiconductor Science and Technology* **1**, 137 (1986).

42. Tung, R. *Physical Review B* **45**(23), 13509 (1992).

43. Sullivan, J. P., Tung, R. T., Pinto, M. R., and Graham, W. R. *Journal of Applied Physics* **70**(12), 7403 (1991).

44. Sze, S., Coleman Jr, D., and Loya, A. *Solid-State Electronics* **14**(12), 1209–1218 (1971).

45. Zhang, Z. Y., Jin, C. H., Liang, X. L., Chen, Q., and Peng, L.-M. *Applied Physics Letters* **88**(7), 073102 (2006).

46. Zhang, Z., Yao, K., Liu, Y., Jin, C., Liang, X., Chen, Q., and Peng, L.-M. *Advanced Functional Materials* **17**(14), 2478–2489 September (2007).

47. Wiesendanger, R. *Scanning Probe Microscopy and Spectroscopy*. Cambridge University Press, (1994).

48. Simmons, J. *Journal of Applied Physics* **34**(6), 1793–1803 (1963).

49. Simmons, J. *Journal of Applied Physics* **34**(9), 2581–2590 (1963).

50. Smit, G. D. J., Rogge, S., and Klapwijk, T. M. *Applied Physics Letters* **80**(14), 2568 (2002).

51. Smit, G. D. J., Rogge, S., and Klapwijk, T. M. *Applied Physics Letters* **81**(20), 3852 (2002).

52. Ruffino, F., Grimaldi, M. G., Giannazzo, F., Roccaforte, F., and Raineri, V. *Applied Physics Letters* **89**(24), 243113 (2006).

53. Appenzeller, J., Radosavljević, M., Knoch, J., and Avouris, P. *Physical Review Letters* **92**(4), 2–5 January (2004).

54. Kubo, O., Shingaya, Y., Aono, M., and Nakayama, T. *Applied Physics Letters* **88**(23), 233117 (2006).

55. Brihuega, I., Dupont-Ferrier, E., Mallet, P., Magaud, L., Pons, S., Gómez-Rodríguez, J., and Veuillen, J.-Y. *Physical Review B* **72**(20), 1–7 November (2005).

56. Dupont-Ferrier, E., Mallet, P., Magaud, L., and Veuillen, J.-Y. *Physical Review B* **75**(20), 1–5 May (2007).

57. Song, J., Ding, T., Li, J., and Cai, Q. *Surface Science* **604**(3-4), 361–365 February (2010).

58. Osvald, J. *Semiconductor Science and Technology* **20**(6), 611–614 June (2005).

59. Mönch, W. *Applied Physics A* **87**(3), 359–366 (2007).

60. Tung, R. T. *Journal of Vacuum Science and Technology B* **11**(4), 1546–1552 (1993).

61. Nakayama, T., Sotome, S., and Shinji, S. *Microelectronic Engineering* **86**(7-9), 1718–1721 July (2009).

62. Ohdomari, I., Kuan, T., and Tu, K. *Journal of Applied Physics* **50**(11), 7020–7029 (1979).

63. Wood, T. J., Bonet, C., Noakes, T. C. Q., Bailey, P., and Tear, S. P. *Physical Review B* **73**(23) (2006).

64. Prutton, M. *Introduction to Surface Physics*. Oxford Science Publications, (1994).

65. Woodruff, D. and Delchar, T. *Modern Techniques of Surface Science*. Cambridge University Press, (1988).

66. Davisson, C. and Germer, L. *Nature* **119**(2998), 558–560 (1927).

67. Binnig, G., Rohrer, H., Gerber, C., and Weibel, E. *Physical Review Letters* **49**(1), 57–61 (1982).

68. Binnig, G., Rohrer, H., Gerber, C., and Weibel, E. *Physical Review Letters* **50**(2), 120–123 January (1983).

69. Goldstein, J., Newbury, D., Joy, D., Lyman, C., Echlin, P., Lifshin, E., Sawyer, L., and Michael, J. *Scanning Electron Microscopy and X-Ray Microanalysis*. Springer, 3rd edition, (2003).

70. Chambers, A., Fitch, R., and Halliday, B. *Basic Vacuum Technology*. IOP Publishing, 2nd edition, (1998).

71. Tung, R. T. *Journal of Vacuum Science and Technology A* **5**(4), 1840–1844 (1987).

72. Van der Pauw, L. *Philips Technical Review* **20**(8), 220–224 (1958).

73. Williams, D. and Carter, C. *Transmission Electron Microscopy: A Textbook for Materials Science 4 vol. set*. Springer, (1996).

74. Tung, R. T., Levi, A., Sullivan, J. P., and Schrey, F. *Physical Review Letters* **66**(1), 72–75 (1991).

75. Liehr, M., Schmid, P., LeGoues, F., and Ho, P. *Physical Review Letters* **54**(19), 2139–2142 (1985).

76. Tung, R. T., Ng, K., Gibson, J., and Levi, A. *Physical Review B* **33**(10), 7077 (1986).

77. Vrijmoeth, J., Van der Veen, J., Heslinga, D., and Klapwijk, T. *Physical Review B* **42**(15), 9598 (1990).

78. Ospelt, M., Henz, J., Flepp, L., and von Kanel, H. *Applied physics letters* **52**(3), 227–229 (1988).

79. Hauenstein, R. J., Schlesinger, T. E., McGill, T. C., Hunt, B. D., and Schowalter, L. J. *Applied Physics Letters* **47**(8), 853–855 (1985).

80. Das, G., Blöchl, P., Andersen, O., Christensen, N., and Gunnarsson, O. *Physical review letters* **63**(11), 1168–1171 (1989).

81. Fujitani, H. and Asano, S. *Physical Review B* **42**(3), 1696 (1990).

82. Ossicini, S., Bisi, O., and Bertoni, C. *Physical Review B* **42**(9), 5735–5743 (1990).

83. Fujitani, H. and Asano, S. *Physical Review B* **50**(12), 8681 (1994).

84. Matthai, C., Rees, N., and Shen, T. *Applied Surface Science* **56-58**, 525–530 (1992).

85. Woodruff, S., Dellas, N., Liu, B., Eichfeld, S., Mayer, T., Redwing, J., and Mohney, S. *Journal of Vacuum Science and Technology B* **26**(4), 1592 (2008).

86. Alptekin, E. and Ozturk, M. C. *Microelectronic Engineering* **87**(11), 2358–2360 November (2010).

87. Cherns, D., Anstis, G., Hutchison, J., and Spence, J. *Philosophical Magazine A* **46**(5), 849 August (1982).

88. Vlieg, E., Fischer, A., Van der Veen, J., Dev, B., and Materlik, G. *Surface Science* **178**(1-3), 36–46 (1986).

89. Robinson, I., Tung, R., and Feidenhans'l, R. *Physical Review B* **38**(5), 3632 (1988).

90. Yang, W., Jona, F., and Marcus, P. *Physical Review B* **28**(12), 7377 (1983).

91. Tung, R. T. and Gibson, J. *Journal of Vacuum Science and Technology A* **3**(3), 987–991 (1985).

92. Tung, R. T. *Materials Chemistry and Physics* **32**, 107–133 (1992).

93. Tung, R. T. *Journal of Vacuum Science and Technology A* **7**(3), 598–605 (1989).

94. Tung, R. T., Gibson, J., and Poate, J. *Physical Review Letters* **50**(6), 429–432 (1983).

95. Tung, R. T. *Journal of Vacuum Science and Technology B* **2**(3), 465–470 (1984).

96. Norde, H. *Journal of Applied Physics* **50**(7), 5052 (1979).

97. McLean, A. *Semiconductor Science and Technology* **1**, 177 (1986).

98. Sato, K. and Yasumura, Y. *Journal of Applied Physics* **58**(9), 3655–3657 (1985).

99. Werner, J. H. *Applied Physics A Solids and Surfaces* **47**(3), 291–300 November (1988).

100. Biber, M., Güllü, O., Forment, S., Meirhaeghe, R. L. V., and Türüt, A. *Semiconductor Science and Technology* **21**(1), 1–5 January (2006).

101. Asubay, S., Güllü, O., and Türüt, a. *Vacuum* **83**(12), 1470–1474 August (2009).

102. Tu, K., Thompson, R., and Tsaur, B. *Applied Physics Letters* **38**(8), 626–628 (1981).

103. Norde, H., de Sousa Pires, J., DHeurle, F., Pesavento, F., Petersson, S., and Tove, P. *Applied Physics Letters* **38**(11), 865–866 (1981).

104. Knapp, J. and Picraux, S. *Applied Physics Letters* **48**(7), 466–468 (1986).

105. Thompson, R., Tsaur, B., and Tu, K. *Applied Physics Letters* **38**(7), 535–537 (1981).

106. Rogero, C., Polop, C., Magaud, L., Sacedón, J., de Andrés, P., and Martin-Gago, J. *Physical Review B* **66**(23), 235421 December (2002).

107. Bonet, C., Spence, D., and Tear, S. *Surface Science* **504**, 183–190 (2002).

108. Duverger, E., Palmino, F., Ehret, E., and Labrune, J. *Surface Science* **595**(1-3), 40–48 December (2005).

109. Perkins, E., Bonet, C., and Tear, S. *Physical Review B* **72**(19), 195406 November (2005).

110. Lohmeier, M., Huisman, W., ter Horst G, Zagwijn, P., Vlieg, E., Nicklin, C., and Turner, T. *Physical Review B* **54**(3), 2004–2009 July (1996).

111. Eames, C., Woffinden, C., Probert, M. I., Tear, S. P., and Pratt, A. *Surface Science* **604**(7-8), 686–691 April (2010).

112. Wetzel, P., Pirri, C., and Gewinner, G. *EPL (Europhysics Letters)* **38**(5), 359 (1997).

113. Kitayama, H., Tear, S., Spence, D., and Urano, T. *Surface Science* **482**, 1481–1486 (2001).

114. Reckinger, N., Tang, X., Bayot, V., Yarekha, D. a., Dubois, E., Godey, S., Wallart, X., Larrieu, G., aszcz, A., Ratajczak, J., Jacques, P. J., and Raskin, J.-P. *Applied Physics Letters* **94**(19), 191913 (2009).

115. Preinesberger, C., Vandré, S., Kalka, T., and Dähne-Prietsch, M. *Journal of Physics D: Applied Physics* **31**(9), L43 (1998).

116. Bowler, D. R. *Journal of Physics: Condensed Matter* **16**(24), R721–R754 June (2004).

117. Ragan, R. *Journal of Crystal Growth* **251**(1-4), 657–661 April (2003).

118. Chen, Y., Ohlberg, D., and Williams, R. S. *Journal of Applied Physics* **91**(5), 3213 (2002).

119. Chen, Y., Ohlberg, D., Li, X., Stewart, D. R., Stanley Williams, R., Jeppesen, J. O., Nielsen, K. a., Stoddart, J. F., Olynick, D. L., and Anderson, E. *Applied Physics Letters* **82**(10), 1610 (2003).

120. Collier, C., Mattersteig, G., Wong, E., Luo, Y., Beverly, K., Sampaio, J., Raymo, F., Stoddart, J., and Heath, J. *Science* **289**(5482), 1172 August (2000).

121. Collier, C., Wong, E., Belohradskỳ, M., Raymo, F., Stoddart, J., Kuekes, P., Williams, R., and Heath, J. *Science* **285**(5426), 391 July (1999).

122. Nogami, J., Liu, B., Katkov, M., Ohbuchi, C., and Birge, N. *Physical Review B* **63**(23), 1–4 May (2001).

123. Ohbuchi, C. and Nogami, J. *Physical Review B* **66**(16), 1–6 October (2002).

124. Yeom, H., Takeda, S., Rotenberg, E., Matsuda, I., Horikoshi, K., Schaefer, J., Lee, C., Kevan, S., Ohta, T., Nagao, T., and Hasegawa, S. *Physical Review Letters* **82**(24), 4898–4901 June (1999).

125. Zeng, C., Kent, P. R. C., Kim, T.-H., Li, A.-P., and Weitering, H. H. *Nature Materials* **7**(7), 539–42 July (2008).

126. Shinde, A., Wu, R., and Ragan, R. *Surface Science* **604**(17-18), 1481–1486 August (2010).

127. Liu, B. *Surface Science* **540**(1), 136–144 August (2003).

128. Cai, Q., Yang, J., Fu, Y., Wang, Y., and Wang, X. *Applied Surface Science* **190**(1-4), 157–160 May (2002).

129. Cai, Q. and Zhou, W. *Journal of Physics: Condensed Matter* **16**(39), 6835–6840 October (2004).

130. Ma, C. L., Picozzi, S., Wang, X., and Yang, Z. Q. *The European Physical Journal B* **59**(3), 297–303 November (2007).

131. Yang, J., Cai, Q., Wang, X.-D., and Koch, R. *Surface and Interface Analysis* **36**(2), 104–108 February (2004).

132. Jun, M., Kim, Y., Choi, C., Kim, T., Oh, S., and Jang, M. *Microelectronic Engineering* **85**(5-6), 1395–1398 May (2008).

133. Hamaya, K., Ueda, K., Kishi, Y., Ando, Y., Sadoh, T., and Miyao, M. *Applied Physics Letters* **93**(13), 132117 (2008).

134. Hortamani, M., Sandratskii, L., Kratzer, P., and Mertig, I. *New Journal of Physics* **11**(12), 125009 December (2009).

135. Kumar, A., Tallarida, M., Hansmann, M., Starke, U., and Horn, K. *Journal of Physics D: Applied Physics* **37**(7), 1083–1090 April (2004).

136. Wang, H. and Zou, Z.-Q. *Applied Physics Letters* **88**(10), 103115 (2006).

137. Nagao, T., Ohuchi, S., Matsuoka, Y., and Hasegawa, S. *Surface science* **419**(2-3), 134–143 (1999).

138. Evans, M., Glueckstein, J., and Nogami, J. *Physical Review B* **53**(7), 4000–4004 February (1996).

139. Reakes, M. B., Eames, C., and Tear, S. P. *Journal of physics: Condensed matter* **21**(26), 265001 July (2009).

140. Reakes, M. B. *The Effect of Cooling on the Growth of Rare Earth Silicides on Silicon and the Growth of Overlayers on 2D Ho Silicide Studied using MEIS and STM*. PhD thesis, University of York, (2010).

141. Yang, J., Rawn, C., Ji, C.-X., Chang, Y., Chen, Y., Ragan, R., Ohlberg, D., and Williams, R. *Applied Physics A* **82**(1), 39–42 November (2005).

142. Eizenberg, M. and Tu, K. *Journal of Applied Physics* **53**(10), 6885–6890 (1982).